UNIVERSITY OF WISCONSIN
DEPARTMENT OF METEOROLOGY

OBSERVED HODOGRAPHS
(TOTAL OF 412 PROFILES)

REDUCED HODOGRAPHS
AND THERMAL WINDS

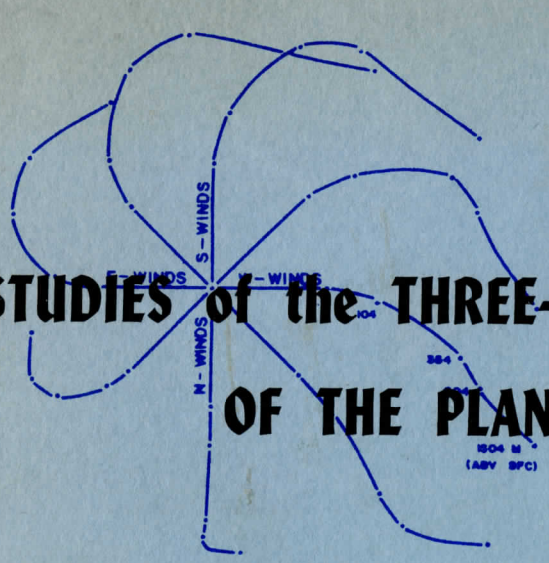

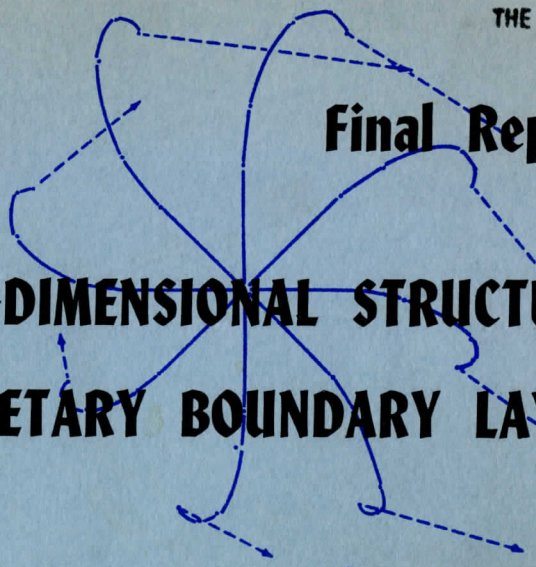

Final Report

STUDIES of the THREE-DIMENSIONAL STRUCTURE OF THE PLANETARY BOUNDARY LAYER

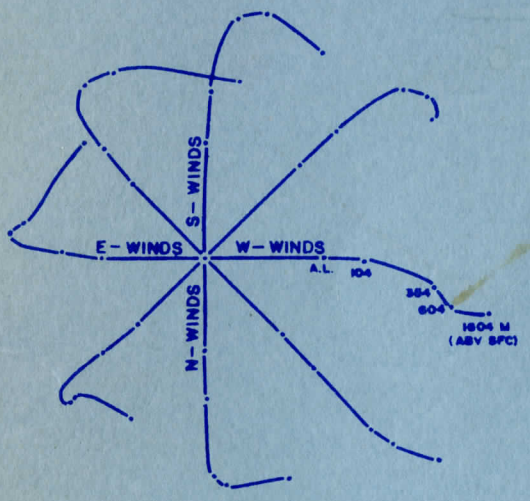

Heinz H. Lettau
PROJECT SUPERVISOR

Contributions by:
JOHN A. DUTTON
HARRY L. HAMILTON, Jr.
WARREN B. JOHNSON, Jr.
DONALD H. LENSCHOW
JAMES K. SPARKMAN, Jr.
CHARLES R. STEARNS
ARLIN B. SUPER

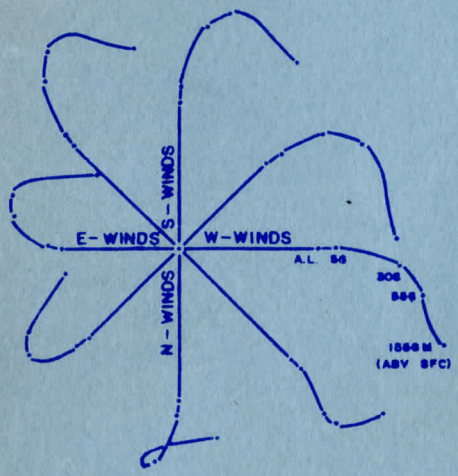

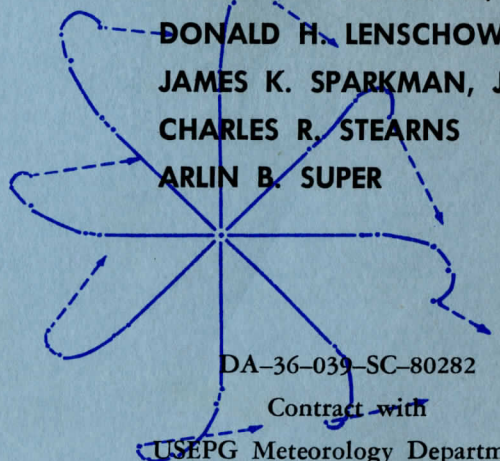

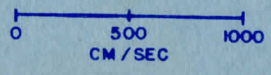

DA-36-039-SC-80282
Contract with
USEPG Meteorology Department
Fort Huachuca, Arizona

Madison, October 1962

UNIVERSITY OF WISCONSIN
DEPARTMENT OF METEOROLOGY

Final Report

STUDIES of the THREE-DIMENSIONAL STRUCTURE OF THE PLANETARY BOUNDARY LAYER

Heinz H. Lettau
Project Supervisor

Contributions by:

John A. Dutton
Harry L. Hamilton, Jr.
Warren B. Johnson, Jr.
Donald H. Lenschow
James K. Sparkman, Jr.
Charles R. Stearns
Arlin B. Super

DA-36-039-SC-80282
Contract with
USEPG Meteorology Department
Fort Huachuca, Arizona

Madison, October 1962

Scanner's note:

This page is blank.

TABLE OF CONTENTS

Page

List of Illustrations v

1. General Introduction - Heinz H. Lettau 1

2. Micrometeorological Installation on Lake Mendota - Charles R. Stearns 7

3. Spatially Continuous Measurements of Temperature Profiles Through an Air-Water Interface - Harry L. Hamilton, Jr. 47

4. Preliminary Report on an Optical Method for Low-Level Lapse Rate Determination - James K. Sparkman, Jr. 69

5. An Airborne Measuring System for Micrometeorological Studies - John A. Dutton and Donald H. Lenschow 81

6. Technique and Results of Surface-Temperature Determinations with an Airborne Bolometer - Donald H. Lenschow 99

7. Climatology of Atmospheric Boundary-Layer Parameters and Energy Dissipation, Derived from Gregg's Aerological Survey of the U. S. - Warren B. Johnson, Jr. 125

8. Equiangular Wind and Current Spirals - Heinz H. Lettau . . . 159

9. Case Studies of Dynamical Interactions at an Air-Water Interface - Arlin B. Super 173

10. Notes on Theoretical Models of Profile Structure in the Diabatic Surface Layer 195

Index of Distribution 227

Scanner's note:

This page is blank.

LIST OF ILLUSTRATIONS

Page

Section 1

Fig. 1 Richardson number in the 80 to 40 cm layer of air above an artificial roughness field of constant obstacle density (one bushel basket per 0.5 m^2 of snow surface), as a function of obstacle-color in the presence of solar heating. Results of experiments on the frozen surface of Lake Mendota, on 3 April 1962 4

Section 2

Fig. 1 Map of Lake Mendota with location of tower and instrument building 10

2 Enlarged map showing Second Point of Lake Mendota with location of tower, Lake Lab buoy, and instrument building (shack) 10

3 Diagram of lake tower 11

4 Vertical diagram of lake tower 12

5 Arrangement of electrical boxes on lake tower 12

6 Wind direction circuits 16

7 SCS cup anemometer counting circuit. 16

8 Construction details of Thornthwaite anemometers . . . 18

9 Anemometer counting circuit and power supply. 18

10 Winter installation of anemometers 20

11 Summer installation of anemometers 20

12 Thermistor power supply 22

13 Basic thermistor circuit 22

14 E_s/E_i versus temperature for thermistors 24

15 Diagram of air temperature equipment 24

List of Illustrations

Page

[Section 2]

Fig. 16 Close-up of temperature profile equipment 26

17 Details of construction of temperature profile equipment . 26

18 Wave detector mounting 28

19 Wave detector circuits 28

20 View of ice block drag detector 30

21 Drag recorder strain gauge mounting at ice block . . . 30

22 Strain-gauge bridge circuit 32

23 Power supply for strain-gauge bridge 32

24 Calibration system for ice block drag measurements . . 34

25 Amplifier input and output at tower 34

26 Tower switch power supply and trigger 36

27 Monostable multivibrator for read-out of digital voltmeter . 36

28 Layout of DVM translator 40

29 DVM translator read-out system 40

30 Read-out of time and wind data 41

31 Method used to prevent double punches on key punch and electric typewriter. 41

32 Operation of key punch and typewriter 42

33 Time switch and card selection 42

34 Method of triggering read-out of time, wind data, and digital voltmeter 44

35 Power supply for delivering 35 vdc pulse to read-out onto cards and typewriter 44

List of Illustrations

Page

Section 3

Fig. 1 Electrical circuitry 50

2 Radiation shields and thermocouples 52

3 Logarithmic profiles as a function of z_0, plotted linearly versus height (z) 58

4 A single downsweep of the sensor, taken at 2: 12 pm on September 9, 1961. 60

5 A downsweep and upsweep of the sensor, taken from 2: 34 to 2: 37 pm on September 9, 1961 60

6 A single downsweep of the sensor, taken at 2: 40 pm on October 21, 1961 62

7 Two downsweeps of the sensor, from 3: 23 to 3: 29 pm on October 21, 1961 64

8 Two downsweeps of the sensor, from 3: 29 to 3: 35 pm on October 21, 1961 64

9 Observed profile from Fig. 7. Smooth curve from Fig. 3, for z_0 = 0.0001 cm 65

10 Two and one-half downsweeps of the sensor, taken at 11: 11 am on November 4, 1961 66

11 Three downsweeps of the sensor, between 9: 27 and 9: 36 pm on November 4, 1961 66

Section 4

Fig. 1 "Looming and stooping" in the air over the ice of Lake Mendota. The almost-undistorted photograph of the boathouse (left) was taken at 09: 18 a.m., 27 March 1962, the other at 03: 00 p.m., 26 March 1962, under conditions of light wind (1 mph) and strong inversion. Exposure time, 1/20 and 1/15 sec, respectively, using film Plus-X, ASA 160. Note the changes in relative position of the lake edge and boathouse, compared with the near target. 74

List of Illustrations

Page

Section 5

Fig. 1 Boom mounted on front of the airplane with net radiometer extending to the right, and the differential pressure ports extending at the tip 86

2 Instrument installation in the rear of the cockpit . . . 88

3 Geometry of the turbulence probe and its motions with respect to space (absolute) and the air (relative) . . . 92

4 The power spectra of turbulent vertical velocities measured with the airborne system 94

Section 6

Fig. 1 Circuit diagram of the Barnes Surface Temperature Bolometer Model 14-310, Serial No. 102 102

2 Calibration curve for surface temperature bolometer . . 104

3 Transmissivity and black-body radiation curves . . . 106

4 Radiation fluxes between ground and surface temperature bolometer. 108

5 Flight path used for bolometric surface temperature measurements in Southern Wisconsin. 114

6 Airborne measurements of surface temperature in Southern Wisconsin on September 7, 1961, in the early morning and early afternoon 116

7 Airborne measurements of surface temperature in Southern Wisconsin during early afternoon flights over the same course on September 7, and October 2 and 5, 1961. . . 122

Section 7

Fig. 1 Mean hodographs for 8 surface-wind directions, Drexel, Nebraska; Winters, 1915-1920 133

2 Mean hodographs for 8 surface-wind directions, Drexel, Nebraska; Summers, 1916-1920. 133

Page

[Section 7]

Fig. 3 Mean hodographs for 8 surface-wind directions, Ellendale, N.D.; Winters, 1918-1920. 134

4 Mean hodographs for 8 surface-wind directions, Ellendale, N.D.; Summers, 1918-1920. 134

5 Winter Ratio of geostrophic drag coefficient for 152
6 Spring non-adiabatic and adiabatic conditions versus 152
7 Summer approximate height derivative of Richardson 153
8 Fall number in atmospheric surface layer 153

Section 8

Fig. 1 A family of equiangular wind spirals and corresponding vertical profiles of eddy diffusivity (K relative to average $\overline{K}$, versus z/H where H = geostrophic wind level), for five selected values of α_0 (angle between surface stress and ambient flow). The special case of the Ekman spiral is illustrated at the center. 168

Section 9

Fig. 1 Free drag, float and marker employed for the measurements of current profiles and divergence in Lake Mendota. . . 176

2 Individual current hodographs in Lake Mendota on 17 August 1961, run 1 through 4 178

3 Direction of 5 cm current in Lake Mendota at indicated hour for the four runs on 17 August 1961 180

4 Individual current hodographs in Lake Mendota on 18 August 1961, run 5 through 10 182

5 Vector-mean current hodograph in Lake Mendota on 18 August 1961 (Day II). 180

6 Individual current hodographs in Lake Mendota on 25 August 1961, run 11 through 15 184

7 15-min averages of windspeed at 40 cm, and temperature difference between air at 20 cm and water; 28 August 1961, for the hours of run 16 to 20 186

List of Illustrations

Page

[Section 9]

Fig. 8 Individual current hodographs in Lake Mendota on 28 August 1961, run 16 through 20 188

9 30-min averages of windspeed at 40 cm, 15-min averages of temperature difference between air at 20 cm and water; 6 September 1961, for the hours of run 21 to 26 . . . 186

10 Time series of current speeds in Lake Mendota at indicated depth, 6 September 1961, run 21 to 26 186

Section 10

Fig. 1 Wind ratio V/V_{go} versus logarithm of height 198

2 Theoretical profiles, of wind ratio V/V_{go} and stress ratio τ/τ_0 versus logarithm of relative height 202

3 Universal profile of the Deacon number versus logarithm of height. 204

4 Theoretical profile of the Deacon number versus metric height 204

5 Empirical relationship between Deacon and Richardson numbers as derived from observations at O'Neill . . . 210

6 Comparison of various theoretical models of mean profile structure in the diabatic surface layer 210

7 Theoretical relation De versus Ri after Swinbank, in comparison with the theoretical relation after Panofsky et al. 214

8 Observational relationship between Deacon and Richardson numbers, from micrometeorological profile measurements over various surface structures 216

General Introduction

Heinz H. Lettau

Department of Meteorology
University of Wisconsin

This volume contains a series of nine individual papers, devoted to micrometeorological research at the University of Wisconsin under the sponsorship of the United States Army Electronic Proving Grounds Meteorology Department, Fort Huachuca, Arizona. The general purpose of the work is the investigation of the three-dimensional structure of the planetary boundary layer. Special attention is given to the horizontal variations of the boundary exchanges of masses, momentum, and energy (or heat) which are induced by surface characteristics. The work accomplished during the three years under the contract has been devoted to the following subtasks:

1. Ground-based instrumentation
2. Airborne instrumentation
3. Micrometeorological measurements, and
4. Theoretical work, including data evaluation and analysis.

Progress has been made in all subtasks. An Annual Report which contains eight individual technical articles was published in 1961. In addition to the listings of scientific papers in Section 1 of the 1961 Annual Report, and to work included in this volume, the following articles (which are, in part, results of research sponsored by the contract) have been published:

K. G. Bauer and J. A. Dutton, "Albedo Variations Measured from an Airplane over Several Types of Surface," Journal of Geophysical Research, 67, No. 6, p. 2367-2376, 1962.

S. M. Robinson, "Computing Wind Profile Parameters," Journal of the Atmospheric Sciences, 19, No. 2, p. 189-190, 1962.

C. B. Tanner, "A Simple Aero-Heat Budget Method for Determining Daily Evaporation," Transactions 7th Congress of Soil Sciences, Madison, Wis., 1960, Vol. I, Section 16, p. 203-209, 1962.

C. B. Tanner and E. R. Lemon, "Radiant Energy Utilized in Evapotranspiration," Agronomy Journal, 54, p. 207-212, 1962.

The research work outlined in the technical requirements of the contract has been advanced on a broad front. Its scope is so wide that this work could not possibly be completed within three years. The term "Final Report" is more or less for administrative convenience only. Continued research in this field is necessary, and in the planning phase.

In the present volume two articles report on achievements concerning instrumentation and equipment. Reference is made to Section 2 by C. Stearns, in which the intricacies of present-day measurement and recording problems of micrometeorological ground-based instrumentation are demonstrated, and ways of practical solutions are shown; and to Section 5 by J. Dutton and D. Lenschow, who describe the correspondingly complex problems of air-borne instrumentation, and their solution by the Cessna-310 system developed at the University of Wisconsin. Direct results concerning the complex structure of surface temperature variations in the region of southern Wisconsin, in measurements made possible only through the use of the airplane, are presented, in Section 6, by D. Lenschow. Obviously, the continuation of field work and of measurement flights is necessary to clarify and explain, quantitatively, how heating or cooling at the lower boundary of the atmosphere affects the three-dimensional structure of the planetary boundary layer. Future work with the airborne system will need to incorporate the measurement of eddy Reynolds stress and heat transfer, at various levels.

For the understanding of the basic problem it is important to investigate the relationship between the small-scale and synoptic-scale processes in the atmosphere. In this respect, significant results were obtained by the refined analysis of climatological windprofile data as reported, in Section 7, by W. Johnson. This work demonstrates how an apparently forgotten treasure of 40-year old data can produce a wealth of significant information, if present-day tools of theoretical analysis are applied. These results seem to agree quite satisfactorily with a theoretical solution of the boundary layer wind profile, proposed in Section 9 of the 1961 Annual Report, as far as barotropic conditions are concerned. Johnson's work, still, is of necessity restricted to steady-state baroclinic conditions. Future work will consider the combination of an observational program of conventional wind profile soundings with airplane measurements of eddy stress.

The obvious similarity between spiral flow in Lake Mendota (see Section 9, by A. Super) and in the atmospheric boundary layer suggests that there is a possibility of utilizing water-current studies as models for non-steady spiral flow, in an empirical approach to the development

problem. A typical difference between wind and water-current spirals stems, however, from the vertical distribution of eddy diffusivity between interface and regions of free fluid flow. In this connection, reference can be made to Section 8, by H. Lettau, in which the basis of a more general practical application of theoretical spiral solutions to atmo- and hydrosphere is prepared.

Two sections of this volume deal with unconventional methods of determination of micrometeorological temperature profiles. In Section 3, H. Hamilton discusses vertically continuous profile measurements, obtained by sweeping a sensor from 2.8 m above to 0.5 m below the air-water interface; in Section 4, J. Sparkman describes tentative work on a simplified technique using optical refraction to determine quasi-horizontal line averages of vertical temperature gradients. The results obtained with these methods, supported by the recordings from the tower station on the lake, have indicated that the thermal structure of the air over the water cannot be satisfactorily explained by vertical transfer of heat alone. It was concluded that a direct appraisal of advection processes is necessary. A program of instrumented cruises parallel to the wind fetch has begun, and results will be reported in due time. The problem is especially interesting in view of the fact that in flow from land to the lake the air experiences not only a change in heating rates (normally, a reversal of sign is involved) but even more significantly, a change in surface stress. After having reached the water the air will be accelerated downstream. This also seems to be the cause for the finding reported, in Section 9, by A. Super, that a positive divergence of surface currents seemed to be a general feature of all cases studied.

A characteristic of what has been referred to as the "Wisconsin-approach" to micrometeorological research is the emphasis on controlled or genuine experimentation. In the 1961 Annual Report a first series of thermal response experiments (involving artificial cycling of natural radiation fluxes) as well as windstress experiments (involving a controlled variation in surface roughness, "bushel-basket experiments") was presented. The weather during the winter of 1961/62 proved to be highly unfavorable for the completion of a new series of controlled windstress experiments, using a systematic exchange of black and white obstacles in order to test the effect of heating on surface drag coefficients and wind profile structure. Of a total of 460 bushel baskets, 230 had been painted white, the other 230 black. The average albedo was 65 and 15%, respectively. The development of the technique was sufficiently perfected only towards the end of the period which permitted working on the ice of Lake Mendota. The sweep apparatus constructed by Mr. Hamilton (see Section 3) proved to be extremely useful for the measurement of temperature profiles over the obstacle field. It was found that area-densities of at least one obstacle per 0.5 m^2 were necessary to produce a significant

Table 1. Richardson number in the 80 to 40 cm layer of air above an artificial roughness field of constant obstacle density (one bushel basket per 0.5 m^2 of snow surface), as a function of obstacle-color in the presence of solar heating. Results of experiments on the frozen surface of Lake Mendota, on 3 April 1962.

CST of Profile Measurement	Number of Obstacles		Richardson Number (80 to 40 cm)
	White	Black	
11: 52-12: 07	230	-	0. 0035
12: 22-12: 37	115	115	-0. 0008
12: 47-13: 02	-	230	-0. 0026
13: 17-13: 22	115	115	-0. 0020
13: 42-13: 57	230	-	0. 0008
14: 12-14: 27	115	115	-0. 0010
14: 37-14: 52	-	230	0. 0000
15: 02-15: 17	115	115	0. 0010
15: 27-15: 42	230	-	0. 0070

effect on the Richardson number. Table 1 is a summary of Richardson number determinations during the last day of the winter season. In the terms of bulk-stability, $\underline{Ri}'$ varied from 6.4 for "all white," to -1.2 for "half black and half white." to -2.3 (in units of 10^{-3} per m) for "all black" obstacle fields. This might be the first quantitative demonstration of a successful stability modification in the air through artificial control of boundary albedo, and subsequent solar heating rates.

A theoretical study was completed in order to appraise the effect of Richardson number variation on windprofile structure; reference is made to Section 10, by H. Lettau. In this section the effect of vertical divergence of momentum flux on windprofile curvature is, for the first time, quantitatively expressed, for adiabatic as well as diabatic conditions. These theoretical results will be considered in future roughness modification experiments. It will also be considered that the most useful information concerning the effect of heating intensity would come from direct stress measurements, employing the ice-block technique described in Section 2, in order to single out the change in drag coefficients due to controlled Richardson number variation.

Scanner's note:

This page is blank.

2

Micrometeorological Installation on Lake Mendota

Charles R. Stearns

Department of Meteorology
University of Wisconsin

Abstract. As a basis and reference station for micrometeorological field experimentation, directed towards the detailed investigation of boundary layer structure in the atmosphere, the Department of Meteorology has installed a tower station on Lake Mendota. The tower is instrumented to record micrometeorological data on a continuous basis, and detailed micrometeorological profile data, including supplementary elements, for periods of field experimentation. The details of installation, instrumentation, and analog and digital automatic recording systems are presented.

List of Contents

2. 0 List of Symbols

2. 1 Site Description and General Features of Installation
- 2. 1. 1 General Purpose of the Installation and Its Location
- 2. 1. 2 Shore Installation, Instrument Building
- 2. 1. 3 Lake Installation, Tower

2. 2 General Description of Methods of Sensing, Signal Transmission and Recording
- 2. 2. 1 Tower Sensors
- 2. 2. 2 Recording Systems
- 2. 2. 3 Cables and Signal Wires
- 2. 2. 4 Winter Installation

2. 3 Details of Measurements and Techniques
- 2. 3. 1 Wind Vane and Standard Anemometer
- 2. 3. 2 Thermistors for Air, Water and Dew Cell Temperature Measurements
- 2. 3. 3 Wind Profile Anemometry

2.3.4 Temperature Profile Equipment
2.3.5 Radiation Measurements
2.3.6 Wave Recorder
2.3.7 Ice Drag Recorder

2.4 Details of Signal Transmission and Recording
2.4.1 Tower Switches and Recording
2.4.2 Digital Voltmeter Recording
2.4.3 Time and Wind Recording for Cards
2.4.4 Key Punch and Typewriter Operation
2.4.5 Time Switch

2.5 References

2.0 List of Symbols

vdc	Volts direct current
milli-vdc	Millivolts direct current
vac	Volts alternating current, normally 60 cycles per sec.
T	Temperature, °K or °C
R_T	Thermistor resistance (ohms) at temperature T
R_0	Thermistor resistance (ohms) at temperature T_0
β	Thermistor material constant, °K
E_i	Input voltage
E_S	Signal voltage
R_S	Signal resistance
i_S	Signal current
σ	Electrical conductivity of water
h	Height of water on wave recorder
E_y	Young's Modulus of elasticity
E	Unit axial deformation of strain
L	Length of unstrained material
ΔL	Change in length due to strain
ΔT	Temperature difference, °C
SR	Solar Radiation
FP	Flux Plate
TS	Tower Switch

2. 1 Site Description and General Features of Installation

2. 1. 1 General purpose of the installation and its location

Basic micrometeorological studies of turbulent air flow near the ground require a uniform surface with horizontal dimensions approximately 100 times the height of the investigated layer. One area available, convenient to the campus of the University of Wisconsin with a reasonably uniform surface, is Lake Mendota (approximately 40 km^2 surface area). Fig. 1 shows the micrometeorological tower location in Lake Mendota and the horizontal wind fetch in several directions. A shallow submarine bar extends 450 m out into Lake Mendota from Second Point. The water depth is 4 m at the tower location shown in Fig. 2. The University administration made a site available at the "Tenting Colony" near the lake shore for the erection of a temporary building to house recording equipment with electric power and telephone service available.

The installation of a structure in the lake required the approval of the City of Madison and the State of Wisconsin Public Service Commission. A hearing was held July 7, 1959, and permission was granted to the University Regents for the installation. Adequate lighting of the tower was required and installed to prevent hazards to boat navigation.

2. 1. 2 Shore installation, instrument building

The temporary building is a 10' by 10' by 10' prefabricated metal shack with one door containing a window, with a view of the tower. The building is insulated by fiber glass. Heating in winter is provided by heat lamps and a thermostatically controlled electric heater. Cooling in summer is necessary for the removal of heat generated by the electronic equipment and is accomplished by a one-horsepower air conditioner. The building is founded on cement blocks with plywood flooring covered with vinyl tile. Shelves and a work bench are permanently installed on the east and south walls. 220 vac available at the building is routed through switch boxes to three external points (Telescope building, Zoology buoy, and Lake Tower). The telescope building is of a 10' by 6' by 8' prefabricated metal building located within a few feet of the lake shore. It houses a 12" reflecting telescope aimed across the lake; reference is made to Section 4 of this report.

2. 1. 3 Lake installation, tower

The tower is of steel construction, triangular in cross section (30 cm on a side), and 6 m tall; see Fig. 3. One meter from the bottom, the cross section commences to taper to a point which may be fixed to a base. The tower serves as a basis for the attachment of equipment and for electrical connections. The tower foundation is a cement block (1 cubic meter)

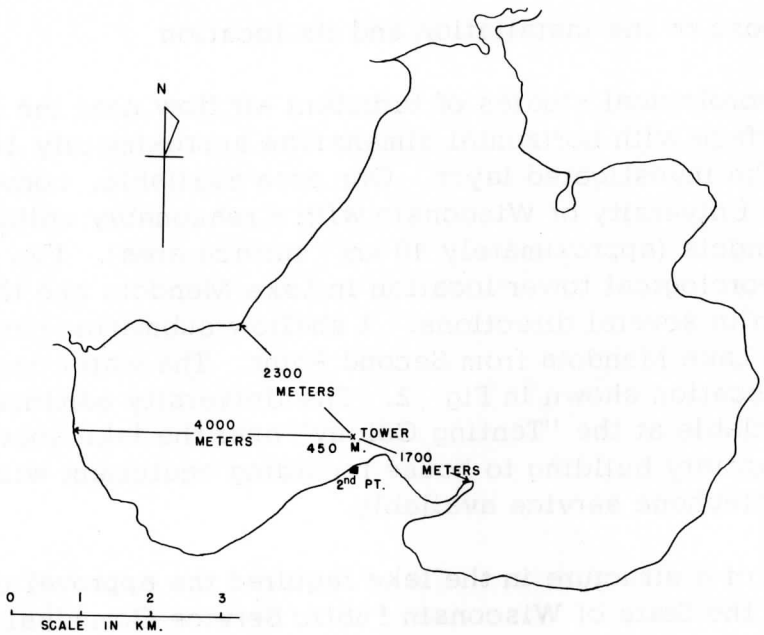

Fig. 1. Map of Lake Mendota with location of tower and instrument building.

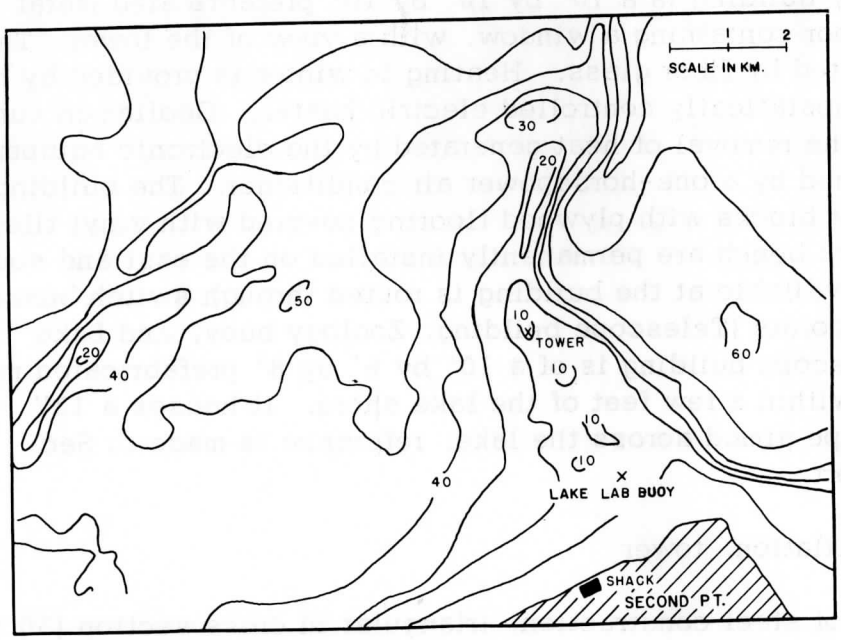

Fig. 2. Enlarged map showing Second Point of Lake Mendota with location of tower, Lake Lab buoy, and instrument building (shack).

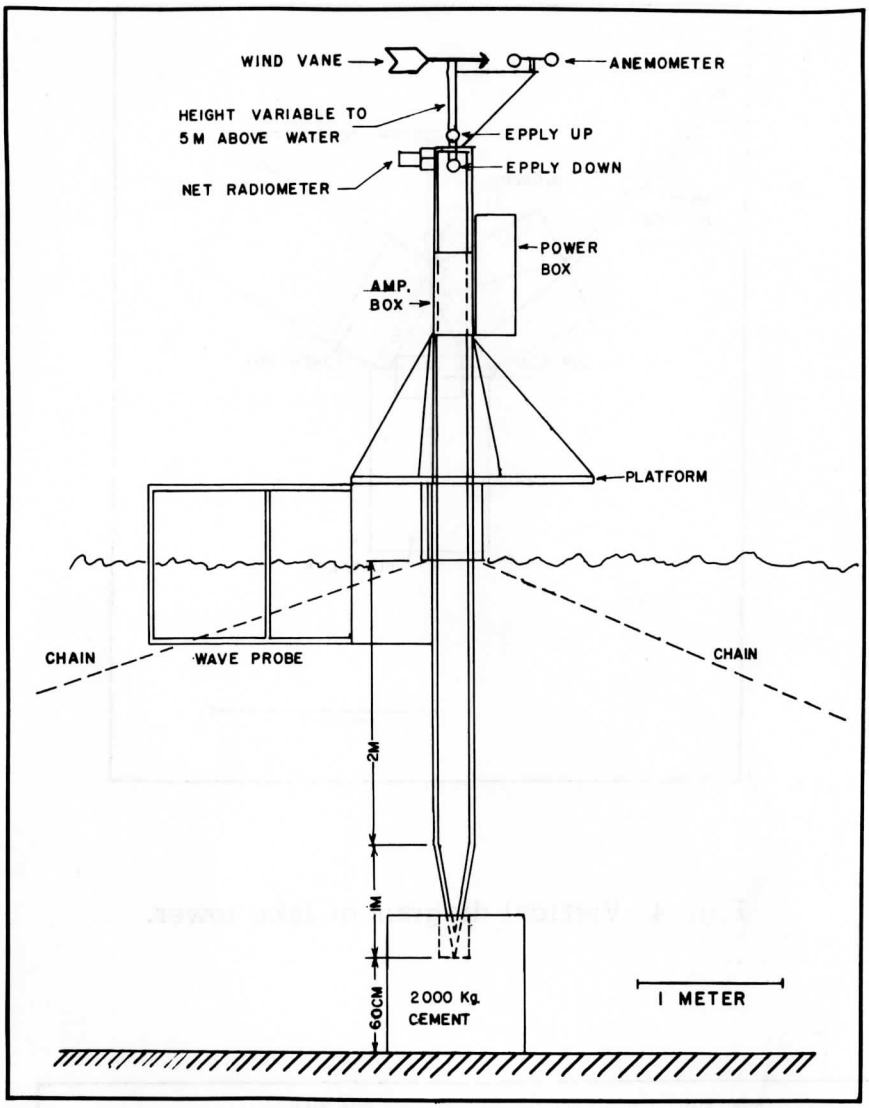

Fig. 3. Diagram of lake tower.

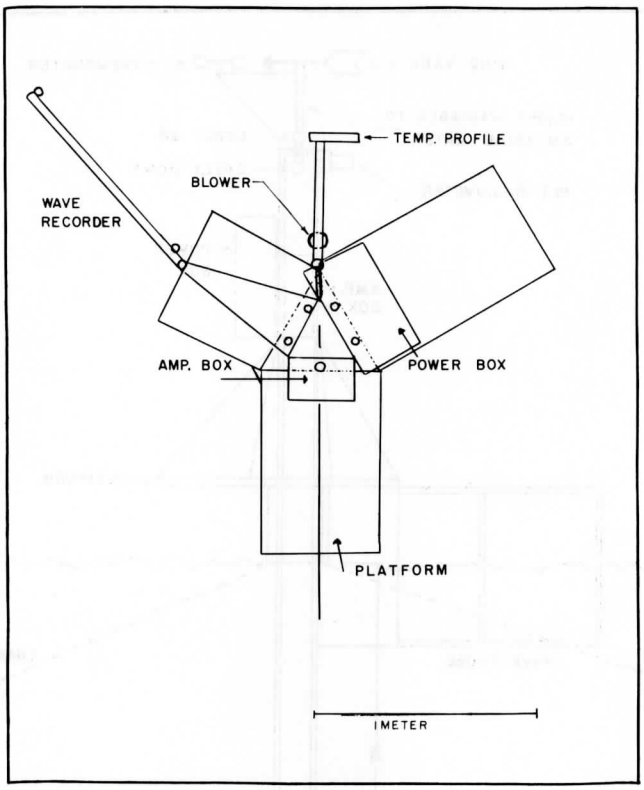

Fig. 4. Vertical diagram of lake tower.

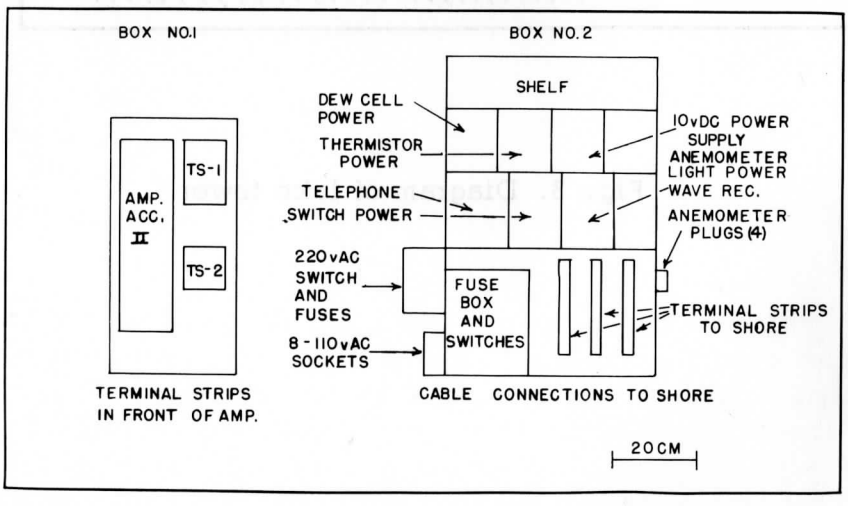

Fig. 5. Arrangement of electrical boxes on lake tower.

weighing approximately 1500 kg in water. The tower is set 30 cm into cement block. Being raised 60 cm off the bottom, the average water level is near the midpoint or 3 m level of the tower. The level of Lake Mendota is regulated so that it varies less than ±30 cm during the year.

Vertical support and tower orientation is by anchors and chains. Five anchors (consisting of 200 liter steel drums filled with cement) are located about 30 m from the tower base, connected by 1/2 cm welded steel chains to the tower at the three-meter point. Viewed from the tower, the anchors are spaced approximately at 72° angles relative to each other. Thus, any four of them will temporarily support the tower. The location of each anchor is marked by a yellow buoy of 20 liters volume fastened to the anchor by chain. The vertical position of the tower is controlled by loosening and tightening the proper chains.

At a point 30 cm above high water level a platform is fixed to the tower extending out over the water for a distance of one meter. This platform can be seen on Fig. 4. It is capable of supporting one or two people working on the tower, and extends out far enough so that it is possible to work at the electrical connection boxes without undue hazard or strain. This is an important consideration inasmuch as an observer may occasionally be required to work on the platform for several hours.

Two sheet metal boxes contain the electrical equipment connections; see Fig. 5. They are mounted on the tower at a height still convenient for working but out of reach of spray from splashing waves. Box No. 1 is 30 cm deep, 100 cm high, and 50 cm wide. This box contains the basic 220 vac outlets, switches, and fuses. In addition, this box contains cable connections for signals above 1 milli-vdc minimum (for example, for anemometer contact counting). Provisions are made for the installation of 10 separate circuits on their own chassis. A telephone and buzzer system allow communications with the building on shore. Box No. 2 is primarily for signals in the range 0 to ±1 milli-vdc requiring amplification to the range 0 to 1 vdc. The box also contains two switches, one with three channels and the other with two channels. The switches have 24 positions, and are triggered as desired from the instrument building.

A shelf (30 cm wide and 100 cm long) extends out from the top of the tower in a southerly direction. Primarily, this shelf is for support of radiation instruments. It can be folded down when the tower is being taken down or erected so as to decrease the cumbersomeness of the tower. Two light fixtures containing 25-watt bulbs are installed near the top of the tower to provide a warning for boat traffic at night. A 5 cm steel pipe extends vertically through the tower for supporting a wind direction

vane and a standard cup anemometer. The pipe is adjustable in height so that the anemometer can be maintained at the 5 m level above the actual air/water interface.

2.2 General Description of Methods of Sensing, Signal Transmission and Recording

2.2.1 Tower sensors

The meteorological elements to be measured on the site are conveniently divided into climatological and micrometeorological elements. The following listing refers to the sensors for continuous or climatological recordings. The sensing method and the height relative to mean water level are also given.

(1) Wind speed; SCS cup anemometer at 500 cm (adjustable)

(2) Wind direction; Gurley Selsyn vane, operating 360° potentiometer; at 500 cm (adjustable)

(3) Air temperature; shaded thermistor at 200 cm

(4) Dew point temperature; dew cell at 200 cm

(5) Water temperature; thermistor at -30 cm

(6) Shortwave radiation from sun and sky; Epply (10 junction) at 315 cm

(7) Reflected shortwave radiation; inverted Epply (50 junction) at 285 cm

(8) Net radiation; Suomi ventilated radiometer at 300 cm.

All climatological elements are recorded on punch cards.

Micrometeorological measurements include wind profile data. A set of 16 Thornthwaite cup anemometers is available. These anemometers are installed near the tower only during special investigations and operate remote counters in the instrument building. Masts, and levels of exposure will be discussed in Section 2.3.1. For air temperature profile studies, ventilated sensors at 20, 40, 80, 160 and 320 cm are provided at the tower. Recording is on punch cards. The temperature differences between adjacent levels are measured by 10-junction thermopiles. The temperature difference between 20 cm and a known reference (normally, the water temperature at -30 cm) is also measured to determine the absolute value of air temperatures. This reference temperature is measured by a thermistor.

For the study of variable surface structure, wave heights are recorded by two vertical silver wires 150 cm long and parallel (1 cm apart) with the average water level near the midpoint of the wires. An ac-voltage applied

to the two wires produces a current which is rectified and recorded. Excepting extreme cases (when large waves cause the water level to rise and fall towards the ends of the wires), this current varies in linear proportion to interface fluctuations.

2.2.2 Recording systems

The main system in the instrument building records analog signals in digital form on punch cards. An amplifier at the tower converts signals of ± 1 milli-vdc to 0 to 1 vdc which is then fed to the digital voltmeter and entered on cards. Signals of 0 to 1 vdc are fed directly to the digital voltmeter. A 24-position switch selects the desired signal. The digital voltmeter reads the signal, then operates the card punch to record the signal. Time and date are entered separately. A second switch at the tower sends signals of less than 1 milli-vdc to the amplifier to be recorded on a separate card. The above system requires one minute to punch a complete card with up to 23 items recorded at 2.4 sec intervals.

Two Brown strip-chart recorders accept signals of 0 to 2.5 milli-vdc. Signals of this level can be sent directly from the tower to the recorder if care is exercised to reject unwanted noise. This is achieved by balancing the load relative to the tower ground. A digital voltmeter and printer will accept signals of 0 to 1 vdc at the rate of 5/sec. An amplifier may be used ahead of the digital voltmeter. Other recording systems available for supplemental data during special observation periods include one 16-channel Visicorder, four 0 to 10 milli-vdc Varians, and a 24-channel Brown Recorder 0 to 2.5 milli-vdc.

2.2.3 Cables and signal wires

The 220-vac electrical power cables include one three-wire No. 12, plastic covered, and three 10-wire No. 20, rubber covered. The 500 m length of one No. 12 wire has a resistance of 2.6 ohm and the ten No. 20 wires have 1.5 ohms resistance in parallel. Each side of the 220 vac consists of one No. 12 and one cable of ten No. 20 wires. The total resistance in parallel is 1 ohm. Thus, 2000 watts of power will cause a drop of 10 volts, which is tolerable. The ground wire also consists of one No. 12 and ten No. 20 wires in parallel.

Three 22-conductor cables of No. 22 wire (vinyl plastic covered) are used for transmitting pulse, or high level ac or dc signals. Resistance to water is about 2 megohm. Each wire has 35 ohm resistance. Between shore and the tower, two 10-conductor No. 20 wire (rubber covered) are used for low level signals. Each wire has 15 ohms resistance between shore and the tower. The resistance to the water is greater than 50 megohms.

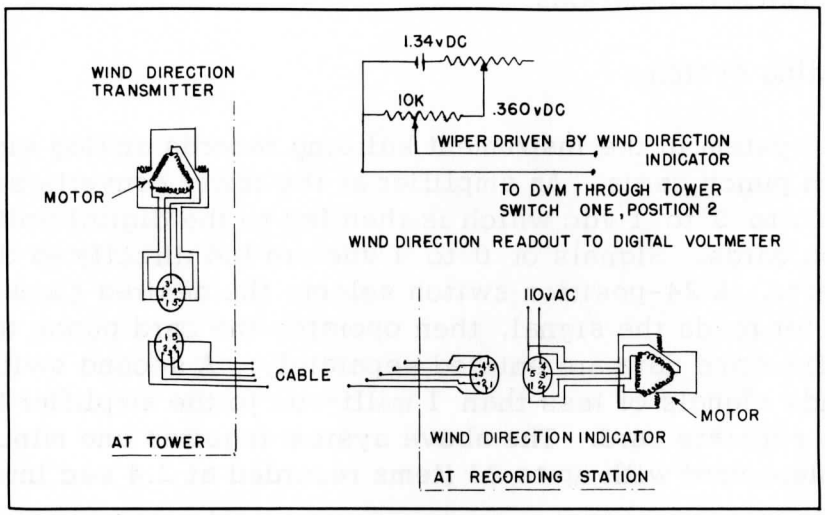

Fig. 6. Wind direction circuits.

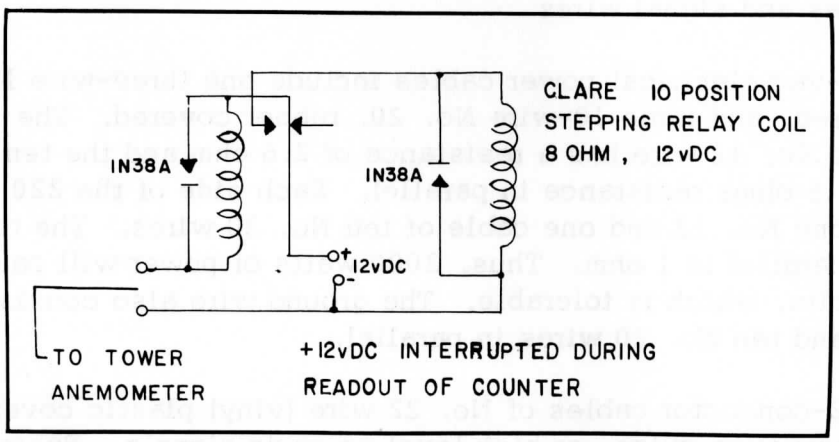

Fig. 7. SCS cup anemometer counting circuit.

The telephone and buzzer, wind vane and anemometer are connected to the building by a 10-conductor No. 20 rubber-covered cable.

2.2.4 Winter installation

The average freezing date of Lake Mendota is 19 December. Thus, in November the tower is removed from the lake before ice forms. All wires are dropped to the lake bottom. After the ice has reached a thickness of 20 cm or more, the tower is reinstalled at the same point by cutting a hole in the ice and submerging the lower 3 meters of the tower. Its weight is supported by 2" by 6" board (2 m long) inserted through the tower and resting on the ice. The tower is held upright by guy ropes to the top of the tower. Sawdust piled around the base retards the melting of the ice from solar radiation absorbed by the tower. Cables are connected in the same manner as during the summer. The tower must be removed from the ice before the spring break up of the lake, which occurs according to the climatological 50-year average on the 6th of April.

2.3 Details of Measurements and Techniques

2.3.1 Wind vane and standard anemometer

The wind vane and indicator is a Gurley model 6533. The indicator is located in the building with five wire connections to the sensor. Read-out is obtained by a one-turn 10,000 ohm potentiometer driven by the indicator. A voltage of 0.360 vdc is applied to the potentiometer and the output is recorded through the digital voltmeter via the tower switch 1, position 2. The potentiometer is accurate to 0.5 per cent, which corresponds to about 2 deg of an arc. This is adequate for climatological purposes considering that, with the sampling rate of once each minute, the wind direction usually varies considerably more than 2 deg during that time. A dead zone of the potentiometer of about 5 deg width is centered at true north and can be neglected. Fig. 6 shows the circuit used to transmit the wind direction from the tower to shore and to convert the wind direction into degrees for the digital recording.

The anemometer is of the standard SCS 3-cup type with 1/60th mile contact, which operates a 12 vdc relay triggering a four-digit counter. The circuit is constructed so that the relay is closed momentarily and will not stay closed if the anemometer stops in contact position for an appreciable length of time as will occasionally occur under conditions of low wind speed and would damage the counters due to heating. The capacitor discharges through the transistor and relay. The resistor is large enough to prevent the coil from remaining closed but small enough to allow the capacitor sufficient charge-up time to fire the relay

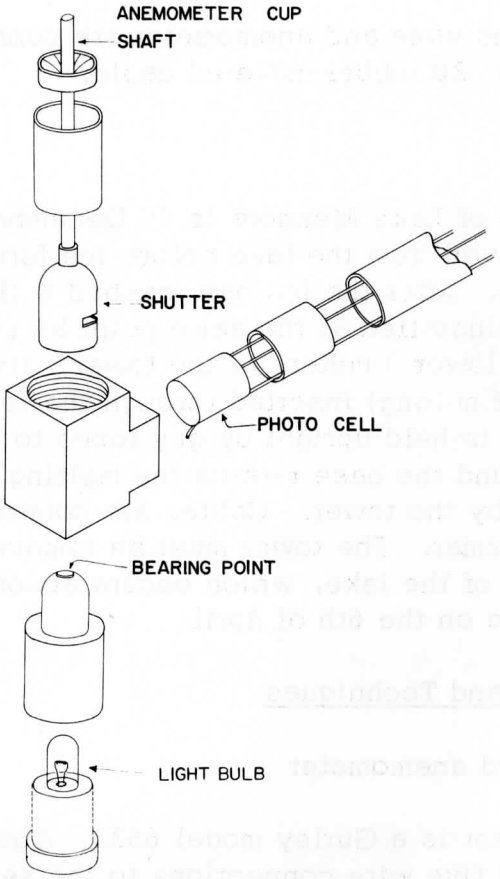

Fig. 8. Construction details of Thornthwaite anemometers.

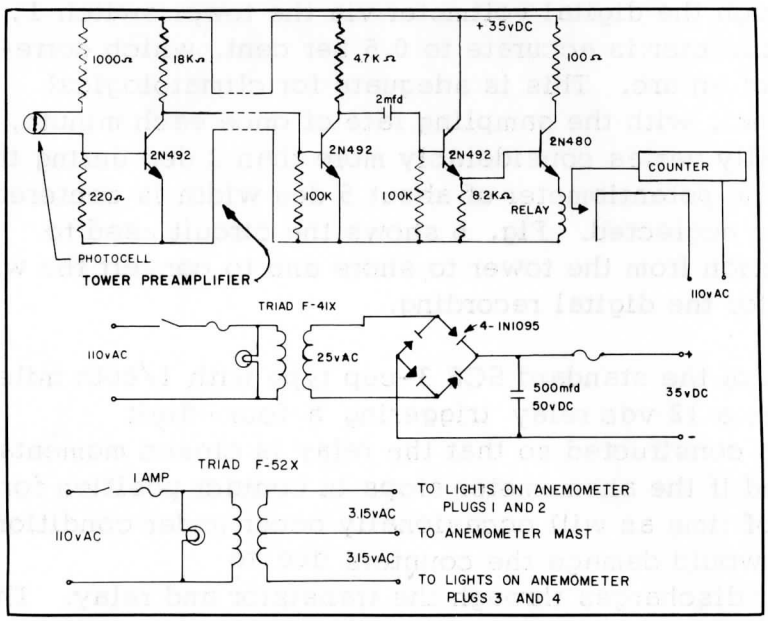

Fig. 9. Anemometer counting circuit and power supply.

if the wind velocity is more than 60 miles per hour. Fig. 7 is a diagram of the circuit.

The relay triggers a 4-decade counter consisting of four Clare ten-position stepping switches. The counts are read out on punch cards when desired; then, the counters are reset to zero. Thus the number recorded is the total of anemometer contacts since the last readout. Dividing the counts by the number of minutes of the period between readouts gives the wind velocity in miles per hour when the anemometer is properly calibrated.

2.3.2 Wind profile anemometry

Sixteen matched cup anemometers manufactured by Thornthwaite Associates are available for the detailed measurement of wind profiles. A shutter at the rotating anemometer shaft alternately shields and exposes a Clarex CP-3 cadmium sulfide photo-cell to a G.E. 323 light bulb. This results in a change in the photo cell resistance from approximately 1 megohm to 10,000 ohms. Fig. 8 shows the details of the anemometer construction. Examples of a winter and summer installation are illustrated in Fig. 10 and Fig. 11, respectively.

Six anemometer masts are presently available with plugs permitting anemometer installation at levels listed below:

One for: 20, 40, 60, 80, 100, 120, 140, 160, 200, 240, 280, 320 cm

One for: 10, 20, 30, 40, 60, 80, 100, 140, 160, 300, 320 cm

Three for: 20, 40, 80, 160 cm

One for: 20, 40, 80, 160, 320, 640 cm.

In addition, a 12-position comparison bar for simultaneous horizontal exposure of up to 12 anemometers at a level of approximately 180 cm is available.

Connections are made to the tower box, then through a preamplifier to the recording station. Power for the anemometer light bulb is supplied by a 6.30 vac transformer centertapped to give 3.15 volts to the individual bulb. Fig. 9 shows the circuit for counting the anemometer revolutions. Sixteen preamplifiers located at the tower are required. At the recording station a second stage of dc-amplification is capacitor-coupled to a pulse-amplification stage triggering the transistor controlling the relay. The relay in turn operates a mechanical counter. By using capacitive coupling it is not possible to hold the relay and counters closed for more than one

Fig. 10. Winter installation of anemometers.

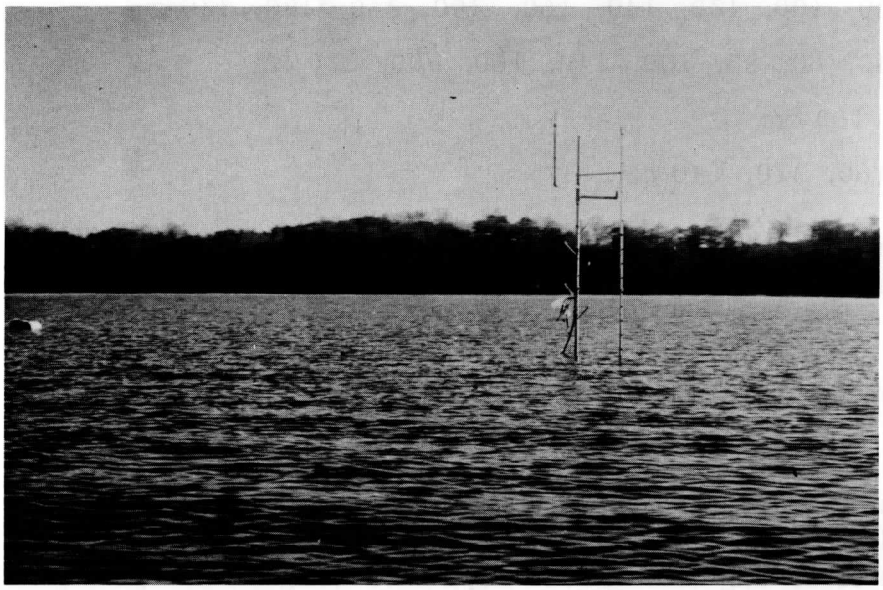

Fig. 11. Summer installation of anemometers.

second. This reduces greatly the danger of overheating when the photo cell is exposed to the light bulb for extended periods which may happen in a very light wind, below 20 cm/sec.

The gain of the system appears to be excessive. However, the photo cell has a finite response time and, at high turning rates (of the order of 8 revolutions per second), the photo cell signal amplitude is reduced as much as 50 per cent. This could result in missing counts if the gain was insufficient.

Frequently, trouble was encountered in profile measurements. A 20-position switch is installed on the power supply panel so that the output of each preamplifier may be examined to help in locating the difficulty. The following is a brief summary based on previous experiences concerning relatively frequent problems, their cause, checking procedures and remedies.

Problem:	Possible causes:
Counter does not trigger Check: Trigger (by shorting at shack)	If counter triggers on shorting: (1) light bulb burned out (2) no cup (3) open circuit; check at mast for triggering (4) bad photo cell; check anemometer (5) no light voltage (6) preamplifier failure. If counter does not trigger on shorting: (1) water across connections (2) preamplifier failure.
Counter misses	Check: connections — (1) loose contacts — particularly plugs preamplifier — (2) gain insufficient; should trigger at 1/4 actual signal relay — (3) contacts are dirty counter — (4) solenoid missing steps.

2.3.3 Thermistors for air, water and dew cell temperature measurement

Thermistors are used as absolute temperature sensors. Individual thermistors may vary widely in terms of absolute resistance value but the ratio of the resistance at one temperature to that of another temperature depends only upon the characteristics of the material used for the thermistor. This is shown by equation (1) which is generally applied to thermistors,

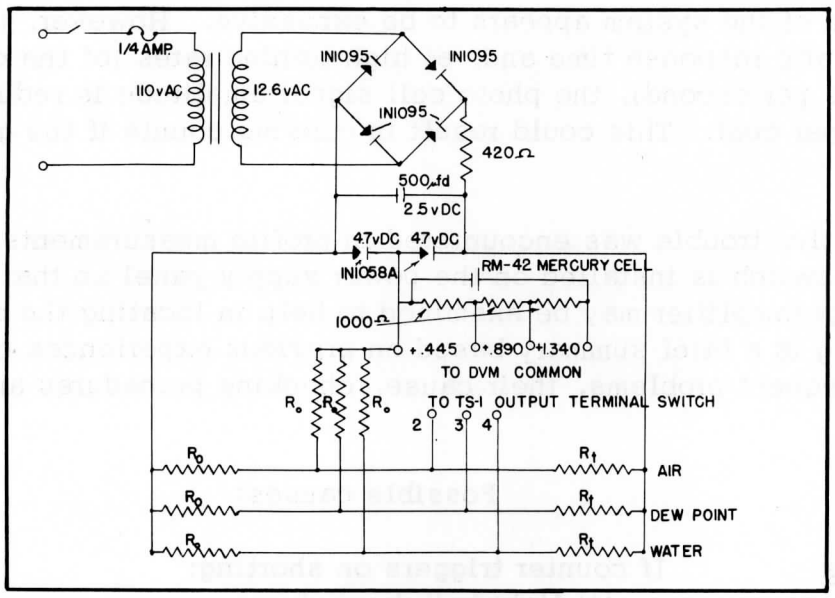

Fig. 12. Thermistor power supply.

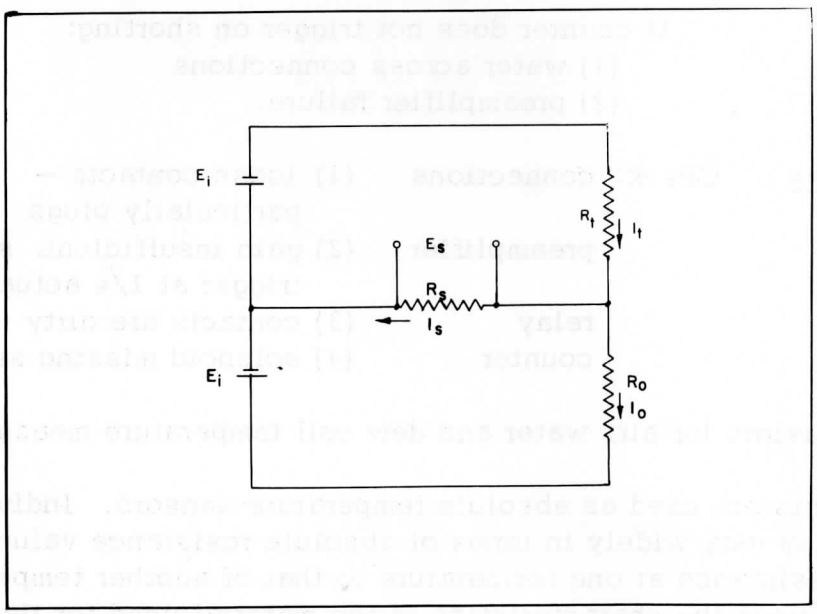

Fig. 13. Basic thermistor circuit.

$$R_T / R_0 = \exp[-\beta(1/T - 1/T_0)] \qquad (1)$$

where T = temperature (deg K), R_T = thermistor resistance at temperature T, R_0 = thermistor resistance at temperature R_0, and β = constant of thermistor material.

This fact suggests matching of the thermistors with a resistor at an arbitrary reference temperature (for example, 0° C) and measuring only the ratio between the thermistor resistance at temperature T and that at 0° C. Thus, the same calibration curve will hold for all thermistors. Fig. 12 shows the power supply and detecting circuit for the thermistors. The value of R is such that a current of 20 ma is drawn when 9.6 volts is across the zener diodes. The power supply delivers 18 vdc, and the desired voltage drop across R is 8.4 volts. Regulation is a 1 per cent change in thermistor voltage for a 10 per cent change in the 110 vac. R_0 is of the order 50,000 ohms while R_T can reach approximately 20,000 ohms. The loading due to each additional thermistor circuit will be less than 0.14 ma. Thus, ten such circuits could be added without appreciably altering the voltage across the zener diodes. The basic thermistor circuit is shown on Fig. 13.

Let E_i = applied voltage, E_s = output voltage, R_s = output resistance, i_T = current through the thermistor, i_0 = current through the reference resistor, and i_s = current through the output resistor. The condition of current continuity is,

$$i_T = i_0 + i_s \quad .$$

Since E_i must equal the sum of voltages around each circuit path, two relationships hold true,

$$E_i = R_T i_T + R_s i_s = R_T i_T + E_s \qquad (3)$$

$$E_i = R_0 i_0 + R_s i_s = R_0 i_0 - E_s \qquad (4)$$

The equation defining E_s can be written with the aid of (2),

$$E_s = (i_T - i_0) R_s \quad . \qquad (5)$$

The sum and the difference of equations (3) and (4) yield

$$2E_i = R_T i_T + R_0 i_0 \qquad (6)$$

$$2E_s = R_0 i_0 - R_T i_T \quad . \qquad (7)$$

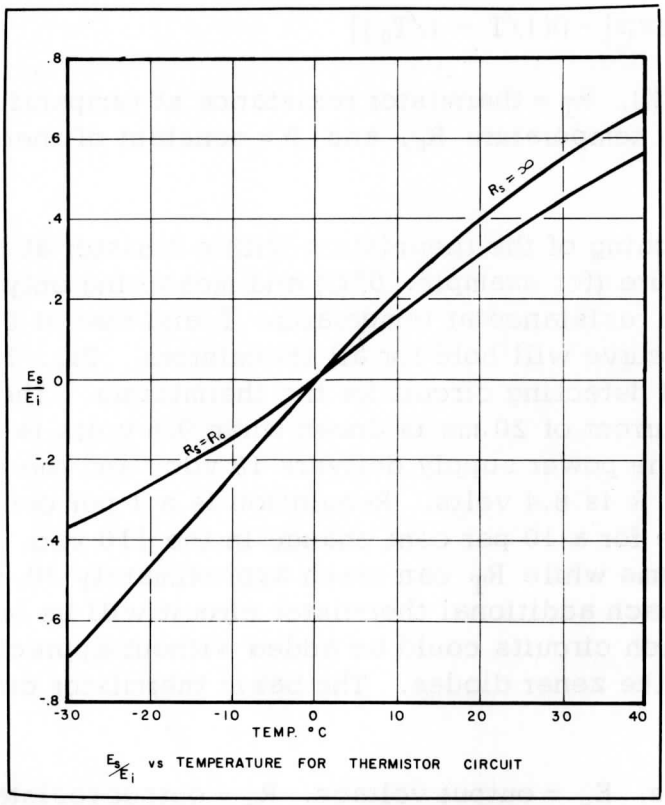

Fig. 14. E_s/E_i versus temperature for thermistors.

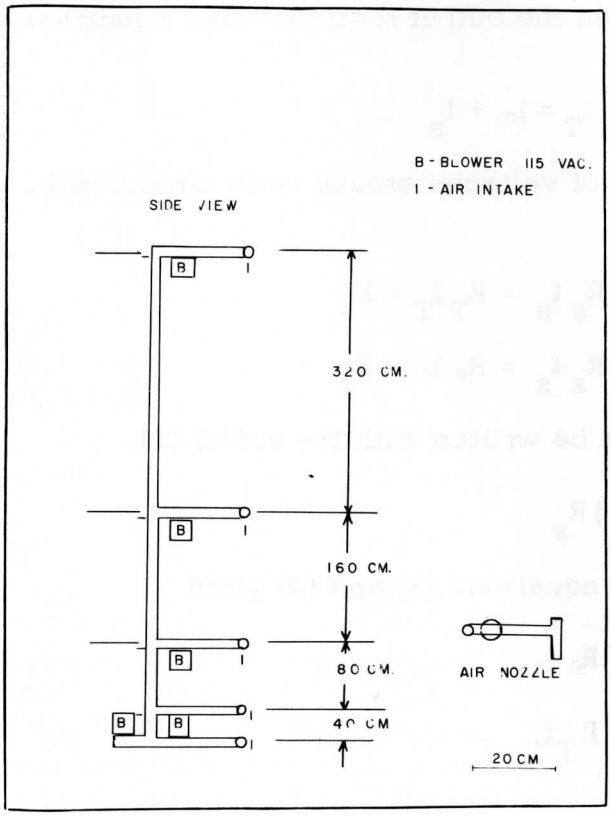

Fig. 15. Diagram of air temperature equipment.

Upon expressing $2E_s$ with the aid of equation (5), and eliminating $2E_s$ in equation (7), and rearrangement of terms,

$$i_0(2R_s + R_0) = i_T(2R_s + R_T) \quad . \tag{8}$$

With the aid of equation (8), equations (6) and (7) can be reformulated as

$$2E_i = i_0[R_0 + R_T(2R_s + R_0)/(2R_s + R_T)] \tag{9}$$

$$2E_s = i_0[R_0 - R_T(2R_s + R_0)/(2R_s + R_T)] \quad . \tag{10}$$

The ratio of equations (10) and (9) yields after some rearrangement of terms,

$$E_s/E_i = (R_sR_0 - R_sR_T)/(R_TR_0 + R_sR_0 + R_sR_T) \quad . \tag{11}$$

Special forms of equation (11) are,

$$E_s/E_i = (R_0 - R_T)/(R_0 + R_T) \; ; \text{ for } R_s = \infty \tag{11a}$$

$$E_s/E_i = (R_0 - R_T)/(R_0 + 2R_T) ; \text{ for } R_s = R_0 \; . \tag{11b}$$

Equation (1) shows that the thermistor relates the ratio R_T/R_0 to the exponential of the temperature inverse. Thus, we solve equation (11) for R_T/R_0 and obtain

$$E_s/E_i = (1 - e^{+\beta(1/T - 1/T_0)})/(1 + e^{+\beta(1/T - 1/T_0)}) , \tag{12a}$$

for $R_S = \infty$; and, correspondingly, for $R_s = R_0$,

$$E_s/E_i = (1 - e^{+\beta(1/T - 1/T_0)})/(1 + 2e^{+\beta(1/T - 1/T_0)}) . \tag{12b}$$

By this method the output becomes independent of the actual resistance of the thermistors and depends only on the matching between R_T and R_0 at the temperature selected for the output to be zero. If not matched at the desired temperature, the result is a displacement of the absolute value of the temperature in one direction or the other. For a material constant of $\beta = 3495°K$, Fig. 14 shows the ratio of E_s/E_i as a function of tempera- for the cases of $R_S = R_0$ and $R_S = \infty$, all for $T_0 = 273°K$.

To insure that R_0 is at the temperature of R_T, the reference resistor and thermistor are potted in the temperature probe with epoxy resin glue. The leads are rubber covered wire and also potted into the temperature probe. The result is a strong waterproof junction which has been found to withstand a great deal of punishment. Rubber-covered wire is used as it permits less water leakage than vinyl-covered wires. Water leakage

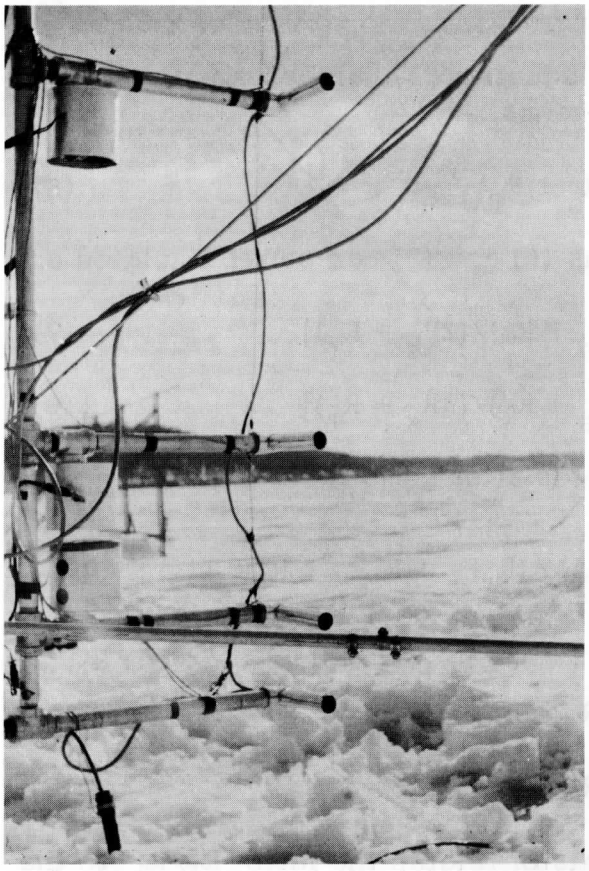

Fig. 16. Close-up of temperature profile equipment.

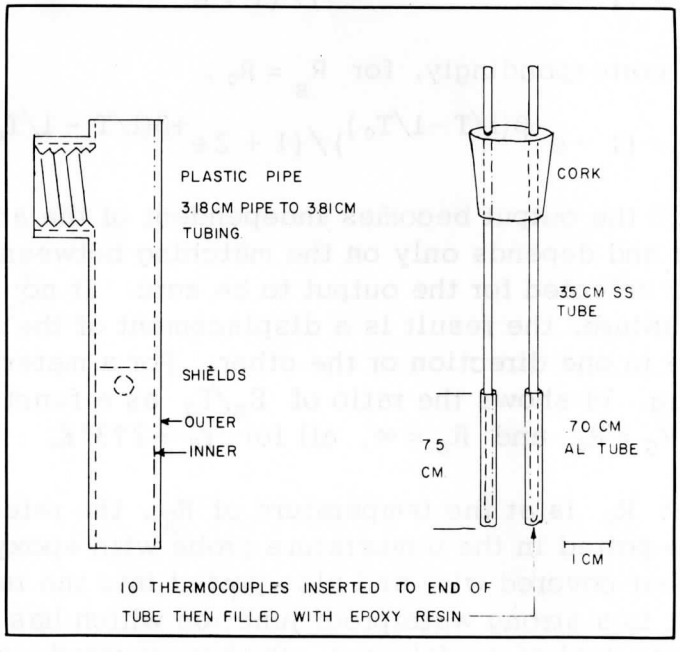

Fig. 17. Details of construction of temperature profile equipment.

could result in resistance reduction of an unknown value across the leads.

The value of R_0 for air and water temperature is selected at 0° C. During periods when the temperature is below zero the signals to the digital voltmeter are negative. Then a bias is added of either 0.445, 0.890, or 1.34 vdc employing the Rm - 42 mercury cell, depending on the mean air and water temperature. The range of temperature measurement is 40° C with an average accuracy of ± 0.025° C. For the dew point temperature using the dew cell a value of R_0 at 20° C was selected as the dew cell temperature runs 20 to 40° C above air temperature. Construction and characteristics of the dew cell are described by Tanner and Suomi (1).

2.3.4 Temperature profile equipment

The temperature difference is measured between adjacent levels by 10-junction copper constantan thermopiles at 20, 40, 80, 160, and 320 cm above the mean water surface. The lowest temperature probe must be out of range of the waves so that no wet bulb effect is measured. The temperature difference from a known reference temperature to the 20 cm level is measured to determine the absolute value of air temperatures. The reference temperature used is that of lake water 30 cm below the surface measured by a thermistor thermometer. Fig. 15 illustrates the scheme and Fig. 16 the lower four levels of the actual profile equipment in an installation over the ice.

The thermopiles are inserted in an aluminum bulb, which is covered with aluminized mylar. Fig. 17 shows the details of the probe construction. The aluminum bulb containing the actual thermopile is 6 cm in length and is pressed onto a stainless steel tube 20 cm long which is supported in a rubber stopper. Stainless steel is used to support the aluminum bulb because of its poor heat conductivity. The thermopile is imbedded in the probe with epoxy cement in the aluminum bulb. The rubber stopper is inserted in one side of a plastic-pipe "tee" which is attached to a 1-1/4 aluminum pipe. The other side of the tee supports the shields for the temperature probe. Two shields are used. The inner shield is painted black on the inside and covered with aluminized mylar on the outside, while the outer shield is covered with aluminized mylar on the inner and outer surfaces. The space between the two shields is ventilated by two 1 cm diameter holes located at the top and bottom of the inner shield next to the plastic tee. The entire assembly is ventilated by a blower which draws air past the thermopile through the aluminum pipe at the rate of 4 m/sec.

The data is collected sequentially in height (commencing with the

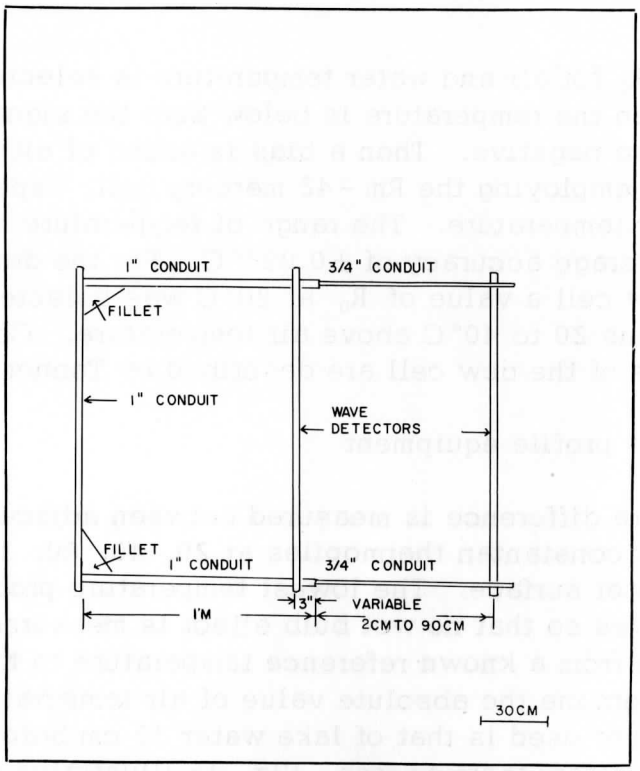

Fig. 18. Wave detector mounting.

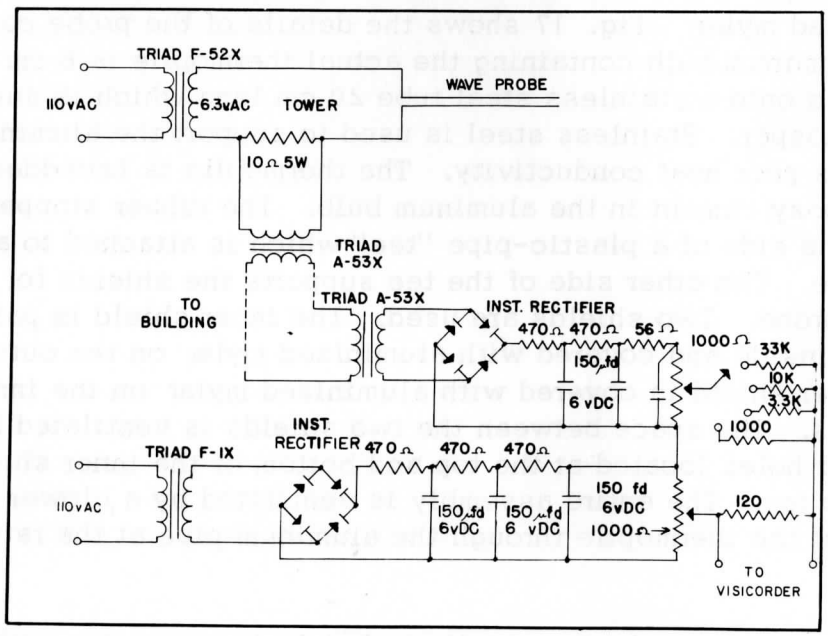

Fig. 19. Wave detector circuits.

reference temperature) and recorded on punch cards at the instrument building. The sampling rate is done a maximum of 1/min producing reliable values of the mean temperature differences.

2.3.5 Radiation measurements

Short wave radiation from sun and sky is measured with Eppley pyrheliometers. A ten-junction model is used for the measurement of downward radiation, and an inverted fifty-junction model is used for reflected (upward) radiation in the summer. In the winter, a ten-junction model may be used for reflected radiation due to the much higher albedo of snow in comparison with the albedo of the water surface. Net radiation is measured with a Suomi-type ventilated radiometer. The heating coil embedded with the thermopile of the flux plate allows adjustment of the ventilation so that heat removal from each side is equal.

During the summer the instruments are mounted on the shelf extending 4 ft from the top of the tower. In the winter, the shelf location is impractical and inconvenient. Therefore, the radiometers are located on a portable shelf approximately 10 m away from the tower where there is no traffic except to service the radiometers.

2.3.6 Wave recorder

The method selected to record wave height is based on the resistance between two parallel silver wires, 1 cm apart and 150 cm long submerged to the midpoint when the water is calm. Fig. 18 shows the mounting, and Fig. 19 the circuit diagram of the system. The electrical current between the two wires is a measure of the water mark or wave amplitude, provided the electrical conductivity of the water is constant with depth and time. Let σ = conductivity of water between two wires of unit length and spaced 1 cm apart, I = total current through wire, and h = length of the submerged part of the wires. Then,

$$I = \sigma h \qquad (13)$$

Trials in a barrel filled with lake water showed that any end effects may be neglected provided that more than 10 cm of the wire length is in the water, with an error of 1 per cent at the 10 cm level. Adhesion of water to the wire causes an error of the order 1 or 2 mm in the height when the water level is descending; it was not measurable when the water is rising.

Alternating current of 60 cps is used because this prevents hydrolytic effects — that is, the formation of hydrogen bubbles on one wire with a resulting decrease in conductivity. At present, wave height is recorded on a Minneapolis Honeywell Visicorder, as it is the only available instrument

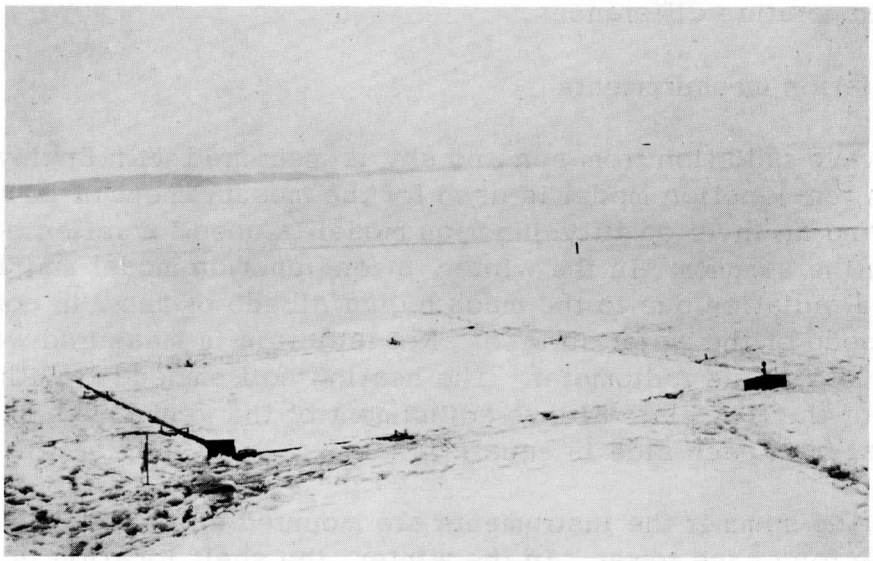

Fig. 20. View of ice block drag detector.

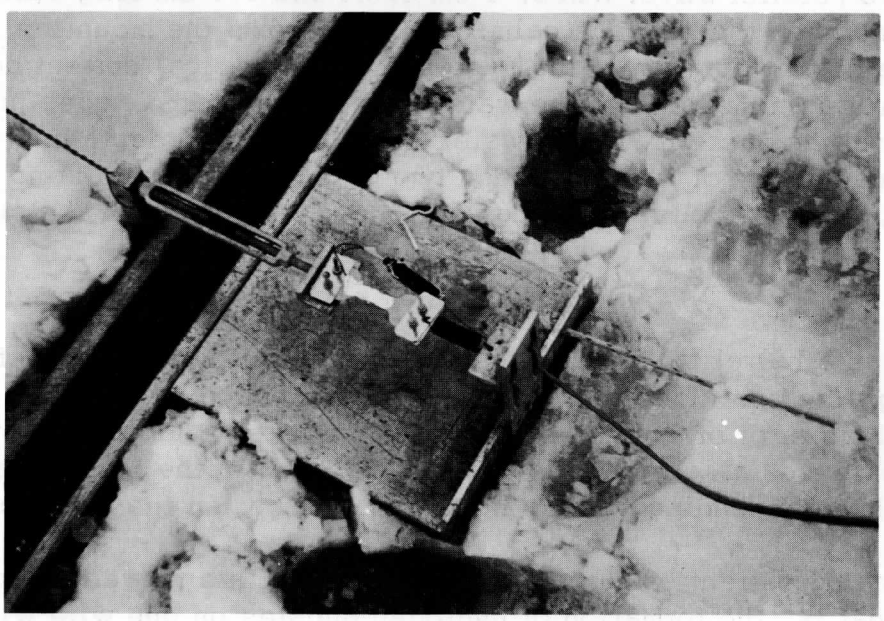

Fig. 21. Drag recorder strain gauge mounting at ice block.

to respond with sufficiently small lag time to all variations in water level. Using three separate sensors properly spaced in the water and three channels on the same chart, details of wave propagation can be studied.

2.3.7 Drag recorder

The problem is to measure the horizontal drag or stress of the wind on the surface of the ice. To achieve this, a square block of ice, ten meters on a side, is cut out with a gap of 10 cm width which was lined with 1" × 12" boards. The gap is bridged at eight equally spaced points with strain gauges (two on each side of the block). Fig. 20 shows the ice block and gauge arrangement.

Baldwin, Lima, Hamilton SR-type FA-100 foil strain gauges are cemented by epoxy resin to strips of titanium 0.005 cm thick and 1 cm wide. One gauge is mounted on each side of the titanium strip and the gauges are connected in series. This eliminates any effects due to bending or vertical vibration of the gauge. After the electrical connections are made, the gauge element and wires are covered with room-temperature vulcanized silicone rubber to protect the gauges from severe bending and moisture. Fig. 21 shows one gauge mounting as used for field measurements.

The strain gauges are connected in a Wheatstone bridge such that the four gauges on each pair of parallel sides of the ice block are in one bridge. The two gauges on one side (being either in contraction or expansion) are bridge-opposite to the two gauges on the other side (being either in expansion or contraction). Figs. 22 and 23 show the strain gauge bridge and the power supply. Torque action on the ice block will cancel out on the gauges, as well as equal tension on all of them, for example due to temperature changes in the ice. The gauges are initially stressed to an estimated 10 kg of force. Any force in the ice block with a component in the direction of the strain gauges will add to the strain on one side and subtract from the other. The difference in strain between the two sides of the ice block was recorded on a Minneapolis-Honeywell potentiometer. Input and output impedance of the bridge was 240 with each FA-100 gauge having a resistance of 120 ± 1 ohm.

The power supply uses a bridge rectifier with capacitor filtering. Output is regulated by a transistor; its base current is controlled by a 9.6 vdc zener diode. A 10 per cent change in input voltage will result in a 0.1 per cent change in output. The power supply will not be harmed by shorting or by absence of load. Two are used, one for each side of the block in order to eliminate any possible cross circuits between the two bridges.

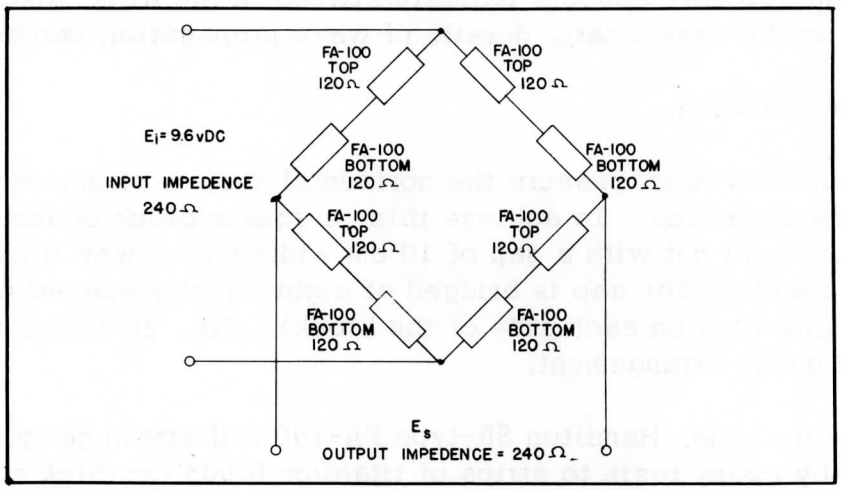

Fig. 22. Strain-gauge bridge circuit.

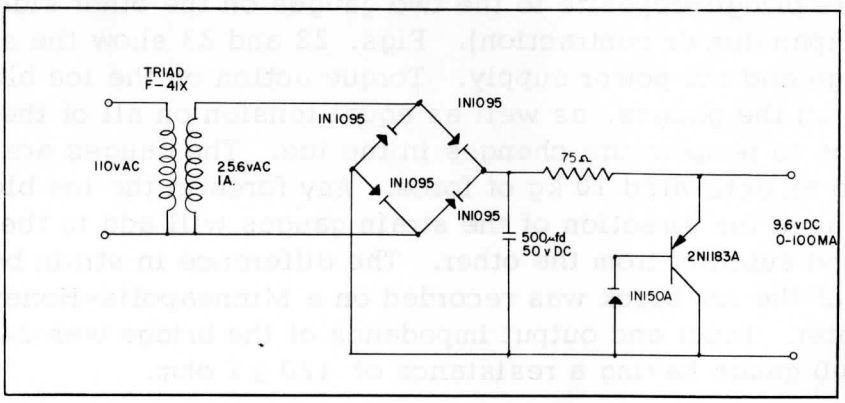

Fig. 23. Power supply for strain-gauge bridge.

The definition of Young's modulus of elasticity gives the following relationship between stress and strain:

$$E_y = S/E \ , \quad \text{with} \quad E = \Delta L/L \quad \text{and} \quad S = F/A \tag{14a}$$

where E = unit axial deformation or strain, E_y = Young's modulus of elasticity, S = unit axial stress, L = length of the material in the stress direction, ΔL = change in L due to the stress, F = total force applied, and A = cross sectional area perpendicular to L. Thus,

$$E_y = (F/A)/(\Delta L/L) = LF/A\Delta L \tag{14b}$$

Strain gauges made of constantan foil with epoxy backing are used to determine the stress by measuring the change in resistance (R) of the strain gauge applied to the strained material,

$$\Delta L/L = C\Delta R/R \ , \tag{15}$$

where C = constant of the strain gauge material (is of the order of 2), ΔR = change in resistance of the gauge due to strain, and R = gauge resistance. Solving for F,

$$F = E_y A C \Delta R/R \ . \tag{16}$$

Four active gauges, two in contraction and two in expansion, are used in a Wheatstone bridge. The relationship between input and output voltage as a function of gauge resistance is

$$e_0 = V \cdot (\Delta R/R) \cdot R_g/(R + R_g) \tag{17a}$$

where e_0 = output voltage of bridge, V = applied voltage, and R_g = detector resistance. When R is small in comparison with R_g, and equation (16) is considered,

$$e_0 = V \cdot \Delta R/R = V \cdot F/(A \cdot E_y \cdot C) \ . \tag{17b}$$

Table 1. Young's modulus and tensile strength for selected material.

Material	Young's Modulus 10^{11} dynes/cm^2	Tensile Strength lbs/inch^2
Aluminum	7.0	30,000
Brass	9.0	50,000
Monel metal	17.0	80,000
Titanium	11.0	50,000

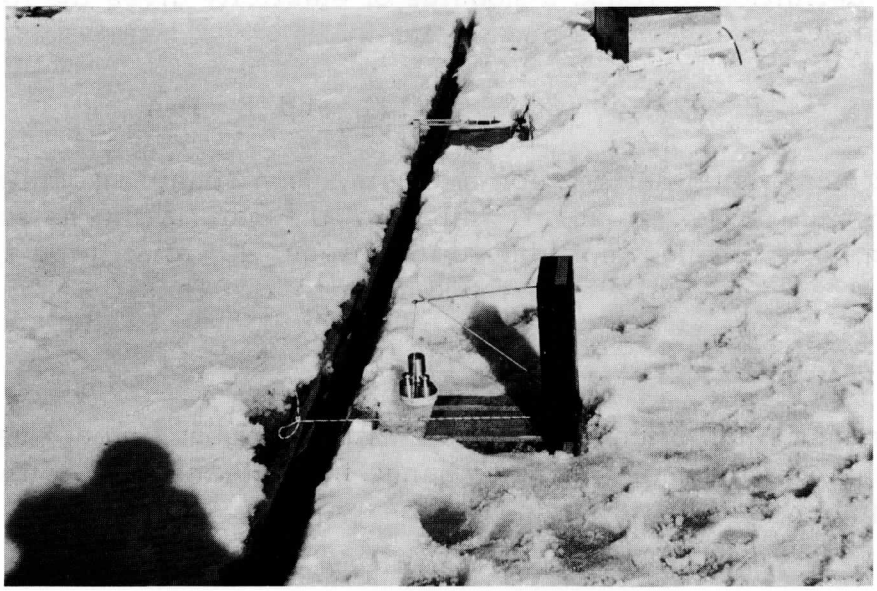

Fig. 24. Calibration system for ice block drag measurements.

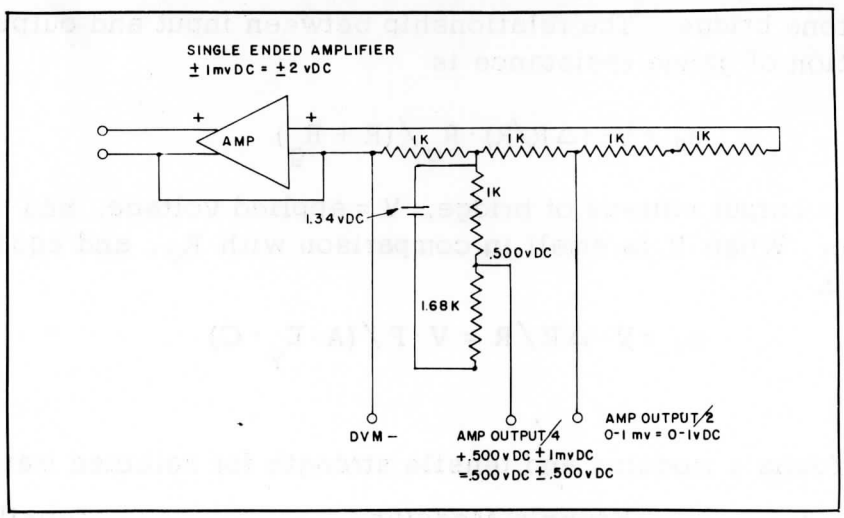

Fig. 25. Amplifier input and output at tower.

Titanium was selected as the strain gauge base material because it was available in sheets 0.005 cm thick. Strips of 1 cm width of this base material were used so that $A = 0.005\ cm^2$. Additional factors such as the bonding cement, epoxy between the base material and strain will contribute to output reduction. Upon solving equation (17b) for F,

$$F = e_0 \cdot A \cdot E_y \cdot C/V; \quad \text{or} \quad F = R_0 A E_y C(R_g + R)/V R_g, \quad \text{when R is not small.} \quad (18)$$

For $V = 10$ vdc and $e_0 = 10^{-3}$ vdc, the force per milli-vdc output is obtained for these titanium strips as 1.1 kg if R is small in comparison with R_g. The sensitivity of 1.1 kg/milli-vdc was not realized in practice. The detecting circuit used had $R_g = 240$ ohms and $R = 240$ ohms, which resulted in $F = 2.2$ kg/milli-vdc. Direct calibration of the ice block gave a value of 10 kg/milli-vdc. This relatively low output may be due to several causes: (1) Epoxy bonding cement materially increased the thickness of the base material and is highly rigid; (2) with thin material the strain gauge itself will increase the values of A and reduce E_y; (3) slow stretching of the titanium base material may have reduced the output by separating the strain gauge from the base material — certainly it shifted the zero value of the strain gauges and may have loosened part of the gauge from the base material.

Titanium cannot be recommended as a base material for future work with strain gauges because, at stresses of less than half the tensile strength, stretching takes place and the material no longer obeys Hook's Law of elasticity. This must result in zero-drifts if the gauges are subjected to high strains. Using the tensile strength of 50,000 lbs/inch^2 and an area of 0.001 inch^2, the maximum strain would be 50 lbs. In the 1962 tests, this was exceeded many times by the gauges used on the ice block. Stretching may occur at stresses of the order of 25 lbs.

Calibration of the drag recorder is aided by a simple lever that converts horizontal tension to vertical pull. This arrangement is shown in operation in Fig. 24. Weights are placed on the pan of the lever which converts vertical to horizontal pull. The frame is placed on the surrounding ice and kept from slipping by nails through the bottom which penetrate the ice. The weight arm is attached to the drag block at the center of one side by a light cord. The recorder reading is noted before and after weights of 1 to 5 kg are placed on the pan during a period of calm air. When one drag component has been calibrated, the process is repeated on the other side of the drag block.

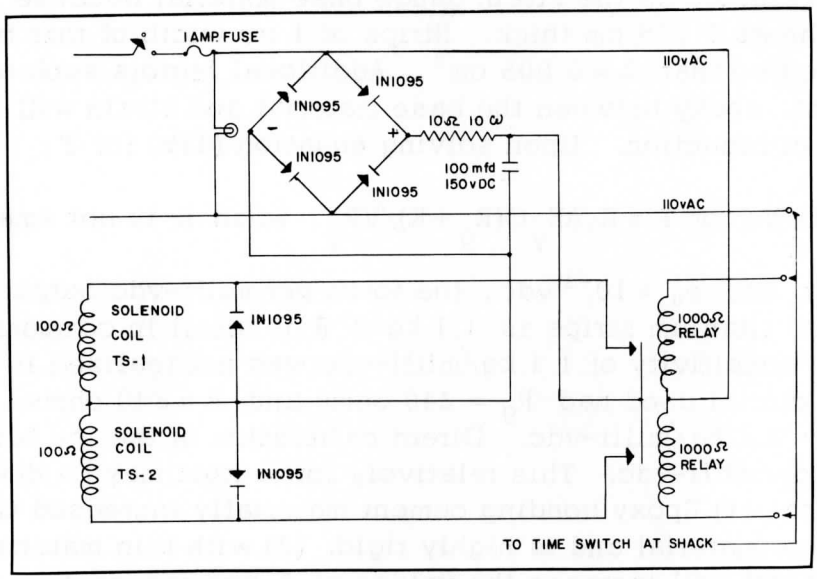

Fig. 26. Tower switch power supply and trigger.

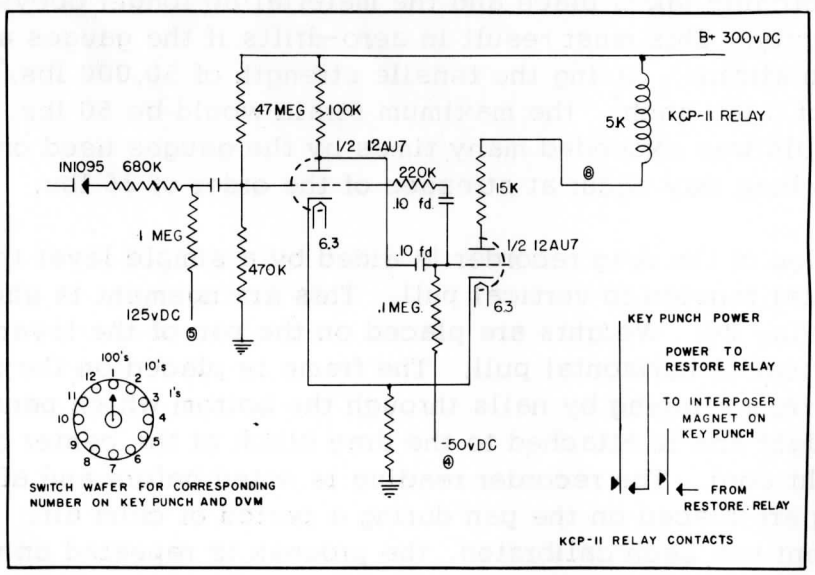

Fig. 27. Monostable multivibrator for read-out of digital voltmeter.

2. 4 Details of Signal Transmission and Recording

2. 4. 1 Tower switches and amplifier

The remote location of the sensors from the recording building requires the amplification of all signals below one milli-vdc. This is achieved by a Minneapolis-Honeywell Accudata II amplifier located at the tower. Fig. 25 illustrates the amplifier input and output circuits. The tower switches operated from shore select the desired channel for recording. Standard signal levels are 0 to 1 milli-vdc, ± 1 milli-vdc, 0 to 1 vdc. The 0 to 1 milli-vdc and ± milli-vdc are converted to 0 to 1 vdc by the amplifier as the signal detected and recorded by the digital voltmeter at the instrument building is in the range 0 to 1 vdc.

Two 24-position solenoid-driven switches are used. One switch provides three sets of terminals, two for inputs to the amplifier and one to provide inputs from either the amplifier or other sensors in the range 0 to 1 vdc for transmission to shore. Thermistors and wind direction are in the range of 0 to 1 vdc. Fig. 26 shows the scheme of the Tower Switch Drive. The second switch provides two sets of terminals for the range of either 0 to 1 milli-vdc or ± milli-vdc to the amplifier. Either the first or second switch may be selected for recording from the instrument building.

The amplifier switches and terminal strips are housed in a metal box which bolts to the south side of the tower. We refer back to Fig. 5 for an illustration of the box layout. A typical connection to the terminal strips may be shown in Table 2.

2. 4. 2 Digital voltmeter recording

Two methods are available for recording the Hewlett Packard 405-AR digital voltmeter output: printer and key punch or typewriter. The printer is a Hewlett Packard 531-B designed for operation from the digital voltmeter. For operation of the key punch and typewriter it was necessary to convert the digital voltmeter output to a form suitable for operating the key punch and typewriter. This will be described in Section 2. 4. 3.

The tower switch is operated every 2.4 sec. One second after the tower switch operation the digital voltmeter is triggered to read. At the same time the read-out of the digital voltmeter is initiated with a 0.2 sec delay to allow the digital voltmeter time to complete reading the signal. The output of the digital voltmeter for either 10^2, 10^1, or 10^0 is 25 vdc if the number is "on" and 125 vdc if the number is "off." The output impedance is 500,000 ohms. A set of 10 multivibrator circuits — one for each digit from 0 to 9 is scanned by a motor-driven switch, beginning with 10^2 to 10^1 and 10^0. One multivibrator is connected in turn to the digit in

Table 2. Typical connection to the terminal strips for tower switches.

Switch Position	Tower Switch 1 0 to 1 or ± 1 milli-vdc	0 to 1 vdc	Tower Switch 2 Ice Therm. 0 to 1 or ± 1 milli-vdc
	Output to Amplifier	Output to DVM	Output to Pos. 23 24 on TS-1
1	short	wind dir.	short
2	short	T air	short
3	short	T water	T air
4	short	T dew cell	T_0 cm
5	short	amp output/2	ΔT_{5-15} cm
6	. 900 milli-vdc	"	T_5 cm
7	Solar rad. (down)	"	ΔT_{5-15} cm
8	Solar rad. (up)	"	FP - 10 cm
9	Net radiation	amp output/4	SR (down)
10	short	T. 500 vdc	SR (up)
11	0. 900 milli-vdc	"	T_{15}
12	$T_{20} - T_w$	"	ΔT_{15-25}
13	$T_{40} - T_{20}$	"	FP 20
14	$T_{80} - T_{40}$	"	SR (down)
15	$T_{160} - T_{80}$	"	SR (up)
16	$T_{320} - T_{160}$	"	T_{25}
17	short	"	$T_{25} - T_{35}$
18	short	"	FP-30
19	short	"	SR (down) 30
20	short	"	SR (up) 30
21	short	"	short
22	short	"	short
23	TS-2 output	"	short
24	TS-2 output	"	short

each of the three decades. The reference voltage from the digital voltmeter for the multivibrator circuits is 125 vdc and, if the voltage applied to the multivibrator is between 125 and 50 vdc, it will not be triggered. If it is 25 vdc corresponding to an "on" number the multivibrator will trigger closing a 2-pole relay for 50 milli-sec. One multivibrator will trigger for each decade of the digital voltmeter. The relay closure will close the appropriate relay for operating the key punch and the typewriter.

Several precautions are taken to prevent punching errors. The power is not applied to the multivibrator relay unless the motor for the scanning switch has been turned on. The motor is turned on by the same pulse that activates the digital voltmeter rather than using the read pulse of the digital voltmeter. Thus, numbers will not be accidentally punched if the digital voltmeter should be triggered by a stray pulse, which will occasionally be encountered. Fig. 27 shows the multivibrator circuit and Fig. 28 the general set-up of the digital voltmeter translator. Fig. 29 illustrates the translator read-out system.

2.4.3 Time and wind read-out to cards

Time, and wind data are recorded on 12 ten-position stepping switches. Time recorded includes year, day (1 to 365), hour and minute. Four decades of wind counts are recorded, then reset to zero after each read-out into card and typewriter. Each position from 0 to 9 corresponds to the same number on the key punch and typewriter. The common wire of each stepping switch is connected to a motor-driven 24-position switch in the proper order for reading time and wind. Recording and read-out details are shown in Fig. 30. The read-out motor allows 50 millisec for each contact-closure and 50 millisec off before the next contact-closure. The contact-closure on deck 1 of the read-out switch closes the relay which operates the key punch and typewriter. Deck 2 resets the wind counters to zero after read-out. This is initiated by turning on the read-out motor by a 35 vdc pulse from the time switch to a relay turning on the motor drive. The motor will make one full revolution, then turn itself off by a cam-operated microswitch. Power to the stepping switches is disconnected during read-out. Read-out time is 2.5 sec for 12 stepping switches and resetting the wind counters to zero.

2.4.4 Key punch and typewriter operation

The key punch is an IBM-024 and the typewriter an IBM-866. The key punch is used to record data on cards for input to a computing machine to convert the data to the proper physical units and to provide averages over desired time intervals. Data is also recorded on the typewriter so that it is immediately available for inspection.

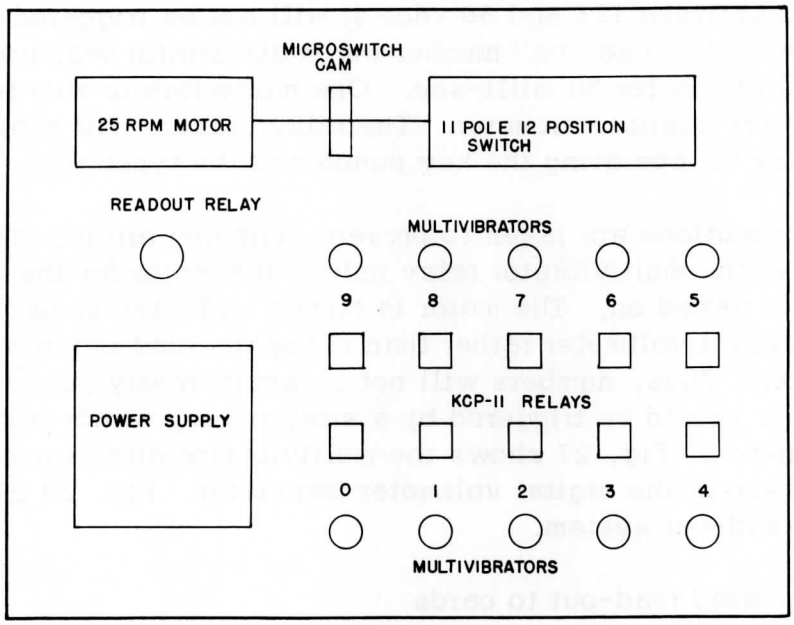

Fig. 28. Layout of DVM translator.

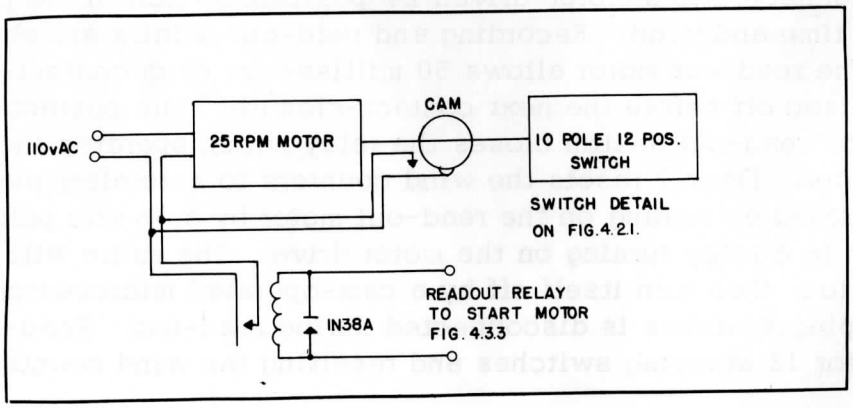

Fig. 29. DVM translator read-out system.
[Fig. 4.3.3 refers to Fig. 30.]

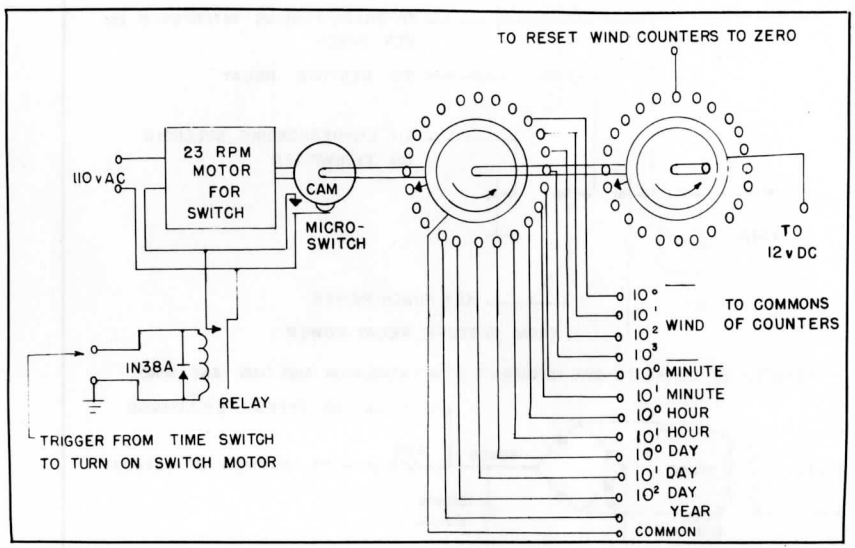

Fig. 30. Read-out of time and wind data.

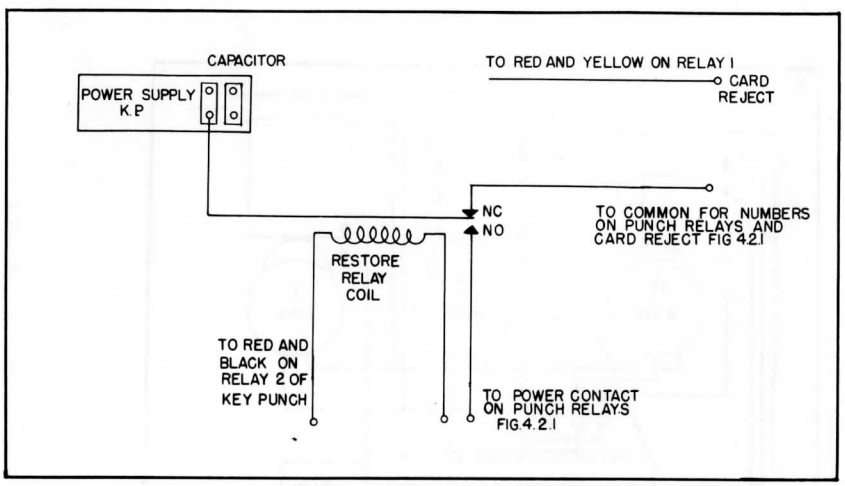

Fig. 31. Method used to prevent double punches on key punch and electric typewriter. [Fig. 4.2.1 refers to Fig. 32.]

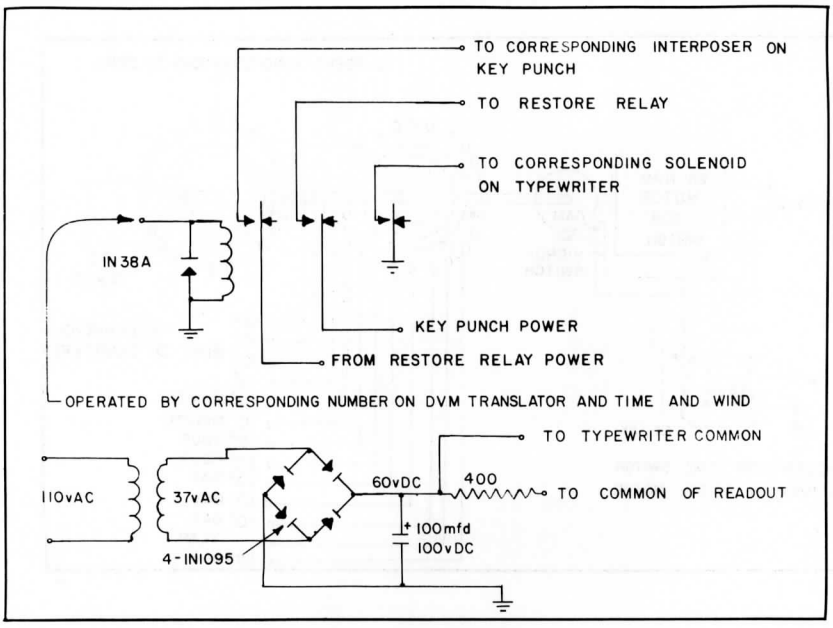

Fig. 32. Operation of key punch and typewriter.

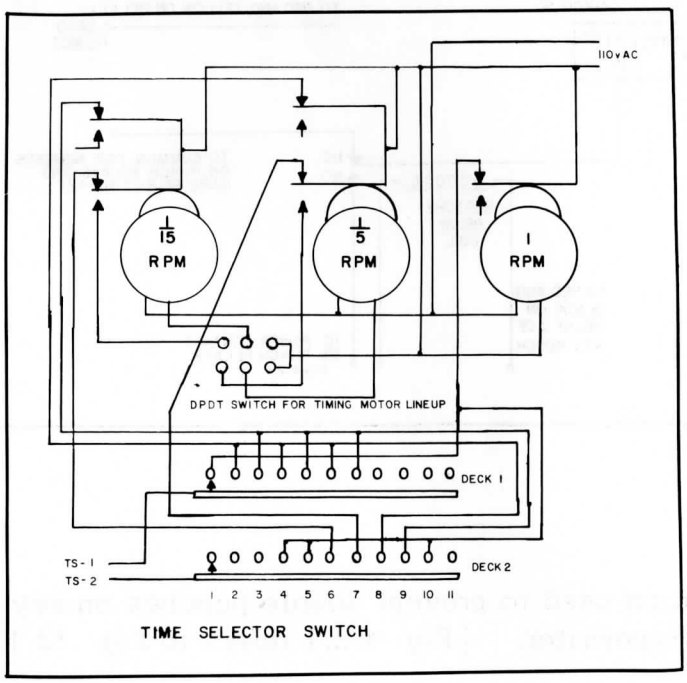

Fig. 33. Time switch and card selection.

The 024 key punch is normally operated from a manual key board. External contact closures with suitable precautions will also operate the key punch. If a lead from the interposer magnet for any number is connected to the negative side of the power supply, the key punch will continuously punch the number until power is disconnected. A cam-operated contact P-4 will close during the last half of the punch cycle, making a connection to the negative side of the power supply. This contact may be used to break the power to the interposer magnet by operating a relay to open the interposer magnet circuit. The relay must keep the power to the interposer magnet disconnected as long as the external contact for the interposer magnet is closed. Fig. 31 shows the details of the key punch restore-relay which is activated by the P-4 contact and remains closed as long as the interposer magnet closure is maintained. The card release circuit is also controlled by the restore relay.

The operation of the IBM-866 typewriter requires a 48 vdc pulse to the appropriate relay to initiate the typing operation. The information for read-out of data to cards and typewriter is a contact closure on the appropriate number. This contact closure operates a 24 vdc relay providing three contact closures. One contact closure operates the key punch interposer magnet. The second contact closure connects power to the restore relay, thence to the key punch and typewriter. The third contact operates the typewriter. Power to the typewriter and key punch is supplied through the restore relay. Thus the restore pulse from the key punch prevents double punches on both the typewriter and key punch. This system is also used for card release and typewriter carriage return. (See Fig. 32.)

2.4.5 Time switch

The punch card and typewriter recording system requires a timing circuit to initiate the recording cycle. This is done by three timing motors of 1/15, 1/5 and 1 rpm, each of which closes a microswitch contact for less than one minute during each revolution. Fig. 33 shows the timing circuit, and the possible combinations of two separate data cards. Selection of the ten possible operations is done by a manually operated switch. It is essential that the motors be timed together. This is done by the motor lineup switch, which when in the operating position allows the 1/15 and 1/5 rpm motors to remain on until they turn themselves off through the cam-operated microswitch. This requires a maximum of fifteen minutes. When the one rpm motor operates its microswitch, the motor lineup switch is returned to the operate position and all microswitches operate together at 15 minute intervals. The second set of microswitches on the 1/5 and 1/15 rpm motors are timed to operate their microswitch more than one minute after the first microswitch in order to initiate the second card recording. Card 1 and card 2 may also be interchanged.

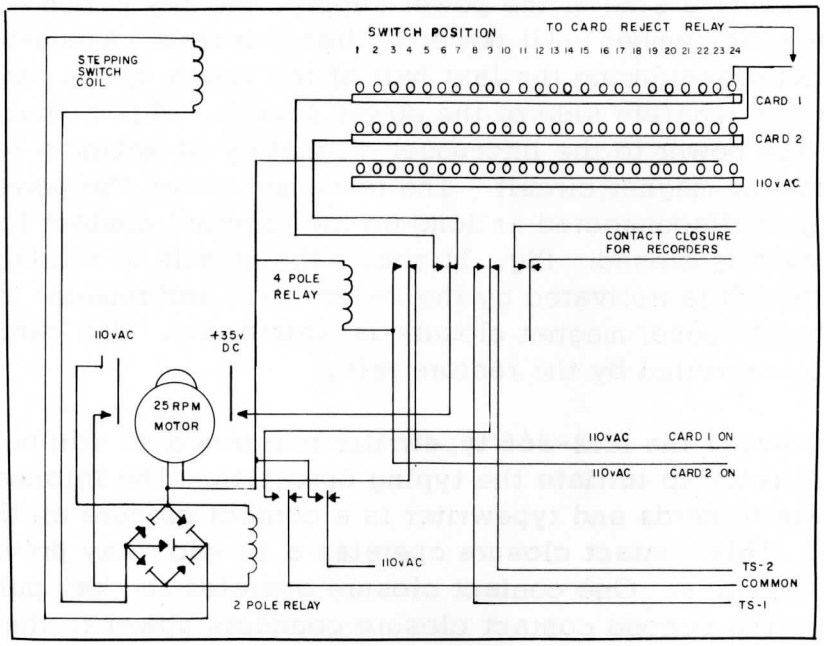

Fig. 34. Method of triggering read-out of time, wind data, and digital voltmeter.

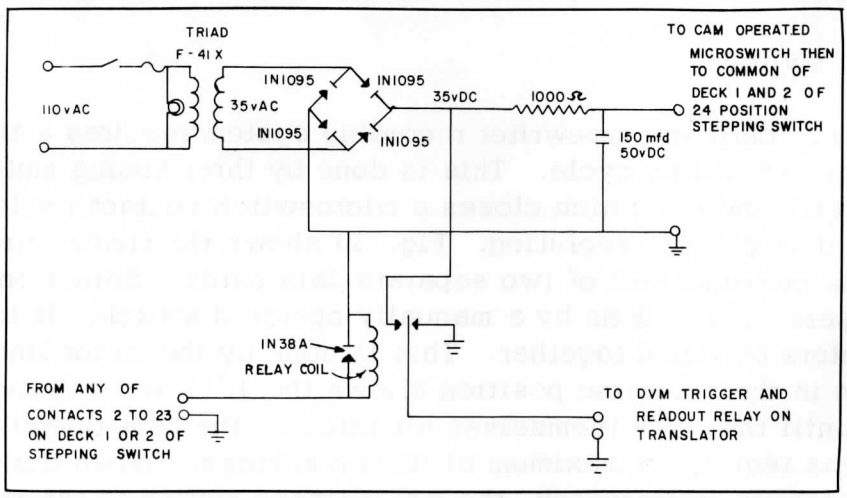

Fig. 35. Power supply for delivering 35 vdc pulse to read-out onto cards and typewriter.

The "on" signal is used to turn on a 25 rpm motor. The motor operates two microswitches, one of which operates a 24-position stepping switch and the other operates the read-out trigger one-half revolution later. Once the stepping switch has been stepped one position, the motor will remain on until a total of 24 steps have been made. A 4-pole double-throw relay is closed for card 1 and remains open for card 2, thus selecting the one of two channels for the read-out pulse, and which of the two tower switches to be triggered in synchronism with the 24-position stepping switch. The 2-pole double-throw relay which triggers the tower switches also maintains the power to the 25 rpm motor as long as the stepping coil microswitch is closed. Otherwise tower switch 2 may be triggered after tower switch 1 and the data will no longer be recorded in the proper sequence. Two channels on the stepping switch are used to direct the 35 vdc read-out pulse for the two separate cards. Position 1 will usually read out time and wind on one card, but may only read time on card 2. Positions 2 to 23 (or less) may read out the digital voltmeter. Position 24 on both cards is used to reject the card from the key punch and to return the typewriter carriage. An additional contact closure on the 4-pole double-throw relay is used to turn on a strip chart recorder for the "on" period during card 1. Details are shown in Fig. 34.

Fig. 35 shows the 35 vdc power supply and the digital voltmeter trigger circuit. Capacitor discharge is used to prevent relay closure for periods of time long enough to cause other parts to overheat.

2.5 References

1. Tanner, C.B., and V.E. Suomi. "Lithium Chloride Dewcell Properties and Use for Dew-Point and Vapor-Pressure Gradient Measurements," TAGU, Vol. 37, No. 4, Aug. 1956.

2. International Business Machines Corp.'s "Wiring Diagram for 024 Key Punch," 1952.

3. International Business Machines Corp. "IBM Input-Output Writer," 1961.

4. Hewlett-Packard Co. "561B Digital Recorder," 1960.

5. Hewlett-Packard Co. "405AR Automatic DC Digital Voltmeter," 1959.

6. C.W. Thornthwaite Associates. "Operating Instructions for Wind Profile Register System," June 1959.

7. Lettau, H.H., and B. Davidson, eds. Exploring the Atmosphere's First Mile, Vol. 1, Pergamon Press, Inc., New York, 1957.

8. Suomi, V.E., M. Franssila, and N.F. Islitzer. "An Improved Net-Radiation Instrument," Journal Meteor., 11, 276-282, 1954.

Scanner's note:

This page is blank.

3

Spatially Continuous Measurements of Temperature Profiles Through an Air-Water Interface*

Harry L. Hamilton, Jr.

Department of Meteorology
University of Wisconsin

Abstract. A piece of apparatus was constructed to sweep a single temperature sensor through a vertical distance of 2.8 m. With this apparatus temperature distributions on both sides of a lake surface, established under various atmospheric conditions, were recorded and studied. The observed distributions were found to be in disagreement with a logarithmic profile close to the water surface.

The most consistent empirical findings were that the temperature in the lowest 20 cm failed to show a gradual approach to the water temperature. Most of the profiles suggested a true discontinuity. With the water warmer, or colder, than the air there appeared to be no gradient-type heat transfer in the investigated layer.

List of Contents

3.0 Introduction

3.1 Equipment
- 3.1.1 Mechanical Lift
- 3.1.2 Electrical System for the Lift
- 3.1.3 Sensing Element
- 3.1.4 Recording System
- 3.1.5 Calibration
- 3.1.6 General Notes

---

*Part of this work was submitted to the University of Wisconsin in partial fulfillment of the requirements for the degree of Master of Science.

3.2 Theoretical Background

3.3 Observations

3.4 Conclusions

3.5 References

3.0 Introduction

It has long been realized that the conventional method of obtaining the temperature distribution in a layer of air near the earth's surface, that of using a series of sensors at fixed levels within the layer, has several defects. These defects include: unknown temperature between sensors, derived only by interpolation; the need to calibrate and know or match the characteristics of several sensing elements; the possibility of dissimilar, erratic pick-up in the cabling of each sensor; and the expense of a multi-channel recorder or the difficulty in synchronizing a series of recorders. Besides encountering the inherent weaknesses of the system, temperature profile studies with fixed sensors above and below water surfaces face added difficulties. If the sensors are inoperable when wet, the experiments can be conducted only during quiescent periods. If immersible sensors are used over a non-stationary water surface, much additional equipment is needed to relate the water level to each sensor at any given time.

Therefore, to study adequately and efficiently the temperature distribution very close to a non-stationary water surface, an instrument is desired whereby a single, immersible sensor may be moved through the entire layer under study. The method would eliminate all spatial interpolation, since the sensor would operate at all levels; only one element need be calibrated; electrical noise could be picked up from only one source; and only one single-channel recorder would be required. By being immersible, the sensor also could be used to study the temperature structure below the surface.

The method of sweeping a single sensor through a layer of air was apparently first described by A. H. Glaser (1957), but similarity between his equipment and that used in this study is in general principles only. Briefly, his procedure was to rotate a temperature sensor on the end of a 3.6 m shaft. The path of the sensor described a vertical circle, extending from near ground-level up to about 7.2 m. The linear speed of the sensor, which had a response time on the order of milliseconds, was 375 cm/sec. The sensor output was amplified and put on the horizontal input of an oscilloscope. A signal proportional to the logarithm of height was put on the vertical input of the oscilloscope. The resulting traces were then photographed with a Polaroid camera for later study.

The procedure reported in this paper was to move fine-wire thermocouples in a straight line through a 2.8 m layer of air and water. The signal from the sensor was amplified and put on the horizontal input of an oscilloscope, and a voltage directly proportional to height was put on the vertical input; the resulting traces were photographed automatically on 35 mm film for study.

3. 1 Equipment

3. 1. 1 Mechanical lift

The frame of the lifting apparatus was constructed of L-shaped, one-eighth inch thick slotted aluminum pieces and had the following dimensions: length, 4 ft.; width, 3 ft.; and height, 8 ft. The 20 ft. boom was made from the same material as the frame. The motor supports and most other moving parts were of rolled steel.

A reversible, 3.6 rpm motor powered a link chain by means of one of three sprocket wheels. The chain was connected to the boom at a point 8 feet from the front end and 4 feet from the pivot point. The rear portion of the boom acted as a counterbalance. Two vertical channel irons forced the boom to move vertically at its point of attachment to the chain. This required that the pivot point be able to move backward and forward a few inches as the boom moved up and down. This was accomplished by having the pivot shaft hinged to the main frame. The sensor-holder was hinged to the boom and connected to an extension of the pivot shaft by means of a thin wire, in order that the sensor be held in the same orientation relative to the ground at all levels of the sweep path. The three sprocket wheels were constructed as a unit. This sprocket assembly and the motor were movable, so that proper chain tension and alignment could be maintained when any one of the three sprocket wheels was in use. The rates of lift were 3.5, 7.0, and 14.0 cm/sec. The size of the frame allowed the chain to move a maximum of 100 cm in lifting the boom.

3. 1. 2 Electrical system for the lift

An electrical system was needed to operate the apparatus. Because of the size of the boom and certain operating conditions, the system was simple but extensive. During each experiment the frame and all accessories were on a barge stationed $\frac{1}{4}$ mile from shore on Lake Mendota. On all but very calm days wave action produced marked stresses and strains on all components.

The lift motor was turned on and off through a 4-pole. 3-position rachet relay. This relay was fired by a 2-pole, 2-position relay, which

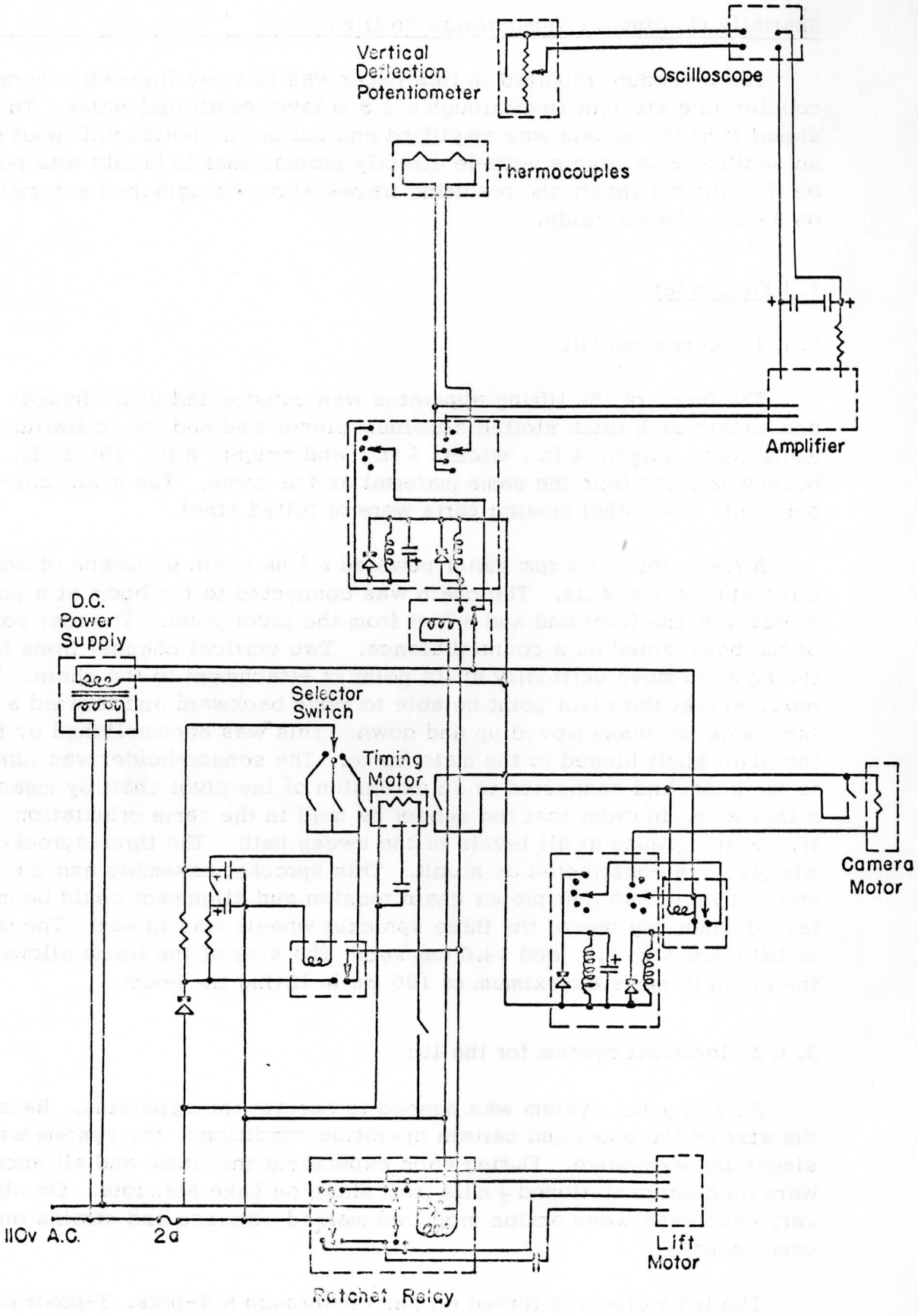

Fig. 1. Electrical circuitry.

was fired by either of two capacitor circuits. One of these circuits, with a charge-up time of about 40 seconds, was fired when the boom, nearly at the bottom of its sweep path, closed a microswitch. The other circuit, with a charge-up time of five seconds, was fired when a timing-cam closed a microswitch. Each sprocket wheel had a cam cut for it such that the sweep path of the boom was the same. Complete up-and-down cycles of the sensor could be made in one minute using the large sprocket, in two minutes using the intermediate size, and in three minutes using the small one. All three cams were driven on the same shaft by a clock motor, each one operating a different microswitch. Selection of the cam and microswitch to be used to fire the capacitor circuit was determined through a selector switch.

Each cycle consisted of four phases: boom moving up; pause at highest position; boom moving down; and pause in lowest position. The times spent in each portion of the cycle were such that the requirements listed above were fulfilled.

The timing cams started the boom up, stopped it at the top, and started it down. The boom stopped itself at the bottom by hitting a microswitch, previously mentioned. It was originally intended that timing cams would give all commands, but this was found to be impossible. Although the boom was counterbalanced, the rate of ascension differed slightly from the rate of decension, the difference depending on which sensor was being used and to what extent the entire frame was being jostled by wave action. Since this difference in rates varied, it was impossible to cut cams to allow for it, and a position switch became necessary. The circuits can be observed in Fig. 1.

3. 1. 3 Sensing element

A temperature-sensing element which could function in water or air, and which had a relatively short response time, was desired. The type constructed to meet these requirements was a set of fine-wire thermocouples. The element consisted of five copper-constantan thermocouples in series. Each junction was made by soldering #44 copper wire to one-mil constantan, resulting in a junction diameter of about four mils. The distance between the measuring junction and the reference junction varied from 8 feet to 12 feet, necessitating long lead-off wires of a heavier gauge. Leeds and Northrup #30 wire was used, being connected to the thermocouple wire about four cm from each junction.

The junctions were in a cross arrangement, supported by $\frac{1}{4}$inch plexiglas, as shown in Fig. 2. To avoid as much solar radiation as possible, four radiation shields were added, two above and two below the junctions. The sides away from the junctions were covered with aluminized mylar, the sides towards the junctions being coated with flat black paint.

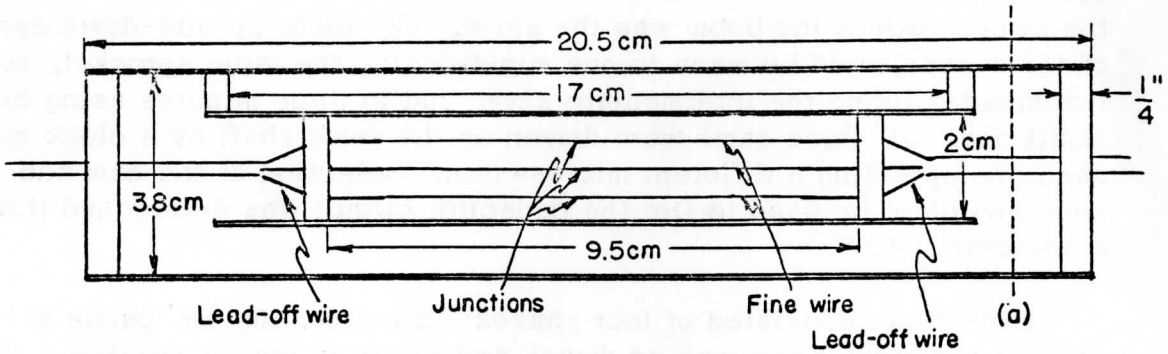

SIDE VIEW

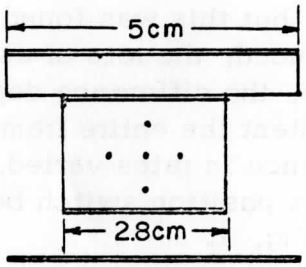

END VIEW through (a)

Fig. 2. Radiation shields and thermocouples.

The thermocouples were made of fine wire for two reasons. First, only a small cross-sectional area would be exposed to any radiation which got past the shields. Second, by having small mass they would respond quickly to slight temperature changes, allowing the small, rapid fluctuations of air temperature to be observed. Tests indicated that the response time, the time taken by the thermocouples to attain a (1 - 1/e)th part of the total change from one output to another, was 0.2 sec.

It was found that thermocouples of this size presented a fairly complete picture of temperature distribution in the air. Smaller wire, having a shorter response time, probably would have revealed a finer structure. But another problem presented itself when this was considered. During each cycle the thermocouples were plunged into and withdrawn from the water. The water exerted a considerable force on the wires, causing frequent breaking. Smaller wire could be even more prone to breaking due to this wear and tear of the water. Further air-water experiments with this apparatus will probably sacrifice some of the current response time for more durable sensors, since the ones described here averaged only some four hours of life on being plunged into the water in this manner.

No artificial ventilation was used. On all observational runs, there was a wind of at least 2 mph; see Section 3. 1. 6. Since the thin radiation shields presented a very small obstacle to the wind, at least 1 m/sec ventilation can be assumed. The vertical motion also produced eddies of air bubbling over the top or bottom of the shields, further assuring that there was no stagnant air at the thermocouples.

3. 1. 4 Recording system

The output of the thermocouples was in the range of millivolts, a voltage too small to be displayed on the oscilloscope. A precision (0.2% accuracy) d-c amplifier served not only to amplify the signal, but also to filter out a great deal of noise. The amplifier was a commercial type, the Accudata II, made by Minneapolis Honeywell. A multiplication factor of 200 was found to be quite satisfactory.

Two noise-suppression features of this amplifier were important. One provided that any noise common to both input leads (positive and negative) would be filtered out and not passed on in the amplified signal. The second was that the amplifier was mounted in two cases, electrically insulated from each other. The outer case was at ground potential. The inner case was connected to one lead of the output. This inner case was also connected to the lake water, so that zero output was actually the ambient potential of the water. This arrangement had the effect of eliminating the numerous stray signals always present in the lake.

After amplification, the signal went through another filter circuit before arriving at the oscilloscope. This circuit consisted of two capacitors and a resistor. The two electrolytic capacitors were in series across the amplifier output, their negative ends connected together. The 100-ohm resistor was in the output line, between the amplifier and the capacitors.

From the final filter circuit, the signal went to the horizontal input of a DuMont oscilloscope. The oscilloscope has settings such that the beam deflection along each axis is proportional to the d-c voltage at each input. The variable voltage of a 10,000-ohm, 10-turn potentiometer, powered by a 1.5 v drycell, was connected onto the vertical input. The potentiometer was geared directly to the chain which moved the boom. Thus the image on the oscilloscope screen traced out a path of temperature T versus height z with z increasing upwards and T increasing to the right. Scales and gains on the scope were adjusted for each run so that a large portion of the screen would be utilized.

For reasons to be discussed later, it was desired to observe the sensor response only during its downward motion. Another pair of relays, whose action was timed by the boom movements, shorted out the amplifier inputs at all times except during the downsweep of the boom, at which time the normal circuitry prevailed. This shorting of the input also gave a reference zero-line on each profile. The straight vertical line traced out while the sensor moved up represented the temperature of the reference junction. Deviations of this zero trace from linear gave an idea as to the oscilloscope noise and drift, and also defined the direction of the oscilloscope's vertical axis.

With a grid superimposed on the oscilloscope face, an observer is able to determine whether lapse, neutral, or inversion conditions exist in the layer being sampled. But since only a moving dot of light is visible at any one time, the general slope of T vs z is all that can be deduced. To note minor changes in slope as conditions within the layer change, and to study the magnitudes of the temperature fluctuations, time-exposures of the trace must be taken. Preliminary work was done using a Polaroid Oscilloscope Camera, but most of the photographs were made with an automated 35 mm camera, specially constructed for this purpose.

A 6 rpm motor was mounted on the side of the camera box, with its drive shaft running into the camera and connecting with the film advance. Also connected to this drive shaft, outside the camera, was an off-center cam arrangement. A lever joined this cam to the shutter mechanism. Each time the shaft rotated one time, the shutter opened and closed. A timing circuit, synchronized with the boom movements, allowed time exposures of 3, 6, or 9 minutes. The cycle was as follows, assuming the shutter open initially: the boom activated a relay, which started the camera motor;

as the film advanced, the shutter closed briefly, then reopened; the relay opened, stopping the motor and the advance of the film. The process took exactly 1 revolution of the camera motor, or about 10 seconds, and advanced the film 1 frame. It was arranged so that the boom was in the lower part of its cycle, and stationary most of the time during picture change.

A minor fault with this system should be noted. For about one second at the beginning of the cycle, and one second at the end, the film was moving while the shutter was open. This was unavoidable unless a much more elaborate mechanical system had been devised. A new system was not attempted because this defect was not too serious.

3. 1. 5 Calibration

Each of the two thermocouple junctions was placed in a large vacuum bottle filled with water. Motor-driven agitators thoroughly mixed the water. Precision mercury-in-glass thermometers, readable to 0.03° C, were used to obtain the water temperatures. The output of the thermocouples was obtained from a digital voltmeter, readable to three places, with ∓ 1 digit accuracy. Warmer water was occasionally added to one bottle. When equilibrium had been reached, the temperature of both baths and the output voltage were recorded. In this fashion a curve of output voltage vs T was obtained over a range of 4° C to 24° C. It was very nearly linear, having a slope of 0.20 mv/° C for the five junctions in series.

To determine the response time of the thermocouples, one junction was placed in a jar of thermally homogeneous water, the other in the air, and the output recorded on a Visicorder. Then the junction in the air was suddenly plunged into another water bath several degrees colder than the air. By repeated trials and a study of the Visicorder trace a consistent value of 0.2 second was derived. The question was then raised as to whether the response time would be the same when the air temperature changed rapidly as when the temperature change occurred as a result of a change of medium. Therefore, another series of tests was run, again with one junction in a jar of thermally homogeneous water, but this time the other junction was moved from very warm air to cool air. The junction was placed in the airstream of a hot air blower, then a shield was dropped between the blower and sensor. The output was studied on a Visicorder, and again a value of 0.2 second was found.

3. 1. 6 General notes

The filter circuits described above eliminated most of the noise that would prevent a coherent signal from being displayed on the oscilloscope, but some noise did get through. At the top and bottom of each trace there was a line shooting off to the left. This was a disturbance picked up

from the relays which started and stopped the boom. It was distracting, but did not render analysis impossible. A more serious stray signal was very erratic and of unknown origin. A sharp spike to the left sometimes appeared as the sensor entered or left the water. Considerable effort to eliminate its appearance failed. On the September 9 run, a broad, light, vertical line was found on most pictures. It appeared on no other runs and its source remains unknown.

This study was mainly qualitative, hence exact calibration of the pictures was not attempted. The apparatus was arranged so that the sensor was upwind to the average flow during each run. The maximum height of the sweeps was about 200 cm above the lake surface, while the minimum was about 80 cm below the surface. Each run was made within 30 ft. of the University of Wisconsin Meteorology Department tower on Lake Mendota; reference is made to Section 2. This tower has thermocouples at 20, 40, 80, 160, and 320 cm, as well as at 15 cm in the water. Their output is monitored every minute. Rough calibration of the pictures in this study was made by assuming that over a one-minute period the air temperature at the moving sensor and the air temperature at the tower would be within 0.1° C of each other.

All wind and temperature values mentioned in this report were obtained from the Meteorology Department tower on Lake Mendota. When the term "water temperature" is used, it refers to the water temperature 15 cm below the surface. "Air temperature" refers to the temperature 20 cm above the surface. Wind direction and velocity were taken at a height of 5 m. Aerodynamically, water is a relatively smooth surface; therefore, wind speed decreases only slightly at lower levels, down to the lowest few centimeters. Direction, velocity, and temperature values are 20 min averages centered on the beginning of any profile to which they refer.

When observations were first taken, the temperature fluctuations were displayed on the oscilloscope when the sensor was moving up from the water as well as when it was moving down from the air into the water. Although the thermocouple wires were very fine, tiny droplets of water clung to them as the sensor left the water. In the air, the droplets quickly evaporated, cooling the thermocouples below air temperature. It was found that the drying of the wires took somewhat less than one minute even on days when the relative humidity was high. After brief analysis of several observational runs with the evaporative effect present, it was decided that this study would not deal with that phenomenon.

An attempt was made to coat the wires with water-repellent material which would not add substantially to the response time of the system. A silicone compound was brushed onto the wires and proved satisfactory as

long as the silicone remained. This method was abandoned when it was found that the repeated immersing of the wires quickly washed away the silicone. The remedy finally adopted for eliminating the evaporation trace was to short out the amplifier input at all times except on the sensor downsweep. The wires had a drying time short enough so that they were dry by the time the sensor was ready to start each downward sweep.

A characteristic of all temperature profiles obtained with a very responsive sensor is the presence of fluctuations. The temperature at any given level is not constant, making it difficult to assign a specific value to it. The best that can be done is to attempt to derive the average temperature about which the fluctuations appear to occur. It is in this sense that the profiles in this report are described. The terms inversions, lapse conditions, maxima and minima refer to actually imaginary curves derived by averaging and smoothing of several recorded profiles, but this was not done using only the photographs shown here. Scores of consecutive photographs were studied, and from them typical profiles inferred. The photographs shown here are ones in which the fluctuations most closely oscillate about the typical profiles.

These profiles illustrate the difficulties that would be encountered if truly quantitative analysis were attempted. Less sensitive components should be used so that the small, rapid fluctuations are not detected, and smoothing is done by the equipment. But for qualitative studies, fast sensors have a great deal to offer.

3.2 Theoretical Background

The generally accepted assumption concerning the temperature distribution above a heated surface is that the profile within the lowest few meters above the surface is similar to the wind profile. This implies that, to a first-order approximation, temperature is proportional to the logarithm of height. The relationship may be expressed as $T(z) \sim \ln z$, where $T(z)$ is the temperature at height z.

It is obvious that this equation breaks down at $z = 0$. To obtain a relationship which is applicable at all levels, the aerodynamic surface roughness length is considered. The equation now takes the form

$$T(z) - T_0 \sim \ln(z + z_0)/z_0 \quad , \qquad (1)$$

where T_0 is surface temperature and z_0 is the aerodynamic surface roughness length. The value of z_0 can vary from the order of 1000 cm for very rough surfaces to the order of 0.001 cm for very smooth surfaces.

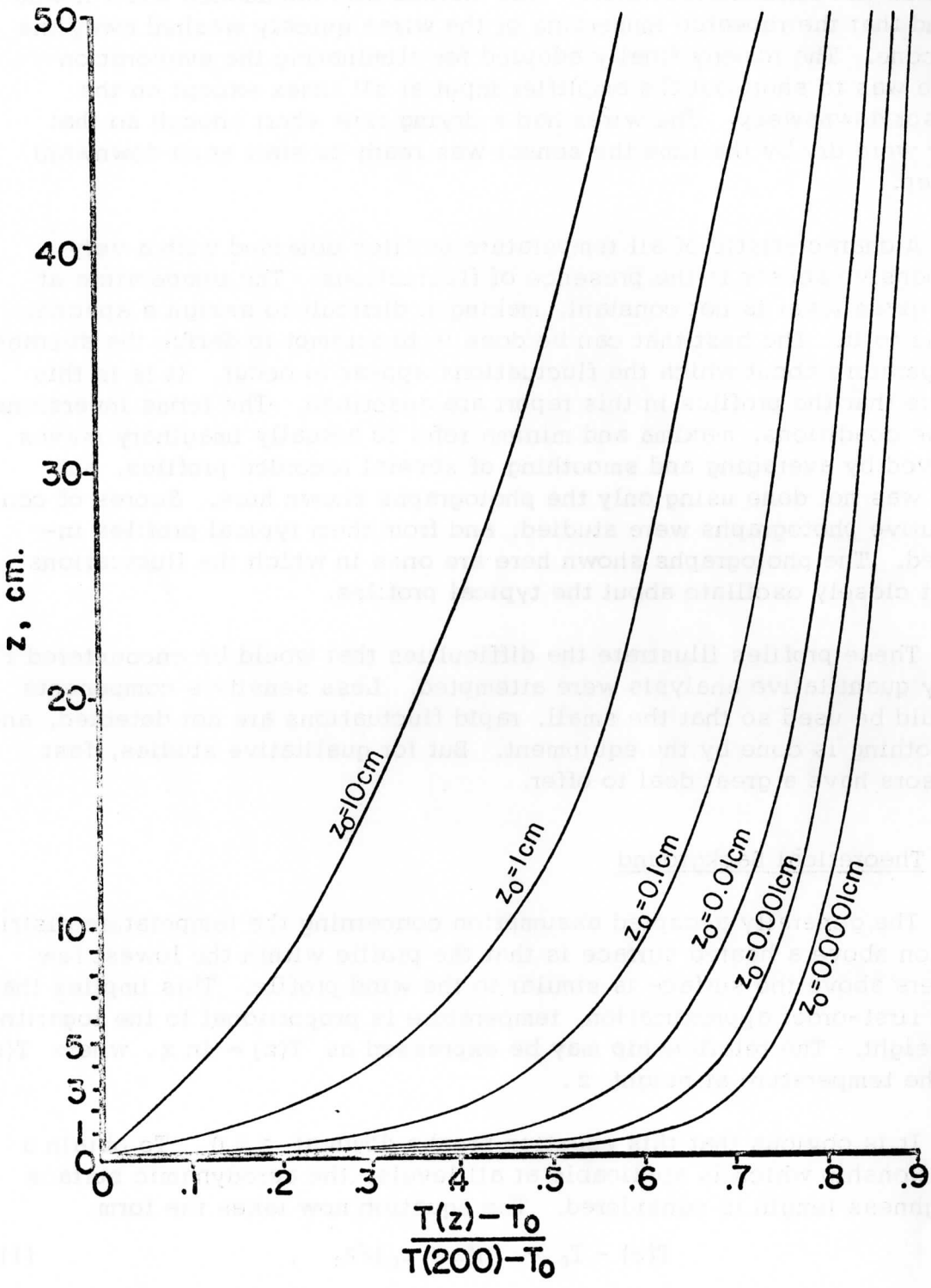

Fig. 3. Logarithmic profiles as a function of z_0, plotted linearly versus height (z).

Sutton (1953, Chapter 3) discusses the results of several investigations into the relationship between surface roughness and turbulent wind flow. Sutton quotes L. Schiller, who found that aerodynamically smooth flow exists when $(\tau_0/\rho)^{1/2} z_0/\nu < 0.2$ (where τ_0 = surface stress, ρ = air density, ν = kinematic viscosity of air, and z_0 is as above); and J. Nikuradse, who found that aerodynamically rough flow requires $(\tau_0/\rho)^{1/2} z_0/\nu > 2.5$. Between these limits is a transition region. During the observational runs, waves on the lake gave ample evidence that the wind was turbulent. For air pressure and temperatures encountered, ν can be taken to be 0.1 cm^2/sec, and if $\sqrt{\tau_0/\rho}$ is assumed to be 10 cm/sec, the smallest value of z_0 that would exclude aerodynamically smooth flow is of the order of 0.002 cm. Wind profile studies at the University of Wisconsin Meteorology Department give z_0 values of 0.01 to 0.001 cm for Lake Mendota, depending on the state of agitation of the water.

These theoretical and observational lower limits for z_0 apply to wind profiles, but it has usually been assumed that the same z_0 would also apply to temperature profiles. However, investigators of temperature distribution over a water surface have rarely used sensors closer to the surface than 20 cm, to avoid wetting the sensors. A search of the literature failed to disclose anyone's empirically checking the logarithmic equation at very low heights.

Small values of z_0 yield logarithmic profiles which have very strong curvature at small values of z, then straighten out and become nearly linear at some distance above the surface. The smaller the value of z_0, the greater the curvature at small z. Fig. 3 shows how the logarithmic profile varies for several values of z_0. To eliminate evaluating the constant of proportionality in the logarithmic distribution, a ratio of temperature differences was used to plot the variation of temperature with height. Since 200 cm was approximately the maximum height of the profile measurement, the temperature difference between this height and the surface was taken as one unit. On the graph is plotted

$$(T_z - T_0)/(T_{200} - T_0) = \log(1 + z/z_0)/\log(1 + 200/z_0) \quad , \qquad (2)$$

for various values of z_0, from $z = 0$ to $z = 50$ cm.

3.3 Observations

Most profiles observed with the moving sensor showed very little curvature. There was an apparent temperature discontinuity between air and water, when the air was warmer than the water as well as when it was cooler. In those cases where some curvature was noticeable, the

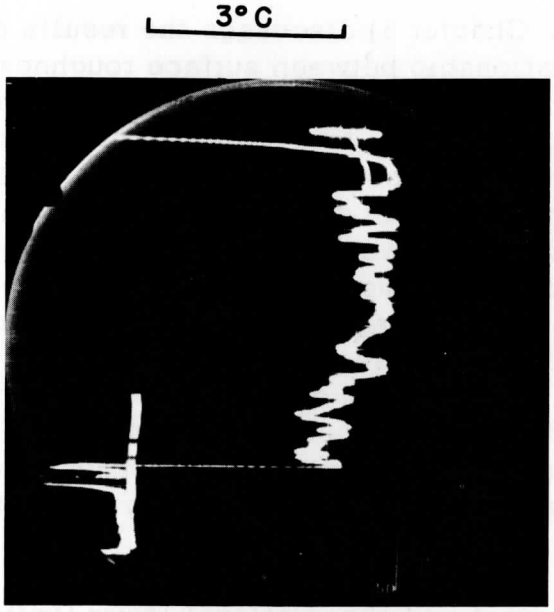

Fig. 4. A single downsweep of the sensor, taken at 2:12 pm on September 9, 1961.

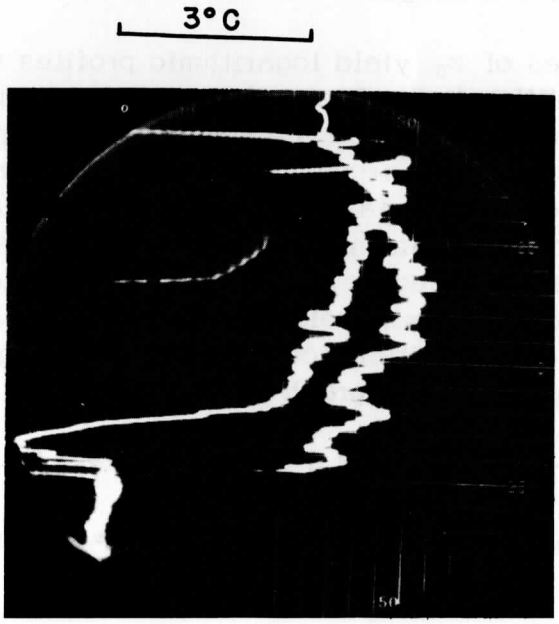

Fig. 5. A downsweep and upsweep of the sensor, taken from 2:34 to 2:37 pm on September 9, 1961.

logarithmic profile agreed with the observation only for an extremely small z_0 of 0.0001 cm or less.

The sensor response time of 0.2 sec could not cause the disagreement. At the speed of travel used for the profile measurements in question, the sensor would cover a distance of 0.7 cm during 0.2 sec. The discrepancies lie not only in the lowest 7 mm, where blurring could conceivably exist, but also in the lowest 5 to 10 cm. If the temperature were actually distributed by the logarithmic relationship, the sensor would detect the curvature, as indeed it did when such conditions apparently existed.

Another explanation could be that warmer (or colder) air was moving out over the water from the land and had not yet reached equilibrium with its new lower boundary when the profiles were observed. This is unlikely in view of the fact that these discontinuities are found when the wind was in a direction such as to give 2 to 3 km of fetch, as well as when an off-land wind gave only $\frac{1}{2}$ km fetch, before reaching the sensor. In all probability a 2 km path over a uniform surface should allow temperature equilibrium to be established, at least in the lower 10 to 20 cm, where the discrepancies arise. However, advective effects cannot be entirely ruled out in view of the fact that the air moves from a relatively rough to a smooth surface and that, actually, neither surface temperature nor roughness structure are completely uniform along the wind fetch over water. A separate investigation of advection processes over Lake Mendota is under way and results will be reported by D. Quick at a later time.

Fig. 4 is an example of this temperature discontinuity. As can be seen, there seem to be two temperature regimes, one in the air and one in the water, with no transition zone between. As a matter of fact, the profile shows the temperature momentarily to increase slightly in the lowest 5 cm of air. At the time of measurement (2:12 p.m., September 9, 1961), the air at 20 cm was about 3.4° C warmer than the water at 15 cm depth. As with all the profiles, about 70 cm of the sensor path was in the water, some 200 cm in the air. Wind was from the southwest, flowing over 2 to 3 km of lake surface before reaching the sensor, at 9 mph. Fig. 4 also shows another interesting detail which frequently occurred when the air was warmer than the water. This is a relative temperature maximum at about 150 cm. The temperature at this height is 1.1° C warmer than the surface air, and 0.4° C warmer than the air at 200 cm.

The day on which this profile was obtained was a warm, sunny day. It is fairly evident that the air sensed by the equipment had passed over long stretches of land which had been heated by the sun. Over the land the profile should show definite lapse characteristics. But upon flowing onto the cooler lake, the lower layers of air began to cool, and eddy motion carried the cooling effect up to about the 150 cm level. It can be

T_{20} = 7.6°C

T_{-15} = 13.6°C

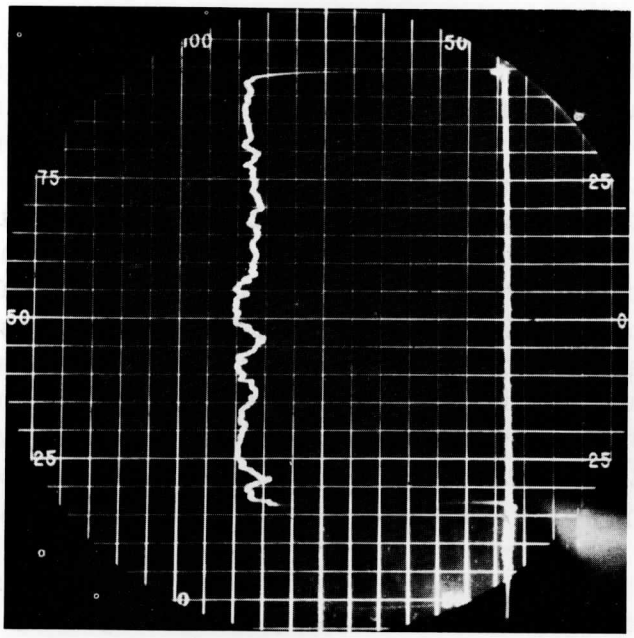

Fig. 6. A single downsweep of the sensor, taken at 2:40 pm on October 21, 1961.

seen on Fig. 4 that the very lowest air layers do not gradually approach water temperature. Note the cooling effect of the water surface due to evaporation. The surface appears about 0.2° C cooler than the water at a depth of 15 cm.

Fig. 5 includes a trace with the sensor moving out of the water as well as going into the water. The upsweep (trace to the left) shows the evaporative effect, a cooling of about 1.7° C. The two traces merge about 180 cm above the surface, indicating that all water has evaporated from the wires by this height. As with Fig. 4, a relative temperature maximum is noted at 150 cm. The profile was observed at 2:34 p.m., September 9, 1961. Water temperature was 24.4° C, air temperature was 28.1° C. Wind was south-southwest at 9.5 mph, having an over-water path of about 1 km.

Fig. 6 was obtained at 2:40 p. m. on October 21, 1961. It represents one of the most clear-cut examples of temperature discontinuity in this study. The air was very nearly isothermal at 7.6° C, while the water was 13.6° C. Wind was almost calm, averaging in speed about 1.5 mph, its direction completely erratic. During the morning there had been a heavy fog, but it was almost entirely gone by the time this profile was taken. With the water warmer than the air, one would expect definite heating through the lower layers, due to turbulence produced by rising warm air from the surface. But there appears to be no gradient-type heat transfer from water to air.

Figs. 7 and 8 are consecutive six-minute exposures. Fig. 7 began at 3:23 p. m., October 21, and Fig. 8 at 3:29 p. m. Two downsweeps of the sensor are recorded on each picture. In spite of their being very close to each other, time-wise, the first profile has a definite, sharp curvature in the lower 10-15 cm, while the second has an apparent discontinuity. Wind direction was erratic, speed nearly 2 mph. Water temperature was 13.5° C, the air was 5.9° C cooler. Fig. 7 represents the profile with probably the weakest curvature of any observed. If a logarithmic profile is compared to it, the z_0 required is approximately 0.0001 cm. Fig. 9 shows the two profiles superimposed.

The first item of note about Fig. 10 is a definite temperature minimum at 45 to 50 cm. The temperature at this level is 0.5 to 0.6° C cooler than it would be by a straight-line interpolation between the water surface and heights about 100 cm. This profile was recorded at 11:11 a. m. on November 4, 1961. A south wind of some 16 mph was almost directly off-land, giving an over-water path of just over $\frac{1}{2}$ km. The water temperature was 8.5° C, the air temperature at 20 cm was 4.5° C. The second point of interest is that Fig. 10 gives some indication as to how an air mass adapts its structure to a non-stationary lower boundary. Waves on Lake Mendota

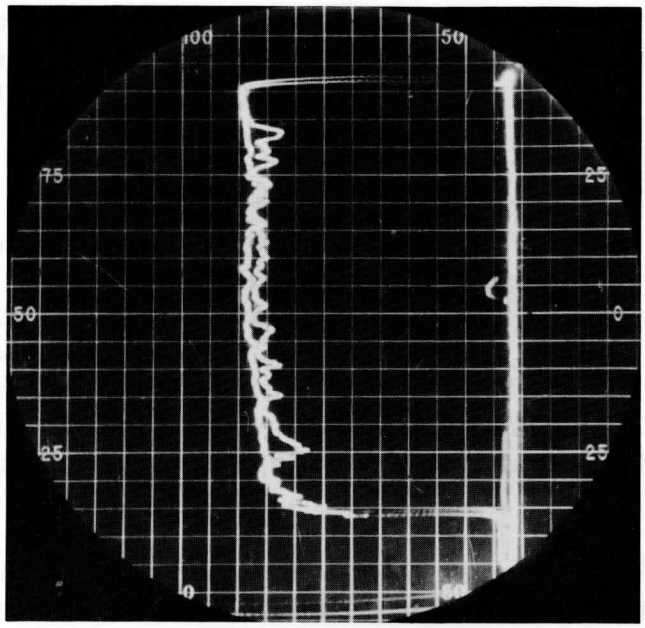

Fig. 7. Two downsweeps of the sensor, from 3:23 to 3:29 pm on October 21, 1961.

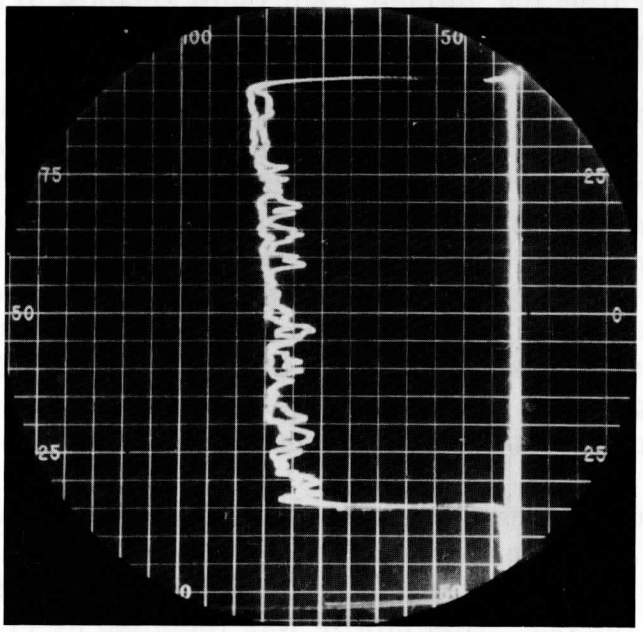

Fig. 8. Two downsweeps of the sensor, from 3:29 to 3:35 pm on October 21, 1961.

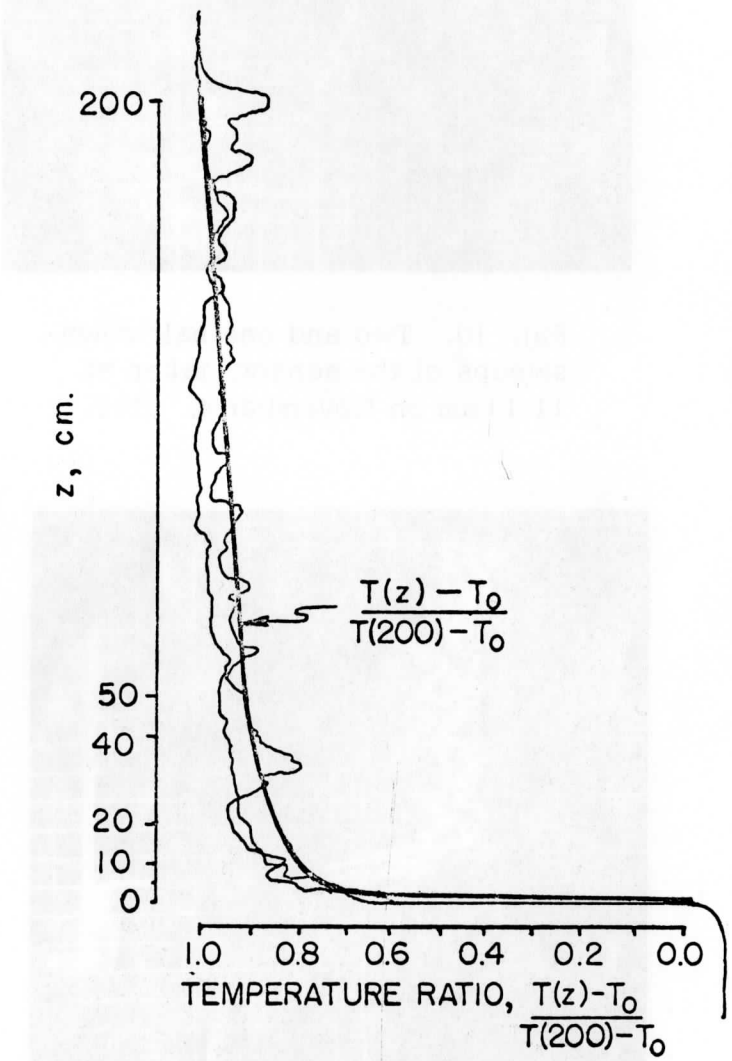

Fig. 9. Observed profile from Fig. 7. Smooth curve from Fig. 3, for $z_0 = 0.0001$ cm.

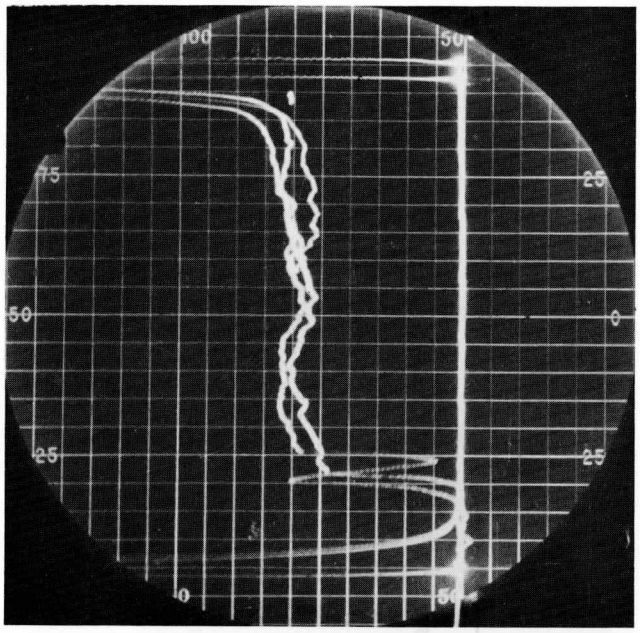

Fig. 10. Two and one half down-sweeps of the sensor, taken at 11:11 am on November 4, 1961.

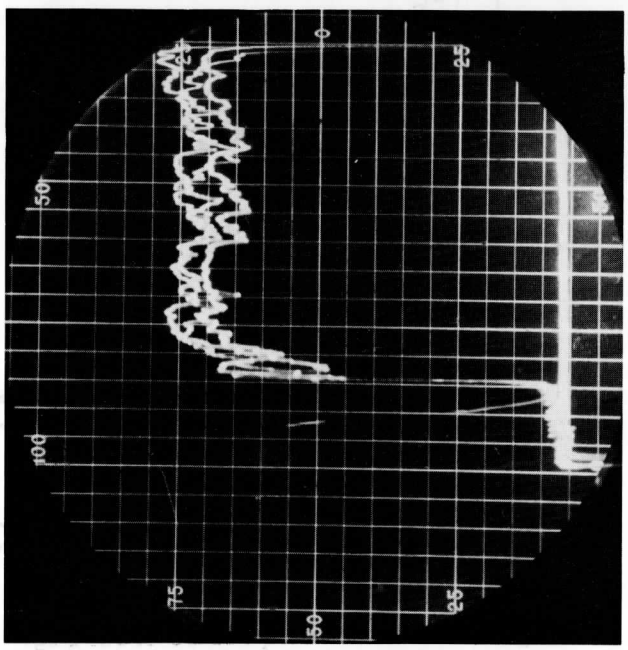

Fig. 11 Three downsweeps of the sensor, between 9:27 and 9:36 pm on November 4, 1961.

were 15 to 20 cm high when the picture was taken. One trace shows the sensor entering the water near the crest of a wave, but the wave rolled by faster than the sensor was lowering. This re-exposed the sensor to the air and evaporation of droplets from the wires dropped the temperature rapidly. Then the sensor went into the water again for the remainder of the sweep. The other trace indicated that the sensor entered the water near a wave trough, almost 12 cm lower than the point of initial entry of the first trace.

The temperature minimum at 50 cm is a good reference point. Up to the level where the two traces merge, the whole thermal structure appears to be lifted with the wave. It is impossible to determine how far above the 100 cm level the effect persists because of the linearity of the profiles in that region. Pictures showing this effect are rare, for two consecutive sweeps of the sensor must enter the water at nearly opposite phases of the wave train. With the barge upon which the apparatus rests rocking in the waves, and the irregularity of the waves themselves, the point of entry becomes a random process.

The profile in Fig. 11 was observed starting at 9:27 p. m. on November 4. Although the curvature appears very great, the logarithmic profile would match this only if z_0 were about 0.0001 cm. The picture contains three traces, over a 9 min period. The envelope of traces is perhaps 0.8° C wide, but the shapes of the profiles are very similar, especially in detecting a slight temperature maximum at 75 cm. A 10 mph wind was from the south-southeast, and the air had an over-water path of slightly more than $\frac{1}{2}$ km. The water temperature was 8.5° C, while that of the air was 2.3° C.

3.4 Conclusions

Weather conditions during runs varied from bright sunshine to heavy overcast; from 1 mph to 12 mph winds; from a $\frac{1}{2}$ km over-water path to one of 3 km; from the air being 3.4° C warmer than the water to its being 6.2° C cooler. No correlation was found between any of these factors and a temperature discontinuity, or the absence of one. These studies were not exhaustive enough to hint at the appropriate mathematical description of the temperature distribution over a water surface. But they do indicate that a logarithmic dependence on height and surface roughness is inadequate in the layers very close to the water surface.

The logarithmic profile assumes vertical heat transfer by conduction. It is possible that heat is transferred between air and water more by infrared radiation than by conduction, or that advection is accompanied by vertical motion. If radiative heating is the dominant process, any tendency

toward curvature in the temperature profile would be suppressed, because the lower layers would be heated only slightly more than higher layers. Future plans call for devising a radiation sensor which could be used with the lifting apparatus from this experiment to determine whether radiation divergence does in fact contribute to the structure of temperature profiles.

3. 5 References

Geiger, Rudolph (1950): The Climate Near the Ground. Cambridge, Mass., Harvard University Press.

Glaser, A. H., W. P. Elliott, and A. J. Druce (1957): "The Study of Small Scale Modification of Air Passing Over Inhomogeneous Surfaces." Texas A & M College Project 85.

Sutton, O. G. (1953): Micrometeorology. New York, McGraw-Hill.

4

Preliminary Report on an Optical Method for Low-Level Lapse Rate Determination

James K. Sparkman, Jr.

Department of Meteorology
University of Wisconsin

Abstract. Data obtained photographically over a 2900 m optical path close to the surface of Lake Mendota is analyzed. Discussion of the optical system used (a Newtonian mirror telescope modified for increased magnification) includes an appraisal of the system and suggestions for a more versatile installation. Examples of photographs taken of targets midway and on the far shore of the lake are presented, and recommendations made for improved target construction. To illustrate the use of the optical method, the Deacon number of the temperature profile, which emphasizes height-changes in stability, is computed.

List of Contents

4. 1 Introduction

4. 2 Theory
- 4. 2. 1 Phenomena
- 4. 2. 2 Ray Curvature and Lapse Rate
- 4. 2. 3 Mathematics and Assumptions of Application

4. 3 Equipment
- 4. 3. 1 Telescopic Camera
- 4. 3. 2 Targets

4. 4 Results
- 4. 4. 1 Raw Data
- 4. 4. 2 Derived Information
- 4. 4. 3 Evaluation

4. 5 Future Possibilities
4. 5. 1 Camera
4. 5. 2 Targets
4. 5. 3 Analysis
4. 6 Acknowledgments
4. 7 References

4. 1 Introduction

The vertical variation of air temperature in the atmospheric boundary layer is both an index of, and a causative factor in, the heat flow across the earth-air interface. Further, near-surface lapse rate is a crucial parameter in the structure of low-level turbulence, wind profiles, and air mass stability, and provides meaningful information about moisture and momentum transfer; reference is made to Sutton (1953). Micrometeorological studies, it is felt, must seek constantly to discover methods to determine the representative lapse rate in the lower atmosphere more quickly, easily and more accurately.

The purpose of this paper is to outline the principles of a simple optical system for obtaining a line-average of lapse rate over a near-linear path (2900 m long) close to the surface, to describe the response of the system in both summer and winter conditions, and to suggest future modifications and additional potentialities.

4. 2 Theory

4. 2. 1 Phenomena

The inferior mirage, best known as "water" visible ahead on a hot pavement, and objects towering or stooping on the far side of a lake during changes of season, are examples of the bending of rays by various temperature gradients. Johnson (1954) and others have discussed these refraction effects and have supplied formulas based on the physical fact that the refractive index (m) of light is a function of air density, and thus a vertical gradient of density leads to bending of light rays in a vertical plane. Density gradients, in turn, are a function of temperature gradients.

The hypothesis of the system to be discussed is that the lapse rate can be determined quantitatively by observing distortions in light transmission. Brocks (1950) and Fleagle (1956) have successfully tested this hypothesis. Yates (1956) has carried out investigation to permit rough correction of distortion based on measurement of temperature gradient.

The goal of this investigation is to build a simple system for use at varying heights which can be moved for use over differing surfaces, and, so far as possible, a system free from dependence on the elevation angle of the sighting instrument.

4. 2. 2 Ray curvature and lapse rate

The bending of light rays in the atmosphere is governed by the density gradient. When the density gradient is zero (at the so-called "autoconvective" lapse rate, 34.1°C/km), rays are transmitted without curvature. For lapse conditions with gradients greater than 34.1°C/km, rays bend upwards, as in total refraction explaining the "water on hot pavement" mirage. With less severe lapse rates and with inversions, rays bend downward. The radius of curvature (r) is directly related to the departure of the lapse rate from the "autoconvective" value.

Computation of curvature begins with the statement, from optics, of the definition of a refractive index:

$$m - 1 = Ap/T \qquad (1)$$

where A (deg/mb) is a constant, p = pressure (mb), and T = temperature (deg Kelvin). Let a prime denote differentiation with respect to height (z). Then

$$m' = A(p'/T - pT'/T^2) = -Ap(T' + g/R)/T^2 \quad , \qquad (2)$$

when the Equation of State (with R = gas constant), and the Hydrostatic Equation (with g = gravity) are considered. Here g/R is the so-called "autoconvective" lapse rate of 34.1°C/km. Solving equation (2) for the temperature gradient,

$$T' = -g/R - m'T^2/Ap \quad . \qquad (3a)$$

For the visible spectrum, the constant A in equations (2) and (3a) equals 77.5×10^{-6} deg/mb. Thus, for the average values of p = 950 mb and T = 271°K,

$$T' = -34.1 - m'10^6 \text{ , deg/km} \quad . \qquad (3b)$$

From geometric optics — see, for example, Johnson (1954, page 9) — it follows that the radius of curvature (r) of a ray is related to the gradient of refractive index:

$$r = -m/m' \approx -1/m' \quad , \qquad (4)$$

since in the atmosphere, m has a value close to unity. Thus, equation (3b) can be written

$$T' = -34.1 + 10^6/r \text{ , deg/km} \quad , \tag{5a}$$

when the radius of curvature is expressed in km.

Using Poisson's Equation it is readily found that the gradient of potential temperature (θ) is

$$\theta' = -24.3 + 10^6/r \quad . \tag{5b}$$

4. 2. 3 Mathematics and assumptions of application

The effect of the ray curvature just described is to distort in some manner the image of a target observed or photographed through the atmosphere close to the surface, except for the unlikely condition of a constant-density region throughout the optical path.

If there is no temperature discontinuity across the air-surface interface and a constant lapse rate is present in the air, proportions of the target are essentially unchanged, but its position in space varies upward with steepness of the gradient (looming). The opposite (sinking) occurs for constant inversion lapse rate. Johnson (1954) shows that looming increases the visual range of a terrestrial observer beyond the geometric horizon.

Given changes in the lapse rate with height, both position in space and target dimensions will be affected. Relatively warm air over cool surfaces lifts the target in space but compresses it vertically (looming and stooping). Cold air over warm surfaces (the "wet pavement" condition) produces upward curving rays that may depict either slight vertical stretching (sinking and towering) or a full inverted image, depending on the intensity of the surface lapse rate. Almost always, as the size of an inverted image increases, greater and greater portions of the target closest to the surface are concealed from the distant viewer, unless he stands sufficiently high above the surface. Typically, a vertically elongated target will be found to be made up of looming upright and inverted portions joined together, hiding ground-level details of the target. Analysis shows that rays from this hidden region leave the target with too great a curvature to find a path to the eye or camera. Position of the composite image, meanwhile, remains at close to its true height in space, as seen by the distant observer.

In using photographs to determine lapse rate, no attempt was made to utilize the target's apparent position in space. Rather, the known heights of the observer and target points above a plane surface (Lake Mendota),

and the determinable path of bent rays over the lake are used to compute ray curvature. Ray paths are ascertained by erecting a small secondary target approximately midway across the lake, and noting what point on the far target appears behind a point at the near target. As curvatures change with air mass movement or diurnal heating and cooling, the midway target seems to rise or sink in relation to the far target. With a series of mid-lake targets set at some known sequence of heights, we can compute a detailed profile of ray curvature with height.

For curvature computation we assume that each ray reaching the observer or camera has a constant radius of curvature throughout its path, determined largely by conditions at its point of origin at the far target. Note that heights measured and computed are relative to the height of the telescope; actual heights above the surface are introduced later after T' results are available. Note also that the height (H) of a point that should be seen behind the near target if no atmospheric effects were present, is a computed value only, and is not identifiable from a photograph.

Ray-curvature formulas are obtained with manipulations involving the discarding of terms small in comparison with the large distances from camera to targets. With D = distance to the far target (2900 m), d = distance to the near target (1023 m), H^* = height of a far-target point optically behind the same near-target point for which height H at the far-target point is seen under no-curvature conditions, the following formula was derived:

$$1/r = 2(H - H^*)/D(D - d) \quad . \qquad (6)$$

4. 3 Equipment

4. 3. 1 Telescopic camera

A parabolic mirror 25 cm in diameter, 180 cm focal length, is used. A larger image is obtained by magnifying the "real image" from the mirror with a macrophotography lens-and-bellows system. A Leica 50 mm lens and III-F body were used to obtain negatives on 35 mm film, the focal length of the entire system averaging about 600 cm. The low f-number resulting (about 27 when lens losses are included) necessitates careful choice of emulsion and processing chemicals, but presented no major problem.

As now mounted on concrete pillars within a pre-fab metal shelter, the telescope is fixed 93 cm above lake level at summertime. This minimum was dictated by problems of winter ice heaving, summer flooding and the near-surface water table. Often a lower or higher viewpoint would be desirable.

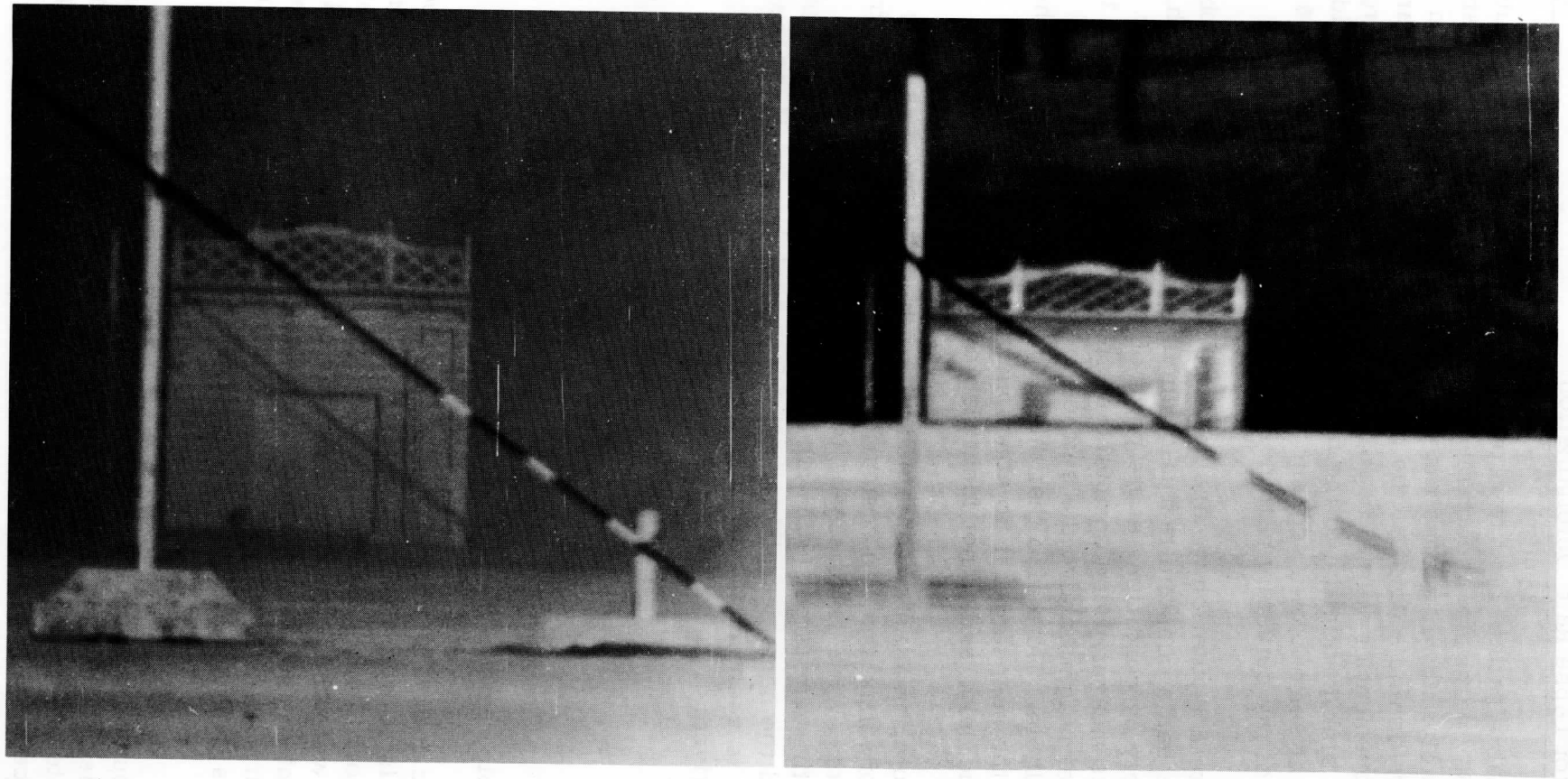

Fig. 1. "Looming and stooping" in the air over the ice of Lake Mendota. The almost-undistorted photograph of the boathouse (left) was taken at 09:18 a. m., 27 March 1962, the other at 03:00 p. m., 26 March 1962, under conditions of light wind (1 mph) and strong inversion. Exposure time, 1/20 and 1/15 sec, respectively, using film Plus-X, ASA 160. Note the changes in relative position of the lake edge and boathouse, compared with the near target.

4. 3. 2 Targets

As constructed, the telescope points toward the front of a privately owned boathouse, ruggedly constructed and located 2900 m NNW across Lake Mendota. Various configurations of lights and wooden targets have been nailed to, bolted to, painted on and otherwise attached to the boathouse.

By far, the most informative of these has been a slanted line across the face of the boathouse consisting of an 8 cm wide strip of web belting stretched tightly from the roof of the boathouse (about 5 m high) across the doorway and into the water (or ice) to one side. The strong brightness contrast between blackened webbing and the white boathouse permits fast-emulsion daylight photography in all but the poorest lighting and visibility. With a slant line, ambiguities of upright versus inverted images can be resolved, and distortion at points at many heights are recorded simultaneously for later analysis.

For the near target, another slanted line was placed on the lake ice in mid-winter, 1023 m from the camera. A 2 × 2 inch strip of oak, approximately 5 m long, was supported on two uprights so as to be parallel to the web belt. It reached from the ice surface to about 3 m high at the upper end. Measured black and white segments painted on the wood strip facilitated identification of points along this line for comparison with boathouse points; see Fig. 1.

4. 4 Results

4. 4. 1 Raw data

Photographs of the distant boathouse vary in clarity with temperature and wind conditions, from sharp pictures in which nails are visible in the wooden sides of the boathouse, to shapeless blobs smeared across the negative sometimes twice the size of a clear image, and fading into a low-contrast background of varying shades of brightness.

Photographs made under inversion conditions generally have better resolution — even strong inversions — than lapse photos, and it is with one of these that this report deals primarily. (Later discussion will include suggestions for improved targets which, it is hoped, will counteract to some degree the "atmospheric boil" effects accompanying the heat flows of lapse situations.) The procedure for analysis, once a photograph is in hand, parallels the computation described: The heights of prominent portions of the boathouse are known — the top rail, the roof edge, the door top, the bottom and various light-boxes and brackets fixed to the boathouse

walls. Some portion of the mid-lake line passes in front of each of these points (or in front of a horizontal line through them, if the far target is offset to one side). We determine the height of a near-target point, compute the height (H) of the point at the far target geometrically behind the selected near-target point, and, using simple trigonometrical formulas, compare H with the height (H^*) of the far-target point optically behind the same near-target point. Table 1 displays the results of several such computations based on visual estimates on 12 by 17 cm prints.

Table 1. Example of determination of ray curvature (given as $1/r$, in units of 10^{-6}/km), gradient of actual and potential temperature (T', θ', °C/km), from estimates of H (cm) and H^* (cm) on 03: 00 p. m., 26 March 1962.

	Far Target		1/r	T'	θ'
Detail	H	H^*	10^{-6}/km	°C/km	°C/km
Rail	456. 7	447. 4	34	0	10
Roof	384. 3	375. 0	34	0	10
Bracket 1	343. 3	322. 0	78	44	54
Light	292. 5	268. 4	88	55	65
Bracket 2	262. 7	205. 0	212	178	188
Door top	254. 5	189. 6	238	204	214
Bracket 3	211. 9	84. 0	470	436	446
Floor	172. 4	0. 0	633	599	609

4. 4. 2 Derived information

The optical method provides direct information on vertical temperature gradients at a variety of more or less continuous heights. Consequently, the Deacon number (DE) of the temperature profile can be derived by taking first-order derivatives. The equation of definition is

$$DE \equiv -\partial \log \theta' / \partial \log z = 1 - \Delta \log (z\,\theta') / \Delta \log z \quad . \qquad (7)$$

The problem is to assign the proper height (z) to θ'-values as listed in Table 1. In a first-order approximation it was assumed that $z = (h + H)/2$, where h = height of the camera (93 cm). From a plot of $z\theta'$-values versus z,

smoothed values of $z\theta'$ have been read off at equidistant height intervals See Table 2 for an example of subsequent Deacon number computation, on the basis of the data given in Table 1.

Table 2. Deacon numbers (DE) computed from interpolated θ'-values (deg/km) at indicated height (z, cm).

z	θ'	DE
450	6	--
400	53	10.0
350	75	4.0
300	165	3.7
250	261	1.4
200	367	1.17
150	473	0.67
100	583	--

The data in Table 2 must be considered tentative. Direct comparison with instrument-tower data are planned in the future.

4.4.3 Evaluation

Perhaps the most difficult decision in the data analysis procedure just related was that of assigning a height in space to ray curvature values. In Wisconsin winters, when ice heaving often litters the shore with piles of crystal wholly hiding the shore line, it is not easy to determine the level of the lake ice with reference to some shore point. Data from the county engineer's office placed the ice surface more than 15 cm below what could be justified by available photos.

On the assumption that some pressure ridge altered mid-lake portions of the ice from the reported heights, computations were made working backward from the least distorted photo at hand to determine what surface height would be required to give the configuration seen. From a sequence of shots made at quarter-hour intervals, one was selected in which the boathouse dimensions most closely approximate those of the actual structure. A ray from the uppermost boathouse rail was assumed to pass through regions of lapse, neutral and inversion conditions en route to the camera,

whatever its curvature along the path. Lack of distortion of rail height dimensions as compared with compression of lower boathouse heights, supports this view. With neutral lapse rate (isothermal) conditions judged to be the average for the whole optical path of this ray, the necessary bending ($H - H^*$) was computed, the requisite surface height then deduced, and this value used in analysis of the strong-inversion photograph.

Vagueness of the edges of portions of the boathouse used as reference points, and poor clarity of the webbed line, particularly in the lower half of the boathouse image, were a noticeable source of errors in the data. For this analysis, no attempt was made either to re-measure, or "best fit." The need for a self-illuminated target set against a dull background appears the best remedy to this problem, to improve signal to noise ratio and permit round-the-clock analysis.

4. 5 Future Possibilities

4. 5. 1 Camera

In many photos, it is readily apparent that from the present camera position 93 cm above the lake, we cannot always see all that we would wish. Often in winter, part of the inverted image is hidden. In summer, we frequently cannot see the lower end of the far target line. For both cases, a telescopic camera capable of being lifted and lowered through several meters would offer far greater versatility. While the present installation, designed almost solely for ruggedness and freedom from thermal movement, could be adapted, some thought might be given to "modified Schmidt" instruments commercially available. In these, insertion of an additional focussing element compresses the length of the light path, and yields an instrument easily handled while retaining good f-number and long focal length. Such a device need not be left in place when not in use, and an optimum camera height could be selected for each thermal condition.

4. 5. 2 Targets

Self-illuminated targets are more easily photographed most of the time than targets relying on color contrast. However, filament bulbs are unreliable over long periods, and the labor of checking and replacing them on the far side of a large lake is prohibitive. This suggests some long-life lamp, with fluorescent or gas-filled tubes now the most readily obtainable. These could be mounted on a 45° slope from horizontal, with coded bright and dark segments provided to facilitate height determination. The whole assembly might be encased in transparent tubing to protect it from moisture. As an additional refinement, the bright segment of the

near-target line could be laid out to match the dark segment of the far-shore line (with changes in length to compensate for the distances). Where high precision placing of both targets is possible, and wave, wind and thermal motion eliminated, any departure of the dot-dash-dot midway line from the dash-dot-dash line on the far shore would represent non-neutral atmospheric conditions graphically.

4. 5. 3 Analysis

Closer approximations to true ray path curvature than our assumption of constant radius between target midway line and camera are desirable, if mathematically feasible.

Further study of available clear photos suggests that with a camera height adjusted for each temperature profile (so as to record both the top and bottom on an inverted image during strong lapse conditions, or the surface end of the slant-line during inversions) it may prove possible to derive all desired thermal profile information without an auxiliary target midway.

4. 6 Acknowledgments

For extensive aid in the initiation and development of this investigation, the author wishes to thank Professor H. H. Lettau of this department, and Mr. F. F. Bowman of Route 1, Waunakee, Wisconsin, whose boathouse often catches my eye.

4. 7 References

Brocks, K. (1950): "Die Lichtstrahlkrümmung im Bodennähe," Deutsche Hydrograph. Z., 3, 241-248.

Fleagle, R. G. (1956): "The Temperature Distribution Near a Cold Surface," Journal of Meteorology, 13, 160-165.

Johnson, John C. (1954): Physical Meteorology. John Wiley & Sons, Inc., New York.

Sutton, O. G. (1953): Micrometeorology. McGraw-Hill Book Co., Inc., New York.

Yates, H. W. (1956): "Atmospheric Refraction Over Water," Report of Project No. NO 284-512, Radiometry II Branch, Optics Division, Naval Research Laboratory, Washington, D. C.

Scanner's note:

This page is blank.

5

An Airborne Measuring System for Micrometeorological Studies

John A. Dutton

and

Donald H. Lenschow

Department of Meteorology
University of Wisconsin

Abstract. Some of the advantages and disadvantages of an airborne measuring system for micrometeorological research are discussed. The instrumentation used in such a system, developed for a light, twin-engine airplane by the Department of Meteorology, University of Wisconsin, is described. Some of the research results to date are presented, and the research potential of the system is outlined.

List of Contents

5. 1 Introduction
- 5. 1. 1 Advantages of an Airborne System
- 5. 1. 2 Quality and Representativeness of Airborne Measurements
- 5. 1. 3 Types of Aircraft

5. 2 General Description of Airborne Measuring System
- 5. 2. 1 Characteristics and Performance of the Airplane
- 5. 2. 2 Modifications of Airframe and Interior
- 5. 2. 3 Recording Equipment
- 5. 2. 4 Electrical Power Supplies
- 5. 2. 5 Electrical Shielding

5. 3 Components of the Airborne System
- 5. 3. 1 Albedo Equipment

5.3.2 Net Radiation Equipment
5.3.3 Surface Temperature Bolometer
5.3.4 System for Turbulent Vertical Component of Air Motion
5.3.5 Hygrometry
5.3.6 Radar Altimeter
5.3.7 Photographic Cameras

5.4 Future Plans and Research Potential of the System

5.5 Acknowledgements

5.6 References

5.1 Introduction

Airborne measuring systems carried on powered aircraft have received increasing recognition and use in meteorology in the past decade. Although measurements from aircraft have been invaluable in the study of synoptic systems (particularly in oceanic and polar regions) during and after World War II, it is primarily since that time that they have been utilized in micro- and meso-meteorological studies. It is the purpose of this paper to describe an airborne measuring system for the study of meteorological and aerodynamic processes in the atmospheric boundary layer, to report in detail on such a system developed at the Department of Meteorology, University of Wisconsin, to discuss a few results of research, and to outline the research potential of the system.

5.1.1 Advantages of an airborne system

Both the advantages and disadvantages of an airborne system compared to the traditional fixed installations lie in the mobility of aircraft. The airborne measuring system operates in the same four-dimensional space upon which physical variables are defined — three spatial coordinates and time. Fixed installations generally operate in only two — the vertical and time. The *a priori* assumption, inherent in the interpretation of data from fixed installations, that time averages are equivalent to spatial averages, is no longer needed with an airborne system. This assumption is generally unstated in the use of results obtained at one point to make physical generalizations.

The airborne system makes possible the study of the horizontal variation of physical variables. As pointed out by Lettau (1959), we must expect that ". . . the wide variety of natural factors including soil type, soil moisture, surface cover, vegetation, terrain variations, albedo, etc., contribute significantly to horizontal variations in boundary layer structure.

. . . the available experimental information permits us to evaluate the relative significance of these factors only in a more or less qualitative manner."

The fixed mast or tower installation, which gives little quantitative information related to the abovementioned variations, is valuable for small scale studies of vertical profiles; the airborne measuring system provides the extension of micrometeorological studies to a horizontal scale of hundreds of miles and a vertical scale much greater than is feasible with towers.

There are further practical advantages. The first is the possibility of taking measurements in areas where neither electrical power nor easy surface transportation exist. Another is the ability to make survey investigations of large areas to determine small regions of particular microclimatological interest. A third is the possibility of following identifiable air masses over a period of time to study modification processes.

Possibilities for the use of airborne measuring systems can be categorized as follows:

(1) Remote measurement or determination of surface variables (such as albedo, surface temperature, net radiation, etc.) and surface structure (such as topography, vegetation types, etc.).

(2) Ambient measurement of atmospheric properties (such as temperature, humidity, net radiation, components of air motion, electric field parameters, visibility, etc.).

(3) Surface to flight level integrations of atmospheric properties (such as radiation absorbed, water content, etc.).

5. 1. 2 Quality and representativeness of airborne measurements

Utilization of airborne measuring systems requires consideration of instrument response to the original signal representing variations of the physical elements under investigation. Certain errors are caused by the portion of the atmosphere between the aircraft and the surface under consideration. On the other hand, atmospheric depletion is the reason for radiation absorption in a column which can be determined by measuring radiation streams at the top and bottom of the column.

The error in albedo determination due to atmospheric depletion has been discussed by Fritz (1948) and by Bauer and Dutton (1962). The error

introduced in surface temperature measurements is considered by Lenschow (1962) (see Section 6).

Assuming perfect transmission through the atmosphere, other errors result from the motion and position of the aircraft. It is possible to study the effect of this type of error in spatial averages when the ground variables are sensed by radiation techniques. Dutton (1962) showed that this error can be minimized by flight planning and that averages can be measured to a good approximation, while the variance spectra of the recorded signals can be corrected to obtain the variance spectra of the observed variable.

5. 1. 3 Types of aircraft

The airborne micrometeorological measuring system to be described in detail here is carried by a light, twin-engine aircraft. There are several reasons for this choice. Lighter-than-air passenger craft have been utilized in meteorological studies, but now play a minor role in aviation and are not generally available. Today, the primary choice of an instrument platform for airborne work will be some type of heavier-than-air vehicle.

Although rotary wing aircraft appear to be useful, Jackson (1959) found a great disadvantage in the excessive vibration. It would also appear that most helicopters are not fast enough to achieve nearly synoptic measurements over relatively large areas. Gliders — which have been used for specialized studies — are not suitable due to restrictions in course planning, and mainly in view of the amount of electrical power required by meteorological instrumentation and recorders.

The large aircraft used for regular synoptic reconnaissance work are generally too heavy for microclimatological research because of the danger and nuisance of operations close to the ground. Single-engine aircraft are also hazardous (because of possible engine failure) both close to the ground and in isolated areas; furthermore, with the exception of "pusher" airplanes, it is not possible to mount either turbulence measuring equipment or radar on the nose of the airplane.

Thus the light, twin-engine airplane appears to be a suitable choice.

5. 2 General Description of Airborne Measuring System

The airborne measuring system to be described in the following sections was developed by the Department of Meteorology, University of Wisconsin, over a period of four years. All modifications to the airframe

were done under our direction; most of the individual instruments were manufactured commercially and altered for compatibility with the airborne system.

5. 2. 1 Characteristics and performance of the airplane

The Cessna 310 airplane used for the Wisconsin airborne measuring system is a five-passenger, twin-engine airplane with a cruising speed of 180 mph, a range of approximately 800 miles, and a service ceiling of about 20,000 feet. The airplane can be operated from runways less than 2500 feet in length. At maximum gross weight of 4600 pounds, the airplane has a climb rate of 1700 feet/min at sea level, and a single-engine climb rate of 380 ft/min. The empty weight of the unmodified airplane is about 3,000 pounds, and a full load of 100 gallons of fuel adds 600 pounds. The airplane as currently modified for airborne measurement, with a full fuel load, pilot, and observer is near maximum gross weight.

5. 2. 2 Modifications to airframe and interior

A streamlined housing, a shell of approximately 1 m length and 0.5 m width, is attached to the bottom of the airplane to provide a platform horizontal in level flight for instrument mounting without cutting the original airplane structure. The housing is designed to protect all downward-sensing instruments from gravel and water thrown by wheels during take-offs and landings. With the landing gear retracted, instruments mounted on the platform have an almost unobstructed downward view. A parabolic reflector, a solarimeter, and a radar altimeter antenna are mounted in the housing.

A cylindrical aluminum boom, 8.7 cm in diameter, was rigidly secured to the front wheel mounting and the main structure of the airplane nose, and extends 77 cm out from the front of the airplane (see Fig. 1). This boom carries sensors for measuring turbulent vertical velocity, extending the total length of the boom and turbulence probe to 1 m. A flux-plate net radiometer and a fast-response thermocouple are also mounted on the boom.

A solarimeter was mounted on the top of the airplane, midway down the fuselage. Essentially the only obstruction to a 2π-steradian upward view is the lateral cross-section of the vertical stabilizer.

The rear seats in the cabin were replaced by facilities for mounting measuring and recording instruments. A two-shelf instrument rack occupies one half of the rear portion of the cockpit, and an interchangeable mounting for either the control and readout unit of the surface temperature bolometer or a third seat occupies the other half (see Fig. 2).

Fig. 1. Boom mounted on front of the airplane with net radiometer extending to the right, and the differential pressure ports extending at the tip.

A camera hole was cut in the floor of the baggage compartment and provided with a door which is operable in flight. Either the surface temperature sensing equipment or an aerial camera can be mounted in the hole. Most of the baggage compartment is used for inverters and a junction-box for funnelling instrumentation outputs to the recorder.

5. 2. 3 Recording equipment

At the present time, data are recorded on a Honeywell 906B Visicorder oscillograph. This is a 12-channel, mirror galvanometer recorder which can be operated at various paper speeds between 0.2 and 25 inches/sec. The galvanometer traces are recorded on light-sensitive paper and can be nearly instantly read due to an automatic development process. The recorder, mounted on a foam-rubber base to reduce vibration from the airframe, requires 500 watts at 100 volts and 60 cps. Amplification is not necessary for most sensor outputs since the galvanometer sensitivity is about 3 microamps/cm. The frequency response of the galvanometers is ±0.5 per cent, for 0 to 24 cps, and the internal resistance is about 30 ohms. A timing unit provides accurately spaced lines on the paper at intervals of 0.01, 0.1, or 1.0 seconds.

It is planned to replace the Visicorder with a magnetic tape system which will make it possible to produce computer input tapes either in the air or on the ground, without laborious manual work.

5. 2. 4 Electrical power supplies

The airplane generators can supply 100 amps of 28-volt dc power. This is converted into the necessary power for running the instruments and recorders by three inverters: (1) a 750 va rotary (110 v, 60 cps, sine wave), (2) a 150 va rotary (110 v, 400 cps, sine wave), and (3) a 200 va solid-state (110 v, 400 cps, square wave). Connectors for the inverter outputs are mounted on a panel at the bottom of the instrument rack. This panel also contains on-off switches and the necessary input and output fuses for the inverters. An ac voltmeter mounted on the instrument rack may be used for monitoring any of the inverter outputs.

5. 2. 5 Electrical shielding

Considerable effort was devoted to reducing electrical noise in the recorded data. All cables and wiring connected with the inverters are shielded with flexible steel conduit, and the power panel is mounted in an aluminum enclosure. The main signal-cables to and from the recorder junction box are covered with flexible copper shielding and plastic tubing and then inserted inside a flexible steel conduit. The copper shielding

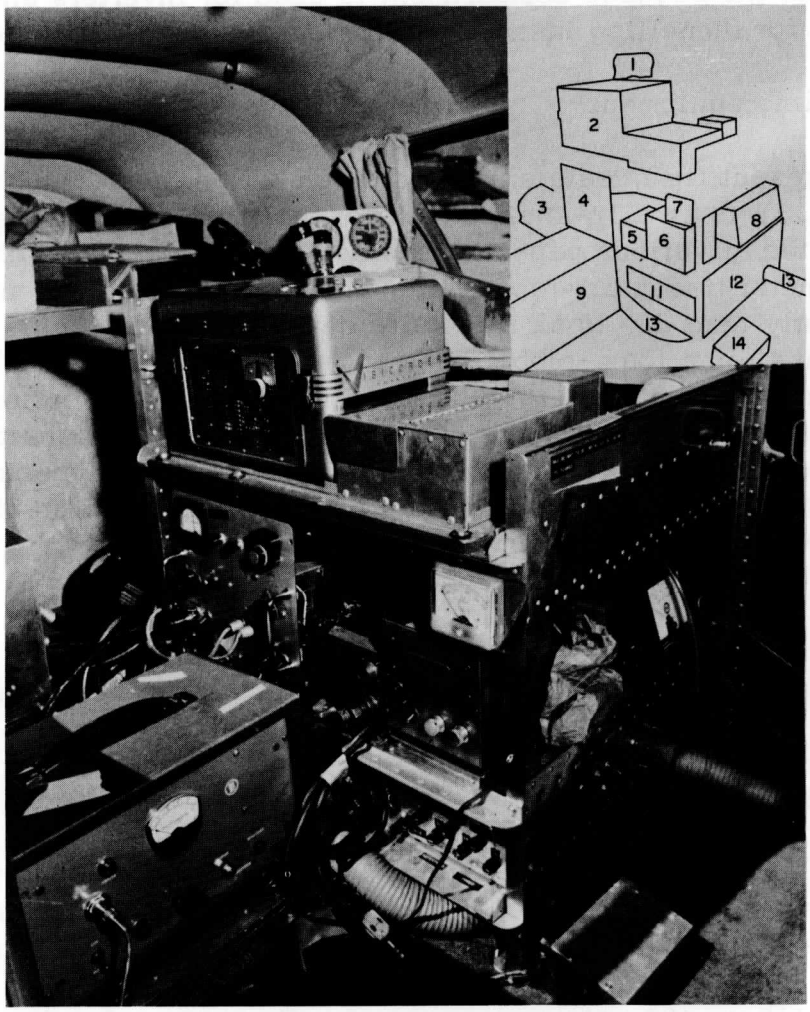

Fig. 2. Instrument installation in the rear of the cockpit. The numbered items in the drawing at upper right corresponding to instrumentation in the picture are: (1) observer's instrument panel with airspeed meter and altimeter; (2) Visicorder; (3) 60 cycle ac inverter; (4) analog computer and gyro for turbulence system; (5) Variac transformer to supply constant voltage to surface temperature bolometer; (6) timing signal generator; (7) voltmeter for monitoring inverter outputs; (8) humidity measuring equipment; (9) control and read-out unit of surface temperature bolometer; (10) omitted; (11) panel for inverter outputs, on-off switches and fuses; (12) controls for recording radar altimeter output and elevator deflection; (13) tube for supplying heat to bolometer sensing head enclosure; (14) event marking signal generator.

connects only to the recorder ground; the conduit is grounded to the airplane at both ends.

5. 3 Components of the Airborne System

The complete airborne measuring system is composed of several individual instruments, which can be recorded separately for special projects or combined to obtain correlations between the various physical processes of the atmospheric boundary layer.

5. 3. 1 Albedo equipment

Short-wave radiometers located on the top and bottom of the airplane permit the determination of the albedo of the ground. The instrument installation consists of: (1) an upward-facing Eppley pyrheliometer (or alternately, a Kipp and Zonen solarimeter) on top of the airplane to measure the down-coming solar plus hemispherical sky radiation; (2) an upward-facing Eppley (or alternately, a Kipp and Zonen) mounted at the focus of a downward-facing parabolic beam reflector on the bottom of the airplane (Kuhn and Suomi (1958)) contained in the instrument housing, to measure up-coming beam radiation reflected by the ground; and (3) a downward-facing Kipp and Zonen hemispherical solarimeter mounted on the bottom of the airplane in the instrument housing to measure up-coming hemispherical radiation reflected by the ground.

Bauer and Dutton (1962) have shown that the albedo obtained from hemispherical sensors must agree with the beam sensors in the presence of isotropic and homogeneous reflected radiation. Fresh snow fields were used to calibrate the two sensors, and the results then agreed over a variety of surfaces, excepting open water bodies.

The Kipp and Zonen solarimeters have several advantages over the Eppley pyrheliometers for airborne use: (1) the time constant is about 2 sec, in comparison with about 10 sec for the Eppleys; (2) the solarimeter is smaller and more rugged; (3) the solarimeter has both outer and inner glass coverings so that the sensing element is still protected if the outer glass is broken in flight.

The results of many flights during a full year over a fixed, standard course encompassing several types of terrain in southwestern Wisconsin are given by Bauer and Dutton (1962). They discussed both temporal and horizontal variations of albedo. The largest contrast was found between snow and snow-free seasons. The authors also describe observations of the effect of clouds on albedo measurements. It is shown that

atmospheric depletion in the first 1000 feet produces less than a five per cent error in albedo determinations.

5. 3. 2 Net radiation equipment

In the initial phase of airplane work, it was planned to utilize the "economical net radiometer" developed at the University of Wisconsin. The instrument was split horizontally into two halves, the upper mounted on the top, the lower on the bottom of the airplane. However, it was found that the response time of the system was too slow.

In 1962, a net radiometer was constructed for airborne use on the boom projecting out of the front of the airplane. The only obstruction to a 4π-steradian view is the lateral cross-section of the airplane and the longitudinal cross-section of the boom. The obstruction is less than $\pm 5°$ above and below the horizon, that is a portion of sky and ground which most likely does not contribute much to net radiation.

The radiometer is a black flux-plate with a time constant of 0.2 sec, constructed with 100 turns of constantan wire on a glass slide, with copper plating on one half, producing 100 thermocouples. The flux plate is mounted in a rectangular box with the top and bottom covered with polyethelene 50 microns thick. The flux plate is 4.6 cm by 2.9 cm and the box is 8.9 cm by 6.7 cm and 1.3 cm thick. Additional details and observed data are given by Lenschow (1962) (see Section 6). The present output of the radiometer does not produce galvanometer deflections large enough for accurate measurement, and data can be read only to 0.05 ly/min.

Although it is virtually impossible to determine surface net radiation with this instrument from reasonable flight altitudes because of atmospheric depletion, the data do provide a quantitative measurement of the strength of heating or cooling processes and its relation to other variables.

5. 3. 3 Surface temperature bolometer

The surface temperature radiometer, constructed by the Barnes Engineering Co., compares the radiation from a 60° C reference cavity with the radiation received in the "atmospheric window" between 8 and 14 microns wavelength to produce a signal proportional to surface temperature. Extensive modifications of the original model were required to make the instrument suitable for airborne use. The instrument is sensitive to the voltage level of the 110 volt 60 cps power supply. Therefore a variable transformer is used to regulate the input voltage. Details of the instrument and results obtained from a year's flight over the same standard course used for the albedo data are given by Lenschow (1962) (see Section 6).

5.3.4 System for turbulent vertical component of air motion

The system for determination of vertical air velocity was designed and constructed by the Giannini Controls Corporation[1] to specifications desired for micrometeorological studies. The system is designed so that the reactions of the airplane to turbulence are theoretically cancelled out, and the vertical component of air motion is measured independent of airplane maneuvers at constant indicated and true airspeed. The system responds to gusts between 0.053 and 26.4 cps. For the cruising speed of the Cessna 310 (180 mph, or approximately 80 m/sec), the above is equivalent to a response to eddies between 1500 and 3 m wavelength. The absolute range is ±120 cm/sec, and the sensitivity is ±15 cm/sec. The system is restricted to gust velocities below 7.3 m/sec. The output of the individual transducers may be recorded simultaneously with the output of an analog computer which computes the vertical component of air motion directly.

The system depends on evaluation of two terms of an identity,

$$w_{p,s} = w_{p,a} + w_{a,s} \quad , \tag{1}$$

where $w_{x,y}$ is the vertical component of motion of x relative to y, while p signifies the probe, a the air, and s space.

From Fig. 3, it follows that

$$\vec{k} \cdot \vec{V}_{p,a} = V_{p,a} \sin \gamma \approx V\gamma = V(\theta - \alpha) \quad , \tag{2}$$

where $\vec{V}_{x,y}$ is a velocity vector and $V_{x,y}$ its scalar magnitude, with the same subscript convention as above. The subscripts are omitted for the velocity of the probe relative to air which equals the true airspeed of the plane, V.

The angle of attack, α, is measured at the tip of the turbulence probe by a pair of pressure ports mounted in the vertical plane at identical angles above and below the longitudinal axis of the airplane. A bidirectional differential pressure transducer converts the pressure difference between the two ports into a voltage directly proportional to that pressure difference. The angle of attack is then determined by the relation

---

[1] The analysis of the measurement technique and system design given here is based on a proposal for the system written by James G. Kyser, Jr., Senior Development Engineer, Giannini Controls Corporation.

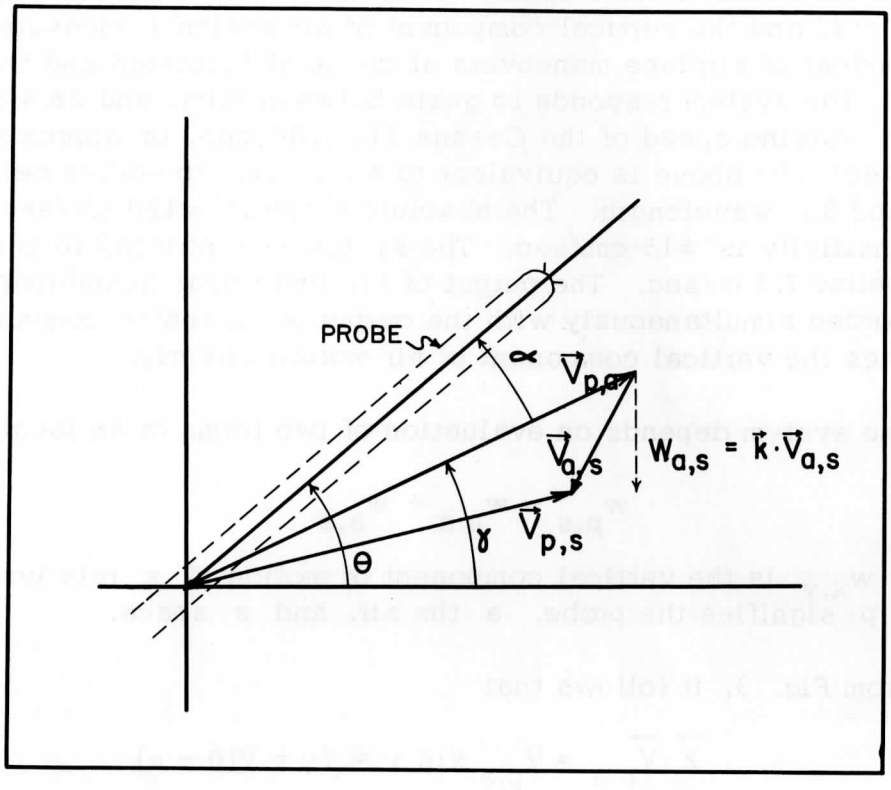

Fig. 3. Geometry of the turbulence probe and its motions with respect to space (absolute) and the air (relative). The notation is explained in the text.

$$\alpha = G\,\Delta p/q \quad , \tag{3}$$

where Δp is the pressure difference, q the dynamic pressure, and G a numerical coefficient which is a function of the Mach number and the configuration of the pressure ports. For Mach numbers less than 0.6, wind tunnel data give $G = 0.186$. Since q is directly related to the indicated airspeed, the output of the pressure transducer is multiplied by $1/q$ in the computer. The multiplication is performed by a variable potentiometer preset with the indicated airspeed to be maintained during the period of measurement.

The pitch angle, θ, is measured by a free gyro mounted in the computer case at the center of gravity of the airplane. The gyro output is directly proportional to θ, and the scale-factor of the angle of attack circuit is adjusted to be identical to the gyro scale factor. The difference, $(\alpha - \theta)$, is computed by a differential amplifier and the output multiplied by the true airspeed of the airplane, V. The multiplication is performed by a variable potentiometer calibrated in units of the true airspeed.

Hence we have obtained an output voltage $E_{p,a}$ which is the electrical equivalent,

$$E_{p,a} = K_V V(\alpha - \theta) \quad , \tag{4}$$

of the negative of the term $w_{p,a} = V\gamma$ of (1), where K_V is the gyro scale factor.

The quantity $w_{p,s}$ is obtained by integration of the output of the accelerometer, $A_{p,s}$, mounted in the probe, in accord with

$$w_{p,s} = \int_o^t A_{p,s}\, dt \quad . \tag{5}$$

It is assumed in (5) that the airplane is flying horizontally at the time the data run is started. An RC integrating circuit is used in the computer. Letting $E_{p,s}$ be the output of the circuit, and denoting Laplace transforms as functions of the variable s with $\hat{}$, we find, for the RC circuit,

$$\hat{E}_{p,s} = K_A \hat{A}_{p,s} / (T_c s + 1) \tag{6}$$

where $T_c = RC$, the time constant of the RC circuit, and K_A is the accelerometer scale factor. However, (6) may be written as

$$\hat{E}_{p,s} = K_A \hat{A}_{p,s} (T_c s) / (T_c s)(T_c s + 1) = K_V \hat{w}_{p,s} (T_c s) / (T_c s + 1) \, , \tag{7}$$

when the accelerometer is calibrated so that $K_A / T_c = K_V$.

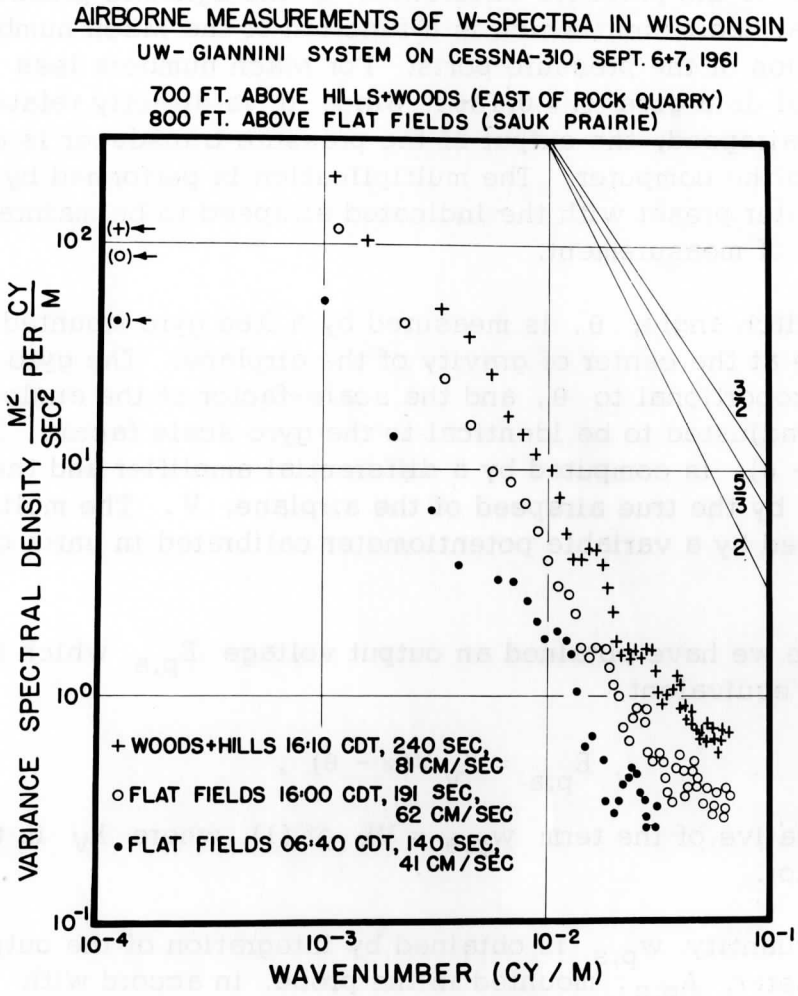

Fig. 4. The power spectra of turbulent vertical velocities measured with the airborne system.

The quantity (4) is passed through an RC differentiating circuit to reduce the effect of gyro drift. Hence the Laplace transform of the output of the differentiating circuit is

$$\hat{E}_{p,a} = K_V \hat{w}_{p,a} \, (T_c s) \, / \, (T_c s + 1) \quad . \tag{8}$$

The output of this differentiator is added to the integrated accelerometer signal by a differential amplifier to produce an output proportional to the vertical velocity. The Laplace transform of the output is obtained by adding (7) and (8),

$$\hat{w}_{a,s} = (\hat{E}_{p,s} + \hat{E}_{p,a})(T_c s + 1) \, / \, K_V T_c s \quad . \tag{9}$$

Equation (9) allows us to correct the variance spectrum of the computer input to obtain the variance spectrum of the vertical velocity (see Dutton (1962)). Replacing the Laplace transforms by Fourier transforms with the substitution $s = i\lambda$, utilizing the fact that the variance spectrum can be represented as the square modulus of the Fourier transform of the velocity, and setting $E_{p,s} + E_{p,a} = E$, we obtain

$$|\hat{w}_{a,s}(\lambda)|^2 = |\hat{E}(\lambda)|^2 [(T_c \lambda)^2 + 1] / (K_V T_c \lambda)^2 \quad . \tag{10}$$

The quantity λ is the frequency; replacing it with $\lambda = \kappa V$ throughout (10) produces the corrected spectrum as a function of wave-number, κ The spectrum correction function in (10) has little effect at high wave-numbers, but becomes increasingly important as the wavelength of the vertical velocity eddies increases.

Fig. 4 shows variance spectra computed from three observation runs made with the turbulence measuring system. The results have not been corrected with the transfer function given by (10). The value of the transfer function is about 1.2 at the wave-number 1/100 m and is about 18 at wave-number 1/1000 m, so that its application to the data shown would extend the validity of the -5/3 slope to smaller wave-numbers.

Two auxiliary instruments are now under development for use with the turbulence measuring system. The first is a fast response thermocouple mounted between the angle-of-attack pressure ports. The averages of the product of the turbulent vertical velocity and the temperature measured by the thermocouple will produce the vertical heat flux. The second additional instrument will measure the fluctuations in true airspeed. Assuming a homogeneous density distribution, the average of the product of the vertical velocity and horizontal velocity deviations will produce a measure of the Reynolds stress.

5. 3. 5 Hygrometry

A humidity-sensing instrument specially constructed by Consolidated Electrodynamics Corporation has been installed. The instrument measures vapor density (g H_2 O per volume of dry air) over the altitude range generally used (1000 to 500 mb). The time response of the instrument is not fast enough for determination of the turbulent water vapor flux, but it does provide a quantitative measure of the moisture conditions of the ambient air.

5. 3. 6 Radar altimeter

A radar altimeter (AN/APN - 22) is installed in the housing at the bottom of the airplane and the output may be simultaneously recorded, or displayed on the pilot's instrument panel. It is accurate to ±5 per cent of the elevation of the surface from 40 to 20,000 feet. The instrument permits the study of correlation between physical processes and topography, and perhaps will be most useful in conjunction with turbulence and surface temperature data. Furthermore, a radar altimeter provides extremely useful information for the pilot when observations are to be taken at a fixed elevation above the ground.

5. 3. 7 Photographic cameras

The airplane was originally equipped with a K-24 camera and intervalometer in order to obtain large negatives (12 cm × 12 cm). Maintenance and operation of this equipment proved expensive and difficult, and the developing of the film rolls requires special equipment. It is now planned to replace the K-24 with a motor-driven 35 mm camera.

The usefulness of continuous photography of terrain over which data is taken is obvious. For example, it would be of interest to determine if conventional photographs can supplement measurements of the albedo, and infra-red photographs that of surface temperature.

5. 4 Future Plans and Research Potential of the System

The current difficulty preventing extensive and effective use of the airborne measurement system for a large variety of research projects is the excessive labor involved in data reduction. The full research potential of the system will be realized only with the installation of an automatic system which will allow computer-input tapes to be produced without manual effort either in the air or on the ground. Planning for such a system is underway.

Possible research products with the airborne system can be divided into categories by the scales of the areas to be studied. The system described here lends itself to studies mainly on two scales: (1) detailed investigations of areas or volumes between 10 and 50 miles in horizontal dimension and up to several thousand feet in height, with emphasis on diurnal and daily changes; (2) survey investigations emphasizing seasonal changes on flight paths between 50 and 500 miles in length.

The second type of study has been emphasized in the work to date (Bauer and Dutton, 1962), although diurnal investigations have recently been started (Lenschow, 1962).

The first type of investigation could yield extremely useful information, with emphasis on turbulence and heat flux in the neighborhood of different types of crops and physical features, such as small mountain ranges, water bodies, and islands.

5. 5 Acknowledgements

We are indebted to Professor H. H. Lettau for his advice and encouragement throughout the development of this system. The project would have been impossible without the cooperation of Mr. Howard Morey, of the Morey Airplane Co., Middleton, and his staff, most particularly Mr. T. A. Waterman and Mr. Sherman Hallen.

5. 6 References

Bauer, K. G., and J. A. Dutton: "Albedo Variations Measured from an Airplane over Several Types of Surface." Journal of Geophysical Research 67, 2367, 1962.

Dutton, J. A.: "Space and Time Response of Airborne Radiation Sensors for the Measurement of Ground Variables." Journal of Geophysical Research 67, 195, 1962.

Fritz, S.: "The Albedo of the Ground and the Atmosphere." Bulletin of the American Meteorological Society 29, 303, 1948.

Jackson, C. I.: "Insolation and Albedo in Quebec-Labrador." McGill Sub-Arctic Research Paper 5, McGill University, Montreal, 1959.

Lenschow, D. H.: "Technique and Results of Surface Temperature Determination with the Aid of an Airborne Bolometer." Master's thesis,

Department of Meteorology, University of Wisconsin, 1962. (See Section 6 of this report.)

Lettau, H.: "Research Problems in Micrometeorology." Final Report, Contract DA-36-039-SC-80063. Meteorology Department, University of Wisconsin, September 1959. U. S. Army Electronic Proving Ground, Fort Huachuca, Arizona, January 1960.

6

Technique and Results of Surface-Temperature Determinations with an Airborne Bolometer*

Donald H. Lenschow

Department of Meteorology
University of Wisconsin

Abstract. The problems and advantages of the bolometric method of measuring surface temperature from an airplane are discussed. The airborne bolometer measures a weighted area-mean temperature that is a function of the surface temperature distribution and emissivity. The effect of atmospheric absorptivity is negligible under ordinary conditions for altitudes above ground of 300 m or less but can be an important consideration for flight levels above 300 m. Micrometeorological data from a series of airplane flights measuring surface temperature over various types of terrain in Southern Wisconsin from late summer to early winter are presented and discussed.

List of Contents

6. 1 Introduction

6. 2 Principles of Operation
- 6. 2. 1 Description of Radiometer
- 6. 2. 2 Techniques of Measurements
- 6. 2. 3 Physics of the Radiometer
- 6. 2. 4 Technique of Airborne Operation

6. 3 Results of Measurements
- 6. 3. 1 Flight Course and Program
- 6. 3. 2 Bolometric Surface-Temperature Variations

6. 4 References

*Part of this work was submitted to the University of Wisconsin in partial fulfillment of the requirements for the degree of Master of Science.

6. 1 Introduction

Instruments for measuring temperature can be classified in either one of two groups: conduction type instruments, or conventional thermometers; and radiation sensing instruments, or bolometers. The radiation flux emitted by a substance is a monotonic function of its temperature, and this is the basis for the bolometric method of temperature measurement. Bolometers have several unique advantages over thermometers. First, because temperature is measured remotely, the radiometer has no effect on the environment under consideration. Second, a weighted area-mean temperature can be measured, whereas a thermometer measures temperature at a point. Third, time response on the order of several milliseconds is possible.

Several disadvantages, however, must also be considered. First, the radiation flux is a function of emissivity as well as temperature. Second, the radiation flux is a function of the medium through which it has passed. Third, the radiation area-mean temperature may not be the true area-mean temperature. Fourth, a reference source of radiation flux must be provided since only differences in radiation flux can be measured. Fifth, the power output of a bolometric detector is relatively small and must be greatly amplified.

Relatively few radiational measurements of surface temperature have been reported in the literature. For example, Albrecht (1952) obtained bolometric measurements of surface temperature from an airplane cruising at 400 m during a few months of 1944. Coombs (1961) made several flights over New Jersey and Greenland and discussed the usefulness and accuracy of measuring surface temperature from an airplane.

Radiation flux in the 7 to 14 micron region has also been measured from a satellite with a bolometer. Fritz and Winston (1962) discuss measurements taken from Tiros II on November 23, 1960, over the United States, and Nordberg et al. (1962) discuss measurements for various parts of the world taken from Tiros III. These are preliminary results, and in general, the radiation temperature measured from outside the atmosphere is not the surface temperature because of atmospheric absorption and emission, especially from cloud tops. An exception to this may be in polar or desert regions, covered with a clear, dry atmosphere.

The value of remote measurements of surface parameters in micrometeorological research is discussed by Lettau (1959). He notes that most micrometeorological experiments have been conducted under the assumption that horizontal variation of the meteorological parameters could be ignored. Therefore, quantitative information concerning these horizontal variations is needed to understand the three-dimensional structure of

the atmospheric boundary layer. Bauer and Dutton (1960) have reported on airborne measurements dealing with the seasonal variation of albedo over Southern Wisconsin. The flight path used by them is identical to the one used for the measurements in this report.

6. 2 Principles of Operation

6. 2. 1 Description of radiometer

The Barnes Sea-Surface Temperature Radiometer Model 14-310, Serial No. 102, is contained in two units with two interconnecting cables. The radiation sensing unit is $4\frac{1}{2}$" high, $5\frac{1}{2}$" wide, and 5" long and weighs about 8 lbs. It contains an infra-red thermistor type detector in a bridge circuit, with 110 vdc bias voltage across both elements. The radiation to be measured is modulated at 90 cps by a two-segmented mirror chopper, belt driven by a 110 vac single-phase synchronous motor rotating at 1800 rpm. The 90 cps output is capacitively coupled to a preamplifier and from the preamplifier is conducted to the control and readout unit by one of the interconnecting cables. This unit is about 24" long, 8" wide and 8" high, and weighs about 30 lbs. The ac signal is further amplified, detected and displayed on two microammeters, one located on the sensing unit and the other on the control and readout panel.

Recorder output terminals are also present; but for the measurements in this report, new recorder output terminals were added to make the unit compatible with the Honeywell 906 B Visicorder Oscillograph. The control and readout chassis also contains a heater circuit to maintain a 60° C reference temperature in a black conical cavity located in the sensing unit. The detector is located at the apex of this cavity. The power requirement is 110 vac 100 watts, and the power supplies for the various components are located in the control and readout unit. See Figure 1.

Originally, the radiometer microammeters were biased with a constant current and the rectified output signal was subtracted from the bias current so that the meters deflected up-scale for increasing temperature. This bias voltage was removed and the meters reversed so that at zero signal input the meter reading is a minimum of about 12 scale divisions. Full scale is 100 scale divisions. In addition, a bias current was added that could be switched on when the surface temperature was below 18° C. Below 18° C the meter reading is off scale, but switching on the bias current moves the signal 80 scale divisions down-scale so the meter could be read to temperatures less than -30° C. See Figure 2.

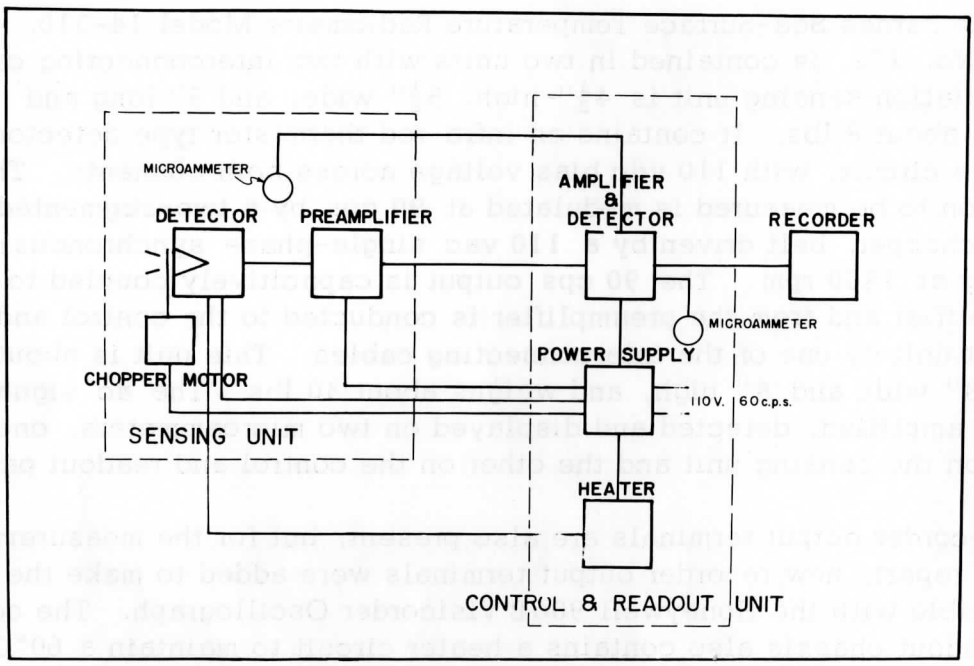

Fig. 1. Circuit diagram of the Barnes Surface Temperature Bolometer Model 14-310 Serial No. 102.

6. 2. 2 Technique of measurements

The radiometer measures the difference in radiation between a black conical cavity held at 60°C by a temperature control circuit and the incoming radiation through an optical filter. The filter excludes radiation outside a 7 to 15 micron pass-band and has half-power points at 7. 7 and 14 microns. The short wavelength cutoff is determined by the absorption of indium antimide; the long wavelength cutoff by the absorption of barium fluoride. The purpose of the filter is to avoid the absorption spectra of atmospheric water vapor and carbon dioxide and the reflected solar radiation.

The thermistor radiation detector is located at the apex of a 20 deg cone and, therefore, the radiometer has a field of view of about 0. 1 steradians. The amplitude of the modulated incoming radiation flux can be calculated according to the following equation,

$$\Delta W = (\rho / \pi) \bar{\tau} \sigma (T_0^4 - T_s^4)$$

where σ = Stefan-Boltzmann's constant = 5.735×10^{-8} watts/($m^2 deg^4$)

ρ = solid angle of field of view = 0.1 steradians

$\bar{\tau}$ = average transmissivity of optical filter = 0.15 at 300°K

T_0 = reference temperature = 333°K

T_s = surface temperature.

For example, a surface temperature of 300°K produces

$$\Delta W = 0.09 \text{ watts}/m^2 \quad .$$

The equivalent noise input to the radiometer with the input grounded is 1.2 microvolts, according to the preamplifier specifications. The output of the radiometer as seen on the panel microammeter with no detector output voltage is approximately 12 scale divisions. The sensitivity of the meter at 300°K is about 2 scale divisions per degree. Therefore, if the preamplifier equivalent noise input is the only input voltage, the sensitivity of the entire system beyond the detector is 10 scale divisions per microvolt, and the sensitivity of the detector is 0.2 microvolt per degree. Using the figure for the energy flux at the detector, the energy sensitivity of the detector is 60 microvolts per watt/m^2, which is of the right order of magnitude according to the specifications. This indicates that the noise level of the radiometer is limited primarily by the equivalent noise input of the preamplifier.

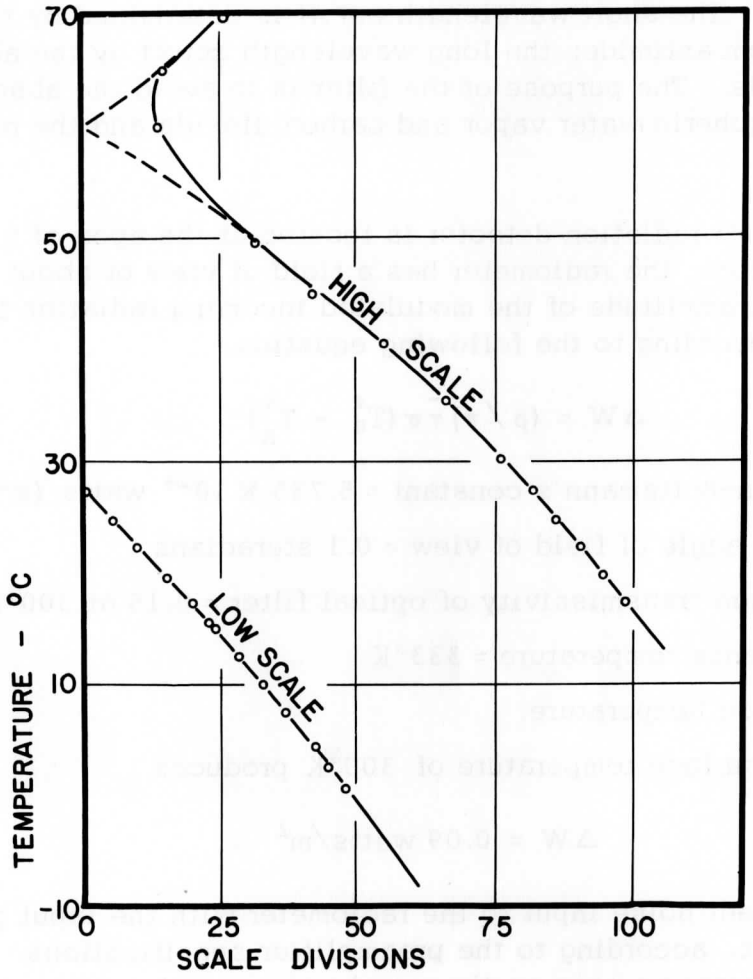

Fig. 2. Calibration curve for surface temperature bolometer.

The voltage input can be expressed as

$$E_i = (E_t^2 + E_n^2)^{\frac{1}{2}}$$

where E_i = preamplifier input voltage, E_t = detector output voltage, and E_n = equivalent noise input voltage. The difference between the actual output and a noiseless output is

$$\Delta E_i = (E_t^2 + E_n^2)^{\frac{1}{2}} - E_t \approx E_n^2 / 2E_t$$

if E_n is small in comparison with E_t. Therefore, as E_t becomes large, the noise voltage will have little effect. At 313°K, for example, E_i = 56 scale divisions, or 7 microvolts, and

$$\Delta E_i = 0.16 \text{ microvolts} .$$

The calibration curve (Fig. 2) verifies this result.

Besides the preamplifier equivalent noise input, at least three other extraneous voltages contribute to the final output voltage. A 60 cps voltage is present but contributes little except at very high temperatures, when the reference temperature is close to the measured temperature. An oscillation with a frequency of less than 3 cps and amplitude less than 0.5°C occasionally appears in the output. This may be due to the second harmonic of the detector voltage mixing with the third harmonic of the 60 cps power supply voltage, since the chopper actually modulates at slightly less than 90 cps.

Mechanical vibrations from the airplane engines result in a noise voltage. This effect is difficult to determine, since it is observed only in the air. With the time-constant of the output at 2.7 sec, the amplitude of the voltage corresponded to less than 0.4°C, but with the time constant at 0.2 sec, the fluctuations were close to 1.0°C.

The heater circuit also contributes an extraneous voltage. The heater is controlled by a thyratron that fires 60 times a second and each time it fires, a voltage pulse is induced in the output. Again the effect is negligible except at high temperatures. To reduce the voltage pulse, a low-pass LC filter was added to the thyratron output.

The time constant of the radiometer for all but one of the measurements reported here was 2.7 sec. Originally, the time constant was 0.2 sec, but in order to filter out more noise, the output capacitance of the full-wave rectifier was increased. The output signal is the average value of

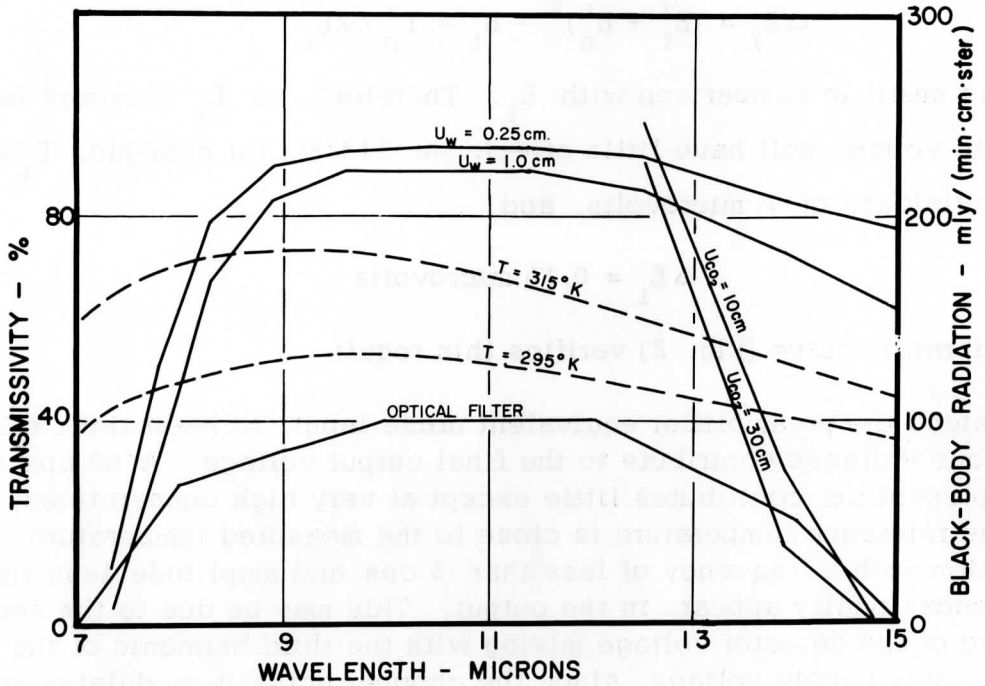

Fig. 3. Transmissivity and black-body radiation curves.

the rectified ac voltage. Thus, much of the noise voltage has no effect on the output, provided the magnitude of the noise voltage is less than the signal voltage. If a synchronous detector had been used, the noise could have been almost eliminated.

6. 2. 3 Physics of the radiometer

The radiometer measures temperature by comparing the radiation flux of a black reference cavity with the radiation flux received through an optical filter. The parallel radiation flux emitted by the surface under investigation can be expressed as a function of wavelength and temperature by Planck's Law for black-body emission,

$$B(\lambda, T) = \frac{c_1 \lambda^{-5}}{\exp(c_2/\lambda T) - 1} \quad \frac{\text{energy}/(\text{time} \cdot \text{area})}{\text{steradian} \cdot \text{wavelength}}$$

where c_1 and c_2 are physical constants. Integrating this equation over all wavelengths produces Stefan's Law,

$$B(T) = (\sigma/\pi) T^4 \text{ watts}/(\text{m}^2 \cdot \text{steradians}) \ .$$

The radiation flux received at the detector will be some function of the parallel radiation flux emitted by the ground. The accuracy of the surface temperature measurement is dependent upon this functional relationship. The variables of this function to be considered here are: (1) atmospheric transmissivity, (2) emissivity of mirror and polyethylene, (3) target emissivity, and (4) non-uniformity of temperature distribution.

The radiometer was calibrated by using water as a target at various known temperatures, and a curve of water temperature versus meter-scale divisions was obtained. Several points were also obtained from a radiator of known emissivity and temperature. The results indicated that the emissivity of water is close to 0.98 in the pass-band of the optical filter; see Brunt (1939). During calibrations, the path length from the target to the radiometer was negligible compared to the airborne measurements, so the effect of atmospheric transmissivity was not evaluated in the laboratory; see Figure 2.

In order to demonstrate the magnitude of atmospheric absorption, five examples have been calculated under various conditions for the simplifying assumptions that the air is isothermal and at constant pressure, and that only water vapor and carbon dioxide are important. A curve of the transmissivity of the optical filter of the radiometer as a function of wavelength, obtained from the radiometer manual, was plotted along with curves of the transmissivity of the atmosphere for 0.25 cm and 1.0 cm

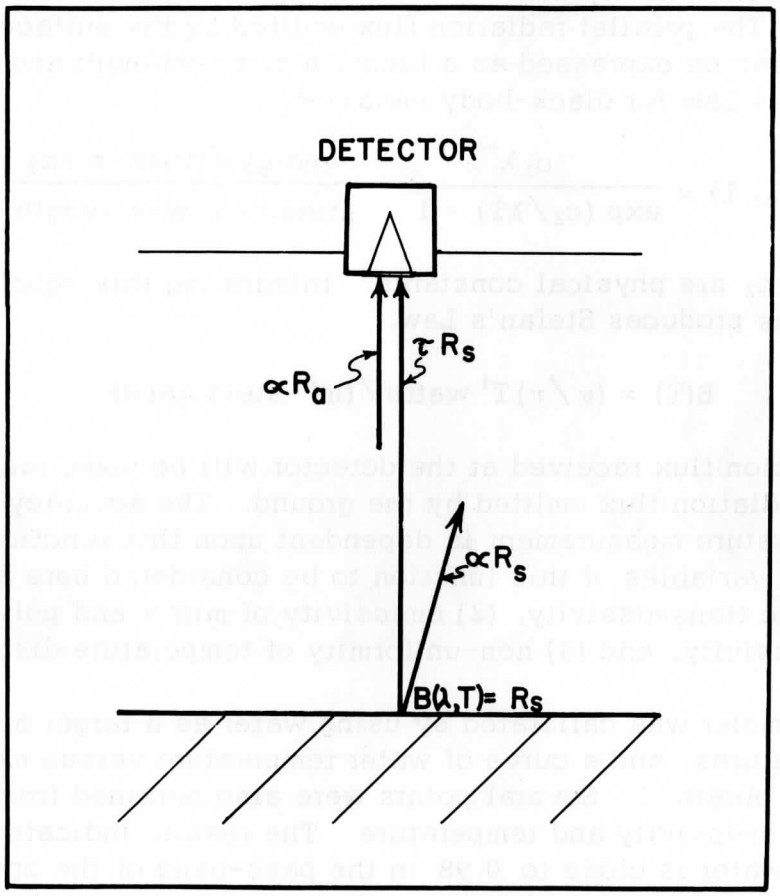

Fig. 4. Radiation fluxes between ground and surface temperature bolometer.

optical depth of water, and 10 cm and 30 cm optical depth of carbon dioxide, obtained from Elsasser (1960); see Figure 3. From Kirchoff's Law, assuming reflectance is negligible, the emissivity, ϵ, is equal to the absorptivity, α. By conservation principles, $\alpha + \epsilon = 1$. Therefore, from Figure 4,

$$R_m = (\tau R_s + \alpha R_a) \cdot \tau_m$$

where R_m = measured radiation, R_s = black-body radiation at surface temperature, R_a = black-body radiation at air temperature, $\tau = \tau_{water} \cdot \tau_{CO_2}$, $\alpha = 1 - \tau$, and τ_m = transmissivity of optical filter.

Curves of $B(\lambda, T)$ are also plotted for temperatures of $T = 315°K$ and $T = 295°K$. The curves were graphically integrated for five cases and the results are summarized in Table 1.

Table 1. Estimate of the effect of water vapor and carbon dioxide on airborne surface temperature measurements for five different combinations of observing conditions. — T_S = surface temperature; T_a = air temperature; T_r = temperature measured by radiometer; U_{wv} = optical depth of precipitable water; U_c = optical depth of carbon dioxide gas; Z = flight level; and W = mixing ratio.

	(1)	(2)	(3)	(4)	(5)	
T_s	295	315	315	315	315	deg K
T_a	315	295	295	295	295	deg K
U_{wv}	1	1	0.25	0	0	cm
U_c	30	30	10	30	10	cm
Z	1000	1000	300	1000	300	m
W	9	9	7	0	0	g/kg
T_r	301.4	309.5	311.5	313.5	313.8	deg K

The first two cases refer to conditions that could exist on a warm spring or cool summer day in Wisconsin with a mixing ratio of 9 gm/kg and a path length of 1000 m. Under these conditions the measured surface temperature may deviate from the actual surface temperature by 30% of the difference between the air and ground temperatures.

The third case is more representative of conditions actually observed in the series of flights presented in this report. These conditions refer to a flight level of 300 m above the ground and a mixing ratio of 7 gm/kg. The measured surface temperature may deviate from the actual surface temperature by 18% of the difference between the air and ground temperatures.

The fourth and fifth cases indicate that carbon dioxide alone has an appreciable effect on the measured temperature. At 300 m the effect is about 6% and at 1000 m about 8% of the difference between the air and ground temperatures.

The largest factor contributing to the temperature difference is the width of the optical filter. The bolometer response extends from 7 to 15 microns, and therefore the 6.2 micron water vapor band on one side, and the water vapor rotational band and also the carbon dioxide 15 micron band, on the other side, overlap the transmissivity curve of the optical filter.

The emissivity of the mirror chopper was not measured, but is assumed to be less than 0.03, since many polished metal surfaces are less than this; see Holden (1951). At 293°K, for an emissivity of 0.03, the chopper will change the measured temperature by 3% of the change in chopper temperature.

The chopper mirror is located outside the controlled temperature cavity but inside the radiometer sensing unit. The opening is covered with a sheet of polyethylene one mil thick, which keeps the chopper blades at a more uniform temperature for various air temperatures, but which contributes another temperature error because of the emissivity of the polyethylene, which, according to Suomi et al. (1958), is about 0.02 in the passband of the optical filter. Therefore, the polyethylene will change the measured temperature by 2% of the change in temperature of the polyethylene. The transmissivity of the polyethylene is about 0.90, so very little attenuation results. The polyethylene was necessary to keep the reference temperature of the cavity at 60°K since the heater circuit was unable to hold the reference temperature during flights in the winter season.

The radiometer was calibrated to read the temperature of a water surface, so that radiational temperatures of the land surfaces will have the same value as their thermodynamic temperature only if the emissivity from 7 to 15 microns is the same as the emissivity of water. The radiation flux emitted by a surface is proportional to T^4 and the emissivity. Differentiation of Stefan's Law for constant radiation flux yields

$$d\epsilon / \epsilon = -4\, dT / T \quad .$$

For example, at 300°K, a 1.3% change in emissivity will change the measured temperature by 1.0°C. This assumes the radiation flux in the pass-band of the optical filter is also a function of T^4.

Fortunately, in the 7 to 15 micron region, most natural surfaces have emissivities between 0.91 and 1.0; reference is made to Holden (1951). Brooks (1952) obtained emissivity values of 0.91 for dry fine sandy loam and 0.99 for wet soil. Geiger (1950) gives values of the emissivity of pine needles at 0.96 and clods of earth with sod at 0.98. Independent determinations of emissivities of various natural surfaces have not been obtained with this instrument, although such measurements would be desirable. All temperatures given in this report are computed under the assumption that the emissivity of all surfaces equals that of water. If it is assumed that a maximum difference of 8% in emissivity can occur between wet and dry conditions, the measured radiation temperature can differ by as much as 6°C for the same surface temperature.

Since radiation flux is proportional to the fourth power of the temperature, the radiometer does not measure the average temperature of a non-uniform surface temperature distribution. The true area-mean of temperature is

$$\overline{T} = (1/A) \int\int_A T(x, y)\, dx\, dy \quad , \quad \text{with} \quad A = \int\int_A dx\, dy \quad ,$$

at some particular instant in time. The area-mean of radiational temperature can be expressed as

$$\overline{T}_r = \{(1/A) \int\int_A \epsilon(x, y)\, [T(x, y)]^4\, dx\, dy\}^{\frac{1}{4}} \quad .$$

If ϵ is equal to 1, it follows from Holder's inequality that

$$\overline{T}_r \geq \overline{T} \quad ,$$

the equality holding when $T(x, y)$ is constant.

In order to show that under most conditions this effect is negligible, a simple example has been calculated for $\epsilon = 1$ and $\partial T/\partial y = 0$, assuming a harmonic variation of T in x,

$$T(x) = T_0 + T_1 \sin x \ .$$

The limits of integration are from $x = -\pi$ to $x = \pi$. The field of view of the radiometer is assumed to be a rectangle. Then it follows that

$$\overline{T} = (1/2\pi) \int_{-\pi}^{\pi} (T_0 + T_1 \sin x)\, dx = T_0 \ ,$$

while

$$\overline{T}_r = [(1/2\pi) \int_{-\pi}^{\pi} (T_0 + T_1 \sin x)^4 dx]^{\frac{1}{4}}$$

$$= T_0[1 + 3(T_1/T_0)^2 - (3/8)(T_1/T_0)^4]^{\frac{1}{4}}$$

Expanding with the aid of the binomial theorem and neglecting terms of $(T_1/T_0)^n$, where $n > 4$,

$$\overline{T}_r = T_0[1 + (3/4)(T_1/T_0)^2 - (21/32)(T_1/T_0)^4] \ .$$

This yields

$$\overline{T}_r - \overline{T} = 0.56°, \quad \text{if } T_0 = 300°K \text{ and } T_1 = 15°C \ .$$

It is improbable that temperature amplitudes of the assumed magnitude ($T_1 = \pm 15°C$) would occur in airborne use. Therefore, possible differences between $\overline{T}_r$ and $\overline{T}$ are not considered in this report. The temperature distribution is a function of time as well as space, but since the space distribution effect is small, the effect of time will also be considered negligible, and the instrument is assumed to have a first-order response in time. Dutton (1962) discusses the averaging of first-order response systems, and his results are assumed to apply to this instrument.

6.2.4 Technique of airborne operation

The airplane used for this program was a Cessna 310, a twin-engine 5 passenger plane, modified for meteorological use. The radiometer sensing unit was mounted in a camera rack, and the control and readout unit was fastened to a seat mounting. At first, the sensing unit was cushioned from airplane vibrations by sheets of foam rubber, but observations indicated that the sensing unit was not affected by vibrations as much as the control and readout unit. The sensing unit was later mounted in an enclosed box, 12" long, 12" wide, and 8" high, with a 2" opening in the bottom that fitted snugly against the bottom of the sensing unit so

that the interior of the box was isolated from the outside air. A 2" diameter flexible tube opened into the top of the box. The other end of the tube was connected to the airplane heater, so that the sensing unit would remain warm when the camera door was opened. In cold weather, the cavity reference temperature could not be maintained by the heater if the radiometer was exposed to the outside air.

The output of the recorder was modified to make the sensitivity and damping resistance compatible with the Visicorder galvanometer. The galvanometer has a flat (±5%) frequency response from 0 to 24 cps. Because of the extended frequency response of the galvanometer, high frequency noise was recorded that was not detectable with low-frequency recorders. Most of the noise was from airplane vibrations and corresponded to less than 0.4°C. The temperature trace was recorded on light-sensitive paper at a speed of 0.2 in/sec.

6.3 Results of Measurements

6.3.1 Flight course and program

The flight path was identical to the one used by Bauer and Dutton (1960). In some cases, however, different sections of the path were analyzed, and in all cases shorter path lengths were chosen and more samples per unit time were used because of the faster time constant of the surface temperature radiometer; see Figure 5.

The Lodi section is a one mile track over uncultivated undulating land, sparsely covered with grass and shrubs, with visible areas of sand, at mile 21 of the course, 4 miles north of Lodi. See Figure 6.

The Arena section is a two mile track over level uncultivated land a few feet above the Wisconsin River, sparsely covered with grass and shrubs with visible areas of sand. It is located from mile 57 to 59 of the course, 2 miles northwest of the village of Arena, less than half a mile from the Wisconsin River.

The Rolling Farmland section is a three mile track over slightly rolling terrain covered primarily with a checkered pattern of cultivated fields and pastures. It is located from mile 8 to 11 of the course on a direct line between Waunakee and Dane.

The Flat Farmland section is a three mile track over level cultivated fields. The individual fields are large and covered with a variety of crops. The soil is dark and fertile and lies in the Wisconsin River floodplain.

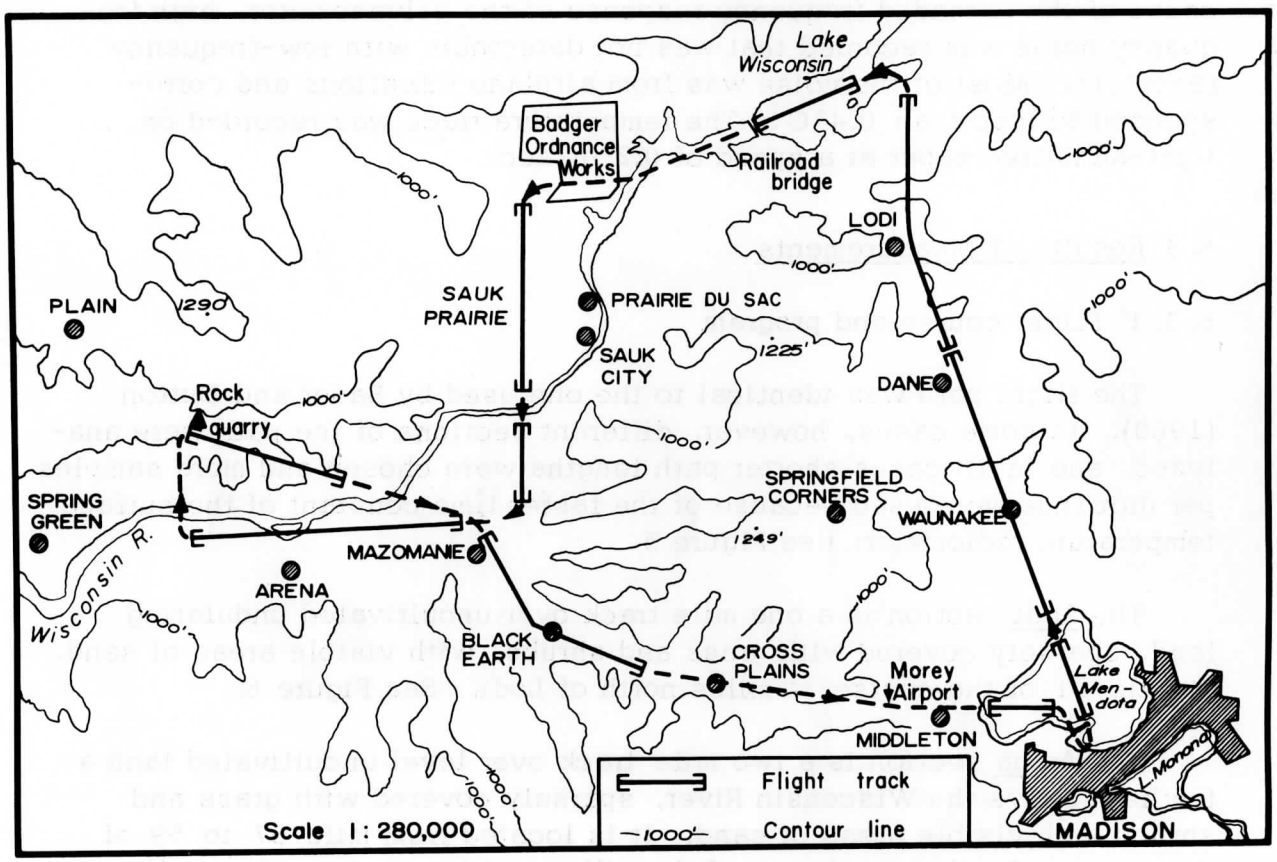

Fig. 5. Flight path used for bolometric surface temperature measurements in Southern Wisconsin. The same track was used by Bauer and Dutton (1960) for albedo studies.

It is located from mile 40 to 43 of the course, one mile south of the Badger Ordnance Works and 3 miles north of the Wisconsin River.

The Hilly Fields and Woods section covers a patchwork of cultivated fields and pastures in the valleys and woods on the steep hillside slopes. This 3 mile length is located from mile 64 to 67 of the course and 4 miles west of the Wisconsin River in typical Southwestern Wisconsin hilly terrain.

The River Bottom Swamp section is a three mile track over swampland, with scattered trees, located from mile 52 to 55 of the course and less than a mile south of the Wisconsin River. It is only a few feet higher than the river; and during high water levels on the river, parts of the area are under water.

Lake Wisconsin is an artificial lake on the Wisconsin River about a mile wide and 4 miles long. Lake Mendota is a natural lake about 5 miles wide, 6 miles long and 10 m deep, with no large incoming river.

6. 3. 2 Bolometric surface temperature variations

Tables 2a and 2b show that the variation of temperature from region to region, and the standard deviation, lessen as the winter season approaches. This is a result of decreased insolation and evaporation. The highest midday temperature occurs usually in a sparsely vegetated sandy area and the lowest midday temperature in a hilly region of scattered woods and fields. Towards the end of fall, the hilly woods and fields region no longer consistently has the lowest midday temperature. This could be expected from the decreased transpiration in the forested regions as the winter season approaches. The maximum standard deviation generally occurred in the region of level, cultivated fields. This was because the fields were covered with a variety of crops, some of which had already been harvested in August. In the harvested grain fields, much of the surface radiation was from the black soil, while the corn and hay fields provided a cover of vegetation.

Figure 6 illustrates the diurnal variation in surface temperature on September 7, 1961. A maximum spread of 25° C exists in a level region of harvested grain fields with exposed black soil. Excepting the lake surfaces, the minimum spread of 9° C exists in a hilly region of woods and fields. The diurnal variation of air temperature at the climatological station on the University of Wisconsin campus was 10.6° C; see Table 3.

In the regions of exposed soil, the variation of emissivity as a function of soil moisture may affect the measured surface temperature. For example, dry sandy loam may give a radiational temperature as much as

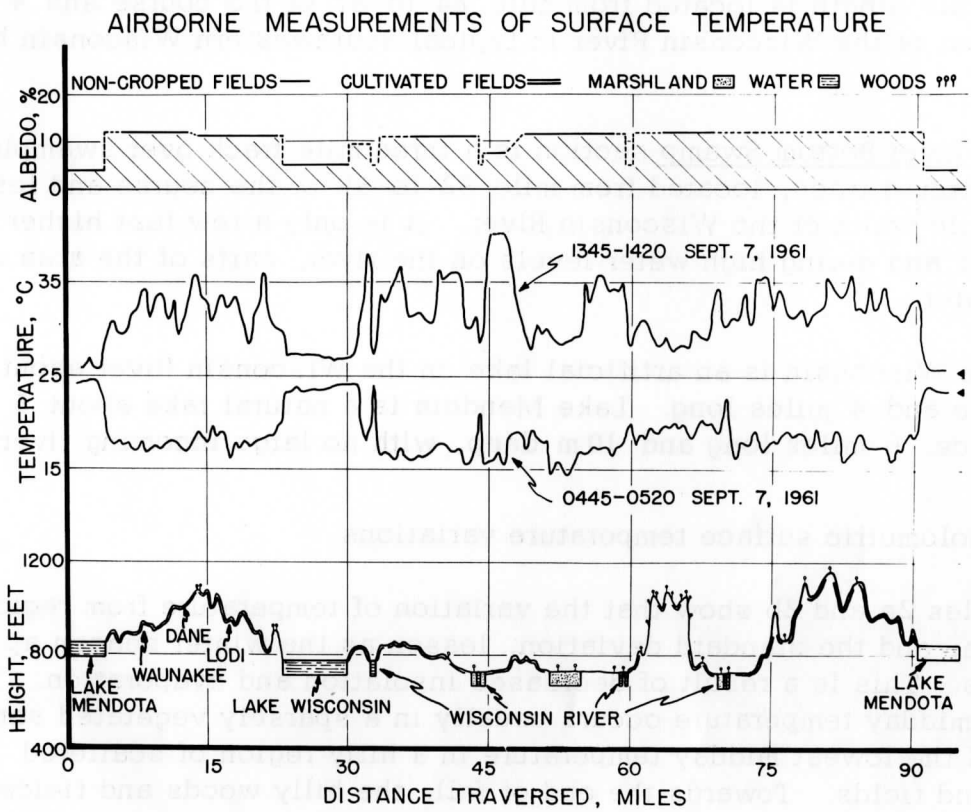

Fig. 6. Airborne measurements of surface temperature in Southern Wisconsin on September 7, 1961, in the early morning and early afternoon.

Table 2a. Average surface temperature and standard deviation (deg C) for various types of terrain in Southern Wisconsin, at indicated date and time of the day.

Date (1961)	Time (CST)	Sandy Areas		Rolling Farmland	Flat Farmland	Hilly Fields and Woods
		Lodi	Arena			
Aug. 31	0450 - 0630	18.3 ± 0.4	19.3 ± 0.2	18.1 ± 0.5	18.6 ± 0.6	20.9 ± 0.7
Sept. 7	0445 - 0525	18.2 ± 0.2	17.3 ± 0.2	17.4 ± 0.4	16.8 ± 0.7	19.6 ± 0.7
Sept. 6	1405 - 1445	33.7 ± 1.2	35.8 ± 1.1	32.1 ± 1.2	29.5 ± 1.8	28.8 ± 1.0
Sept. 7	1345 - 1425	35.2 ± 1.4	35.2 ± 0.5	32.6 ± 1.4	32.6 ± 2.2	28.9 ± 0.9
Sept. 14	1350 - 1430	21.2 ± 0.5	18.0 ± 0.4	19.6 ± 0.6	19.5 ± 0.6	15.5 ± 0.8
Sept. 15	1415 - 1455	30.2 ± 0.6	28.9 ± 0.6	28.4 ± 0.8	26.9 ± 1.0	23.4 ± 1.0
Sept. 25	1445 - 1525	21.8 ± 1.0	20.7 ± 0.8	19.8 ± 0.4	19.6 ± 0.9	17.9 ± 0.9
Sept. 28	1410 - 1450	16.4 ± 1.8	18.0 ± 1.8	14.0 ± 0.9	14.2 ± 1.6	9.3 ± 1.3
Oct. 2	1425 - 1505	18.7 ± 1.1	18.9 ± 0.7	16.8 ± 1.5	17.8 ± 1.2	15.1 ± 1.3
Oct. 5	1420 - 1500	26.7 ± 0.8	28.1 ± 0.6	24.2 ± 0.5	24.9 ± 0.7	24.6 ± 0.6
Nov. 1	1325 - 1405	16.6 ± 0.8	17.2 ± 0.5	15.2 ± 0.2	15.4 ± 0.7	17.2 ± 0.7
Nov. 6	1340 - 1420	---	2.4 ± 0.2	---	2.8 ± 0.3	1.4 ± 0.4
Nov. 9	1340 - 1420	11.6 ± 0.7	10.5 ± 0.6	9.2 ± 0.4	10.1 ± 0.5	11.1 ± 1.1
Nov. 27	1445 - 1525	0.7 ± 0.6	-2.5 ± 0.4	1.2 ± 0.3	-1.3 ± 0.2	-2.6 ± 0.9

Table 2b. Average surface temperature and standard deviation (deg C) for various types of terrain in Southern Wisconsin, at indicated date and time of the day. $T_{L.M.}$ = temperature of Lake Mendota several feet under the surface, measured independently by a thermistor.

Date (1961)	Time (CST)	Swamp Areas	Lakes		$T_{L.M.}$
			Wisconsin	Mendota	
Aug. 31	0450 - 0630	17.8 ± 0.7	24.5	25.0	25.6
Sept. 7	0445 - 0525	15.0 ± 0.8	23.5	24.0	25.2
Sept. 6	1405 - 1445	28.8 ± 0.9	26.2	24.0	25.6
Sept. 7	1345 - 1425	29.0 ± 0.7	27.0	25.7	25.7
Sept. 14	1350 - 1430	16.3 ± 0.4	25.5	22.5	23.8
Sept. 15	1415 - 1455	25.5 ± 0.7	24.5	22.0	22.8
Sept. 25	1445 - 1525	18.7 ± 0.6	19.0	19.5	20.2
Sept. 28	1410 - 1450	12.9 ± 1.3	11.0	13.7	16.0
Oct. 2	1425 - 1505	15.4 ± 0.6	15.3	17.5	18.0
Oct. 5	1420 - 1500	25.7 ± 0.6	15.3	17.2	17.6
Nov. 1	1325 - 1405	16.5 ± 0.8	9.0	11.2	13.3
Nov. 6	1340 - 1420	2.2 ± 0.3	8.0	9.5	9.3
Nov. 9	1340 - 1420	9.8 ± 0.6	6.0	8.0	---
Nov. 27	1445 - 1525	-2.0 ± 0.2	2.0	4.5	---

Table 3. Climatological station data and weather conditions for days with bolometric surface temperature measurements. T_{max} = maximum air temperature and T_{min} = minimum air temperature at the climatological station on the University of Wisconsin campus (deg C); T_F = temperature during flight-time.

Date (1961)	T_{max}	T_{min}	T_F	Weather Conditions
Aug. 31	31.8	19.4	23.8	clear
Sept. 7	30.6	20.0	22.7	5/10 stratus; WSW 5
Sept. 6	27.2	16.1	23.8	clear; SW 10
Sept. 7	30.6	20.0	28.2	8/10 Ci; almost calm
Sept. 14	12.8	7.8	9.9	OVC & SHWRS; WSW 15
Sept. 15	20.0	7.2	18.2	1/10 Cu
Sept. 25	15.0	9.4	12.7	3/10 Cu
Sept. 28	11.7	3.3	10.4	clear; W 10
Oct. 2	12.8	1.1	9.3	8/10 Cu
Oct. 5	23.2	12.8	21.6	clear; W 5
Nov. 1	10.6	5.6	6.6	6/10 Cu; SW almost calm
Nov. 6	-0.6	-3.3	-2.3	OVC
Nov. 9	7.2	-4.4	4.3	clear
Nov. 27	0	-3.9	-3.4	3/10 Cu; NE 15

Table 4. Precipitation records for days previous to flights over Southern Wisconsin from the climatological station on the University of Wisconsin campus.

Flight Date (1961)	Date and Amount of Previous Precipitation
Sept. 6	Sept. 5; 0.1"
Sept. 7	Sept. 5; 0.1"
Sept. 14	Sept. 12; 2.7", Sept. 13; 2.3"
Sept. 15	Sept. 12; 2.7", Sept. 13; 2.3"
Sept. 25	Sept. 23; 0.1", Sept. 24; 0.01"
Sept. 28	Sept. 27; Trace
Oct. 2	Sept. 30; 0.70"
Oct. 5	Oct. 3; Trace
Nov. 1	Oct. 29; 1.0"
Nov. 6	Nov. 2; 1.28"
Nov. 9	Nov. 6; Trace
Nov. 27	Nov. 6; Trace

5° C lower than the actual surface temperature. If the same soil were moist, the measured temperature would be very close to the actual surface temperature. Previous precipitation records for each flight date are therefore summarized in Table 4. The table indicates that the soil was probably moist on Sept. 6, 14 and 15, and Oct. 2. For the rest of the flight dates the soil was probably dry at the surface, so temperatures, especially in the sparsely vegetated areas, may be actually somewhat higher than measured with moister soil.

In general, the surface temperature is a complicated function of many variables, which include air temperature, insolation, cloud cover, albedo, soil moisture, evaporation, vegetative cover, elevation contours, soil type, and wind velocity. As a result, the surface temperature over a region of variable terrain cannot be easily inferred from a few measurements. For example, the lowest midday temperature on a clear dry day may be found in a swamp, a region of hilly fields and woods, or a region of rolling farmland.

Figure 7 illustrates that the surface temperature distribution can change considerably within a few days. Part of the change may be due to slight variations in flight course. This effect was minimized by selecting an easily identifiable flight path and by selecting specific fields and woodlots to fly over. The temperature distribution was observed to change considerably from flight to flight over these specific surface features.

The record on April 16, 1962 (Table 5) included the measurement of hemispheric net radiation. The net radiation was measured with an unventilated flux plate, calibrated with a ventilated net radiometer described by Suomi et al. (1954). The flux plate was covered with a flat sheet of polyethylene about a quarter inch away from the flux plate and therefore is inaccurate at low sun angles. The calibration, however, compares favorably with the ventilated net radiometer under clear conditions at high sun angles, and under uniform overcast conditions.

Several interesting results are observed. In the rolling farmland and Lodi areas, the net downward radiation was relatively low (0.45 and 0.32 ly/min, respectively) due to partial obscuring of the sun by a thin deck of cirrus. The other regions were clear and the net radiation was greater than 0.55 ly/min. The net radiation is a maximum over Lake Mendota because of the lower albedo and decreased upward long-wave radiation flux. Over Lake Wisconsin, the net radiation fluctuated because of variable cloudiness, but was higher than the surrounding land. At Arena, the net radiation was less than the surrounding region, probably due to a higher albedo.

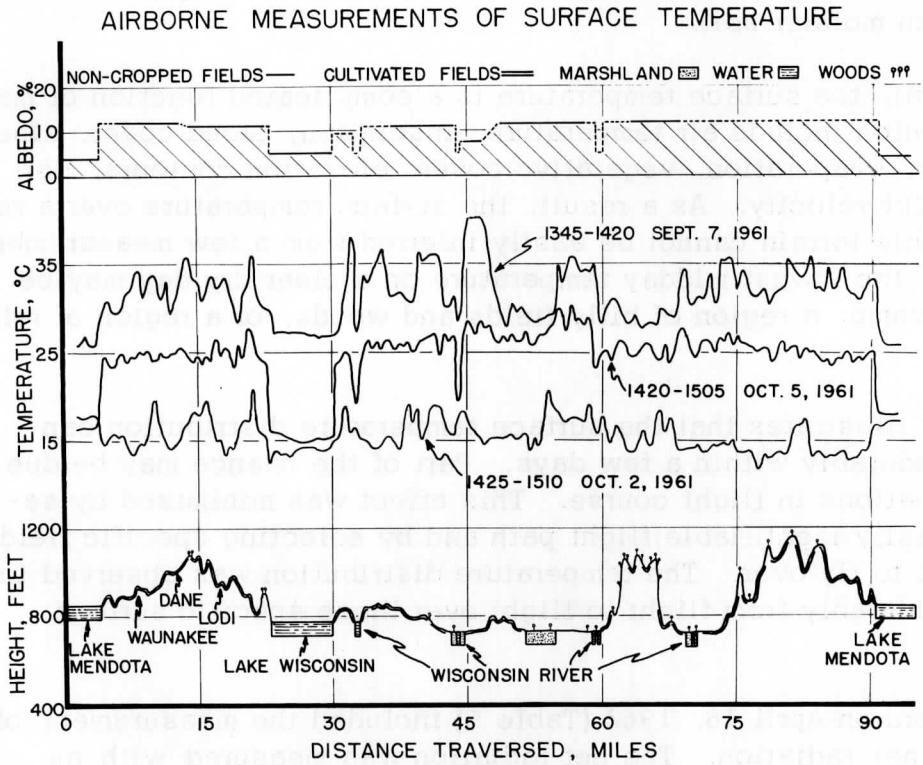

Fig. 7. Airborne measurements of surface temperature in Southern Wisconsin during early afternoon flights over the same course on September 7, and October 2 and 5, 1961.

Table 5. Average surface temperature and net radiation for various types of terrain in Southern Wisconsin. The time-constant of the radiometer is 0.2 sec. Time of flight, April 16, 1962, 1400 to 1445 CST.

Location	Temperature °C	Net Radiation (ly/min)
Lodi	13.2 ± 1.1	(0.32)*
Arena	22.8 ± 1.3	0.55
Rolling farmland	13.1 ± 1.5	(0.45)*
Flat farmland	21.8 ± 2.0	0.65
Hilly fields and woods	18.8 ± 2.9	0.65
Swamp areas	15.8 ± 1.4	0.65
Lake Wisconsin	3.0	---
Lake Mendota	3.0	---

*Under Ci cloud.

6.4 References

Albrecht, F.: "Mikrometeorologische Temperatur Messungen vom Flugzeug aus," Ber. Deutsch. Wetterdienst, Bad Kissingen, 38, 332, 1952.

Bauer, K.G., and J.A. Dutton: "Flight Investigations of Surface Albedo," University of Wisconsin, Department of Meteorology, Technical Report No. 2, Contract DA-36-039-SC-80282, Madison, Wis., 1959.

Brooks, F.A.: "Atmospheric Radiation and Its Reflection from the Ground," J. Meteor., 9, 41, 1952.

Brunt, D.: Physical and Dynamical Meteorology, Cambridge University Press, Cambridge, England, 1939.

Combs, A.C.: "Techniques and Results of Infrared Surface Temperature Measurements in New Jersey and Greenland," USASRDL Technical Report 2193, DA Task 3A99-07-001-01, Fort Monmouth, N.J., 1961.

Dutton, J. A.: "Space and Time Response of Airborne Radiation Sensors for the Measurement of Ground Variables," J. Geophys. Research, 67, 195, 1962.

Elsasser, W. M.: "Atmospheric Radiation Tables," Meteorological Monographs, 4, 1960.

Fritz, S., and J. S. Winston: "Synoptic Use of Radiation Instruments from Satellite Tiros II," Monthly Weather Review, 90, 1, 1962.

Geiger, R.: The Climate Near the Ground, Harvard University Press, Cambridge, Mass., 1950.

Holden, T. S., and J. J. Greenland: "The Coefficients of Solar Absorptivity and Low Temperature Emissivity of Various Materials," Report No. 6, Commonwealth Scientific and Industrial Research Organization, Division of Building Research, Melbourne, Australia, 1951.

Lettau, H. H.: "Research Problems in Micrometeorology," University of Wisconsin, Department of Meteorology, Final Report, Contract DA-36-039-SC-80063, Madison, Wisconsin, 1959.

Nordberg, W., W. R. Bandeen, B. J. Gonrath, V. Kunde, and I. Persano: "Preliminary Results of Radiation Measurements from the Tiros III Meteorological Satellite," J. Atmos. Sciences, 19, 20, 1962.

Suomi, V. E., M. Fransilla, and N. Isletzer: "An Improved Net Radiometer," J. Meteor., 11, 276, 1954.

Suomi, V. E., D. O. Staley, and P. M. Kuhn: "A Direct Measurement of Infra-Red Radiation Divergence to 160 mb," Quart. J. Roy. Meteor. Soc., 84, 360, 1958.

Additional reference (published after completion of this work):

Lorenz, D.: "Messungen der Bodenoberflaechen Temperator vom Hubschranber aus" (Measurements of Groundsurface Temperature from a Helicopter), Berichte Deutsch. Wetterdienst, 82, Offenbach a. M., Germany, 1962.

7

Climatology of Atmospheric Boundary-Layer Parameters and Energy Dissipation, Derived from Gregg's Aerological Survey of the U.S. *

Warren B. Johnson, Jr.

Department of Meteorology
University of Wisconsin

Abstract. A graphical-numerical method, developed by Lettau (1962), for eliminating the thermal wind from observed wind profiles in a baroclinic boundary layer, is applied to mean hodographs obtained by meteorological kites at four stations in the United States during the years 1915 to 1920, summarized by Gregg (1922). In the analysis, the assumption of a height-independent thermal wind permits the approximate determination of the surface geostrophic wind and the surface shearing stress. These quantities are used to compute the angle between surface wind and isobars, the geostrophic drag coefficient, and the total energy dissipation in the boundary layer. The results are compared seasonally and regionally, and in most cases show tolerable agreement with theoretical values. An attempt to investigate the dependence of the geostrophic drag coefficient upon stability is made, using Richardson-number estimates based on geostrophic advection.

List of Contents

7.1 Introduction

7.2 Data Description and Transformation

---

* Part of this work was submitted to the University of Wisconsin in partial fulfillment of the requirements for the degree of Master of Science. In addition to sponsorship by the U.S. Army Electronic Proving Ground, Fort Huachuca, Arizona, Meteorology Department, this work was supported by the Ford Foundation under the terms of a Graduate Student Fellowship for the author.

7.3 Development of Theory and Method of Analysis
7.3.1 Theoretical Background
7.3.2 Determination of Geostrophic Wind Components
7.3.3 Determination of Boundary Layer Parameters
7.3.4 Estimate of Richardson Numbers

7.4 Discussion of Results
7.4.1 Reliability of Data
7.4.2 Discussion of Hodographs
7.4.3 Discussion of Diabatic Effects
7.4.4 Comparison with Theoretical Windprofile

7.5 Acknowledgements

7.6 References

7.1 Introduction

Modern-day balloon soundings of the atmosphere are designed with rapid ascent speeds of the order of 1000 feet per minute to increase the simultaneity of the observations at various tropospheric and stratospheric levels. Information on upper-air conditions as obtained from these observations is vitally important for use in forecasting and in the study of the large-scale features of the atmosphere. Data obtained from these soundings, however, is of limited use in the study of the atmospheric boundary-layer (which is the lower portion of the troposphere) because the rapidly-ascending balloons do not sample in sufficient detail the characteristic changes in wind speed and direction which occur in this region. Thus, an investigator who wishes to study the detailed structure of the atmospheric boundary layer, or layer of frictional influence, must turn to other sources of data.

One means of detailed low-level sounding — and, unfortunately, one of the most neglected in recent years — is the meteorological kite. Instrument-carrying kites were commonly used by the U.S. Weather Bureau during the period 1910 to 1930. Gregg (1922) summarized in a very thorough fashion the observations made by means of kites up to and including the year 1920, at six kite stations in the U.S. Portions of these data have formed the basis for this investigation.

Gregg's summary has been used by other researchers. Humphreys (1940) compared theoretical wind profiles for the two cases of (1) gradient wind the same at all levels, and (2) gradient wind increasing linearly with height, with wind profiles obtained from the kite observations at Drexel, Nebraska, for summer and winter, respectively. The shapes of these two sets of curves were shown to be roughly the same. In a later section of the present study, Humphreys' results will be confirmed.

Priestley (1959) concluded that a shortcoming of many of the previous attempts to explain the height-variation of the wind in the boundary layer is that insufficient consideration was given to the thermal wind. The present study is a new attempt to evaluate windprofile data for baroclinic conditions (geostrophic wind changing in speed and/or direction with height) in the atmosphere. A method, suggested by Lettau (1962), is used which separates from the total height-variation of the wind vector an estimate of that variation attributable to the thermal wind. This estimate is based on theoretical principles, although it is to a degree limited in validity by the assumption of constant thermal wind.

When the estimated effects of baroclinicity are separated from the observed wind profiles, as is done in this study, the remaining data approximately describe the frictional effects. Using this information and theory largely developed by Lettau (1950, 1957a, 1957b, 1959, 1961, 1962), various boundary-layer parameters, including energy dissipation, have been computed for the four seasons at four locations in the United States.

7.2 Data Description and Transformation

Gregg's summary covers the results of daily kite observations at the following six U.S. Weather Bureau stations maintained during the period 1915-1920: Broken Arrow, Oklahoma; Drexel, Nebraska; Ellendale, North Dakota; Groesbeck, Texas; Leesburg, Georgia; and Royal Center, Indiana. The data for the first four stations were chosen for this study, principally because of the greater number of observations at these sites. Table 1, most of which was taken from Gregg's report, summarizes the essential facts concerning each of these kite stations. It may be noted that Drexel has by far the longer record of observations, and as expected, in most cases these data seem to give the most reliable results.

According to Gregg, the kite flights were made daily during the periods shown, except when lack of wind, extremely high wind, or other conditions made kite-flying impossible. Thus the data are biased in that cases of very low or very high winds are excluded. This fact may slightly reduce the value of the observations for strictly climatological purposes, but does not make the data less suitable for use in the present study. Also it should be remembered that the data represent daytime observations only. Gregg does not report explicitly the time of day the kites were regularly flown, although at one point he remarks that a majority of the flights were made ". . . near the time of primary pressure maximum," indicating mid-morning.

For each of the four seasons Gregg tabulated the average wind speed and direction at each station at anemometer level, 500, 750, 1000, 2000,

Table 1. Data on station location and period of observations for Gregg's Aerological Survey.

Station	Alt. m MSL	N Lat.	W Long.	Period of Observations (inclusive)
Ellendale, N. Dakota	444	45°59'	98°34'	Jan. 1918 - Dec. 1920
Drexel, Nebraska (12 mi. WNW of Omaha)	396	41°20'	96°16'	Oct. 1915 - Dec. 1920
Broken Arrow, Okla. (15 mi. SE of Tulsa)	233	36°02'	95°49'	Aug. 1918 - Dec. 1920
Groesbeck, Texas (25 mi. E of Waco)	141	31°30'	96°28'	Oct. 1918 - Dec. 1920

3000, 4000, and 5000 m above mean sea level, grouping the profiles according to sixteen surface-wind directions (the sixteen points of the compass). In this study, the sixteen groups were reduced to eight (for surface-wind directions N, NE, E, SE, S, SW, W, NW) by averaging sets of three surface-wind directions. For example, the groups of observations for NNW, N, and NNE surface-wind directions were averaged to obtain a single class of data for surface-wind direction N. Since the observations become rather sparse above 2000 m, and also because the frictional influence of the earth's surface is generally conceded to be very small at and above approximately 1500 m above station level (Lettau, 1959), the present study did not consider winds above 2000 m MSL.

The climatological means thus obtained consist of horizontal wind speed and direction at five levels (station, 500, 750, 1000, and 2000 m MSL), classed according to eight surface-wind directions, for the four seasons, at all four kite stations. For each wind vector, the component parallel with the surface wind and the component perpendicular to the surface wind (taken as positive when directed to the right of the surface wind) were computed. These data are presented in Tables 2 to 5. The surface observations were assumed to be taken at a normal anemometer level of 3 to 5 m. The wind speed at the earth-air interface ($z = 0$) is of course equal to zero. However, to conserve space in the tables, values of the derived surface geostrophic wind components were entered opposite $z = 0$. The method by which surface geostrophic wind components were obtained, as well as the theory used in the computation of the boundary-layer parameters, will be explained in Section 7.3.1.

Table 2. Wind-profile data for eight surface-wind directions at Drexel, Nebraska. z is height (m) above surface; A.L. is anemometer level; u, v are wind components (cm/sec) perpendicular to and parallel with surface wind; underlined values signify estimated geostrophic wind components.

	N		NE		E		SE		S		SW		W		NW	
z	u	v	u	v	u	v	u	v	u	v	u	v	u	v	u	v
2.1: Winter																
1604	-138	1249	454	746	895	496	1277	202	1247	720	1145	1019	728	1511	-62	1768
604	35	1177	299	904	626	884	772	944	688	1138	625	1143	457	1257	151	1433
354	25	1103	155	880	354	949	459	1030	401	1164	409	1168	313	1166	125	1254
104	9	743	20	670	56	741	87	782	73	840	95	862	63	771	24	813
A.L.	0	563	0	553	0	543	0	550	0	597	0	630	0	527	0	583
0	300	1020	270	890	470	990	510	1210	460	1220	390	1100	340	990	320	1090
2.2: Spring																
1604	-286	1276	62	811	400	806	666	928	682	1150	625	1283	317	1449	-285	1568
604	-37	1283	85	1047	243	1144	290	1061	277	1301	326	1245	238	1155	8	1270
354	-27	1170	17	1000	128	1156	175	1154	133	1261	214	1174	154	1099	-7	1177
104	9	773	9	727	31	889	30	859	11	923	64	911	41	866	0	863
A.L.	0	577	0	590	0	713	0	657	0	723	0	760	0	700	0	690
0	310	1100	330	1040	360	1180	220	1150	250	1230	270	1120	260	920	280	990
2.3: Summer																
1604	-374	992	-270	729	520	544	672	459	506	913	258	1149	245	1260	-97	1377
604	-100	1008	-25	867	164	816	301	890	261	1099	184	1207	213	1097	0	1183
354	-46	970	-31	882	107	871	171	938	140	1081	81	1158	133	1029	18	1067
104	-10	613	18	613	30	836	32	672	35	742	10	803	12	703	8	690
A.L.	0	410	0	427	0	467	0	473	0	523	0	590	0	517	0	490
0	270	890	220	830	170	870	230	990	400	1060	430	1110	350	890	310	940
2.4: Fall																
1604	-277	1201	-146	728	449	634	911	669	714	1099	625	1082	319	1247	-20	1637
604	20	1203	93	935	290	891	534	1019	396	1322	317	1181	324	1038	133	1333
354	19	1107	28	950	203	928	361	1008	240	1275	211	1158	206	1026	84	1191
104	9	713	8	630	36	626	57	698	25	850	29	822	39	756	23	783
A.L.	0	490	0	420	0	440	0	467	0	590	0	603	0	550	0	550
0	500	1050	560	920	630	870	380	1050	340	1260	280	1100	370	860	430	1010

Table 3. Wind-profile data for eight surface-wind directions at Ellendale, North Dakota. z is height (m) above surface; A. L. is anemometer level; u, v are wind components (cm/sec) perpendicular to and parallel with surface wind; underlined values signify estimated geostrophic wind components.

	N		NE		E		SE		S		SW		W		NW	
z	u	v	u	v	u	v	u	v	u	v	u	v	u	v	u	v
3. 1: Winter																
1556	44	1066	400	525	798	254	1216	-259	1140	250	1180	777	854	1349	105	1497
556	270	954	365	715	567	708	727	647	748	861	685	933	586	1238	223	1311
306	187	959	281	750	329	802	422	829	433	957	425	953	363	1094	159	1185
56	19	840	0	697	61	654	50	621	32	672	50	658	26	732	5	867
A. L.	0	807	0	670	0	593	0	537	0	577	0	560	0	630	0	787
0	350	890	320	790	440	890	470	1000	540	1070	440	950	510	1070	390	1130
3. 2: Spring																
1556	103	1035	185	827	660	683	747	969	463	1088	652	1299	241	1468	0	1317
556	200	1062	224	971	409	891	341	1112	302	1154	393	1211	270	1135	170	1157
306	112	1058	138	983	194	940	227	1036	159	1085	184	1163	127	1033	83	1087
56	6	940	5	857	5	833	0	840	10	810	10	830	0	787	0	920
A. L.	0	910	0	820	0	800	0	780	0	743	0	733	0	717	0	883
0	260	1030	250	1000	260	960	250	1080	290	1090	290	1080	290	910	290	1030
3. 3: Summer																
1556	-173	862	280	430	339	367	497	795	523	848	649	721	430	1182	-116	1171
556	130	971	209	744	244	751	217	1050	215	1068	243	908	205	1091	61	1055
306	107	964	138	809	149	742	125	972	124	1010	86	819	75	984	69	988
56	9	747	18	630	13	580	12	730	9	733	29	626	-4	697	-5	763
A. L.	0	693	0	573	0	530	0	670	0	660	0	550	0	620	0	707
0	360	940	230	830	270	840	290	1040	240	1050	150	900	290	930	270	920
3. 4: Fall																
1556	177	788	393	509	849	354	935	505	910	890	613	1063	501	1239	203	1332
556	246	876	335	803	513	800	559	1035	521	1226	476	1069	392	1138	247	1161
306	187	880	245	852	321	808	276	1031	313	1166	300	1045	278	1088	174	1100
56	13	740	34	652	80	595	34	732	23	810	16	713	13	753	5	833
A. L.	0	703	0	593	0	533	0	647	0	700	0	607	0	650	0	767
0	300	880	330	890	380	920	390	1170	400	1240	410	980	360	1000	310	1000

Table 4. Wind-profile data for eight surface-wind directions at Groesbeck, Texas. z is height (m) above surface; A. L. is anemometer level; u, v are wind components (cm/sec) perpendicular to and parallel with surface wind; underlined values signify estimated geostrophic wind components.

	N		NE		E		SE		S		SW		W		NW	
z	u	v	u	v	u	v	u	v	u	v	u	v	u	v	u	v
4. 1: Winter																
1859	-209	1011	334	871					857	941	542	1112	368	1474	-119	1558
859	169	928	287	454					802	1283	288	1186	310	1186	95	1166
609	188	913	251	523					520	1357	199	1170	193	1131	108	1085
359	150	911	198	595	Insufficient data				358	1246	124	1116	141	1094	60	1031
A. L.	0	643	.0	410					0	533	0	580	0	623	0	663
0	440	840	--	--					720	1330	250	1120	270	930	300	840
4. 2: Spring																
1859	-563	988	-322	574	418	340	680	688	584	1025	277	1057			-523	1575
859	-75	990	122	774	483	634	528	939	349	1243	134	1213			-139	1396
609	-76	994	116	862	425	767	383	999	311	1214	14	1207	Insufficient		-44	1253
359	-56	958	56	876	280	845	245	983	143	1165	7	1173	data		-13	1063
A. L.	0	663	0	587	0	497	0	527	0	713	0	710			0	780
0	--	--	530	900	450	860	410	1030	200	1240	370	1230			--	--
4. 3 Summer																
1859							143	600	126	671	-26	502				
859							180	759	144	875	14	800				
609							156	754	119	889	25	847				
359	Insufficient data						130	739	65	857	-10	840	Insufficient data			
A. L.							0	533	0	520	0	490				
0							240	800	280	910	270	930				
4. 4: Fall																
1859	-168	986	154	703	466	424	694	678	533	973					-222	1326
859	153	867	237	809	438	759	601	913	452	1198					0	1155
609	150	880	261	838	398	829	485	966	332	1184					81	1153
359	118	882	183	837	290	873	308	990	196	1110	Insufficient data				47	1069
A. L.	0	567	0	463	0	363	0	433	0	487					0	545
0	390	780	330	830	380	930	490	1010	450	1180					590	930

Table 5. Wind-profile data for eight surface-wind directions at Broken Arrow, Oklahoma. z is height (m) above surface; A. L. is anemometer level; u, v are wind components (cm/sec) perpendicular to and parallel with surface wind; underlined values signify estimated geostrophic wind components.

	N		NE		E		SE		S		SW		W		NW	
z	u	v	u	v	u	v	u	v	u	v	u	v	u	v	u	v
5. 1: Winter																
1767	-384	1229							964	997	663	996	368	1372	106	1650
767	123	1113							671	1243	343	1098	311	1214	244	1341
517	54	1046							476	1288	293	1049	204	1152	79	1235
267	34	966							262	1168	162	1011	97	975	54	1039
A. L.	0	790	Insufficient data						0	740	0	697	0	673	0	793
0	830	950							510	1280	180	1070	410	980	--	--
5. 2: Spring																
1767	-312	1020	61	456	607	481	936	639	746	1065	352	1175				
767	-97	878	252	731	571	750	489	933	407	1280	0	987				
517	-90	908	154	849	392	939	335	1030	252	1296	-54	935				
267	-57	895	63	830	211	888	167	946	108	1152	0	853	Insufficient data			
A. L.	0	863	0	710	0	663	0	747	0	863	0	693				
0	--	--	360	900	470	940	190	1050	270	1280	--	--				
5. 3: Summer																
1767									258	672	424	705				
767									232	848	418	797				
517									135	887	173	891				
267			Insufficient data						75	804	84	799	Insufficient data			
A. L.									0	583	0	540				
0									360	880	430	810				
5. 4: Fall																
1767	-176	1073	78	783			926	549	564	1118	569	1133			-110	1449
767	189	972	171	829			537	917	317	1157	428	1042			193	937
517	142	969	133	873	Insufficient		286	1021	261	1164	370	1054	Insufficient		102	917
267	98	882	109	810	data		198	959	130	1060	158	964	data		96	872
A. L.	0	697	0	530			0	633	0	717	0	597			0	690
0	510	850	330	800			340	1080	210	1080	330	910			--	--

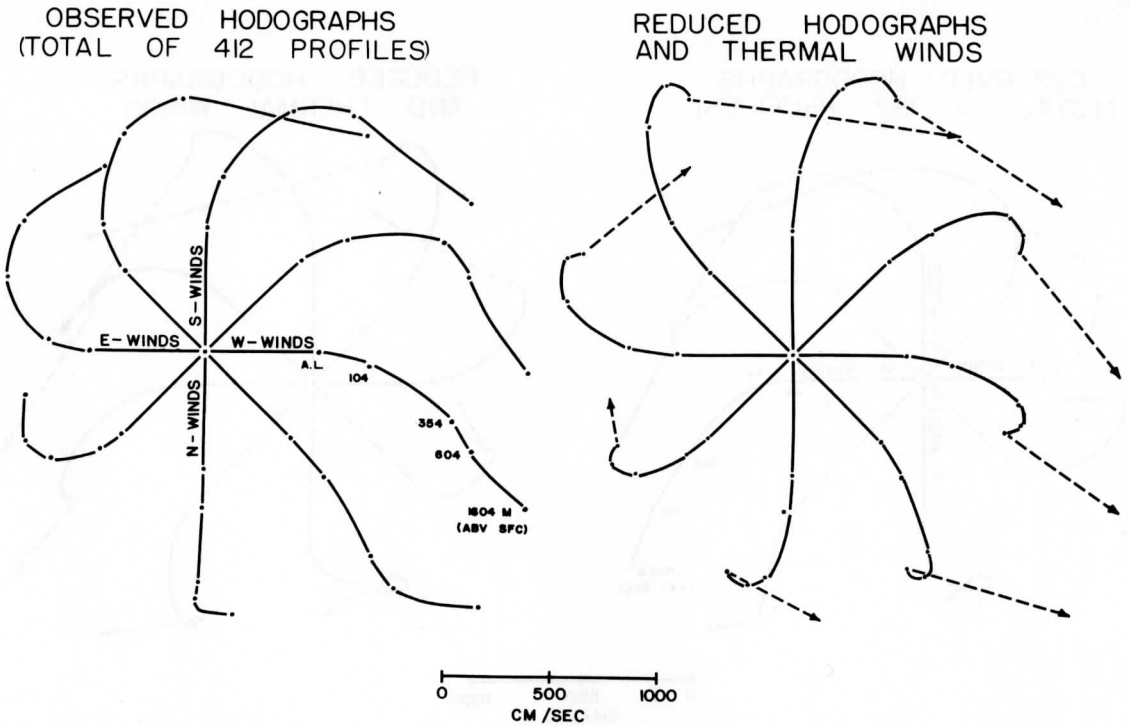

Fig. 1. Mean hodographs for 8 surface-wind directions, Drexel, Nebraska Winters, 1915-1920

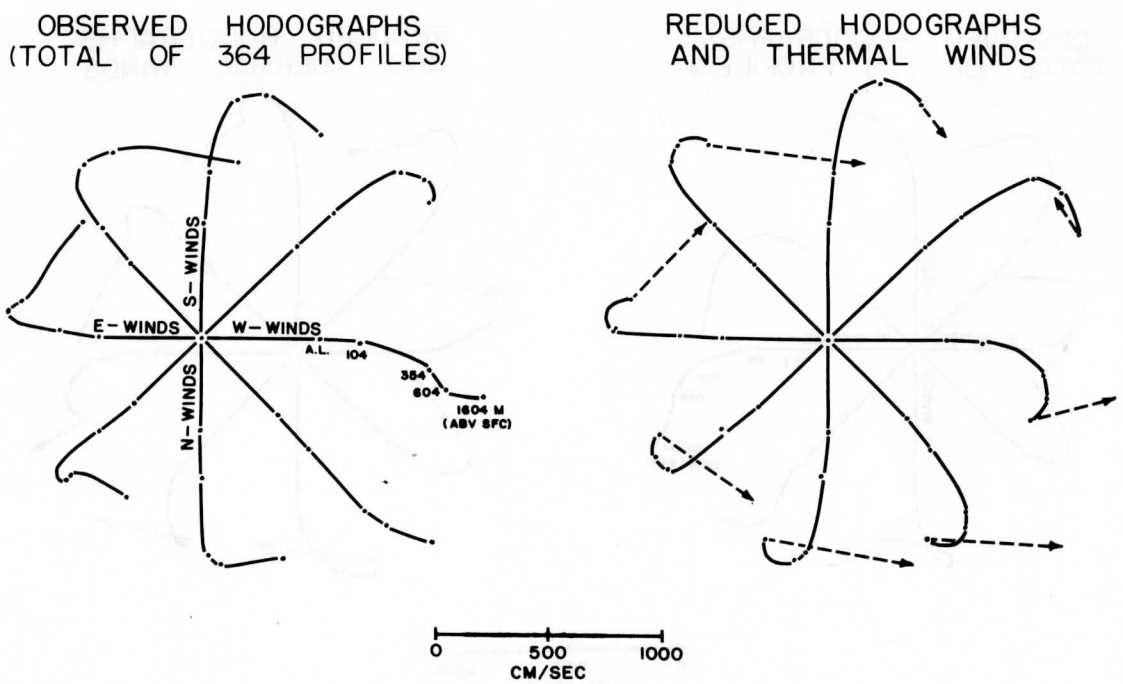

Fig. 2. Mean hodographs for 8 surface-wind directions, Drexel, Nebraska Summers, 1916-1920

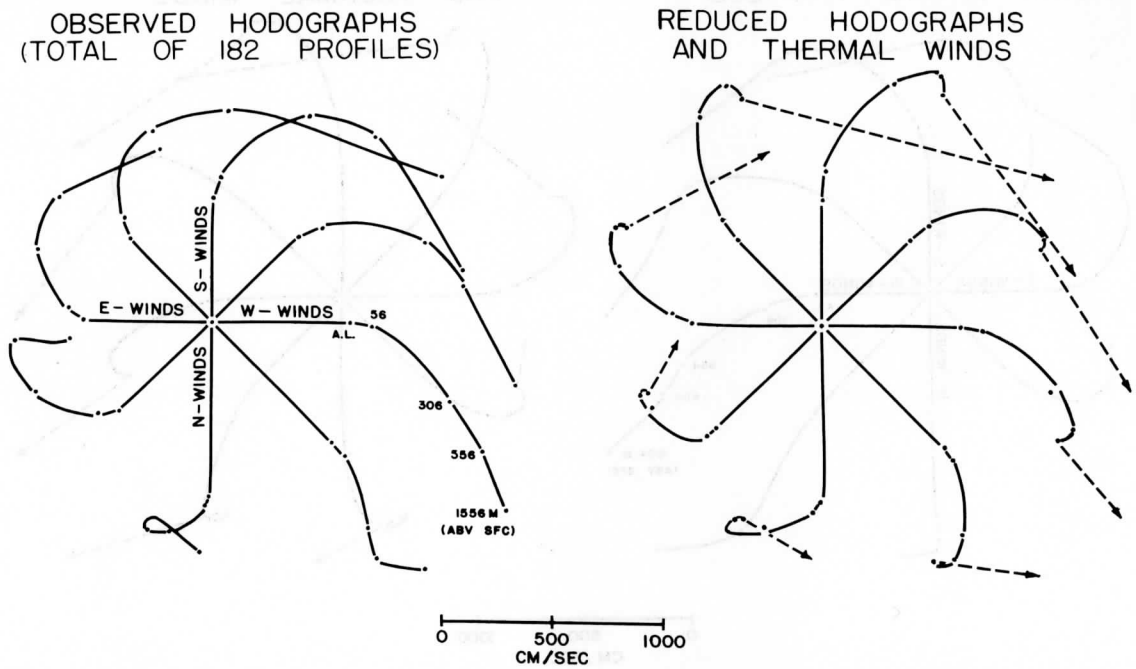

Fig. 3. Mean hodographs for 8 surface-wind directions, Ellendale, N. D. Winters, 1918-1920

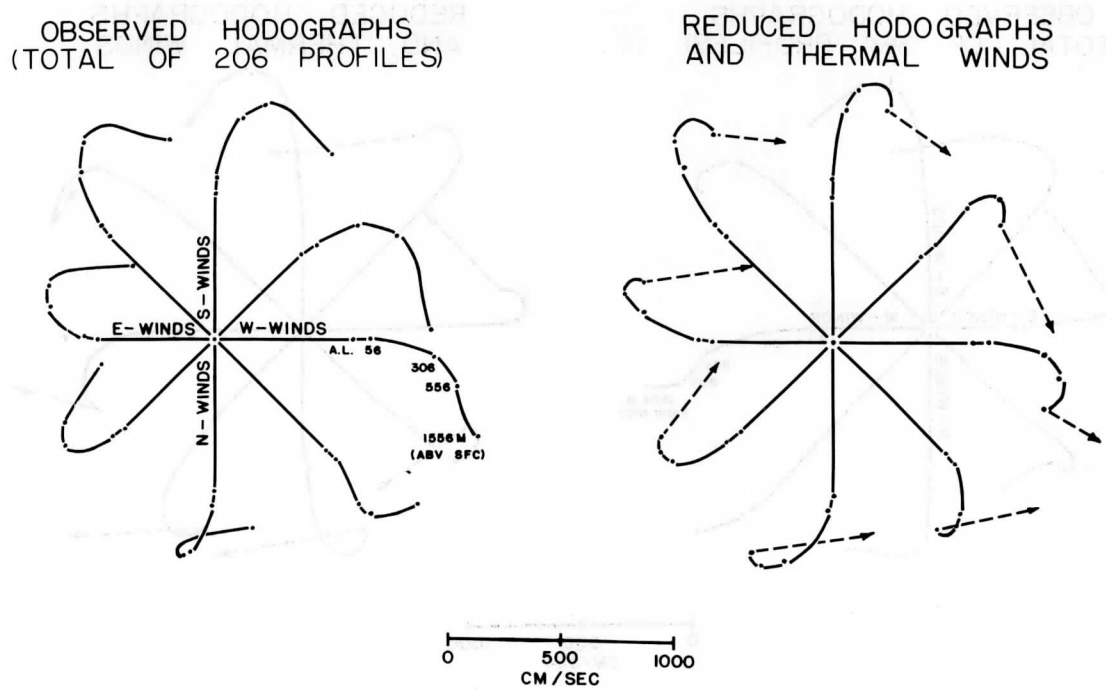

Fig. 4. Mean hodographs for 8 surface-wind directions, Ellendale, N. D. Summers, 1918-1920

7.3 Development of Theory and Method of Analysis

7.3.1 Theoretical background

In his analysis of the Leipzig and Scilly Island wind profiles, Lettau (1950, 1957b) showed that an accurate value of the geostrophic wind vector (including the thermal wind) can be obtained with the aid of a representative actual wind profile, which does not necessarily have to extend to the top of the boundary layer. The method used essentially consists of a trial-and-error orientation of the coordinate system in the assumed direction of the geostrophic wind, the orientation being correct (in the exact direction of the geostrophic wind) when certain deviations are minimized.

Lettau (1962) has suggested a closely-related method of analysis which is simpler and can be used when sufficiently detailed wind-profile data up to and beyond the top of the boundary layer are available. In this analysis, the coordinate system is oriented in the direction of the surface wind (which is also the direction of the vector of surface stress). This method and the manner in which it has been applied to the Gregg data will be explained in the succeeding paragraphs.

In the equations to follow, CGS units are applicable unless otherwise stated. Assuming (1) steady, horizontally-uniform, large-scale air motion over level terrain of uniform surface roughness; (2) no accelerations; (3) no inertia forces; (4) no mean vertical motion; and (5) the variation of density with height (in the boundary layer) small enough to be neglected; the equation of motion for the boundary layer can be written

$$\rho f i\vec{V} + \nabla_h p = \vec{\tau}' \qquad (1)$$

where ρ = density, f = Coriolis parameter, $i = \sqrt{-1}$ (complex vector notation), $\vec{V}$ = horizontal wind vector, $\nabla_h p$ = horizontal pressure gradient, $\vec{\tau}$ = horizontal vector of shearing stress, and the prime (') represents partial differentiation with respect to height. For the same assumptions applied above the boundary layer, we have the geostrophic equation,

$$\rho f i\vec{V}_g + \nabla_h p = 0 \quad . \qquad (2)$$

Subtracting Equation (2) from Equation (1), we obtain

$$\rho f i(\vec{V} - \vec{V}_g) = \vec{\tau}' \quad . \qquad (3)$$

Let a coordinate system be defined as shown below, where $\vec{a}$ is a unit vector which points 90 degrees to the right of the wind vector in the

surface layer. Then the unit vector $\vec{ia}$ is parallel to the vectors of surface stress and surface wind. The following identities explain the component notation.

$$\begin{aligned}
\vec{\tau}_o &= \vec{a}(\tau_{ox} + i\tau_{oy}) = \vec{ia}\tau_{oy} \quad , \quad (\tau_{ox} = 0) \quad , \\
\vec{\tau} &= \vec{a}(\tau_x + i\tau_y) \quad , \\
\vec{V} &= \vec{a}(u + iv) \quad , \quad \vec{V}_g = \vec{a}(U + iV) \quad , \text{ and} \\
G &= |\vec{V}_g| = |U + iV| = (U^2 + V^2)^{\frac{1}{2}} \quad .
\end{aligned} \tag{4}$$

Using these expressions in Equation (3) gives

$$\tau'_x + i\tau'_y = \rho f[(V - v) + i(u - U)] \quad . \tag{5}$$

Separating the real and imaginary parts of each side of Equation (5), we obtain

$$\tau'_x = \rho f(V - v) \quad , \tag{6a}$$

and

$$\tau'_y = \rho f(u - U) \quad . \tag{6b}$$

Integrating Equation (6a) from the surface ($z = 0$) to the top of the boundary layer ($z = H$) yields

$$\tau_{Hx} - \tau_{ox} = \rho f \int_0^H (V - v)\,dz \quad . \tag{7a}$$

Since the shearing stress at the top of the boundary layer is very small, τ_{Hx} may be neglected. In addition, $\tau_{ox} = 0$ due to the orientation of the coordinate system. Thus

$$\rho f \int_0^H (V - v)\,dz = 0 \quad . \tag{7b}$$

An integration of Equation (6a) between the limits 0 and z yields

$$\tau_x = \rho f \int_0^z (V - v)\,dz \quad . \tag{8a}$$

Proceeding in a similar manner, when Equation (6b) is integrated between the limits $z = 0$ and $z = H$, the result is

$$\tau_{Hy} - \tau_{oy} = \rho f \int_0^H (u - U)\,dz \quad . \tag{8b}$$

Neglecting τ_{Hy}, and remembering that $\tau_{ox} = 0$, we have

$$\tau_{oy} = \tau_0 = \rho f \int_0^H (U - u)\,dz \quad . \tag{9}$$

If Equation (6b) is integrated from $z = 0$ to $z = z$, we obtain

$$\tau_y - \tau_{oy} = -\rho f \int_0^z (U - u)\,dz \quad .$$

Substituting Equation (9) into this expression yields

$$\tau_y = -\rho f \int_0^z (U - u)\,dz + \rho f \int_0^H (U - u)\,dz = \rho f \int_z^H (U - u)\,dz \quad . \quad (10)$$

7.3.2 Determination of geostrophic wind components

When wind profile data through the boundary layer are available, Equation (7b) can be used to determine the component of the geostrophic wind parallel to the surface wind. In this study, the geostrophic (frictionless) wind is assumed to change linearly with height, or in other words, a constant thermal wind is assumed. In addition, the observed wind at 2000 m MSL is assumed to be geostrophic. The wind components at this level are denoted by V_H and U_H.

With these assumptions, and using profile data for v (i.e., a linear v versus z graph), the surface geostrophic wind component V_0 parallel to the surface wind may be found graphically. This is done by pivoting a straight line about the point $(H, v_H = V_H)$ such that Equation (7b) is satisfied, i.e., such that the algebraic sum of all areas from $z = 0$ to $z = H$ between the observed v-profile and the assumed linear V-profile (the straight line) is zero. The point of intersection of the straight line and the level $z = 0$ determines V_0. In addition, the lowest point of intersection of the straight line and the observed v-profile determines a level (which is denoted by z^*) at which τ_x is a maximum, since τ_x increases up to this height and then decreases in the interval between $z = z^*$ and $z = H$, to a value of zero at $z = H$. Thus, from Equation (8a),

$$(\tau_x)_{max} = \tau_x^* = \rho f \int_0^{z^*} (V - v)\,dz \quad . \quad (11)$$

Let K^* = eddy diffusivity at the level z^*. When $(u')^*$ is the slope of the u-profile at $z = z^*$, we have

$$\tau_x^* = \rho K^* (u')^* \quad .$$

Now, at any level, the coefficient K should be independent of the direction of the stress component, hence

$$\tau_x / u' = \rho K = \tau_y / v' \quad ,$$

or at the level $z = z^*$,

$$\tau_x^* / (u')^* = \tau_y^* / (v')^* \quad . \quad (12)$$

Equation (12) can be solved for τ_y^*, which is the only unknown. The quantities $(u')^*$ and $(v')^*$ are constructed graphically as the slopes of the respective wind-profile curves at the level $z = z^*$. With the aid of Equation (10), τ_x^* is obtained as the product of the density, the Coriolis parameter, and the area enclosed on the curve sheet by the observed v-profile and the V-profile between the levels $z = 0$ and $z = z^*$.

With τ_y^* determined from Equation (12), Equation (10) can be written

$$\tau_y^* = \rho f \int_{z^*}^{H} (U - u)\,dz \quad . \tag{13}$$

Using the same assumption of constant thermal wind as before, the straight line representing the assumed profile of U, the component of the geostrophic wind perpendicular to the surface wind, may be constructed. This line, as in the previous case, is drawn from the value of the observed wind at 2000 m MSL, which is taken as U_H, to the surface level, using the condition imposed by Equation (13). This condition is that the area enclosed by the linear U-profile and the observed u-profile between the levels $z = z^*$ and $z = H$ must be equal to the value computed for $\tau_y^*/\rho f$ from Equation (12). The intersection of the straight line and the surface level $z = 0$ is U_0, the component of the surface geostrophic wind perpendicular to the surface wind. The values obtained from the Gregg data for V_0 and U_0 in this graphical-numerical manner are shown in the rows for $z = 0$ in Tables 2 to 5.

Using this method, the differences $(V_H - V_0)$ and $(U_H - U_0)$ represent the components of the total thermal wind vector in the boundary layer from $z = 0$ to $z = 2000$ m MSL. The thermal wind can be eliminated from the observed wind by performing computations at each level z using the relationships

$$v_c = v - (V_H - V_0)\,z / H$$

and

$$u_c = u - (U_H - U_0)\,z / H \quad ,$$

where z, H are measured from the surface. The profiles of the reduced values v_c and u_c then approximately represent the variation of wind with height due to the frictional effects.

Reduced hodographs obtained in this way for Drexel, Nebraska, and Ellendale, North Dakota, using the Gregg data for winter and summer seasons, are compared in Figures 1 to 4 with hodographs plotted from the original data. The total thermal wind vector (components $U_H - U_0$ and $V_H - V_0$) are also illustrated. In most instances the variation of the wind with height as shown by the reduced hodographs appears to describe a

conventional wind spiral. Figures 1 to 4 will be discussed more fully in Section 7. 4. 2.

7. 3. 3 Determination of boundary layer parameters

Using the geostrophic wind components thus derived, certain boundary layer parameters may be found. The absolute value of the surface geostrophic wind vector is given by

$$G_0 = (V_0^2 + U_0^2)^{\frac{1}{2}} \quad . \tag{14}$$

The angle between the surface wind and the isobars is

$$\alpha_0 = \tan^{-1}(U_0 / V_0) \quad . \tag{15}$$

The magnitude of the surface shearing stress is given by Equation (9) as the product of ρ, f, and the area enclosed by the profiles of U and u between $z = 0$ and $z = H$. If this area is denoted by R (dimensions of m^2/sec), we have

$$\tau_0 = \rho f R \quad . \tag{16}$$

The geostrophic drag coefficient is defined as

$$C \equiv (\tau_0 / \rho)^{\frac{1}{2}} / G_0 \quad . \tag{17a}$$

Using Equation (16), this becomes

$$C = (Rf)^{\frac{1}{2}} / G_0 \quad . \tag{17b}$$

Lettau (1961) has developed a convenient expression for the total value of energy dissipation in the boundary layer. In addition, he has worked out and suggested (1962) an approximate formula for computing the energy dissipation in the boundary layer when thermal winds are present. The discussion to follow details Lettau's work.

In the boundary layer, the total energy dissipation (E) is given by a vertical integration of the dot product of the vectors of shearing stress and vertical wind shear:

$$E = \int_0^H \vec{\tau} \cdot \vec{V}' \, dz \quad . \tag{18}$$

But $\vec{\tau} \cdot \vec{V}' = (\vec{\tau} \cdot \vec{V})' - \vec{V} \cdot \vec{\tau}'$, and $\vec{V} \cdot \vec{\tau}' = \vec{V}_g \cdot \vec{\tau}'$, when reference is made to Lettau (1961). Thus we obtain

$$E = \int_0^H [(\vec{\tau}\cdot\vec{V})' - \vec{V}\cdot\vec{\tau}']\,dz = [\vec{\tau}\cdot\vec{V}]_0^H - \int_0^H \vec{V}_g\cdot\vec{\tau}'\,dz \quad . \tag{19}$$

If we assume, as before, that the geostrophic wind changes linearly with height in the boundary layer,

$$\vec{V}_g' = \text{Constant} \equiv \vec{S}_g \quad ,$$

and we may write

$$\vec{V}_g = \vec{V}_{g,o} + z\vec{S}_g \quad . \tag{20}$$

Again using the assumption that the wind at the level $z = H$ is geostrophic, we obtain

$$\vec{V}_H = \vec{V}_{g,o} + H\vec{S}_g \quad . \tag{21}$$

Substituting Equation (20) into Equation (19) yields

$$E = [\vec{\tau}\cdot\vec{V}]_0^H - [\vec{V}_{g,o}\cdot\vec{\tau}]_0^H - \vec{S}_g\cdot\int_0^H z\vec{\tau}'\,dz \quad . \tag{22}$$

Using the identity

$$z\vec{\tau}' = (z\vec{\tau})' - \vec{\tau} \quad ,$$

Equation (22) becomes

$$E = [\vec{\tau}\cdot\vec{V}]_0^H - [\vec{V}_{g,o}\cdot\vec{\tau}]_0^H - \vec{S}_g[z\vec{\tau}]_0^H + \vec{S}_g\cdot\int_0^H \vec{\tau}\,dz \quad .$$

Evaluating the terms,

$$E = \vec{\tau}_H\cdot\vec{V}_H - \vec{V}_{g,o}\cdot\vec{\tau}_H + \vec{V}_{g,o}\cdot\vec{\tau}_o - H\vec{S}_g\cdot\vec{\tau}_H + \vec{S}_g\cdot\int_0^H \vec{\tau}\,dz$$

$$= \vec{\tau}_o\cdot\vec{V}_{g,o} + \vec{\tau}_H\cdot(\vec{V}_H - \vec{V}_{g,o} - H\vec{S}_g) + \vec{S}_g\cdot\int_0^H \vec{\tau}\,dz \quad .$$

Using Equation (21),

$$E = \vec{\tau}_o\cdot\vec{V}_{g,o} + \vec{S}_g\cdot\int_0^H \vec{\tau}\,dz \quad . \tag{23}$$

The integral in Equation (23) may be approximated by

$$\int_0^H \vec{\tau}\,dz \approx H(\vec{\tau}_o + \vec{\tau}_H)/2 \quad .$$

Now Equation (23) becomes

$$E \cong \vec{\tau}_o \cdot \vec{V}_{g,o} + H\vec{S}_g \cdot (\vec{\tau}_o + \vec{\tau}_H)/2 \quad .$$

Using Equation (21) again,

$$E \cong \vec{\tau}_o \cdot \vec{V}_{g,o} + (\vec{V}_H - \vec{V}_{g,o}) \cdot (\vec{\tau}_o + \vec{\tau}_H)/2$$

$$= \vec{\tau}_o \cdot (\vec{V}_{g,o} + \vec{V}_H)/2 + \vec{\tau}_H \cdot (\vec{V}_H - \vec{V}_{g,o})/2 \quad .$$

But $\vec{\tau}_H$ is much smaller than $\vec{\tau}_o$. Hence

$$E \cong \vec{\tau}_o \cdot (\vec{V}_{g,o} + \vec{V}_H)/2 = \tau_o(V_o + V_H)/2 \quad , \qquad (24)$$

where V_0 and V_H are the geostrophic wind components parallel to $\vec{\tau}_0$ at $z = 0$ and $z = H$. Equation (24) may be used to estimate the boundary-layer energy dissipation when the surface stress and the geostrophic wind components parallel to the surface stress are known.

7.3.4 Estimate of Richardson numbers

It is known that the boundary layer parameters are functions of the thermodynamic stability of the lower layers of the atmosphere, although in some instances the exact nature of the dependence has not been well established. Various forms of the Richardson number, which is the ratio of buoyancy force to inertia force, have commonly been employed as a measure of stability. Use of the conventional form of the Richardson number requires knowledge of the temperature profile in the lower layers. Lettau (1962) has developed an approximate form for the Richardson number for steady states of a baroclinic atmosphere when the temperature profile is not known. This new form provides a measure of the stability under the assumption that vertical convection is balanced by horizontal warm-air or cold-air advection. A development of Lettau's expression follows.

Near the earth's surface, the Richardson number is defined by

$$\underline{Ri} = g\,\theta'/T_m(v')^2$$

where g is the acceleration due to gravity, T_m the mean temperature of the layer under consideration, θ the potential temperature, and v the horizontal wind speed in the surface layer. Multiplying the right side of this equation by K/K, where K is the eddy diffusivity, we obtain

$$\underline{Ri} = g(K\theta')/T_m v'(Kv') \quad . \tag{25}$$

In the surface layer, the height variation of shearing stress can be neglected; thus

$$\tau/\rho = \tau_0/\rho = Kv' \quad \text{and} \quad (Kv')' = 0 \quad .$$

Also, in the surface layer, $K\theta'$ may be considered constant, hence

$$K\theta' = (K\theta')_0 \quad \text{or} \quad (K\theta')' = 0 \quad ,$$

where the subscript refers to the interface.

The logarithmic law is assumed to describe the wind profile in the surface layer:

$$v = k^{-1}(\tau_0/\rho)^{\frac{1}{2}} \log_e (1 + z/z_0) \quad ,$$

where k = von Karman constant = 0.4 and z_0 = aerodynamic roughness length of the interface. Differentiating, we get

$$v' = k^{-1}(\tau_0/\rho)^{\frac{1}{2}}/(z + z_0) \quad .$$

Substituting these expressions into Equation (25) gives

$$\underline{Ri} = (kg/T_m)(K\theta')_0(\tau_0/\rho)^{-\frac{3}{2}}(z + z_0) \quad , \tag{26}$$

and differentiation with respect to height yields

$$(\underline{Ri}')_0 = (kg/T_m)(K\theta')_0(\tau_0/\rho)^{-\frac{3}{2}} \quad . \tag{27}$$

When z_0 is small in comparison to z it can be neglected in Equation (26), so that

$$\underline{Ri} = z(\underline{Ri}')_0 \quad . \tag{28}$$

In the boundary layer, for the conditions of steady states ($\partial T/\partial t = 0$) and no mean vertical motion, the horizontal temperature advection must be balanced by vertical heat convection. Assuming that K can be taken as the eddy diffusivity of heat, we obtain

$$\vec{V} \cdot \nabla T = (K\theta')' \quad ,$$

or, integrating through the boundary layer,

$$(K\theta')_H - (K\theta')_0 = \int_0^H \vec{V} \cdot \nabla T \, dz \quad .$$

Assuming $(K\theta')_H = 0$, the above expression reduces to

$$(K\theta')_0 = -\int_0^H \vec{V} \cdot \nabla T \, dz \approx -H(\overline{\vec{V} \cdot \nabla T}) \quad , \tag{29}$$

where the bar denotes a vertical average.

Now, using the fact that the temperature gradient on a constant-pressure surface is approximately equal to the horizontal temperature gradient, the thermal wind equation may be written

$$\nabla T = -\frac{T_m f}{g} i\vec{V}'_g \quad .$$

It is assumed that the actual average advection can be substituted by the geostrophic advection, whereupon, for constant thermal wind,

$$\vec{V} \cdot \nabla T \approx \vec{V}_g \cdot \nabla T \approx -\frac{T_m f}{g} \overline{\vec{V}_g} \cdot i\vec{V}'_g \quad . \tag{30}$$

Since $$\overline{\vec{a} \cdot \vec{V}_g} = \overline{U + iV} = \tfrac{1}{2}[(U_0 + U_H) + i(V_0 + V_H)] \quad ,$$

and $$\vec{a} \cdot \vec{V}'_g = U' + iV' = (1/H)[(U_H - U_0) + i(V_H - V_0)] = \text{const} \quad ,$$

then $$\overline{\vec{V}_g} \cdot i\vec{V}'_g = (1/2H)[(U_0 + U_H) + i(V_0 + V_H)] \cdot [(V_0 - V_H) + i(U_H - U_0)]$$

$$= (1/H)(U_H V_0 - U_0 V_H) \quad . \tag{31}$$

Combining Equation (30) and Equation (31), we obtain

$$\overline{\vec{V} \cdot \nabla T} \approx -\frac{T_m f}{g H}(U_H V_0 - U_0 V_H) \quad . \tag{32}$$

The combination of Equations (29) and (32) yields

$$(K\theta')_0 = f T_m (U_H V_0 - U_0 V_H)/g \quad .$$

Now, using Equation (27), we obtain

$$(\underline{Ri}')_0 = k f (\tau_0/\rho)^{-\frac{3}{2}} (U_H V_0 - U_0 V_H) \quad . \tag{33}$$

Since $k = 0.4$, and by Equation (16), $(\tau_0/\rho) = Rf$, we finally have

$$(\underline{Ri}')_0 = 0.4(U_H V_0 - U_0 V_H)/R\sqrt{Rf} \quad . \tag{34}$$

Equations (14), (15), (16), (17b), (24), and (34) have been used in this study to compute the values shown in Tables 6 to 9 of G_0, α_0, τ_0, C, E, and $(\underline{Ri}')_0$, respectively. In the tables, $\overline{\alpha}_0$ denotes "smoothed" values obtained by averaging the value of α_0 for the surface-wind direction shown, with the values of α_0 for the two adjacent directions, in those cases where these adjacent values were available. Values for the advectional term $(U_H V_0 - U_0 V_H)$ have also been tabulated. An attempt is made in the next section to draw certain conclusions about these derived parameters. In addition, the errors involved in their computation will be discussed.

Table 6. Derived boundary layer parameters for Drexel, Nebraska, based on data of Table 2. G_0 = surface geostrophic wind (cm/sec); $\bar{\alpha}_0$ = surface deviation (deg arc); $A_{0,H} = U_H V_0 - U_0 V_H$ = geostrophic advection term m^2/sec^2); τ_0 = surface stress (dynes/cm^2); C = geostrophic drag coefficient (number); $(\underline{Ri}')_0$ = rate of Richardson number change with height (10^{-3}/m); $E_{0,H}$ = energy dissipation (watts/m^2).

Surface Wind Direction	G_0	$\bar{\alpha}_0$	$A_{0,H}$	τ_0	C	$(\underline{Ri}')_0$	$E_{0,H}$
6.1: Winter							
N	1064	16.7	-51.5	1.60	.035	-38.0	1.82
NE	930	19.8	20.3	1.21	.035	22.8	0.99
E	1096	22.2	65.3	1.52	.033	51.6	1.13
SE	1313	22.8	144.2	1.67	.029	99.6	1.18
S	1304	20.9	119.0	1.80	.030	73.2	1.75
SW	1167	20.0	86.2	1.33	.029	83.6	1.41
W	1046	18.3	20.7	1.07	.029	27.6	1.34
NW	1137	17.2	-63.3	1.00	.026	-94.8	1.42
6.2: Spring							
N	1152	15.1	-71.3	1.49	.032	-54.4	1.78
NE	1092	16.5	-20.3	2.20	.041	-8.8	2.03
E	1234	15.0	18.2	2.08	.035	8.4	2.06
SE	1171	13.2	56.2	1.43	.031	45.6	1.48
S	1255	12.1	55.1	2.03	.034	26.4	2.42
SW	1153	13.4	35.4	1.33	.030	32.0	1.60
W	956	15.0	-8.5	0.95	.031	-12.8	1.13
NW	1029	15.5	-72.1	1.18	.032	-78.4	1.50
6.3: Summer							
N	930	16.9	-60.1	1.80	.044	-32.8	1.70
NE	859	14.4	-38.4	0.95	.035	-54.8	0.74
E	886	13.1	36.0	1.60	.044	23.2	1.13
SE	1017	15.6	56.0	1.41	.036	44.0	1.02
S	1133	18.4	17.1	2.63	.044	5.2	2.60
SW	1190	20.9	-20.8	2.86	.044	-5.6	3.23
W	957	20.1	-22.3	1.88	.044	-11.2	2.02
NW	990	18.8	-51.8	2.20	.046	-20.8	2.55
6.4: Fall							
N	1163	26.8	-89.	2.88	.044	-25.2	3.24
NE	1077	30.5	-54.2	3.20	.050	-13.2	2.63
E	1074	28.7	-0.9	2.06	.041	-0.4	1.55
SE	1116	23.0	70.2	1.36	.032	60.8	1.17
S	1305	16.2	52.6	1.73	.031	32.0	2.03
SW	1135	17.1	38.4	1.54	.033	27.6	1.68
W	936	20.0	-18.7	1.26	.036	-18.0	1.33
NW	1098	23.9	-72.4	2.18	.041	-30.8	2.88

Table 7. Derived boundary layer parameters for Ellendale, North Dakota, based on data of Table 3; see Table 6 for explanation of symbols.

Surface Wind Direction	G_0	$\bar{\alpha}_0$	$A_{0,H}$	τ_0	C	$(\underline{Ri}')_0$	$E_{0,H}$
7.1: Winter							
N	956	20.4	-33.4	0.64	.025	-106.8	0.63
NE	853	23.3	14.8	0.81	.031	33.2	0.53
E	993	24.7	59.8	1.10	.031	85.2	0.63
SE	1105	25.9	133.8	1.35	.031	140.4	0.50
S	1198	25.4	108.5	1.61	.031	87.4	1.07
SW	1046	25.9	77.9	1.44	.034	74.0	1.25
W	1185	23.2	22.6	1.92	.034	14.0	2.32
NW	1195	22.2	-46.5	1.83	.033	-31.2	2.40
7.2: Spring							
N	1062	14.8	-16.3	0.80	.025	-34.8	0.83
NE	1031	14.6	-2.2	0.79	.026	-4.8	0.72
E	994	13.9	45.6	0.86	.028	87.6	0.71
SE	1108	14.6	54.5	1.45	.033	48.0	1.48
S	1128	14.4	18.9	1.35	.031	18.4	1.47
SW	1118	15.7	32.7	1.16	.029	40.0	1.38
W	955	16.0	-20.6	0.98	.031	-32.8	1.16
NW	1070	15.8	-38.2	1.08	.029	-52.0	1.27
7.3: Summer							
N	1007	17.9	-47.3	1.27	.034	-48.8	1.14
NE	862	18.4	13.3	0.87	.033	23.6	0.55
E	882	16.1	18.6	1.10	.036	23.6	0.66
SE	1080	15.4	28.6	2.07	.041	14.0	1.89
S	1077	13.0	34.6	1.72	.037	22.4	1.63
SW	912	13.5	47.6	1.14	.036	56.8	0.92
W	974	14.6	5.7	1.97	.044	3.2	2.08
NW	958	18.5	-42.3	1.38	.038	-37.6	1.44
7.4: Fall							
N	930	18.6	-8.1	0.85	.030	-15.6	0.71
NE	950	20.7	18.2	0.89	.030	32.8	0.62
E	996	20.5	64.7	1.14	.032	81.2	0.73
SE	1233	19.3	89.7	1.43	.029	79.6	1.20
S	1302	19.5	77.2	1.64	.030	56.0	1.75
SW	1062	20.0	16.5	1.14	.030	20.4	1.17
W	1063	20.0	5.5	1.05	.029	7.6	1.18
NW	1047	18.5	-21.0	1.00	.029	-3.2	1.17

Table 8. Derived boundary layer parameters for Groesbeck, Texas, based on data of Table 4; see Table 6 for explanation of symbols.

Surface Wind Direction	G_0	$\bar{\alpha}_0$	$A_{0,H}$	τ_0	C	$(\underline{Ri}')_0$	$E_{0,H}$
8.1: Winter							
N	948	23.8	-62.0	0.96	.031	-75.6	0.89
NE	--	--	(Insufficient data)		--	--	--
E	--	--	(Insufficient data)		--	--	--
SE	--	--	(Insufficient data)		--	--	--
S	1513	21.5	46.2	2.26	.030	15.6	2.57
SW	1148	20.0	32.7	1.50	.032	20.4	1.67
W	969	15.7	-5.6	0.86	.029	-8.0	1.03
NW	892	21.4	-56.7	1.07	.034	-59.2	1.28
8.2: Spring							
N	--	--	(Insufficient data)		--	--	--
NE	1045	28.6	-59.4	1.84	.040	-25.6	1.36
E	971	26.3	-51.2	0.82	.028	-74.8	0.49
SE	1108	18.6	42.5	1.37	.032	28.8	1.18
S	1256	15.8	51.9	0.86	.018	70.4	0.97
SW	1284	12.8	-5.0	2.97	.041	-1.2	3.39
W	--	--	(Insufficient data)		--	--	--
NW	--	--	(Insufficient data)		--	--	--
8.3: Summer							
N	--	--	(Insufficient data)		--	--	--
NE	--	--	(Insufficient data)		--	--	--
E	--	--	(Insufficient data)		--	--	--
SE	835	16.7	-3.0	0.71	.031	-5.2	0.50
S	952	17.1	-7.3	1.41	.038	-4.8	1.11
SW	968	16.2	-16.0	1.89	.044	-6.4	1.36
W	--	--	(Insufficient data)		--	--	--
NW	--	--	(Insufficient data)		--	--	--
8.4: Fall							
N	870	27.4	-51.5	0.92	.034	-63.2	0.81
NE	893	23.5	-10.4	0.82	.031	-15.2	0.63
E	1004	23.5	27.2	0.82	.027	39.6	0.56
SE	1123	23.0	36.9	1.27	.030	28.0	1.07
S	1263	23.1	19.1	1.71	.031	9.2	1.84
SW	--	--	(Insufficient data)		--	--	--
W	--	--	(Insufficient data)		--	--	--
NW	1102	29.9	-98.9	3.44	.051	-16.8	3.88

Table 9. Derived boundary layer parameters for Broken Arrow, Oklahoma, based on data of Table 5; see Table 6 for explanation of symbols.

Surface Wind Direction	G_0	$\bar{\alpha}_0$	$A_{0,H}$	τ_0	C	$(\underline{Ri}')_0$	$E_{0,H}$
9.1: Winter							
N	1262	40.6	-138.5	3.73	.046	-24.0	4.07
NE	--	--	(Insufficient data)		--	--	--
E	--	--	(Insufficient data)		--	--	--
SE	--	--	(Insufficient data)		--	--	--
S	1378	16.7	72.5	1.88	.030	35.2	2.14
SW	1085	19.4	53.0	0.74	.024	102.8	0.77
W	1062	15.9	-20.2	2.03	.041	-8.8	2.39
NW	--	--	(Insufficient data)		--	--	--
9.2: Spring							
N	--	--	(Insufficient data)		--	--	--
NE	969	24.0	-10.9	0.90	.030	-16.0	0.61
E	1051	19.5	34.4	1.09	.030	37.6	0.77
SE	1067	15.9	86.1	0.72	.024	172.4	0.61
S	1309	12.5	66.7	1.51	.028	44.0	1.77
SW	--	--	(Insufficient data)		--	--	--
W	--	--	(Insufficient data)		--	--	--
NW	--	--	(Insufficient data)		--	--	--
9.3: Summer							
N	--	--	(Insufficient data)		--	--	--
NE	--	--	(Insufficient data)		--	--	--
E	--	--	(Insufficient data)		--	--	--
SE	--	--	(Insufficient data)		--	--	--
S	951	22.3	-1.5	1.67	.042	-0.8	1.30
SW	917	28.0	4.0	1.54	.041	2.4	1.17
W	--	--	(Insufficient data)		--	--	--
NW	--	--	(Insufficient data)		--	--	--
9.4: Fall							
N	991	31.0	-69.7	1.55	.038	-44.4	1.49
NE	866	22.4	-19.6	1.30	.040	-16.4	1.03
E	--	--	(Insufficient data)		--	--	--
SE	1132	14.6	81.3	1.49	.033	55.2	1.21
S	1101	15.9	37.4	0.91	.026	52.8	1.00
SW	968	15.3	14.4	0.95	.030	19.2	0.97
W	--	--	(Insufficient data)		--	--	--
NW	--	--	(Insufficient data)		--	--	--

7. 4 Discussion of Results

7. 4. 1 Reliability of data

In discussing the reliability of the data in his summary, Gregg states that, although there may be appreciable errors in individual observations, these errors should be eliminated in the main by the method used of averaging large numbers of observations. Unfortunately, however, due to the short period of observation for Broken Arrow and Groesbeck (see Table 1), the total number of observations for these stations is much smaller than would be desired. Table 10 shows the number of wind profiles (surface to 2000 m MSL) which formed the basis for the climatological means taken, at all four stations and for each season.

Table 10. Number of individual complete wind profiles observed in Gregg's survey.

Season	Ellendale	Drexel	Broken Arrow	Groesbeck
Winter	182	412	60	129
Spring	213	387	118	132
Summer	206	364	97	77
Fall	223	420	123	146

When the total observations for a season at Broken Arrow and at Groesbeck are divided into eight groups according to the direction of the suface wind, it can be seen that the number of soundings becomes small. This reduces the representativeness of the means. Also, the surface winds at these two stations exhibit strong directional tendencies for each season, and most of the observations are concentrated in a few surface-wind groups. The remaining groups contain so few observations that a mean cannot be considered representative. Hence, gaps will be found in Tables 2 to 9.

Due to the fact that the Gregg data gives winds for only five levels (station, 500, 750, 1000, and 2000 m MSL), the wind-profile curves drawn for use in this study were necessarily subjective. Each curve had to be drawn through all of the points, since there was not enough information to justify doing otherwise. The large gap in the data from the level

1000 m MSL to 2000 m MSL particularly caused arbitrariness in the drawing of the curves in this region. Of course, effort was made to draw each curve as smoothly and as objectively as possible.

For the most part, the resulting wind profiles for Ellendale and Drexel turned out to be smooth curves. For Broken Arrow and Groesbeck, however, the curves in many instances were somewhat irregular, probably reflecting the lower degree of reliability of these means.

Since the shapes of the wind-profile curves were subjective to a certain degree, the graphical determination of the slope at the level $z = z^*$ (required for use in Equation (12)) certainly admits of some uncertainty. This uncertainty stems both from the lack of confidence in the shape of the curve and from the normal error involved in drawing a tangent to the curve.

The area R, used in several of the computations, was determined by the simple numerical-integration method of "counting squares." Small errors in the determination of this area are to be expected. However, these errors caused by the integration method are certainly much smaller than those caused by the uncertainty in the exact shapes of the wind profiles.

In order to reduce the effect of taking the density constant with height in the integrations of Equation (6a) and Equation (6b), an average density computed from values given by Gregg was used.

7. 4. 2 Discussion of hodographs

An examination of the hodographs (Figures 1 to 4) reveals several interesting features. As would be expected, the thermal winds for winter at the two stations are roughly parallel. In winter, cold-air advection occurs for northerly and northwesterly surface winds, while warm-air advection is associated with easterly, southeasterly, southerly, and southwesterly surface winds. Approximately neutral advection exists for the westerly surface winds; and slight warm-air advection is occurring for northeasterly flow at the surface.

This latter situation may be visualized by considering that a northeasterly surface wind is likely to occur at either of the two stations when a surface low-pressure center is located to the south-southeast of the station. For this synoptic situation, isotherms in the boundary layer above the station would normally be oriented in a general NE to SW direction (possibly N to S), with cold air to the west. The thermal wind vector in

this case would be directed approximately as shown by the winter hodographs for northeasterly surface winds.

It may be noticed on the reduced hodographs that the angles α_0 between the surface wind and the surface geostrophic wind in many cases seem to be smaller than might be expected. This will be discussed in Section 7.4.4.

Since the thermal winds for summer are relatively weak, it can be seen that Humphreys (1940) made a reasonable approximation when he identified typical summer wind-profile structure with conditions of no thermal wind. His association of typical winter wind-profile structure with conditions of constant thermal wind conforms with the assumption made in this study. The results show that this assumption obviously does not hold in all cases, but seems to be reasonable in most of them.

In particular, for cold-air advection at Drexel, the assumption of the geostrophic wind changing linearly with height produced very unlikely results. Accordingly, values of U_0 for those cases had to be obtained by interpolating between U_0-values for adjacent surface-wind directions. However, the U_0-values obtained for cold-air advection at Ellendale seemed realistic enough so that no interpolations were necessary.

All observed hodographs were drawn tangent to the thermal wind at the level 2000 m MSL. This was done because the observed wind at this level was considered to be geostrophic, and thus the shear at this level must be considered to be entirely due to the thermal wind.

7.4.3 Discussion of diabatic effects

The manner in which the geostrophic drag coefficient depends upon stability has been examined, and the results are illustrated in Figures 5 to 8. In these graphs, values of $(\underline{Ri}')_0$ greater than zero represent inversion (stable) conditions, while negative values represent lapse (unstable) conditions. The geostrophic drag coefficient for adiabatic conditions, C_a, was evaluated for each season at each site by plotting C versus $(\underline{Ri}')_0$ and drawing a straight trend line by eye. The value of C where the trend line crossed the zero value for $(\underline{Ri}')_0$ was taken to be C_a. This procedure, of course, is subjective to some extent.

It will be noted that the same curve appears in each of Figures 5 to 8. This curve represents a mean trend line drawn by taking the data as a whole (for all seasons and all stations). Thus the curve serves as a reference by which the data for each season may be compared on a more objective basis.

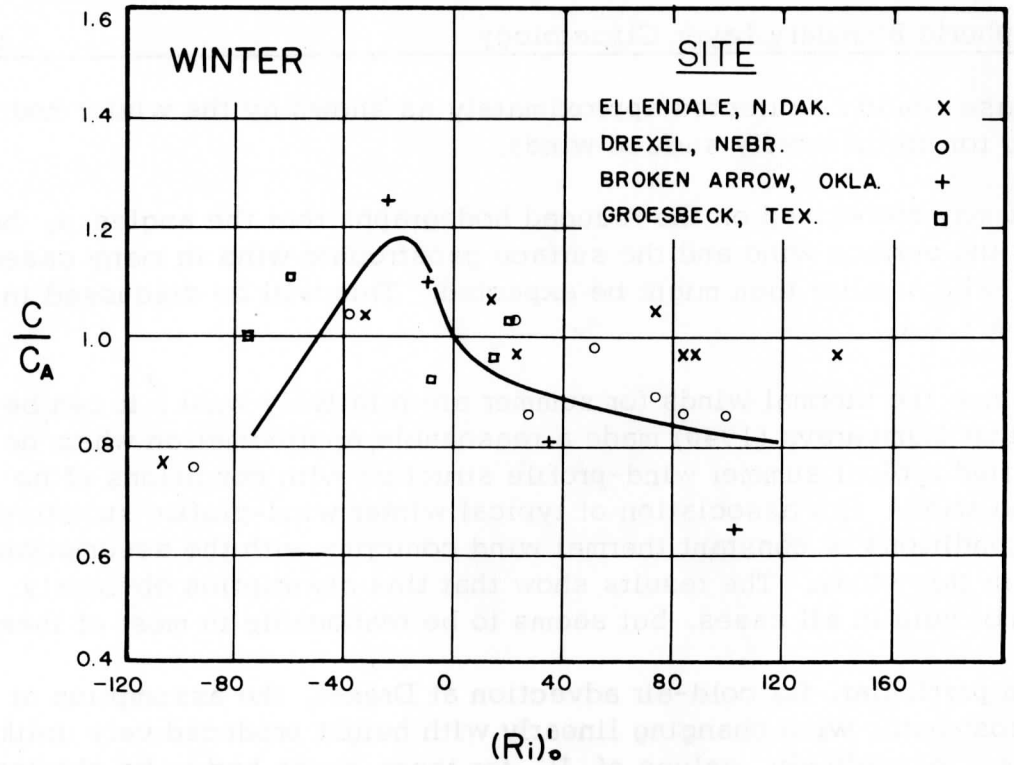

Figure 5

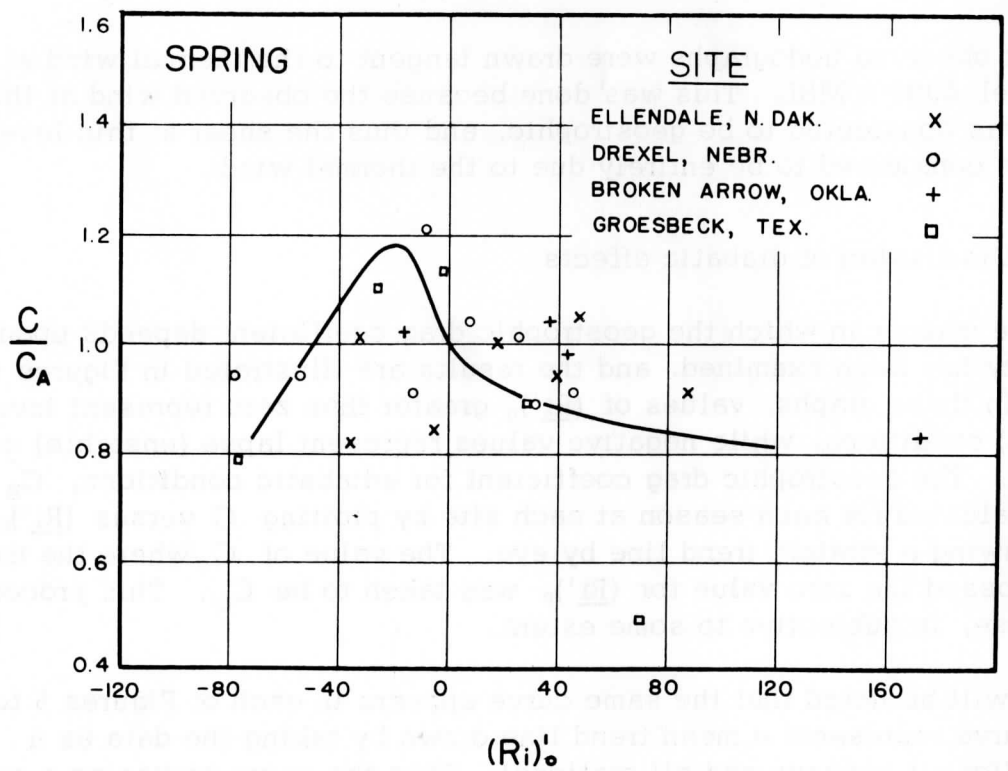

Figure 6

Ratio of geostrophic drag coefficient for non-adiabatic and adiabatic conditions versus approximate height derivative of Richardson number in atmospheric surface layer.

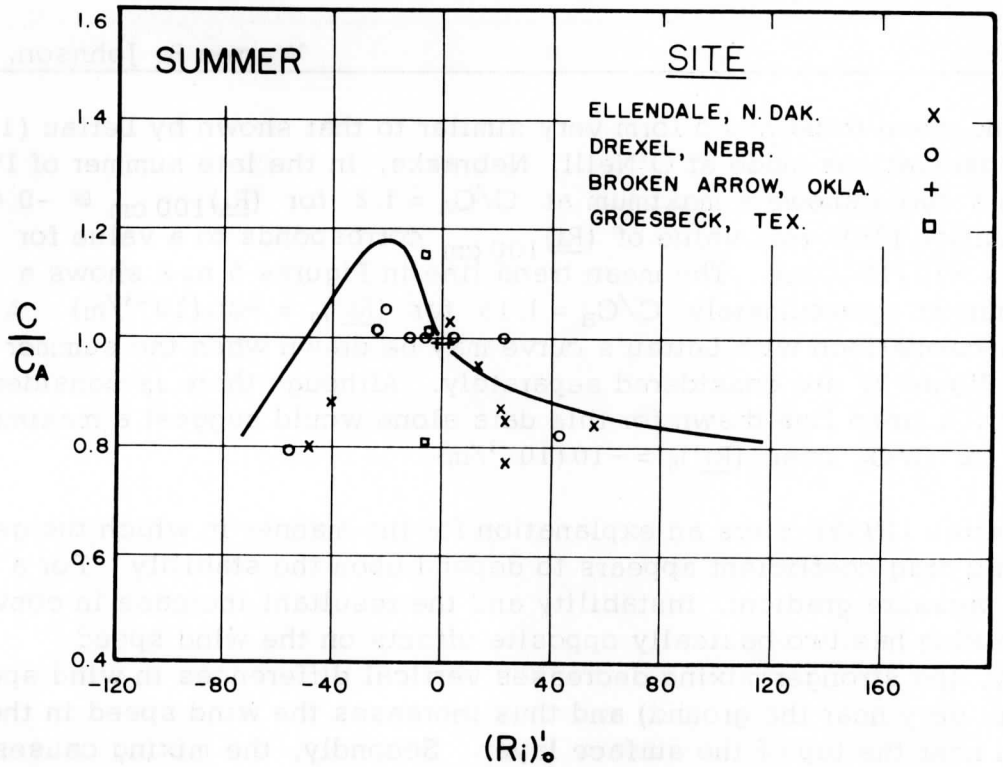

Figure 7

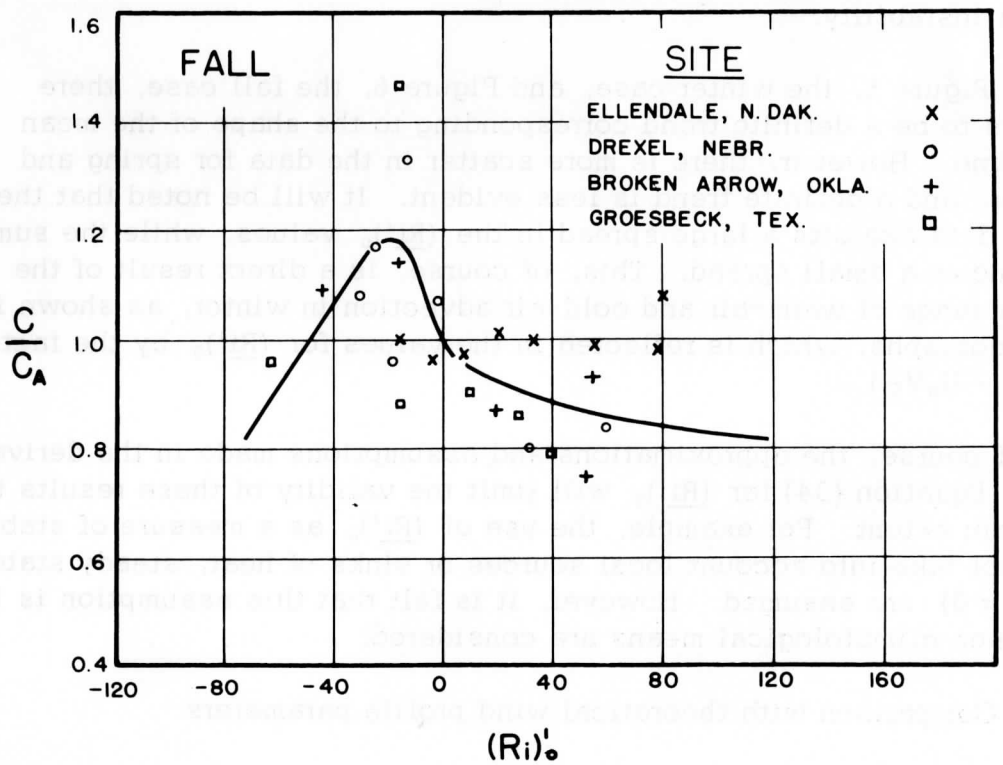

Figure 8

Ratio of geostrophic drag coefficient for non-adiabatic and adiabatic conditions versus approximate height derivative of Richardson number in atmospheric surface layer.

The mean trend has a form very similar to that shown by Lettau (1958) from observations made at O'Neill, Nebraska, in the late summer of 1953. Lettau's curve shows a maximum at $C/C_a = 1.2$ for $(\underline{Ri})_{100\,cm} \cong -0.01$. By Equation (28), this value of $(\underline{Ri})_{100\,cm}$ corresponds to a value for $(\underline{Ri}')_0 = -10(10^{-3}/m)$. The mean trend line in Figures 5 to 8 shows a maximum at approximately $C/C_a = 1.15$ for $(\underline{Ri}')_0 = -20(10^{-3}/m)$. A closer comparison with Lettau's curve may be drawn when the summer data, Figure 7, are considered separately. Although there is considerable scatter, a trend line drawn for this data alone would suggest a maximum value for C/C_a near $(\underline{Ri}')_0 = -10(10^{-3}/m)$.

Lettau (1959) offers an explanation for the manner in which the geostrophic drag coefficient appears to depend upon the stability. For a given pressure gradient, instability and the resultant increase in convective mixing has two basically opposite effects on the wind speed. Firstly, the stronger mixing decreases vertical differences in wind speed (except very near the ground) and thus increases the wind speed in the region near the top of the surface layer. Secondly, the mixing causes an increase in the thickness of the boundary layer, which can effect a reduction in the wind speed at all levels in what was the boundary layer for less mixing. Lettau concludes that the first effect predominates for slight instability, while the second effect becomes more important for greater instability.

In Figure 5, the winter case, and Figure 6, the fall case, there appears to be a definite trend corresponding to the shape of the mean trend line. However, there is more scatter in the data for spring and summer, and a definite trend is less evident. It will be noted that the winter data exhibits a large spread in the $(\underline{Ri}')_0$ values, while the summer data shows a small spread. This, of course, is a direct result of the greater range of warm-air and cold-air advection in winter, as shown in the hodographs, which is reflected in the values for $(\underline{Ri}')_0$ by the factor $(U_H V_0 - U_0 V_H)$.

Of course, the approximations and assumptions made in the derivation of Equation (34) for $(\underline{Ri}')_0$ will limit the validity of these results to a certain extent. For example, the use of $(\underline{Ri}')_0$ as a measure of stability does not take into account local sources or sinks of heat; steady states $(\partial T/\partial t = 0)$ are assumed. However, it is felt that this assumption is justified when climatological means are considered.

7.4.4 Comparison with theoretical wind profile parameters

Using his proposed new theoretical form for the length-scale of turbulence, Lettau (1961) has developed a universal wind spiral solution for

the barotropic atmospheric boundary layer, and has illustrated the dependence of the parameters of the theoretical wind spirals upon the surface-Rossby number, $\underline{Ro}_0 = G_0/z_0 f$. Utilizing values of roughness-length (z_0) for each of the sites, derived by Kung (1962), these theoretical parameters can be compared with average climatological values of the parameters obtained in the present study. This comparison is made in Table 11. The values for $\overline{G}_0$, $\overline{C}_a$, and $\bar{\alpha}_0$ are averages of the derived, or empirical values for spring and winter only. $\bar{z}_0$ is an average roughness length for spring and winter and was derived for a 100 mile radial distance around Drexel by Kung, as the result of an analysis of regional land-use data similar to that reported for Wisconsin (Kung and Lettau, 1961). However, for the other three stations, regional $\bar{z}_0$ values for larger areas (10 deg longitude by 10 deg latitude) were derived by Kung.

Table 11. Boundary layer climatology and comparison between empirical and theoretical values of geostrophic drag coefficients and surface wind deviation angle.

	Ellendale	Drexel	Broken Arrow	Groesbeck	
$\overline{G}_0$	1062	1131	1148	1113	(cm/sec)
$\bar{z}_0$	2.3	9.5	38.5	67.5	(cm)
f	1.05	0.963	0.859	0.764	(10^{-4}/sec)
$\log_{10} \underline{Ro}_0$	6.65	6.09	5.54	5.33	
C_a (theor.)	0.034	0.037	0.041	0.043	
$\overline{C}_a$ (emp.)	0.034	0.032	0.033	0.034	
α_0 (theor.)	23.1	25.7	28.7	29.9	(deg)
$\bar{\alpha}_0$ (emp.)	18.6	18.7	22.4	20.9	(deg)

There is some correspondence between the theoretical and empirically derived parameters. The derived values for $\bar{\alpha}_0$, however, are consistently smaller than the theoretical values. An overestimate of z_0 values for Oklahoma and Texas is possible.

It is appropriate here to mention that one of the shortcomings of the analysis method is that the development of the equations used in evaluating the surface geostrophic wind components was based on several assumptions, one of the most important being the assumption of a height-

independent thermal wind. Some error, then, is certainly present in the values found for U_0 and V_0. Since $\alpha_0 = \tan^{-1}(U_0/V_0)$, it may be expected that considerable variation will occur in the derived α_0 values. This was found to be the case in this study.

The topography of the land surrounding each site was examined in an attempt to discover any dependence of α_0 upon surface-wind direction, but no clear-cut relationship was discovered. For example, it was found that the Drexel station was located near the edge of a plateau, about a mile east of a rather steep drop-off to the Platte River valley. However, no unusual behavior of the derived values of α_0 for westerly surface winds at Drexel is evident.

The seasonal averages of α_0 (derived in this study) and z_0 (from Kung, 1962) at the four sites are shown in Table 12.

Table 12. Relationship between empirical wind deviation angle and regional value of aerodynamic roughness parameter for the seasons.

	Ellendale		Drexel		Broken Arrow		Groesbeck	
	$\bar{\alpha}_0$ (deg)	$\bar{z}_0$ (cm)	$\bar{\alpha}_0$ (deg)	$\bar{z}_0$ (cm)	$\bar{\alpha}_0$ (deg)	$\bar{z}_0$ (cm)	$\bar{\alpha}_0$ (deg)	$\bar{z}_0$ (cm)
Winter	23.9	1	19.7	8	23.1	33	20.5	58
Spring	15.0	5	14.5	11	18.0	44	20.4	77
Summer	15.9	31	17.3	28	25.2	64	16.7	99
Fall	19.6	12	23.3	14	19.8	44	25.1	75

It is known that the surface wind angle generally increases with (1) increasing surface roughness, (2) increasing stability, and (3) decreasing latitude. If one or the other of these effects is presumed to predominate for a certain season at each station, the variations of $\bar{\alpha}_0$ might be "explained"; however, this would be bordering on conjecture.

Table 13 compares averages (for all seasons) of the directly-derived, or empirical values of surface stress at the four stations with theoretical values computed using the geostrophic drag coefficient (Lettau, 1961). The derived values seem to be systematically smaller than the theoretical values.

Table 13. Mean surface geostrophic speed, aerodynamic roughness parameter, and surface stress.

Station	$\bar{G}_0$ (cm/sec)	$\bar{z}_0$ (cm)	$\bar{\tau}_0$ (dyne/cm^2)	
			Empirical	Theoretical
Ellendale	1040	12	1.24	1.92
Drexel	1129	15	1.73	2.27
Broken Arrow	1074	46	1.47	2.44
Groesbeck	1060	77	1.45	2.55

The derived values of energy dissipation (E) shown in Tables 6 and 9 are of the order 1 to 2 watts/m^2, which is also smaller than might be expected for land; e.g., Lettau (1961, Fig. 4, page 164) gave meridional E profiles for the North American continent which result, for the latitude range from 35 to 45°N, in E = 1.5 watts/m^2 in July, and E = 4.5 watts/m^2 for January. A directly obtained value for relatively high wind speed was E = 8.3 watts/m^2 for the Leipzig wind profile. This apparent disagreement may be explained as follows. When Equation (17a) and Equation (18) are considered, and the geostrophic wind is taken to be constant, it can be shown that

$$E = \rho C^2 G_0^3 \cos \alpha_0 \quad . \tag{35}$$

To compute mean energy dissipation, Equation (35) may be written

$$\bar{E} = \rho \overline{C^2 G_0^3 \cos \alpha_0} \quad .$$

However, the quantity $(\bar{G}_0)^3$ was essentially inherent in the values of E obtained in this study. Since

$$\overline{(G_0^3)} \geq (\bar{G}_0)^3 \quad ,$$

the method of computing E from mean winds, as used here, would be expected to produce smaller values.

To conclude, it may be stated that the method used in this study, although subject to some error, should prove useful when applied to more detailed wind profile data, as this data becomes available in the future.

7.5 Acknowledgements

I would like to extend my sincere appreciation to Dr. H. H. Lettau, whose expert instruction and kind guidance made this paper possible. Thanks also go to Mr. Ernest C. Kung, who provided the regional surface-roughness information used in this study.

7.6 References

Gregg, W. R., 1922: An Aerological Survey of the United States; Part 1, Results of Observations by Means of Kites. Monthly Weather Review, Sup. No. 20, 78 pp.

Humphreys, W. J., 1940: Physics of the Air, 3d ed. New York, McGraw-Hill, 676 pp.

Kung, E. C., and Lettau, H. H., 1961: Regional and Meridional Distributions of Continental Vegetation Cover and Aerodynamic Roughness Parameters. Sec. 5 of Studies of the Three-Dimensional Structure of the Planetary Boundary Layer, Department of Meteorology, Univ. of Wisconsin, Annual Report, Contract DA-36-039-SC-80282.

Kung, E. C., 1962: Oral communication.

Lettau, H. H., 1950: A Re-examination of the "Leipzig Wind Profile" Considering Some Relations between Wind and Turbulence in the Frictional Layer, Tellus, Vol. 2, pp. 125-129.

Lettau, H. H., 1957a: Computation of Richardson Numbers, Classification of Wind Profiles, and Determination of Roughness Parameters. Sec. 7.4 of Exploring the Atmosphere's First Mile, Vol. I (H. Lettau and B. Davidson, eds), New York, Pergamon Press, pp. 328-336.

Lettau, H. H., 1957b: Windprofil, innere Reibung und Energieumsatz in der unteren 500 m über dem Meer, Beitr. Phys. d. Atmosphäre, Vol. 30, pp. 78-96.

Lettau, H. H., 1959: Wind Profile, Surface Stress, and Geostrophic Drag Coefficients in the Atmospheric Surface Layer. In Atmospheric Diffusion and Air Pollution (F. N. Frenkiel and P. S. Sheppard, eds), Vol. 6 of Advances in Geophysics, New York, Academic Press.

Lettau, H. H., 1961: Theoretical Wind Spirals in the Boundary Layer of a Barotropic Atmosphere. Sec. 9 of Studies of the Three-Dimensional Structure of the Planetary Boundary Layer, Dept. of Meteorology, Univ. of Wisconsin, Annual Report, Contract DA-36-039-SC-80282.

Lettau, H. H., 1962: Unpublished lecture notes. Department of Meteorology, University of Wisconsin.

Priestley, C. H. B., 1959: Turbulent Transfer in the Lower Atmosphere. Chicago, University of Chicago Press, 130 pp.

8

Equiangular Wind and Current Spirals

Heinz H. Lettau

Department of Meteorology
University of Wisconsin

Abstract. A generalized spiral solution of the equations of motion and momentum transfer is presented for steady and horizontally homogeneous states under the action of Coriolis forces. The class of equiangular spirals is discussed which includes, as special cases, the Ekman and the Rossby spirals. The derived generalized form of equiangular spirals permits more flexibility in applications to observed hodographs than previously realized, especially in the interpretation of wind-induced current-spirals in lakes, or in the ocean.

List of Contents

8. 1 Introduction
8. 2 Generalized Spiral Solution
8. 3 Equiangular Spirals
8. 4 The Special Rossby Spiral
8. 5 Illustration and Application of Equiangular Spirals
8. 6 Conclusions, and Outlook for Future Work
8. 7 References

8. 1 Introduction

Typical of the atmosphere and hydrosphere is that the flow structure is significantly affected by the Coriolis force. This causes that the flow near boundaries not only changes speed but also direction, with increasing distance from the surface. The result of such combined shearing and veering is a typical wind or current hodograph which is of the spiral type.

Correspondingly, the vectors of horizontal shearing stress form a spiral between the lower extreme of surface drag, and an ideal zero value in the region of free, or geostrophic, flow at some large distance from the boundary.

The general properties of wind and stress spirals resulting from the use of semi-theoretical concepts of turbulence structure have been investigated in a previous paper; reference is made to Lettau (1961). However, there is still a need for a simple, but reasonably reliable, practical method for estimating certain derived flow parameters (such as eddy diffusivity, or shearing stress, at various levels) on the basis of directly observable parameters (such as intensities of shear, and rate of veering) in atmospheric or hydrospheric boundary layers.

Previously, the classical Ekman solution was nearly exclusively used for this purpose. Due to the restricted nature of this solution the interpretation of observational facts has often lead to erroneous conclusions. The purpose of the following discussion is to show that the classical Ekman solution is only one special case in a certain class of elementary spiral solutions. Their basic structure will be discussed in a form suitable for various geophysical applications. While the mathematical developments will be presented in the terms of wind and stress variations (which can be directly applied to problems of air and water currents) it should be noted that they apply likewise to a number of diffusion problems, especially the harmonic case of temperature and heat flux variations in a semi-infinite conductor.

8. 2 Generalized Spiral Solution

The discussion is restricted to cases of steady and horizontally uniform large-scale motion above level boundaries. At any point in the fluid a perfect balance between the pressure gradient force, the Coriolis force, and the friction force is assumed. This excludes inertia forces, and mean vertical components of motion. The resulting mean flow is a strictly horizontal vector ($\vec{V}$) independent of horizontal coordinates, but possibly changing direction and speed from level to level. At sufficient distance from the ground level, the friction force approaches zero. The resulting vector of geostrophic motion ($\vec{V}_g$) is assumed independent of height.

In the boundary layer the motion increases generally with height (z), from the boundary value of $\vec{V}_0 = 0$ at the ground ($z = 0$) asymptotically approaching the geostrophic motion at large distance from the ground ($z \geq H$). Vertical differences in fluid density (ρ) will be neglected.

When f = Coriolis parameter and $\vec{\tau}$ = vector of shearing stress at height z, the equation of motion reduces for the above formulated assumptions to

$$\rho f i(\vec{V} - \vec{V}_g) = \vec{\tau}' \quad , \tag{1}$$

where complex vector notion is used, $i = \sqrt{-1}$, and the prime denotes differentiation with respect to z. It is assumed that the vector of shearing stress is horizontal, and at any level proportional to the vector of shear ($\vec{V}'$). Then the factor of proportionality is a scalar quantity (function of height) which defines the effective dynamic viscosity (ρK) or, the effective kinematic viscosity (K) which is also referred to as "eddy diffusivity." Since $\vec{V}_g' = 0$, the equation which defines K can also be written in terms of geostrophic departure $(\vec{V} - \vec{V}_g)$,

$$\vec{\tau} = \rho K \vec{V}' = \rho K (\vec{V} - \vec{V}_g)' \quad . \tag{2}$$

Equations (1) and (2) are the basic equations of the problem. The similarity to the equations of heat continuity and heat conduction is obvious. The two dependent variables can be separated, which results in the new system of two equations,

$$if(\vec{V} - \vec{V}_g) = K(\vec{V} - \vec{V}_g)'' + K'(\vec{V} - \vec{V}_g)' \quad , \tag{3}$$

$$if\vec{\tau} = K\vec{\tau}'' \quad . \tag{4}$$

The problem is to integrate the basic equations (1) and (2), or the equivalent system (3) and (4). Obviously, the solution depends exclusively on the analytical formulation of the height dependency of K. If $K(z)$ would be <u>a priori</u> known, the problem would be of a mathematical nature only. However, in large-scale geophysical motions the problem, first of all, is to gain empirical knowledge of possible $K(z)$, by evaluation of observed wind profiles. This will be greatly facilitated when useful relationships between K and certain directly observable quantities are established. In view of the spiral nature of any solutions to equations (3) and (4), it is most promising to deal directly with observable angular quantities. Therefore, consider the following definitions, which agree with those introduced previously (Lettau, 1961b):

α = angle between $\vec{V}$ and $\vec{V}_g$, (5a)

β = angle between $\vec{V} - \vec{V}_g$ and $-\vec{V}_g$, (5b)

γ = angle between $\vec{\tau}_0$ and $\vec{\tau}$, and (5c)

ψ = angle between $(\vec{V} - \vec{V}_g)'$ and $-(\vec{V} - \vec{V}_g)$, with (5d)

$r \equiv \tan \psi$. (5e)

From equations (1) and (2) it follows that ψ is also the angle between $\vec{\tau}$ and $i\vec{\tau}'$. The physical boundary conditions at $z = 0$ are $\vec{V}_0 = 0$, $\vec{\tau}_0 \neq 0$, and $K_0 > 0$; or, for the above angles, $\beta_0 = 0$, $\gamma_0 = 0$, while $\alpha_0 = \psi_0 > 0$, thus $r_0 > 0$. At great heights the spiral-radius vectors reduce to the points $\vec{V} = \vec{V}_g$ and $\vec{\tau} = 0$, respectively, and the angular quantities are undetermined.

It can be shown that with the aid of three of the above defined angles, i. e., β, γ, and $\psi = \tan^{-1} r$, generalized spiral solutions are obtained as

$$\vec{V} - \vec{V}_g = -\vec{V}_g \exp - \int_0^{\beta} (i + 1/r)\, d\beta \quad , \tag{6}$$

$$\vec{\tau} = \vec{\tau}_0 \exp - \int_0^{\gamma} (i + r)\, d\gamma \quad , \tag{7}$$

with the following derivatives:

$$(\vec{V} - \vec{V}_g)' = -(\vec{V} - \vec{V}_g)\,\beta'(i + 1/r) \, , \tag{6'}$$

$$(\vec{V} - \vec{V}_g)'' = (\vec{V} - \vec{V}_g)[\beta'^2 (i + 1/r)^2 - \beta''(i + 1/r) + \beta' r'/r^2] \, , \tag{6''}$$

$$\vec{\tau}' = -\vec{\tau}\gamma'(i + r) \tag{7'}$$

$$\vec{\tau}'' = \vec{\tau}[\gamma'^2 (i + r)^2 - \gamma''(i + r) - \gamma' r']$$

$$= \vec{\tau}[\gamma'^2 (r^2 - 1) - \gamma'' r - \gamma' r' + i(2r\gamma'^2 - \gamma'')] \, . \tag{7''}$$

The separation of real and imaginary parts as carried out by the transformation from the first to the second form of equation (7'') is omitted, for brevity, in equation (6''), but will be considered later. Also, using the rules for division and multiplication of complex numbers, it is possible to establish other equations, for example, one which relates the curvature term $(\vec{V} - \vec{V}_g)''$ to the shear term $(\vec{V} - \vec{V}_g)'$.

From the definitions, boundary conditions, and basic equations, the geometrical relationship can be derived

$$\beta - \gamma = \psi - \psi_0 = \psi - \alpha_0 \quad , \tag{8}$$

with the subsequent derivative form,

$$\beta' - \gamma' = \psi' = r'/(1 + r^2) \quad . \tag{8'}$$

To establish the relationship between K and the angular quantities, consider equation (1), substitute on the right-hand side equation (7'), then express $\vec{\tau}$ by equation (2),

$$i\rho f(\vec{V} - \vec{V}_g) = -\vec{\tau}\gamma'(i + r) = -\rho K(\vec{V} - \vec{V}_g)'\gamma'(i + r)$$

$$= \rho K(\vec{V} - \vec{V}_g)\beta'(i + 1/r)\gamma'(i + r). \quad (9a)$$

In the last form of the right-hand side of equation (9a) the real part is identically zero, and the imaginary part yields

$$K = f / \beta'\gamma'(r + 1/r); \quad \text{or,} \quad f/K = \beta'\gamma'(r + 1/r). \quad (9b)$$

The last equation is the equivalent of the formula for thermal diffusivity in the soil, as derived and discussed by Lettau (1954). Corresponding equations for f/K can be obtained in terms of either β or γ. For example, consider equation (4) and introduce on its right-hand side equation (7''). Imaginary and real parts of the resulting complex equation yield

$$f/K = -\gamma'' + 2r\gamma'^2 , \quad (10a)$$

$$0 = -\gamma''r - \gamma'r' - \gamma'^2(r^2 - 1) , \quad (10b)$$

or, upon elimination of γ'' in equation (10a) with the aid of equation (10b),

$$f/K = \gamma'^2(r + 1/r) + \gamma'r'/r . \quad (10c)$$

Finally, consider equation (3) and introduce on its right-hand side equations (6'') and (6'). Upon separation of real and imaginary parts, after some elementary transformations,

$$f/K = -\beta'' + 2\beta'^2/r - \beta'K'/K , \quad (11a)$$

$$0 = -\beta''r + \beta'r' - \beta'^2(r^2 - 1) - r\beta'K'/K , \quad (11b)$$

or, after solving for K'/K,

$$K'/K = -\beta''/\beta' - \beta'(r - 1/r) + r'/r , \quad (11c)$$

and, upon elimination of β'' and K',

$$f/K = \beta'^2(r + 1/r) - \beta'r'/r . \quad (11d)$$

It can be verified that equations (11d) and also (10c) could have been directly derived from equation (9b) when the geometrical relationship (8') is utilized to eliminate either β' or γ'. More interesting is the fact that equation (11c) can be readily integrated, yielding, with the proper boundary conditions,

$$K/K_0 = (r\beta_0'/r_0\beta') \exp - \int_0^z \beta'(r - 1/r)\,dz . \quad (12)$$

The integration constant K_0 can be expressed with the aid of equations (9b), (10c), or (11d).

Obviously, the actual analytical shape of the relation (12) will be determined completely by the mathematical nature of the functions $\beta'(z)$ and $r(z)$. The reversal of this statement holds true also. Thus, the problem mentioned in Section 8. 1 is formally solved. In the following section a significant mathematical simplification will be introduced.

8. 3 Equiangular Spirals

By generally accepted definition, an equiangular spiral is characterized by the condition that the angle formed by the radius vector, and the tangent at the spiral, is independent of any turning of the radius vector. Recalling the defining statement (5d) it follows that $\psi = \text{const} = \psi_0 = \alpha_0$, for an equiangular wind spiral, and, in view of (5e),

$$r' = 0 \; ; \quad \text{or,} \quad r = r_0 = \tan \alpha_0 \quad . \tag{13a}$$

For convenience of writing let us define a parameter (q) in the identity

$$q \equiv r_0 - 1/r_0 = \tan \alpha_0 - \cot \alpha_0 \quad , \tag{13b}$$

so that $q = 0$ for $r_0 = 1$, q being positive for $r_0 > 1$ and negative for $r_0 < 1$. In other words, q is positive for $\alpha_0 > 45°$, negative for $\alpha_0 < 45°$, and zero for $\alpha_0 = 45°$.

From equations (8) and (8'), also from comparing equation (10c) with equation (11d), it follows for $r' = 0$ that

$$\gamma' = \beta' \; ; \quad \text{and} \quad \gamma = \beta \quad . \tag{14}$$

Thus, equation (10b) reduces to

$$\gamma''/\gamma' = q\,\gamma' \quad , \tag{15a}$$

which can be solved, for the proper boundary condition, yielding

$$\gamma = -(1/q) \log_e (1 + z/D) = \beta \quad , \tag{15b}$$

where the length D represents the integration constant. Upon differentiation,

$$\gamma' = \beta' = -1/q(z + D) \; ; \quad \text{with} \quad \beta_0' = -1/qD \; . \tag{15c}$$

Equation (15c) gives $D = -1/q\beta_0'$. We can restrict the discussion to spirals with clockwise turning of the radius vector. That means that β' is always positive. Thus, D in equation (15c) is positive only for $q < 0$. For $q > 0$, let us use a positive $D^* = -D$. Finally, we find

$$\gamma = \beta = \frac{r_0}{1 - r_0^2} \log_e \frac{z + D}{D} \quad , \quad \text{for } r_0 < 0 \ , \tag{16a}$$

$$\gamma = \beta = \frac{r_0}{r_0^2 - 1} \log_e \frac{D^*}{D^* - z} \quad , \quad \text{for } r_0 > 0 \ . \tag{16b}$$

When $r_0 = 1$, that means, $q = 0$, equation (15a) reduces to $\gamma'' = 0$, or $\gamma' = \text{const} = \beta' = \beta_0' = \gamma_0'$. Then, the classical Ekman solution applies, and from equations (9b), (10c), or (11d), it follows that

$$\beta'_{\text{Ekman}} = \sqrt{f/2K_0} \quad , \tag{17}$$

or, β as well as γ are linear functions of height. In other words, the rate of turning of the radius vectors with height is constant for $r_0 = 1$. Equations (6) and (7) show that $r = r_0 = 1$ is the only existing special case for which the wind spiral is similar to the stress spiral.

Another interesting theorem can be derived from equations (11c), (14), and (15a) in that, for $r' = 0$,

$$K'/K = -\beta''/\beta' - q\beta' = -2q\beta' \quad . \tag{18}$$

Equation (18) indicates that, in view of $\beta' > 0$, any height-increasing eddy diffusivity ($K'/K > 0$) requires that $\alpha_0 < 45°$, while for height-decreasing eddy diffusivity ($K'/K < 0$), $\alpha_0 > 45°$. The Ekman spiral requires $K' = 0$, i.e., $K = K_0$ and $\alpha_0 = 45°$.

The vertical profile of eddy diffusivity follows from equations (9b), (10c), or (11d), and is given by

$$K/K_0 = (1 + z/D)^2 \quad , \quad \text{for } r_0 < 1 \ , \tag{19a}$$

$$K/K_0 = (1 - z/D^*)^2 \quad , \quad \text{for } r_0 > 1 \ , \tag{19b}$$

with

$$K_0 = q^2 D^2 f/(r_0 + 1/r_0) \quad , \tag{19c}$$

since $D^2 = D^{*2}$. Thus, all equiangular spirals require that the eddy diffusivity is a parabolic function of height. This includes the Ekman spiral, for the extreme case of an infinitely large D-value. The wind components can be computed with the aid of the following formulas:

$$u/V_g = 1 - (1 + z/D)^{1/qr_0} \cos \beta \quad , \tag{20a}$$

$$v/V_g = (1 + z/D)^{1/qr_0} \sin \beta \quad . \tag{20b}$$

For an illustration of a family of equiangular wind spirals see Fig. 1. A more detailed discussion of practical applications will be presented in Section 8. 5.

8. 4 The Special Rossby Spiral

When equation (6') is differentiated with respect to z, the result can readily be expressed as a relationship between the curvature term $(\vec{V} - \vec{V}_g)''$ and shear term $(\vec{V} - \vec{V}_g)'$, rather than geostrophic departure as in equation (6''). If we restrict the discussion to equiangular spirals, i. e., $r' = 0$, the following is obtained

$$(\vec{V} - \vec{V}_g)'' = (\vec{V} - \vec{V}_g)' (\beta''/\beta' - \beta'/r_0 - i\beta') \quad . \tag{21}$$

In an attempt to apply a similarity hypothesis originally introduced by Kármán — reference can be made to the discussion in Lettau (1961a, page 125) — Rossby (1932) postulated that at all levels the vector $(\vec{V} - \vec{V}_g)''$ should be perpendicular to the vector $(\vec{V} - \vec{V}_g)'$. This requires that the real part of the complex equation (21) must be zero, whereupon

$$\beta''/\beta' = \beta'/r_0 \quad , \tag{22a}$$

or, when equations (14) and (15a) are recalled,

$$\beta'/r_0 = q\beta' = (r_0 - 1/r_0)\beta' \quad , \tag{22b}$$

which is satisfied only when $r_0^2 = 2$.

The special case of an equiangular spiral with $r_0 = \sqrt{2}$, i. e., $\alpha_0 = 54.7°$, can be referred to as the Rossby spiral. According to a theorem discussed in Section 8.3, the Rossby spiral requires monotonically height-decreasing eddy diffusivity. In shape it is intermediate between the two lowest spirals depicted on Fig. 1.

For the understanding of turbulent duct-flow, Kármán's hypothesis has been shown to be of no value; see Lettau (1961a, page 132). Correspondingly, no empirical facts or theoretical developments are known which justify the singling out of a special equiangular spiral with the fixed value of $\alpha_0 = 54.7°$. On the contrary it must be emphasized that it is just the possibility of α_0-variation which makes the discussion of equiangular spirals interesting, and opens the road to fruitful geophysical applications.

8. 5 Illustration and Application of Equiangular Spirals

Fig. 1 shows five individual members of the family of equiangular spirals. The representation follows conventional lines in that geostrophic motion is plotted as a horizontal vector. The direction of surface stress (and of wind nearest to the ground) is indicated by the dashed vector, with values of α_0 written in. Three intermediate wind vectors at levels of $H/4$, $H/2$, and $3H/4$ are indicated in most of the spirals; for the definition of H see below. An estimate of β and its rate of change with height can be obtained by constructing vectors of $(\vec{V} - \vec{V}_g)$ in Fig. 1 at $H/4$, $H/2$, and $3H/4$. It can be readily verified that β' decreases systematically with height for $\alpha_0 < 45°$, is constant for the Ekman spiral (the spiral in the center of Fig. 1, with $\alpha_0 = 45°$), and increases rapidly with height for $\alpha_0 > 45°$.

In wind spiral solutions it is customary to define the "geostrophic wind level (H)" as the lowest height at which the actual wind vector attains the direction of the geostrophic motion. The mathematical condition for this is that, at $z = H$, the angle β equals 180° which is π radians. Thus, from equations (16a) and (16b),

$$-q\pi = \log_e(1 + H/D) \quad , \quad \text{for } q < 0 \ , \tag{23a}$$

$$-q\pi = \log_e(1 - H/D^*) \quad , \quad \text{for } q > 0 \ . \tag{23b}$$

In equation (23b) it is obvious that H must be smaller than $D^* = -D$. With the aid of the last two equations the parameter D can be computed for any given H and q, i. e., α_0. When D is obtained, K_0 can be computed with the aid of equation (19c).

Note that the super-geostrophic wind-component (the excess of actual wind component parallel to the isobars, beyond geostrophic speed) at and near $z = H$ increases systematically with increasing α_0. This is related to the corresponding relative and absolute decrease of eddy diffusivity in the region near H, which will be discussed below.

In view of equation (19a) the height-average of eddy diffusivity between ground and level H is

$$\overline{K} = (K_0/H) \int_0^H (1 + z/D)^2 \, dz = K_0(1 + H/D + H^2/3D^2) \ . \tag{24a}$$

Remember that D is negative for $\alpha_0 > 45°$ so that, using D^*,

$$\overline{K} = K_0(1 - H/D^* + H^2/3D^{*2}) \ . \tag{24b}$$

Vertical profiles of $K/\overline{K}$ in the region $0 \leq z/H \leq 1$ are also illustrated

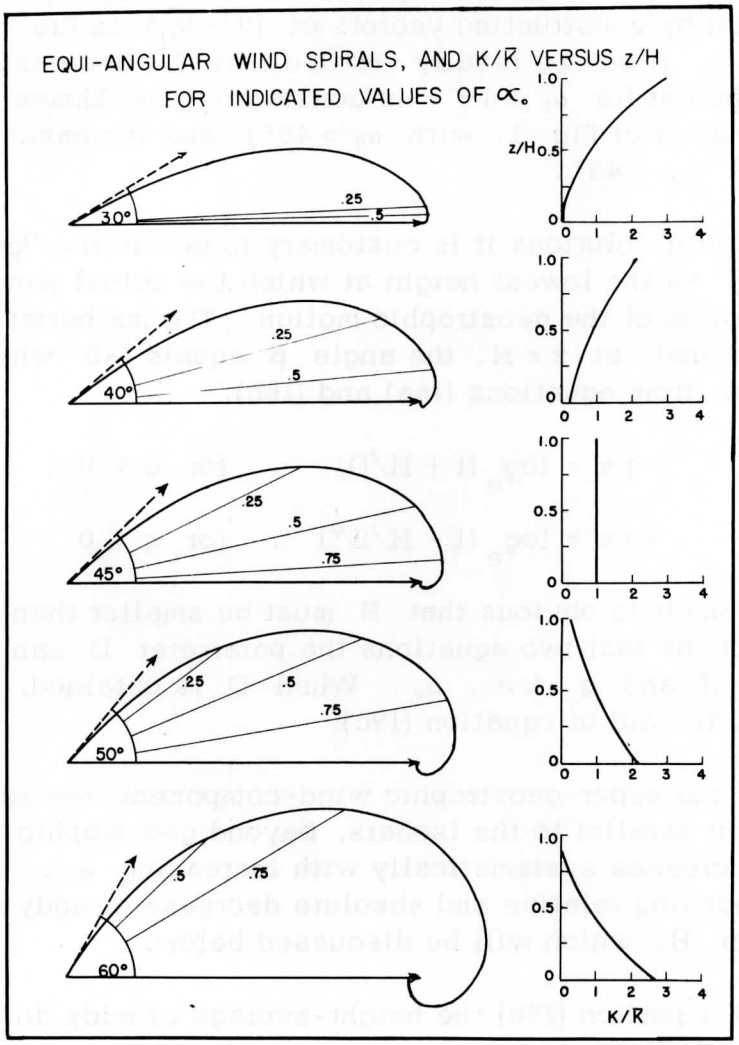

Fig. 1 A family of equiangular wind spirals and corresponding vertical profiles of eddy diffusivity (K relative to average $\overline{K}$, versus z/H where H = geostrophic wind level), for five selected values of α_0 (angle between surface stress and ambient flow). The special case of the Ekman spiral is illustrated at the center.

in Fig. 1, for each of the five selected α_0-values. A summary of computed data is given in Table 1.

Table 1. Characteristic dimensionless parameters of equiangular wind spirals, as a function of α_0, also dimensional quantities assuming $f = 10^{-4}\,\mathrm{sec}^{-1}$ and $H = 1000$ m.

α_0 deg	r_0	q	D/H	$K_0/H^2 f$	$\bar{K}/K_0$	D m	K_0 m^2/sec	$\bar{K}$ m^2/sec
30	0.577	-1.155	0.0273	4.29×10^{-4}	485.1	27	0.043	20.8
40	0.839	-0.353	0.4926	1.48×10^{-2}	4.303	493	1.48	6.5
45	1.000	0.000	∞	0.0507	1.000	∞	5.07	5.1
50	1.192	0.353	-1.4926	0.1362	0.480	-1493	13.6	6.5
60	1.732	1.155	-1.0273	0.6080	0.342	-1027	60.8	20.8

The dimensionless quantities listed in Table 1 are defined, or given, by equations (13a), (13b), (23a,b), (19c; after dividing both sides by $H^2 f$ and using 23a,b to express D^2/H^2), and (24a,b). The dimensional quantities D, K_0, and $\bar{K}$ are computed for $f = 10^{-4}$ sec^{-1} (a mid-latitude value), and by arbitrarily assuming $H = 1000$ m. A certain symmetry relative to Ekman-spiral values can be noted. It is evident that the values of $\bar{K}$ agree with atmospheric conditions, at least by order of magnitude. For example, the Ekman value in Table 1 corresponds to $\rho\bar{K} = 60\,\mathrm{g\,cm^{-1}\,sec^{-1}}$ when $\rho = 0.00118\,\mathrm{g/cm^3}$.

It seems to be possible to remove the arbitrariness in dealing with spiral solutions of this nature. Lettau (1961a) has suggested that in turbulent flow the average eddy diffusivity is adjusted so as to keep the effective Reynolds number of the flow just below a universal critical value. If we define the effective Reynolds number as

$$\underline{\mathrm{Re}}_{\mathrm{eff}} \equiv \underline{\mathrm{RE}} = V_g H/\bar{K} \quad , \tag{24}$$

the critical value ($\underline{\mathrm{RE}}^*$) must be expected to be close to 2000, since V_g is ambient flow and not an average speed of actual boundary layer motion, while H is more nearly the full profile height and not a displacement thickness.

Reynolds' criterion in the form

$$V_g H / \bar{K} < RE^* = 2000 \qquad (25a)$$

yields, after certain transformations involving the dimensionless relationships summarized in Table 1,

$$H > (V_g / RE^* f) \cdot \Phi \quad , \text{ where} \qquad (25b)$$

$$\Phi = \Phi(r_0) = (H/D)^2 \cdot (K_0/\bar{K}) \cdot (r_0 + 1/r_0)/q^2 \quad . \qquad (25c)$$

A summary of computed data is given in Table 2. Note that $\Phi_{Ekman} = 2\pi^2$.

Table 2. Minimum values of H = geostrophic wind level (in equiangular wind spirals, as a function of α_0) which satisfy condition (25a); H_{10} for $V_g/f = 10^5$ m, and $H_{0.1}$ for $V_g/f = 10^3$ m.

α_0 deg	Φ	H_{10} m	$H_{0.1}$ m
30	4.80	240	2.4
40	17.00	850	8.5
45	19.74	987	9.9
50	17.00	850	8.5
60	4.80	240	2.4

Letting again $f = 10^{-4}$ sec^{-1} the H-values in Table 2 refer to ambient speeds of 10 and 0.1 m/sec, respectively. It is interesting to note that the Reynolds criterion permits the largest H-values to exist for Ekman spiral conditions.

A monotonic (parabolic) height variation of eddy diffusivity is highly unlikely in atmospheric boundary layers. A more realistic and satisfactory spiral solution (with eddy diffusivity first increasing then decreasing with height) has been found which, of course, is not of the equiangular type; reference is made to Lettau (1961b, page 154). However, spiral flow in wind-driven ocean or lake currents offers a field for application. When no pressure gradients are involved, the surface current corresponds to V_g. Super (1962, see Section 9) reports on observations of wind-driven spiral flow in Lake Mendota, with 0.1 m/sec as the order of magnitude of the surface current, and α_0 values of approximately 60°. The resulting H (in the case of water currents H is referred to as "frictional depth") of

2.3 m, as predicted in Table 2, seems to conform with actual data. A maximum eddy diffusivity at the air/water interface (due to wind action and irregularities superimposed on waves) is most likely to exist. For further detail, reference is made to Section 9.

Finally, the relationship between the absolute magnitudes of boundary stress (τ_0) and ambient speed (V_g) will be established. We introduce equation (7') on the right-hand side of the basic equation (1), whereupon, at $z = 0$,

$$-\rho f i \vec{V}_g = -\vec{\tau}_0 \gamma_0' (i + r_0) \; ; \quad \text{or,} \quad \rho f \vec{V}_g = \vec{\tau}_0 \gamma_0' (1 - i r_0) \, , \tag{26a}$$

which gives, in terms of vector magnitudes,

$$\tau_0 = \rho f V_g / \gamma_0' \sqrt{1 + r_0^2} = \rho f V_g \cos \alpha_0 / \gamma_0' \quad , \tag{26b}$$

since, geometrically, $1 + r_0^2 = 1/\cos^2 \alpha_0$. The relations (26a, b) hold true for any generalized wind spiral solution. For equiangular spirals a significant simplification occurs in that $\gamma_0' = \beta_0'$. In contrast to γ_0' which is difficult to estimate, the rate of turning of the geostrophic departure (β_0') can be estimated from observational data. As an example let us consider data on current profiles in Lake Mendota observed by Super (see Section 9), i.e., $f = 10^{-4} \text{sec}^{-1}$, $\rho_w = 1 \text{ g/cm}^3$, $V_g = V_{w,o} = 10$ cm/sec, $\alpha_0 = 61°$, $\cos \alpha_0 = 0.485$, and $\beta_0' = 0.0089$ rad/cm. Application of equation (26b) produces in this case $\tau_0 = 0.055$ dynes/cm^2 which is the same value as discussed by Super. If the water surface remains level (i.e., no wind-slope is induced) the above τ_0 must be equal to the momentum transfer from the air to the water, and the surface current will deviate by $90 - \alpha_0 = 29°$ to the right of the air motion in the surface layer.

8.6 Conclusions, and Outlook for Future Work

It can be concluded that the derived generalized form of equiangular spiral solutions permits more flexibility in various applications to observed hodographs than was previously possible, with only the special cases of the Ekman and Rossby spirals known. Especially, this statement applies to the interpretation of wind-induced current spirals in lakes or in the ocean, where depth-decreasing eddy diffusivity must be expected. An important feature of generalized equiangular spiral flow is that all restrictions concerning the value of α_0 and, subsequently, the angle of deviation between air motion above, and the surface current below the interface, are removed.

A shortcoming of equiangular spiral flow is the fixed mathematical structure of the function describing the height variation of eddy diffusivity.

We refer to the parabolic profiles of K and the fact that both K and K' approach zero, for $\alpha_0 > 45°$, at a level slightly above H. Even though K_H will be small (relative to K_0), it cannot be smaller than the finite value of molecular diffusivity. Below the bottom of the friction layer in lakes and the ocean, the parabolic K-profile will not be realistic.

Future work in this field will deal with spiral solutions in which the parameter r is height-dependent in a mathematically defined and physically realistic manner.

8.7 References

Lettau, H. (1954): "Improved Models of Thermal Diffusion in the Soil," Transactions, American Geophys. Union, 35, 121.

Lettau, H. (1961a): "A Generalized Mathematical Model of the Mean-Velocity Distribution in Turbulent Duct Flow," Sec. 8, Annual Report, Studies of the Three-Dimensional Structure of the Planetary Boundary Layer, Contract DA-36-039-SC-80282, USEPG, Fort Huachuca, Arizona.

Lettau, H. (1961b): "Theoretical Wind Spirals in the Boundary Layer of a Barotropic Atmosphere," Sec. 9, Annual Report, Studies of the Three-Dimensional Structure of the Planetary Boundary Layer, Contract DA-36-039-SC-80282, USEPG, Fort Huachuca, Arizona.

Rossby, C. G. (1932): "A Generalization of the Theory of the Mixing Length with Applications to Atmospheric and Oceanic Turbulence," Mass. Inst. Tech. Meteor. Papers, 1, No. 4.

Super, A. (1962): "Case Studies of Dynamical Interactions at an Air-Water Interface," Thesis for the M. S. degree in Meteorology at the University of Wisconsin.

9

Case Studies of Dynamical Interactions at an Air-Water Interface[1]

Arlin B. Super

Department of Meteorology
University of Wisconsin

Abstract. This empirical study was undertaken to gain a better understanding of the processes involved in the transfer of horizontal momentum from the air to a body of water (Lake Mendota). Attempts were made to obtain the time sequence of accurate measurements of vertical profiles of current speed and direction in the upper 150 cm layer of Lake Mendota. These measurements were also utilized to calculate horizontal divergence in the surface-to-10 cm layer. This information was then related to supporting wind profile, wind direction, and temperature profile measurements in the air above the lake. The time sequence of wind velocity, current profile, divergence, and degree of stability was studied in detail on five particular days during August and September, 1961.

Positive divergence was generally found in the region of the lake studied. Negative divergence occurred only once when the angle between the wind and the 0 to 10 cm current exceeded 90°. A high correlation was found between wind and current velocities, with thermal stratification in the air as an additional factor in the relationship. The Coriolis force also appeared to be an important factor in the modification of current hodographs, in that inertia oscillations occurred under conditions of weakening winds (under about 4 mph).

---

[1] Part of this work was submitted to the University of Wisconsin in partial fulfillment of the requirements for the degree of Master of Science.

List of Contents

9. 1 Introduction

9. 2 Techniques of Measurements
- 9. 2. 1 Equipment and Apparatus
- 9. 2. 2 Procedure for Collecting Data

9. 3 Development of Data

9. 4 Individual Case Studies
- 9. 4. 0 General Remarks
- 9. 4. 1 Day I (17 August)
- 9. 4. 2 Day II (18 August)
- 9. 4. 3 Day III (25 August)
- 9. 4. 4 Day IV (28 August)
- 9. 4. 5 Day V (6 September)
- 9. 4. 6 Summary
- 9. 4. 7 Discussion of Errors

9. 5 Recommendations

9. 6 Acknowledgements

9. 7 References

9. 1 Introduction

The problem of momentum transfer through an air-water interface has for some time been the subject of theoretical work. Ekman (1905) has shown that in a fluid of infinite depth and constant viscosity the hodograph of current velocities under steady state conditions would have the form of a logarithmic spiral. Rossby (1936) has discussed a specialized theoretical equiangular spiral for eddy viscosity decreasing parabolically with depth. Lettau (1962; see Section 8) has developed a more general system of equiangular spirals and expressed the eddy viscosity as a function of the angle between the surface current and the surface stress, and the change with respect to depth of the angle β which is formed by the tangent at the spiral and the radius vector (current vector).

Unfortunately, empirical work on this problem is inconclusive. Shulman and Bryson (1961) have conducted a study of variations of lake currents with depth in Lake Mendota. By employing free-floating drags, they were able to construct vector-averages of currents down to 3m depth, and discussed mean hodographs for various ranges of wind speed. It was felt that the next step was to make case studies of time variations in wind and current velocity. A similar method, also employing free-floating drags, was used. As additional information, simultaneous measurements

of the air temperature and wind profile were made, and wind direction was recorded in detail.

9. 2 Technique of Measurements

9. 2. 1 Equipment and apparatus

A distance meter, designed for this study, consisted of a propeller mounted on a horizontal shaft which, through a 20: 1 worm gear, drove a vertical shaft. These shafts turned on ball bearings which were contained in an oil-filled housing. A cam fixed to the vertical shaft caused one electrical contact per revolution in a 12 V.D.C. counter circuit. The distance meter was mounted about one foot off the side of an outboard motor boat equipped with remote controls. The propeller was about 30 cm below the water surface so that it remained immersed even in rough water. A pitot tube was attached to the distance meter. This made it possible to make all measurements at the same boat speed.

To calibrate the distance meter several runs were made between two points of known distance (approximately one mile). The average of these runs was taken as the true distance. To check the reliability of measurements over distances comparable to those encountered in the actual study, several runs were made between two buoys about 250 m apart. On a calm day the largest deviation from the mean was 0.5%, and, on the roughest water experienced in this study, 1.5%.

A stopwatch with sweep second hand and dial calibrated to 1/5 second was used. Time was estimated to the nearest 1/10 sec. The watch was coordinated with that of the micrometeorological base station. The region in which the current profile and horizontal divergence was obtained was located approximately one mile from the micrometeorological tower; reference is made to Section 2, concerning tower equipment and supporting data.

The free-floating drags were constructed from two pieces of 1/4" waterproof plywood (each 10 cm × 30 cm) in the form of a cross. Ordinary cotton fishing line was used to suspend the drags from small "pencil" floats ("markers") of about 16 cm^2 cross-sectional area. Lead weights of varying sizes were suspended from the drag until about 2/3 of the float was immersed. A 2" × 2" yellow flag was attached to the float to facilitate spotting the drags. Fig. 1 illustrates schematically the equipment.

The three drags used to measure divergence in the 0 to 10 cm layer were matched and tested for similarity on a moderately rough day. When dropped simultaneously in a circle of about one foot diameter, several trials showed that 5 minutes after release the three drags could be found in a circle of about 3 feet in diameter.

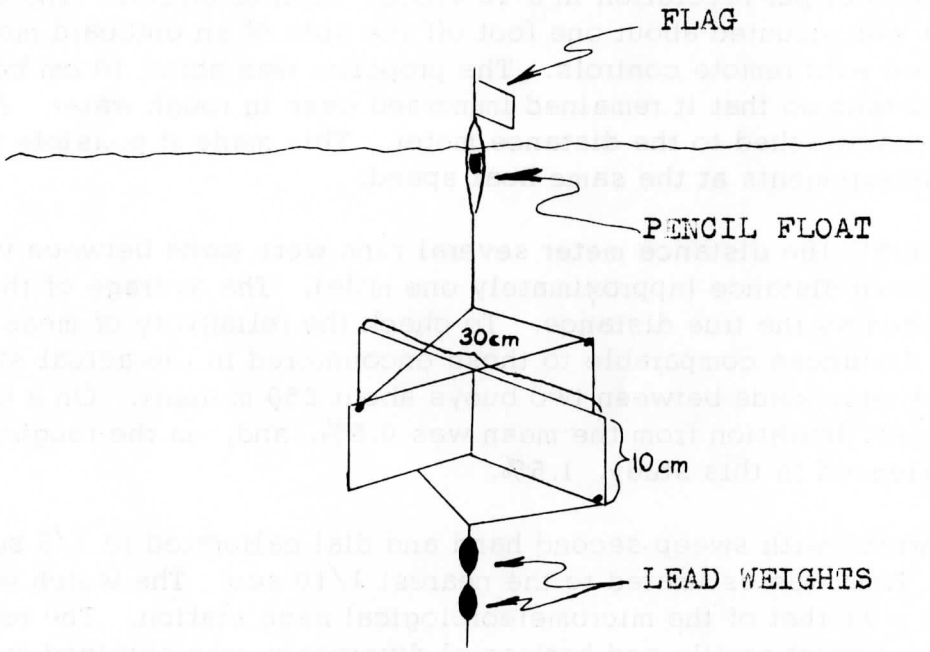

Fig. 1. Free drag, float and marker employed for the measurements of current profiles and divergence in Lake Mendota.

9. 2. 2 Procedure for collecting data

Three buoys, designated I, II, and III, were anchored in the middle of the western basin (of 65' depth) of Lake Mendota. These buoys formed an equilateral triangle with sides of about 100 m. Before a set of measurements the throttle of the boat engine was carefully adjusted with the aid of the pitot tube while traveling perpendicular to the surface current.

Two closed courses, a counterclockwise and clockwise circuit, were now made around the triangle, the time of passing each buoy, and the distance between the buoys, being noted. The 0 to 10 cm drags were dropped during the last circuit, one at each buoy. Immediately after, the additional profile drags were released simultaneously at Buoy I, responding to the current at 20 to 30 cm, 50 to 60, 100 to 110, and 150 to 160 cm depth. For brevity these measurements will be referred to as 5, 25, 55, 105, and 155 cm current measurements employing the mean depth of the drags as index. Alternately, the 0 to 10 cm (or 5 cm) level will be referred to as surface level.

Approximately three minutes later, the first measurement of the sides of the triangle formed by the three surface drags was begun. This was accomplished by a counterclockwise, followed by a clockwise, circuit. The length of each side of the triangle was thus obtained for opposite directions of travel, which is necessary to eliminate drift. Time of passage by each drag was also noted.

The current profile measurement was now begun. The distances between the individual profile drags and buoys were measured in the following sequence: Buoy III to the 5 cm drag; 5 cm drag to Buoy III; 5 cm drag to Buoy I; Buoy I to 5 cm drag; 5 cm drag to 25 cm drag; 25 cm drag to 5 cm drag; 25 cm drag to Buoy I; etc. . . . A final check was made by measuring the distance between the deepest drag and Buoy II, and by making a rough sketch of the relative positions of the various drags and buoys. After the current profile measurements were accomplished (normally, 20 to 25 minutes after the beginning) the sides of the triangle formed by the three surface drags were again measured in the previously described manner.

All drags were now collected and another set of measurements was normally begun. On days when the water was rough, it was found necessary to return to shore after each set of measurements to drain the boat. One set of the above described measurements will be referred to as one "run." A total of 26 runs during five days (4 to 6 runs per individual day) will be discussed in the following sections.

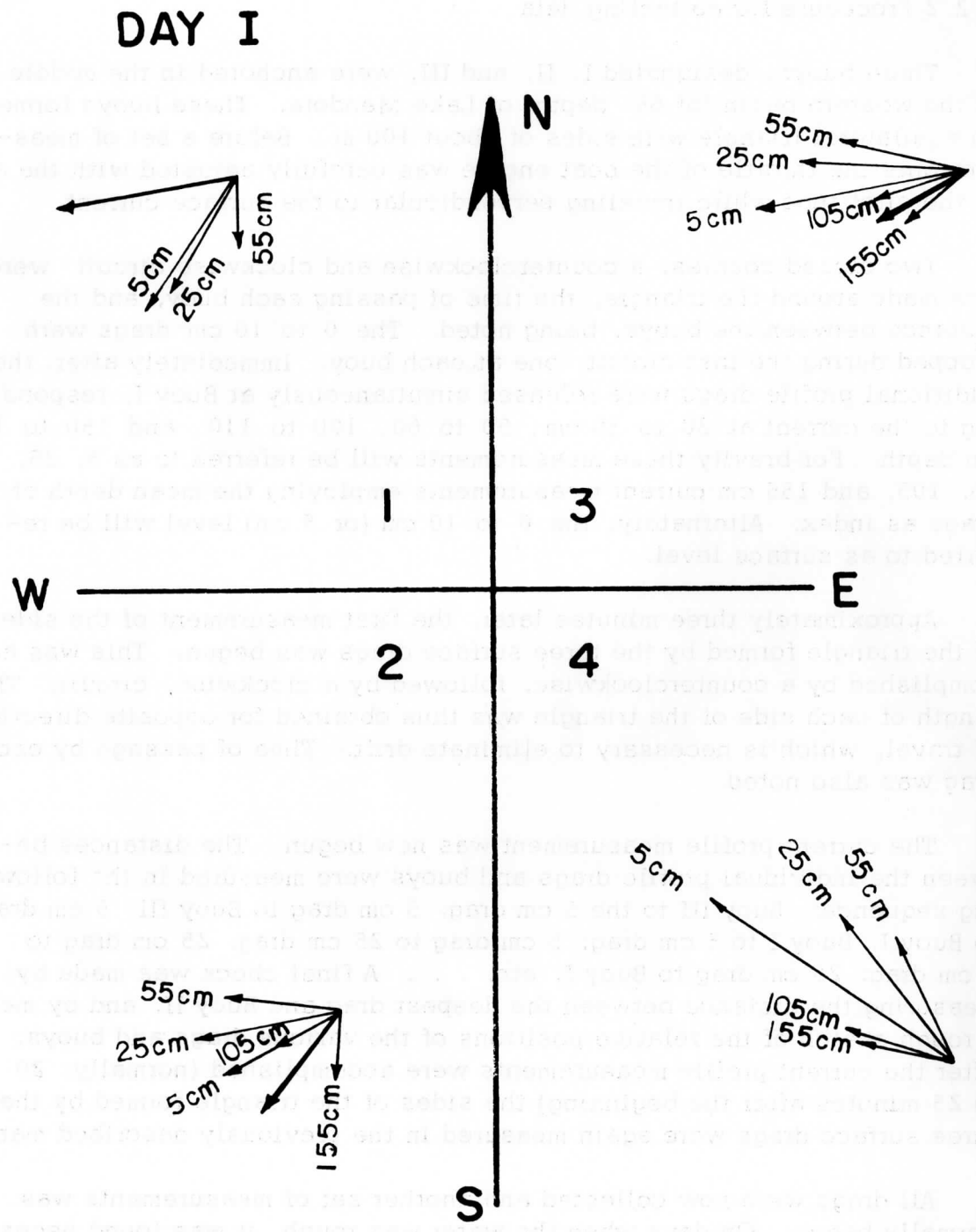

Fig. 2. Individual current hodographs in Lake Mendota on 17 August 1961, run 1 through 4.

9. 3 Development of Data

Graphical methods were employed. All constructions were based on the mean of the two measurements of each distance. For example, the mean of the distances measured between the surface drag and Buoy III, and Buoy III and the surface drag, was considered valid at the mean time (t_1) of the two distance measurements.

The speed of the 5 cm current was considered to be the mean of the speeds calculated from the two measurements between the 5 cm drag and Buoy I. This mean speed, along with the mean distance between Buoy III and the 5 cm drag, was used to determine the position of this drag at time t_1 and, therefore, the direction in which it was traveling.

The velocities of the other drags were calculated in the same manner, and the mean speed was obtained in all cases. The direction of their travel was found graphically using mean separation from the nearest "reference drag." The 5 cm drag served as the "reference drag" for the 25 cm drag, the 25 cm for the 55 cm drag, etc. Once all the directions and speeds were determined, a vector diagram or hodograph was drawn.

The horizontal divergence (D) of the surface currents is given by

$$D = A^{-1} dA/dt \approx \Delta A / \overline{A} \Delta t \quad , \tag{1}$$

where A = area of the triangle formed by the three surface drags, $\overline{A}$ its mean value, and ΔA its change during the time interval Δt. Normally, Δt was close to 25 minutes. The area was calculated using the trigonometric formula

$$A^2 = s \cdot (s - a) \cdot (s - b) \cdot (s - c) \quad , \tag{2}$$

where $s = (a + b + c)/2$ and a, b, c are the lengths of the sides of the triangle. The means of the measurements of a, b, c for clockwise and counterclockwise circuit were used.

9. 4 Individual Case Studies

9. 4. 0 General remarks

Data from five selected days of 1961 was studied in detail. Each of the five days had good supporting data. Moreover they showed individually interesting conditions. Day I (August 17) was chosen as a good example of a calm day. Days II and III (August 18 and 25) had relatively steady state conditions. Day IV (August 28) was characterized by a rapid buildup and recession of wind speed following the passage of a squall

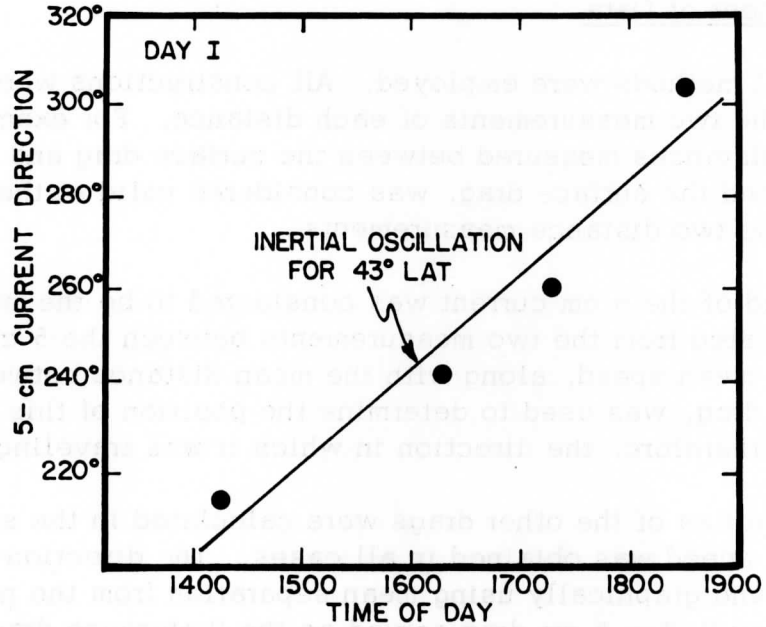

Fig. 3. Direction of 5 cm current (full dots) in Lake Mendota at indicated hour for the four runs on 17 August 1961. Note the systematic veering which is compared with the theoretical rate of rotation for an inertia oscillation at this geographical latitude.

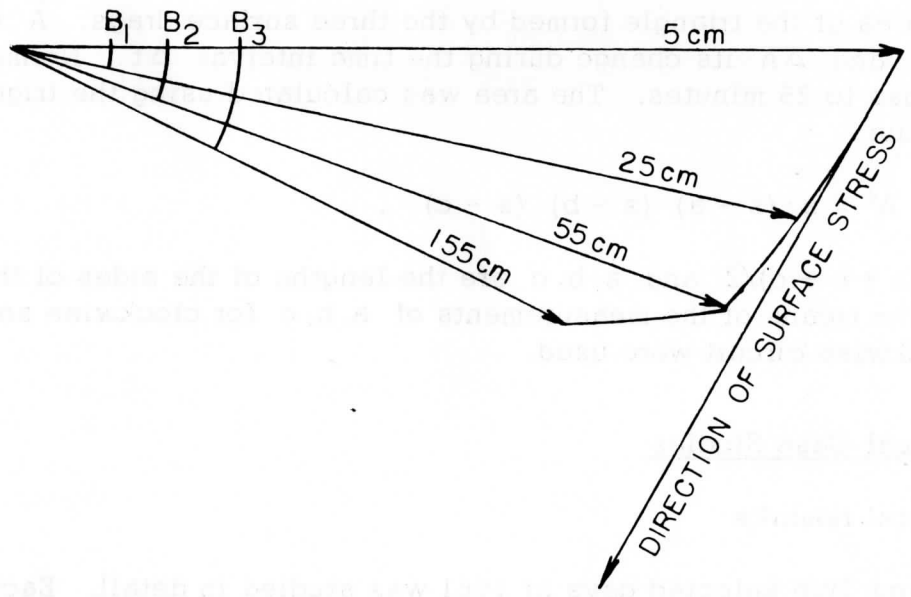

Fig. 5. Vector-mean current hodograph in Lake Mendota on 18 August 1961 (Day II).

line. Day V (September 6) exhibited a gradual buildup and recession of wind velocity in a typical diurnal trend.

The results of the measurements for all five days are summarized in Table 1. Because wind direction is the most important factor in the set-up of lake currents, detailed data covering completely the five observational periods are listed in Table 2. Other supporting data from the micrometeorological tower installation are presented in graphical form, only for those days at which conditions changed in a significant manner. In the individual hodographs the wind vector (at 40 cm height) appears as a bold line and was drawn to the scale 1" = 200 cm/sec. Current vectors are drawn to the scale 1" = 4 cm/sec. For the sake of appearance they are labeled with the average depth (in cm) at which the current measurement was made. For example, the numeral 5 represents to 0 to 10 cm current.

9. 4. 1 Day I (17 August 1961)

On this day (also on the preceding day) the wind was light and variable. The thermal stratification in the air remained stable throughout the period of measurement with the degree of stability gradually increasing as the day progressed. The current speeds were relatively low compared to the other days studied. During the period of measurements the current direction veered at a rate which closely approximated that of an inertial oscillation at this geographic latitude. For detail of results, see Table 1, also Figs. 2 and 3.

In the period between the first and second run the wind direction was quite far to the left of the surface current, while just previous to and during the last run it was to the right of the current; see Fig. 2. As the surface current would be expected to align itself about 20 to 30 deg to the right of the wind, a slowing down in the general trend of rotation in the former case and a speeding up in the latter case could be expected.

The rate of veering — see Fig. 3 — followed rather closely that of an inertial oscillation (i. e., 360° per one-half pendulum day, which is 20.5° per hour, at 43° latitude), especially between the second and third measurements when the wind direction remained roughly at 20 deg to the left of the surface current. In this position the wind would not be expected to affect the rate of oscillation to any appreciable degree.

It is possible that the increase in current velocity during the later part of this day was due to a favorable alignment of wind and current directions. The current velocity during the first run is relatively low compared to the other measurements of this day even though the wind velocity is relatively high. It will be noted, however, that the wind direction is almost

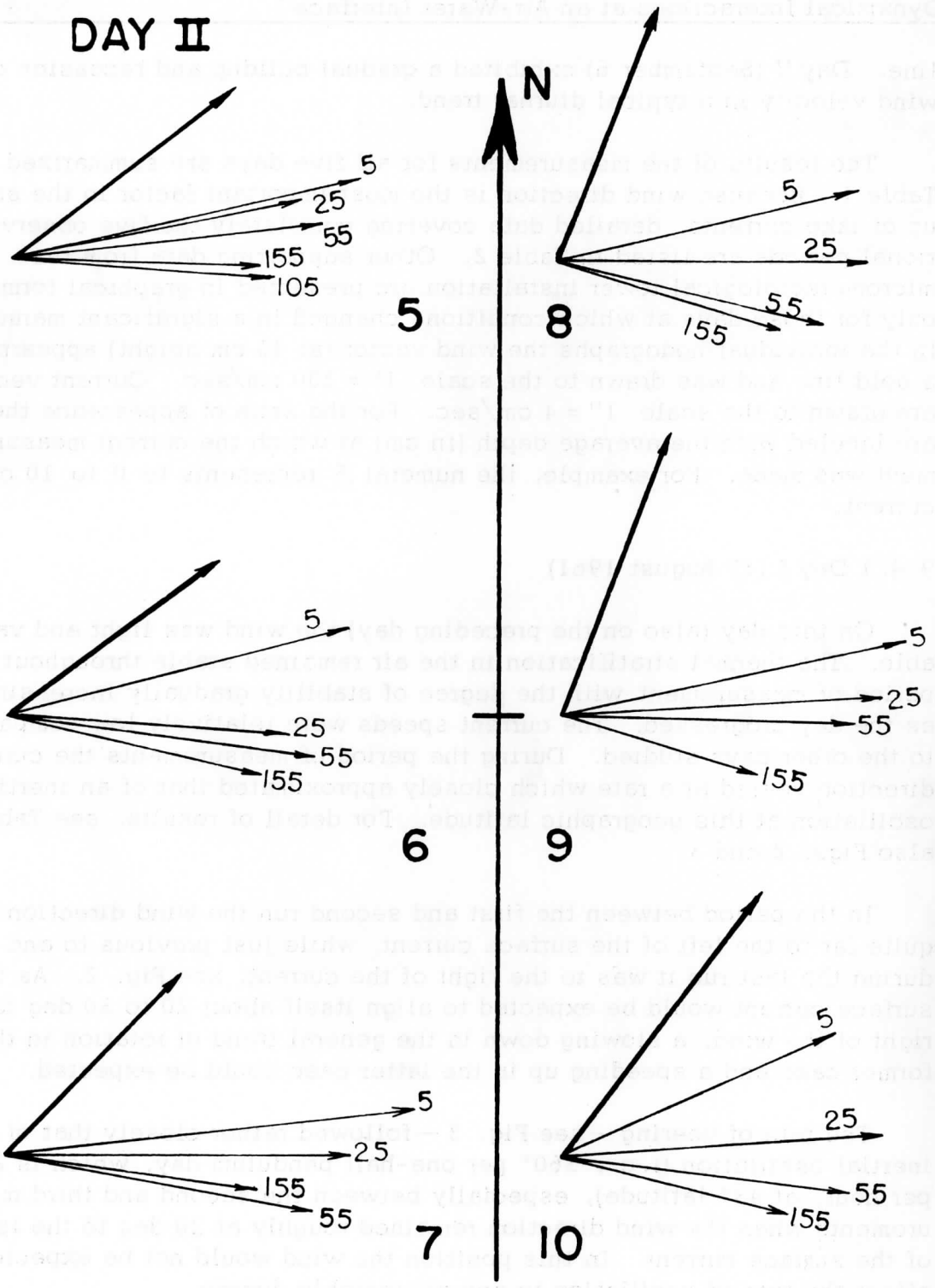

Fig. 4. Individual current hodographs in Lake Mendota on 18 August 1961, run 5 through 10.

90 deg to the right of its "steady state" position in the current hodograph. Hence, the wind would not be expected to contribute significantly to the current velocity during or just previous to this measurement. Later in the day the alignment of wind and current directions appears to cause an acceleration in current speed.

Another noteworthy feature of this day is the average rate of divergence of $3 \times 10^{-4}\,\mathrm{sec}^{-1}$. This is significantly higher than that obtained for the other case studies.

9.4.2 Day II (18 August)

This day showed the closest approximation of steady state conditions. In comparison to the other days, the air was markedly stable. The resulting current velocities also showed little change in direction and speed as the day progressed; see Fig. 4. A slight increase in wind speed occurred during the latter part of the day. The stability also increased during this period and apparently more than compensated for the wind effect on the current velocity, since the current velocity decreases slightly during this period. It is noteworthy that the last three hodographs of this day resemble theoretical spirals derived for steady state condition. In view of these facts this day was selected for a calculation of surface stress. This calculation was made by utilizing the theoretical development of Lettau (1962; see Section 8). The hodograph of the vector average of all the current profiles measured on this day was constructed; see Fig. 5.

In Lettau's theoretical model the eddy diffusivity at the surface, K_0, is given by

$$K_0 = f r_0 / (1 + r_0^2)(\beta_0')^2 \quad , \tag{3}$$

where f is the Coriolis parameter, r_0 the tangent of α_0 which is the angle between the surface current and the surface stress; β is the angle formed by the current at some depth with the surface current, and β_0' the surface value of the change of β with depth. The surface stress τ_0 is given by $\rho K_0 V_0'$ where ρ is the density of water (assumed to equal $1\ \mathrm{g/cm^3}$) and V_0' the rate of change in current speed with respect to depth in the layer nearest to the surface.

From the indicated β values, β_0' was determined as $0.0089/\mathrm{cm}$. The value of α_0 was measured as 61 deg so that r_0 is equal to 1.804. The Coriolis parameter at this latitude is $10^{-4}/\mathrm{sec}$. By using these values K_0 was found to be $0.536\ \mathrm{cm^2/sec}$. The value of V_0' was approximated by the change in speed between the 0 to 10 cm and 20 to 30 cm layers. This shear value was found to be $0.096/\mathrm{sec}$.

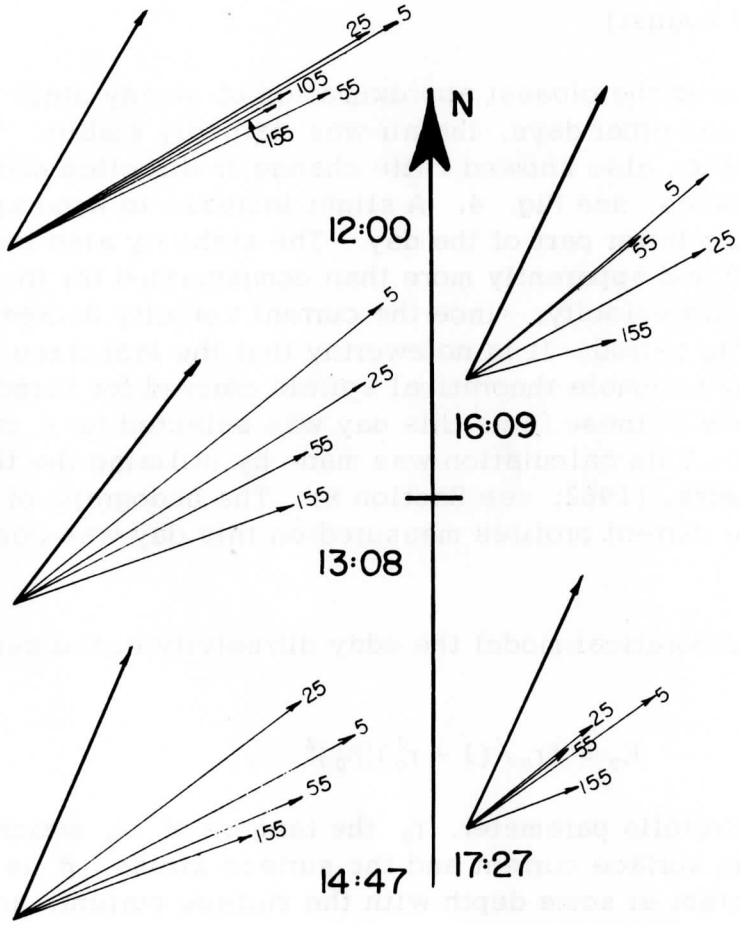

Fig. 6. Individual current hodographs in Lake Mendota on 25 August 1961, run 11 through 15.

The surface stress, τ_0, was then calculated and was found to have a magnitude of 0.051 dynes/cm^2. This average value of surface stress for the periods of measurement on this day is in agreement with values obtained by Shulman and Bryson (1961). Their values were calculated by fitting by eye the Ekman spiral solution to their hodographs.

9. 4. 3 Day III (25 August)

This day is similar to Day II in that wind direction and speed are relatively steady. However, the stability of the air changed gradually from unstable just prior to the taking of measurements to moderately stable late in the afternoon. At no time was the degree of stability of Day II attained. Current speeds, after peaking at about 1300 hours, decreased for the remainder of the afternoon. Apparently, the change in stability was primarily responsible for this decrease. The current direction, however, remained relatively constant throughout the day as would be expected with a strong steady wind; see Fig. 6.

Besides the degree of stability, two other important dissimilarities are apparent between Days II and III. One is the magnitude of wind velocity (recorded at 2 m above the lake surface), which averages about 3.5 m/sec on Day II and 4.75 m/sec on Day III. The other is the contrast between the relatively smooth hodographs of Day II to those of Day III which are quite distorted. It is probable that these two dissimilarities are closely related. Reference is made to Shulman and Bryson (1961), who noted a breakdown in current profiles and called attention to theoretical developments by Munk (1943), Rossby (1936), and Sverdrup (1946). These authors suggest the existence of a critical value of wind velocity in the approximate range of 450 cm/sec to 550 cm/sec. Above this critical value an abrupt increase in the degree of instability of the water currents occurs.

9. 4. 4 Day IV (28 August)

A squall line passage occurred about 1400 hours, after which the wind direction remained relatively constant; see Table 2. The wind speed increased until about 1500 to 1645 hours, after which it decreased rapidly. The stability of the air also showed a rapid increase until about 1440 to 1600 hours, after which it decreased to a degree that instability occurred at about 1700 hours. After this time the air remained slightly unstable for the remainder of the day; see Fig. 7.

A strong correlation apparently exists between wind speed and current speed. However, the angle between the wind direction and the 0 to 10 cm current, while relatively steady during the first part of the day, changes rapidly after about 1745 hours; see Fig. 8. After this time the rate of

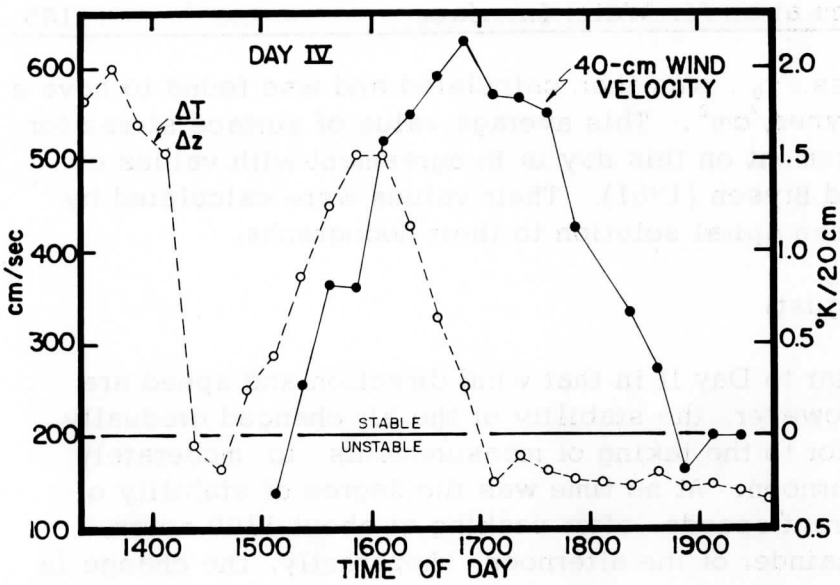

Fig. 7.
15-min averages of windspeed at 40 cm, and temperature difference between air at 20 cm and water; 28 August 1961, for the hours of run 16 to 20.

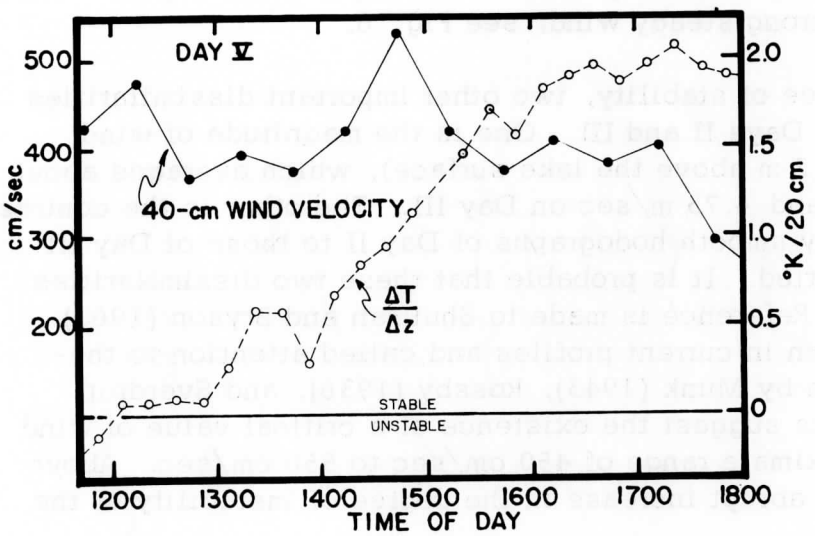

Fig. 9.
30-min averages of windspeed at 40 cm, 15-min averages of temperature difference between air at 20 cm and water; 6 September 1961, for the hours of run 21 to 26.

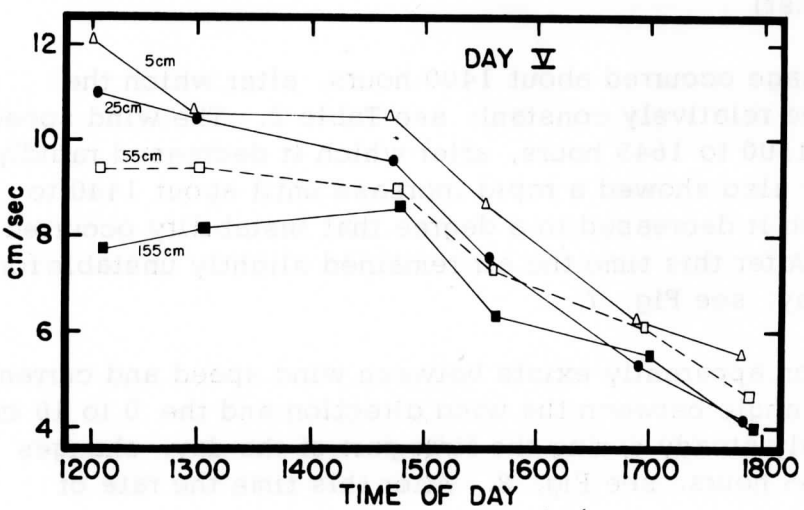

Fig. 10.
Time series of current speeds in Lake Mendota at indicated depth, 6 September 1961, run 21 to 26.

veering of the 0 to 10 cm current is almost three times that of an inertial oscillation at this latitude. This rapid rate of turning might be explained by a gradient flow. It can be expected that a component of the wind stress acting upon the surface will maintain a pressure gradient in the lake. That is, part of the wind stress will cause a slight tilt of the lake surface with water levels increasing downwind. It can be expected that as the wind accelerates, this tilt will increase. If a constant wind velocity is maintained, the lake tilt will remain constant. If a deceleration in wind speed occurs, this tilt will decrease. This will either cause the currents in the upper layers of the lake to slow down or will act to change their direction or, more likely, both. The effect will depend upon the relative directions of gradient currents and initial currents.

It is worthy of mentioning that negative divergence (convergence) was measured only once in this entire study. This single measurement occurred late on Day IV when, also for the only time in this study, the angle between the wind direction and the 0 to 10 cm current exceeded 90°.

It can be seen in Fig. 8 that the first two hodographs on this day are quite similar to theoretical models even though the wind velocity was about 540 cm/sec during the second run. Apparently, the stability of the air was sufficient to prevent a breakdown in the hodographs as was observed on Day III. However, during the last three runs the air is unstable and the hodographs do break down. It is interesting to note that the first two hodographs are not distorted even though a squall line with associated wind shift occurred shortly before the profile measurements. Apparently, recovery in current direction is quite rapid.

9. 4. 5 Day V (6 September)

On this day a continuous backing of the wind direction was observed. The wind speed was relatively high before and during the first run, after which it slowed down slightly only to rise again from about 1400 to 1500 hours. After about 1500 hours, it gradually decelerated throughout the remainder of the day. The air, which had been unstable during the morning, increased in stability from noon till about 1730 hours, after which stability decreased rapidly; see Fig. 9.

The highest current speed recorded on this day was observed during the first run; see Fig. 10. This was apparently due to the instability that existed previous to the measurement along with the relatively high wind speed. The anemometer located on the micrometeorological tower recorded wind speed of about 490 cm/sec from 1100 to 1130 hours and about 450 cm/sec from 1130 to 1145 hours. An increase in wind speed between 1300 and 1445 hours on the 0 to 10 cm current speed was apparently just compensated for by the increase in stability. After 1445 hours the current speed decreased rather steadily.

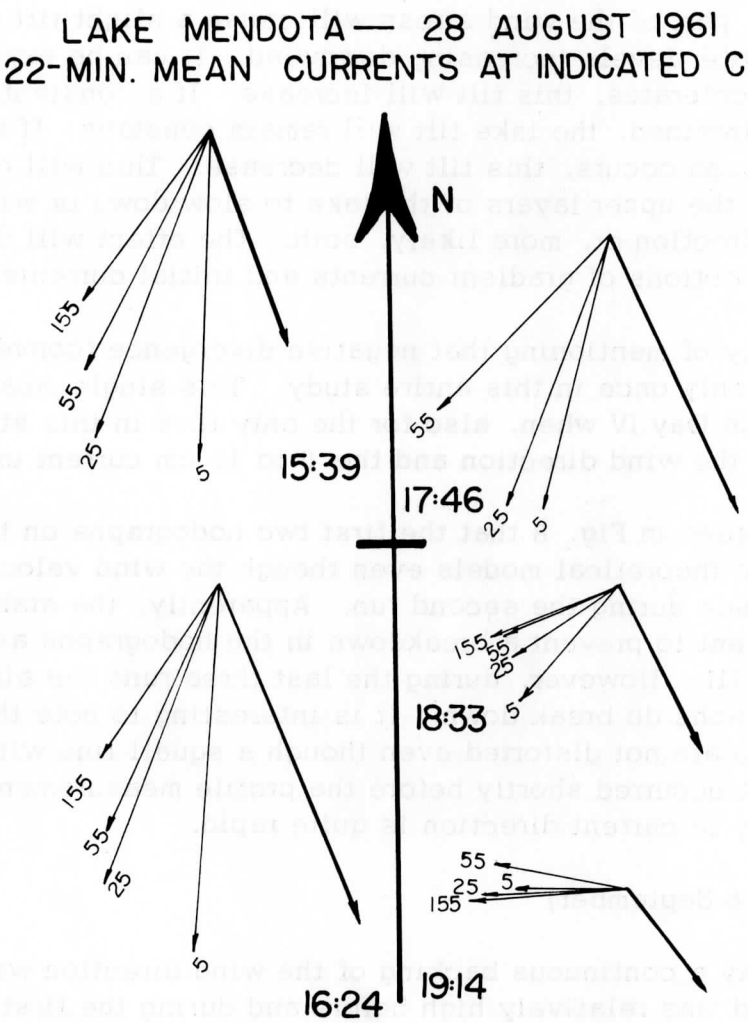

Fig. 8. Individual current hodographs in Lake Mendota on 28 August 1961, run 16 through 20.

The current hodographs were distorted throughout the day even though the wind speed remained below 450 cm/sec after 1500 hours. A slight gradient flow might be responsible for this continued distortion. After the first run, an unusually large angle persists for the remainder of the day between the 0 to 10 cm current and the wind direction. A slight gradient current might also help account for this large angle.

9. 4. 6 Summary

A definite directional shear (turning with depth) of the wind-driven lake currents is apparent. Under relatively steady atmospheric conditions the hodographs seem to take the general shape of theoretical spiral flow. The hodographs apparently become distorted in conditions of rough water and associated instability. A gradient flow may also distort these hodographs.

A good correlation generally exists between the time series of wind and current speed. However, this correlation is affected by variations in the degree of stability. The correlation appears to be completely disrupted when inertia oscillations occur in periods of relative calm.

Divergence was generally positive in the area of the lake studied. However, no correlation was found between divergence and the other variables studied. Negative divergence occurred only once when the angle between the wind direction and the 0 to 10 cm current was greater than 90 degrees.

The 20 to 30 cm, 50 to 60 cm, and 150 to 160 cm currents were calculated as percentages of the 0 to 10 cm current for all sets of measurements with the exception of those taken on Day I. The results of the calculations are as follows: 20 to 30 cm, 89%; 50 to 60 cm, 82%; 150 to 160 cm, 69%, which is in good agreement with the data obtained by Shulman and Bryson (1961). Their percentage values for these same respective currents were 83%, 76%, and 69%.

The theoretical spiral solution of Lettau (1962) was applied to the vector average of the hodographs of Day II. The average wind speed on this day was about 350 cm/sec. The value of surface stress for this day was calculated to be 0.051 dynes/cm.

9. 4. 7 Discussion of errors

Although it is felt that the data are generally reliable, several sources of error do exist. The float and associated flag to which the drag is attached will generally cause a deviation to the left of the true current at any level, because the portion of the float which is above water will

attempt to follow the wind. The major portion of the float will try to follow the surface current. As the surface current is normally faster than the currents at lower levels, this effect can cause error unless the silhouette area of the float is very small in comparison with the drag. It has been noticed by observing particles near the surface that on calm days the uppermost thin layer (approx. 1" deep) of water travels considerably faster than the water below. This layer also moves at an angle of roughly 20 degrees to the left of the layer below it. This could lead, at least on calm days, to certain errors in current measurements.

A non-linearity of the distance meter can also be a source of error in rough water, as the boat alternately accelerates and decelerates when riding over wave crests. The profile and divergence measurements would be less affected than the calculated magnitudes of the current velocity.

Differences may exist in the wind and temperature conditions as recorded at the instrument tower and the conditions that actually existed at the study site. It was felt that these errors would be much less than others which would occur if the study site were near the instrument tower, because the tower is located on an underwater ridge which rises to about ten feet below the surface. This ridge must be expected to disturb the current profile significantly.

Failure to steer the boat on a truly straight course would also be a source of error. However, any errors due to this cause cannot be serious, as evidenced by the small deviations from a mean distance experienced on the calibration runs.

9.5 Recommendations for Further Studies

There was some evidence that lake currents react quite rapidly to changes in wind speed and direction. Rapid changes in stability also appear to have an immediate influence on currents. This can be clarified by faster sampling rates. A sampling rate of the order of once every five minutes should be sufficient for a more detailed study. This rate could not be attained with the equipment and procedure employed in this study. Other methods should be investigated.

One method would be to use three stations with several current meters each. These stations would consist of masts fixed to the lake bottom, each equidistant from the other two. For low velocity currents a meter such as the Stevens Midget current meter with starting velocity of 2 cm/sec, or the Pygmy Price meter are commercially available. In most instances a standard type current meter such as the Price meter used by the U. S. Geological Survey should suffice. These meters would be attached to the

forward ends of vanes which would operate in the same manner as wind vanes, and indicate direction by waterproofed potentiometers.

Such a network of sensors used along with similar supporting equipment to that used in this study would permit a very detailed study to be made. The time sequence of air-water interactions could be recorded on a continuous basis. Changes in divergence and vorticity could also be studied in detail.

9. 6 Acknowledgements

The author expresses his sincere gratitude to Charles P. Stearns of the Department of Meteorology for his unselfish contributions in the way of supporting data, cooperation and general guidance. Without the tower installation and associated recording system, largely developed by him, this experiment would not have been possible.

Sincere thanks also to Dr. Heinz Lettau, Professor of Meteorology, under whose benevolent guidance this paper was written.

9. 7 References

Ekman, V. W. (1905): "On the influence of the earth's rotation on ocean currents," Ark. F. Mat. Ast. och Fysik., Stockholm, 2 (11), 1-52.

Lettau, H. (1962): "Equiangular Wind and Current Spirals" (Unpublished lecture notes); see Section 8.

Munk, W. H. (1943): "A critical wind speed for air-sea boundary processes," J. Mar. Res., 6, 203-218.

Rossby, C. G. (1936): "On the friction force between air and water and on the occurrence of a laminar boundary layer next to the surface of the sea," Pap. Phys. Oceanogr., 4 (3), 1-20.

Shulman, M. D., and R. A. Bryson (1961): "The vertical variation of wind driven currents in Lake Mendota," Limnol. Oceanogr., 6(3), 347-355.

Stearns, Charles R. (1952): "The stress of the wind on Lake Mendota," unpublished master's thesis, University of Wisconsin.

Sverdrup, H. U., M. W. Johnson, and R. H. Fleming (1946): The Oceans. Prentice Hall, New York, pp. 498-498.

Taylor, G. I. (1916): "Skin friction of the wind on the earth's surface," Proc. Roy. Soc., London, A92, 196-199.

Woodcock, A. H. (1944): "A theory of surface water motion deduced from the wind induced motion of the Physalia," J. Mar. Res., 5, 196-205.

Table 1. Results of current and divergence measurements in Lake Mendota, 1961. Included are $\Delta V = |\vec{V}_5 - \vec{V}_{155}|$ = magnitude of vector shear (10^{-2} sec^{-1}); d = wind direction (deg); δ_5 = angle (deg) between wind direction and 5 cm current; D_5 = divergence of 5 cm current (10^{-4} sec^{-1}).

			Current Speeds (cm/sec)								
Run	Date	DST	5 cm	25 cm	55 cm	105 cm	155 cm	ΔV	d	δ_5	D_5
1	8/17	1350-1423	4.00	2.34	1.70	--	--	--	80	-46	3.4
2	8/17	1603-1630	3.18	3.61	2.88	1.75	1.67	1.73	62	1	2.5
3	8/17	1654-1727	5.19	4.14	3.19	2.37	1.99	2.38	40	40	--
4	8/17	1753-1850	7.05	4.51	3.40	2.76	2.45	3.22	145	-21	3.1
5	8/18	1351-1414	8.82	7.25	7.61	--	6.08	2.20	232	25	2.3
6	8/18	1436-1459	8.66	6.90	7.65	--	6.48	2.78	223	32	1.9
7	8/18	1517-1539	10.18	8.58	7.68	--	6.30	2.90	224	39	0.6
8	8/18	1619-1640	7.58	7.62	6.64	--	5.64	2.65	202	55	3.1
9	8/18	1700-1722	8.67	7.90	7.27	--	5.13	3.26	208	50	1.2
10	8/18	1739-1759	7.38	7.97	7.23	--	5.83	3.04	217	29	0.1
11	8/25	1146-1215	14.34	13.44	11.35	--	9.67	3.12	211	29	2.0
12	8/25	1257-1320	15.05	13.28	10.58	--	9.59	4.51	218	14	2.1
13	8/25	1436-1458	12.44	11.44	10.07	--	8.12	3.05	204	38	0.5
14	8/25	1558-1620	9.99	8.66	7.18	--	4.99	3.90	206	24	4.8
15	8/25	1715-1739	7.46	5.32	4.25	--	3.91	2.52	205	30	1.1
16	8/28	1529-1549	10.20	10.18	8.37	--	6.65	4.04	341	22	2.5
17	8/28	1613-1635	11.20	9.73	8.22	--	6.38	4.37	338	27	3.1
18	8/28	1735-1758	8.64	8.98	7.66	--	5.99	2.82	337	38	1.0
19	8/28	1822-1844	4.72	3.78	3.79	--	4.26	1.44	335	69	2.4
20	8/28	1903-1924	3.44	4.45	4.19	--	4.88	-0.75	323	132	-0.2
21	9/6	1158-1223	12.09	11.02	9.40	--	7.74	4.50	257	21	3.2
22	9/6	1252-1314	10.57	10.48	9.42	--	8.15	1.88	249	39	1.9
23	9/6	1435-1457	10.44	9.53	8.96	--	8.60	2.98	244	35	0.5
24	9/6	1525-1550	8.62	7.51	7.26	--	6.32	2.04	229	59	1.1
25	9/6	1646-1705	6.22	5.29	6.10	--	5.52	1.45	231	48	1.6
26	9/6	1741-1801	5.52	4.19	4.65	--	3.97	2.43	222	74	2.1

Table 2. 15-min average of wind direction recorded at Mendota Tower Station. Values in parentheses are 30-min averages; squall line passage at about 2 p. m., 28 September 1961.

CDT	8/17	8/18	8/25	8/28	9/6
1130-1144	---	---	---	---	252
1145-1159	---	---	206	---	264
1200-1214	---	---	217	---	259
1215-1229	---	---	198	---	257
1230-1244	---	---	208	---	259
1245-1259	---	---	216	---	256
1300-1314	---	243	218	---	248
1315-1329	---	222	200	282	243
1330-1344	---	243	204	290	252
1345-1359	---	229	202	269	245
1400-1414	79	221	196	321	245
1415-1429	78	221	201	331	246
1430-1444	85	220	206	332	243
1445-1459	85	227	197	332	245
1500-1514	23	218	188	327	245
1515-1529	---	230	193	331	232
1530-1544	27	212	199	341	222
1545-1559	40	196	214	347	239
1600-1614	34	219	201	337	230
1615-1629	49	210	206	337	229
1630-1644	(47)	209	202	353	219
1645-1659	(47)	214	209	352	232
1700-1714	54	219	206	343	230
1715-1729	74	210	207	353	223
1730-1744	(99)	208	(199)	331	222
1745-1759	(99)	206	(199)	342	221
1800-1814	143	---	198	335	211
1815-1829	---	---	198	335	216
1830-1844	---	---	---	334	---
1845-1859	---	---	---	316	---
1900-1914	---	---	---	320	---
1915-1929	---	---	---	311	---
1930-1944	---	---	---	297	---
1945-1959	---	---	---	291	---

Scanner's note:

This page is blank.

10

Notes on Theoretical Models of Profile Structure in the Diabatic Surface Layer

Heinz H. Lettau

Department of Meteorology
University of Wisconsin

Abstract. The vertical distribution of wind profile curvature in the atmospheric boundary layer for adiabatic and steady-state conditions is discussed. It is shown that the Deacon number of the wind profile decreases gradually with height, from unity at the ground to a minimum value at intermediate levels whereupon it re-curves (increases again) towards the geostrophic wind level. Theoretical models of profile curvature in diabatic surface layers proposed by various authors are summarized, and it is shown that none of them predicts the typical changes in Deacon numbers indicated by observational findings at positive Richardson numbers. It is concluded that this discrepancy cannot be removed by a modification or revision of the mathematical structure of surface layer models, since the reason of the failure seems to be the appearance of momentum-flux divergence, and a significant reduction in surface layer thickness in cases of strong inversion. A synthetic wind profile is used to demonstrate and discuss these effects.

List of Contents

10. 1 General Definitions
10. 2 Deacon Number Distribution in the Adiabatic Boundary Layer
10. 3 Model Assumptions in Terms of Diabatic Influence Function
10. 4 Discussion of a Synthetic Windprofile Derived from Diabatic Surface Layer Theory
10. 5 Conclusions
10. 6 References

10. 1 General Definitions

For steady-state conditions in the adiabatic surface layer above horizontally uniform sections of the earth/air interface, it is generally assumed that the mean horizontal wind speed (V, cm/sec) varies with height (z, cm or m) as expressed by the logarithmic law

$$V_a = k^{-1} V_a^* \log_e (1 + z/z_0) \quad , \tag{1a}$$

where the subscript a refers to adiabatic conditions, z_0 = surface roughness length (cm), k = Karman constant, and $V^* = (\tau_0/\rho)^{1/2}$, with τ_0 = surface stress (dynes/cm^2) and ρ = air density (g/cm^3). With the aid of the geostrophic drag coefficient (C) the wind profile equation (1a) can be reformulated as

$$V_a/V_{go} = k^{-1} C_a \log_e (1 + z/z_0) \quad , \tag{1b}$$

where V_{go} = geostrophic wind speed at the earth/air interface, and $C = V^*/V_{go}$, or, $C_a = V_a^*/V_{go}$. Lettau (1959, 1961) has shown that for adiabatic conditions the geostrophic drag coefficient C_a is a unique-valued function of the surface-Rossby number $\underline{Ro}_0 = V_{go}/z_0 f$ where f = Coriolis parameter. Consequently, given f and V_{go} for a region (either from a synoptic map, or climatology), the fully developed steady-state wind distribution in the surface layer can be predicted for adiabatic conditions when only a representative value of the aerodynamic surface roughness length (z_0) is given for a site, or prescribed for an interface-section of that region.

The purpose of this paper is to investigate the effect of a steady rate of boundary heating (or cooling) on the structure of the mean wind profile in the lower atmosphere. In comparison to adiabatic surface layer conditions, boundary heating is known to produce two interrelated effects. These are: (1) change in profile curvature, and (2) change of average profile steepness (wind gradient, or shear). The mathematically simplest form which illustrates the two effects is the "power law" suggested by Deacon (1953),

$$V = k^{-1} V^* (1 - \beta)^{-1} [(1 + z/z_0)^{1-\beta} - 1] \tag{2a}$$

where β is a height-independent parameter which is larger than unity for surface heating, smaller than unity for surface cooling, while $\beta = 1$ applies to adiabatic conditions. The logarithmic law (1a) is the asymptotic form of the power law (2a) for $1 - \beta$ approaching zero. The two effects mentioned above are evidenced by the fact that the quantity $1 - \beta$ appears twice (i. e., as a factor as well as an exponent) in equation (2a). The numerical parameter β can be separated out by considering the wind-shear

profile obtained by differentiation (denoted by the prime) of equation (2a), with respect to height, in view of $\beta' = 0$,

$$V' \equiv \partial V/\partial z = k^{-1} V^* (z + z_0)^{-\beta} \quad , \tag{2b}$$

and, upon logarithmic differentiation of equation (2b),

$$-\partial \log V' / \partial \log (z + z_0) = \beta = \text{const.} \tag{2c}$$

Actually, the logarithmic curvature of observed wind profiles in diabatic surface layers is not independent of height. This restricts the applicability of Deacon's power law, and it must be classified as an interpolation formula.

During the last decades various authors have proposed expressions for the mean wind profile in diabatic surface layers. A partial list of authors who contributed to this field includes the names of Rossby and Montgomery (1935), Sverdrup (1936), Holzman (1943), Lettau (1949, 1952), Businger (1955, 1959), Monin and Obukhov (1954), Elliott (1957), Ellison (1957), Kao (1959), Priestley (1955), Panofsky, Blackadar, and McVehil (1960), Swinbank (1960), Neumann (1961), and others. The various proposed mathematical forms show a considerable range in analytical complexity, from Deacon's relatively simple power law to modifications of the logarithmic law which culminate in extremely complicated formulas such as those derived by Kao (1959). Because most authors use different starting points it is not easy to compare the results and to judge the relative merits of the various proposed solutions.

To add just another formula to the existing list is not the author's intention. In view of the present state of affairs it was considered more imperative to unify the existing theories, to clarify the common physical basis of the mathematical developments, and to demonstrate their relative value for the problem of predicting diabatic wind profile structure, on the basis of given external conditions.

Consideration of external conditions is an especially important point. It was stated above that a change from adiabatic to diabatic conditions affects not only profile curvature but also the average profile steepness. However, profile steepness is, first of all, dependent on the over-all driving force of air motion, i. e. , the horizontal pressure gradient and the resulting geostrophic speed. Consequently, the singling out of the purely diabatic effects requires the investigation of the ratio V/V_{go}, that is to say, use of equation (1b) rather than equation (1a). As a fairly representative illustration of purely diabatic effects, see Fig. 1, where V/V_{go} is plotted versus the logarithm of height for various degrees of thermal stability, and instability, in the surface layer over prairie country.

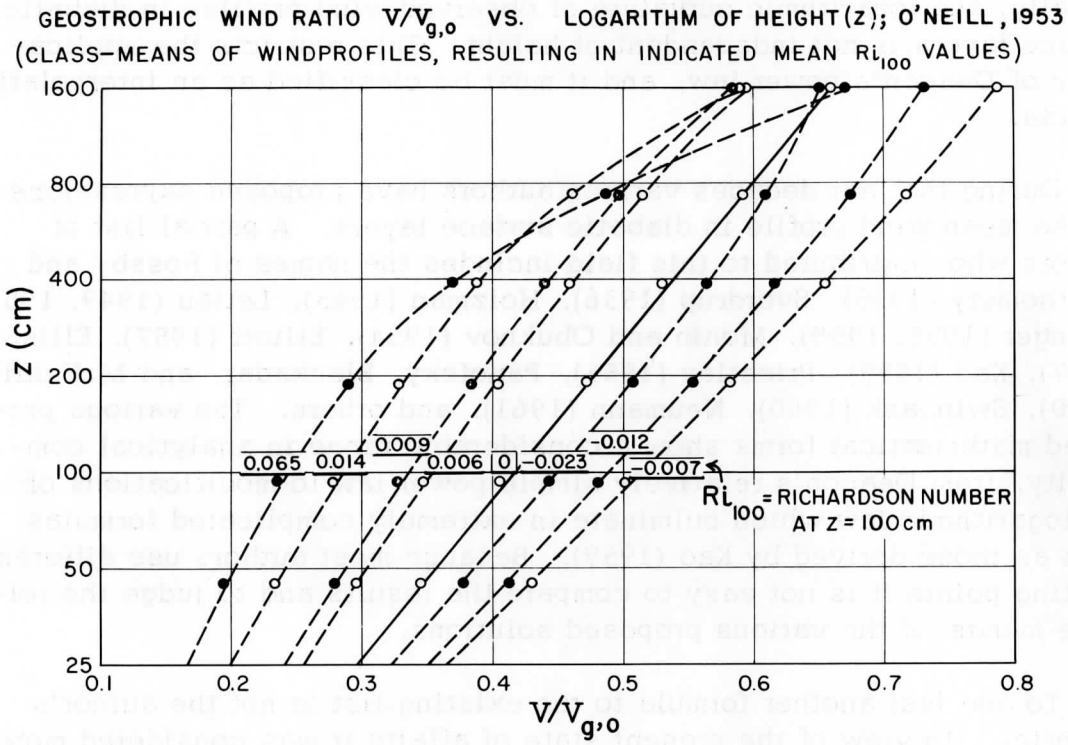

Fig. 1. Wind ratio V/V_{go} versus logarithm of height. Empirical data obtained during the "Great Plains Turbulence Field Program," O'Neill, 1953. The wind profiles are averaged according to classes of bulk-stability resulting in the indicated mean values of Richardson number at z = 100 cm.

It is recognized that a truly satisfactory theory of mean profile structure in diabatic shear flow can ultimately be obtained only as an integral part of a universal turbulence theory which explains also the statistical properties of the details of flow — that is, the eddy spectrum. However, the contributions of eddies of various sizes to the over-all mechanism of mean shear flow are still not clearly understood, even for the homogeneous fluid, or an adiabatic atmosphere. In comparison with the relatively adequate information concerning the structure of mean profiles the accuracy and representativeness of present-day knowledge concerning spectra, as well as fundamental principles of turbulence structure, is still wanting. Therefore, it seems permissible to omit references to eddy structure and to limit the discussion to the representative shape of diabatic profiles of mean wind speed (V) and mean potential temperature (θ, deg K).

Basically, any theory in the physical sciences consists of a set of definitions, one or several model assumptions (postulates), and various conclusions and predictions, or applications, which are logically derived therefrom. A model assumption may be suggested by empirical relationships or it may intuitively be based on a postulated relationship which has not been observed and may not even be directly observable. The conclusions of a theory must be tested, and proved to be in agreement, with independent observations; they must enable us to predict new observable relationships which in turn can be tested by suitably designed new experiments. It is necessary to examine the assumptions and the logical structure of a theory if a model suggested by empirical relationships fails to coincide with reality in another range of external conditions, or if predictions cannot be confirmed. Then, it is necessary to modify the assumptions or correct the logic so that the conclusions do agree with observed facts, at least within defined limitations of model-applicability.

These general statements apply, of course, to the theory of representative mean profile structure in diabatic surface layers of the atmosphere. In this case, it can be stated that the model assumptions are most efficiently formulated in terms of first-order derivatives (i.e., vertical gradients) of mean wind speed and potential temperature. That means that the model assumptions deal with the structure of the height functions V' and θ', where the primes denote differentiation with respect to z (or $z + z_0$). This is related to the fact that the prominent scale factor in diabatic surface layer theory, namely, the Richardson number (Ri) is a combination of these two gradients,

$$\underline{Ri} = (g/T_m)\,\theta'/V'^2 \quad , \qquad (3)$$

where g = gravity (980 cm/sec^2), and T_m = mean Kelvin temperature of the considered air layer.

The testing of model assumptions is most conclusively based on second-order derivatives or profile-curvature characteristics. As such let us define the Deacon numbers of the wind profile (De) and potential temperature profile (DE), in the identities

$$De \equiv -\partial \log V' / \partial \log z = -(z + z_0)V''/V' \quad , \tag{4a}$$

$$DE \equiv -\partial \log \theta' / \partial \log z = -(z + z_0)\theta''/\theta' \quad . \tag{4b}$$

Two special cases of interest are when the Deacon number equals unity, or zero, respectively. The first case indicates a strictly logarithmic, the second a strictly linear profile (as a function of height).

In contrast to β in equation (2c), De and DE in equations (4a, b) are unspecified functions of height. However, concerning dependency on both height and Richardson number, it follows directly and without restrictions from the defining equations (3, 4a, and 4b) that

$$\partial \log Ri / \partial \log z \equiv (z + z_0)Ri'/Ri = 2\,De - DE. \tag{5}$$

Several special cases of equation (5) are of interest; the most prominent of these are included in the following statements. The Richardson number is:

(i) strictly linear in z when $2\,De - DE = 1$,

(ii) independent of height when $2\,De = DE$, and

(iii) inversely proportional to wind shear when $De = DE$.

Case (iii) involves a similarity assumption which is especially important and frequently used. A straightforward and most crucial test of any diabatic surface layer theory is that the model assumption must lead to the same dependency between Ri and De (also, between Ri and DE) as is empirically known to exist, from the analysis of the most reliable and complete micrometeorological data available, regardless of where and by whom they were collected.

Applications of the diabatic surface layer theory employ, predominantly, certain integrated forms such as the profile equations for wind speed and potential temperature, which are obtained from the gradients as

$$V = \int_{z_0}^{z+z_0} V' \, dz \quad , \tag{5a}$$

$$\theta - \theta_0 = \int_{z_0}^{z+z_0} \theta' \, dz \quad . \tag{5b}$$

The prediction of diabatic surface layer structure requires, supplementary to V_{go} and z_0 (and f), the knowledge of boundary fluxes, that is, the ratio τ_{oa}/τ_0 (or C/C_a), and also the rate of surface heating ($\pm Q_0$, ly/min or ly/sec). In addition to equations (5a and b) this requires the investigation of eddy diffusivities for momentum (K, cm^2/sec) and for heat (K_Q, cm^2/sec), which relate the gradients to the flux quantities. The diffusivities are defined by the equations

$$K = \tau/\rho V' \quad , \tag{6a}$$

$$K_Q = -Q/\rho c_p \theta' \quad , \tag{6b}$$

where c_p = specific heat of the air (0.24 cal/g per deg).

It shall be shown that the major problem is to clarify the mathematical nature of what we shall refer to as the diabatic influence function, which expresses the shear ratio V'/V'_a as a function of the Richardson number. Before this is done it will be necessary to investigate the concept of the surface layer as the lowest stratum of the entire atmospheric boundary layer. Basically, this requires an appraisal of how the adiabatic wind profile in the surface layer (specifically, the logarithmic law) ties in with more general solutions of the equation of motion, considering the vector nature of both horizontal air motion and shearing stress in the "spiral" layer, i. e., from the surface layer up to the geostrophic wind level.

10. 2 Deacon Number Distribution in the Adiabatic Boundary Layer

Equations (1a and 1b) refer to scalar wind speed as a function of height. However, due to the action of the Coriolis force it is typical for conditions in the atmospheric boundary layer that the wind direction changes with height. While the surface stress is instrumental in reducing wind speed in comparison with the close-to-geostrophic speed in the free atmosphere, it also causes, in the interaction of frictional and pressure gradient with Coriolis forces, that a component of the horizontal air

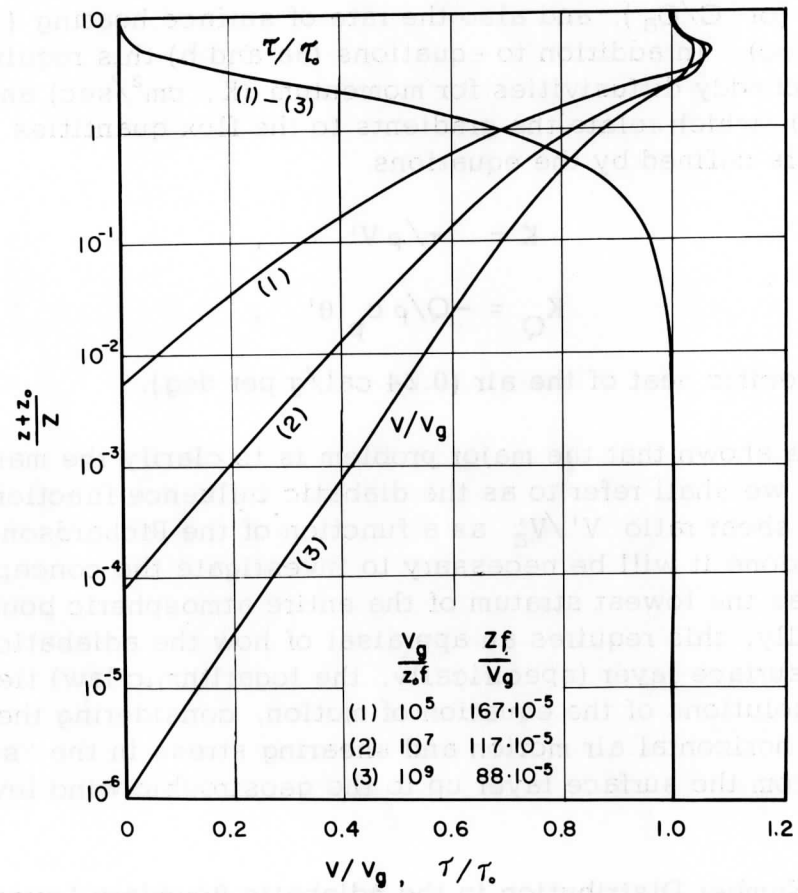

Fig. 2. Theoretical profiles, of wind ratio V/V_{go} and stress ratio τ/τ_0 versus logarithm of relative height, through the entire atmospheric boundary layer in adiabatic states. The numbers at the curves refer to three indicated surface-Rossby numbers and subsequent coefficients for conversion from relative to metric height.

the wind-height Z is defined as the level where the eddy diffusivity has its maximum value and where in the basic solution the cross-isobar flow has its maximum value, too.

motion blows across the isobars toward lower pressure. Thus, the vector of surface stress forms an angle (α_0) with the vector of air motion at the top of the boundary layer, and the wind direction shifts with height so as to align itself with geostrophic conditions in the free atmosphere. This makes it necessary to depict the complete wind distribution in the atmospheric boundary layer in vector form (hodograph), which leads to the concept of a wind spiral. For illustrations of average wind spirals in the atmosphere above the North American continent, reference is made to the study of boundary layer climatology by Johnson (1962; see Section 7 of this report). Conditions in the adiabatic case for a barotropic atmosphere were discussed by Lettau (1961). The author's theoretical model can readily serve to investigate typical height distributions of scalar wind speed for the entire boundary layer.

With the notation introduced by Lettau (1961; pages 151 to 153), i.e., r = absolute value and β = relative azimuth of the dimensionless geostrophic departure, the ratio of scalar wind speed (V) and geostrophic speed ($V_g = V_{go}$) is

$$V/V_{go} = [(r/r_0)^2 - (2r/r_0)\cos(\beta - \beta_0)]^{\frac{1}{2}} , \qquad (7)$$

where r_0 and β_0 denote values at the boundary ($z = 0$). Sample computations can be based on the tabulations given in Lettau (1961; Table 2). Fig. 2 illustrates results for surface-Rossby numbers of 10^5, 10^7, and 10^9. A logarithmic scale of relative height $(z + z_0)/Z$ is used. The conversion of relative to metric heights can be made with the aid of the unit-height coefficient in the equation $Z = C_Z V_{go}/f$. The unit height coefficient as defined by Lettau (1961, Table 4, page 156) is a unique-valued function of the surface-Rossby number, and subsequent values are indicated on Fig. 2. Also illustrated is the height distribution of intensity of shearing stress (τ) relative to ground drag (τ_0). In this relationship the dependency on the external conditions summarized by the value of the surface-Rossby number is so slight that practically the same theoretical curve applies to all three Ro_0 values used on Fig. 2.

It can be seen that for the major portion of the atmospheric boundary layer the V/V_{go} profile deviates significantly from the straight line suggested by the logarithmic law(1b); the latter is only the asymptotic form of the profile for small height. Interestingly, the slope of the V/V_g curves on Fig. 2 first increases with height before it decreases in the final approach to conditions in the free atmosphere. The slight overshoot, or super-geostrophic wind in the upper half of the atmospheric boundary layer is a well-known effect of the Coriolis force. It can also be noted on Fig. 2 that the deviation of τ/τ_0 from unity appears to precede, in height, the deviation of V/V_{go} from a straight line. The reason for this will be discussed below.

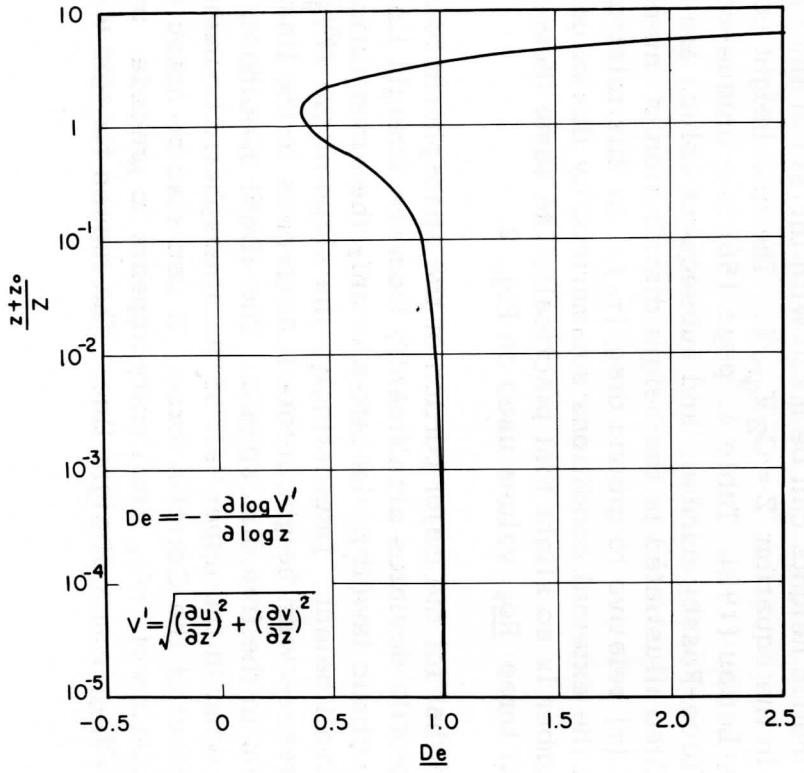

Fig. 3. Universal profile of the Deacon number versus logarithm of height, derived from the theoretical wind spiral solution in an adiabatic boundary layer.

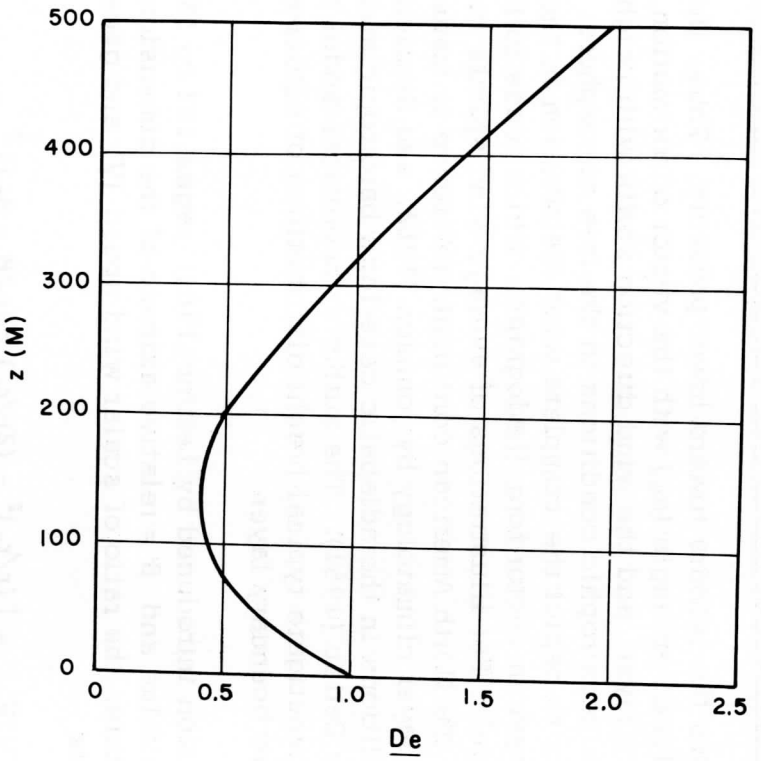

Fig. 4. Theoretical profile of the Deacon number versus metric height, derived from the theoretical wind spiral solution in an adiabatic boundary layer, assuming $Z = 100$ m.

To investigate in detail the curvature of the profile of scalar wind speed in the atmospheric boundary layer, we consider the Deacon number as defined in equation (4a). Using the notation introduced by Lettau (1961; pages 146 to 148), with ℓ = dimensional, and F = non-dimensional Eulerian length-scale of turbulence, ζ = non-dimensional height = $(z + z_0)/Z$, where Z = unit height of the order of 100 m, T = non-dimensional friction velocity (proportional to $(\tau/\rho)^{1/2}$), the defining equation $\ell = (\tau/\rho)^{1/2}/V'$ yields, upon logarithmic differentiation,

$$\underline{De} = d(\log F)/d(\log \zeta) - d(\log T)/d(\log \zeta). \qquad (8)$$

With the aid of the universal spiral solution and the detailed data tabulated by Lettau (1961; Tables 1 and 2), the universal dependency of the wind-profile Deacon number was computed and is summarized in Table 1. This universal result is illustrated in Fig. 3 (using a logarithmic height scale) and in Fig. 4 (using a linear height scale and assuming an average value of Z = 100 m). It can be seen that the Deacon number of the adiabatic wind profile in the entire boundary layer first decreases and reaches a minimum value of 0.40 at a relative altitude of ζ approximately equal to 1.4, which lies close to half-way between the levels of maximum eddy diffusivity (at $\zeta = 1.0$) and maximum length-scale of turbulence (at $\zeta = 2.0$). At higher levels $\underline{De}$ re-curves and becomes large in the approach to the top of the boundary layer.

Especially important is the surprisingly rapid decrease of the Deacon number in the lowest atmosphere. Without exception the previous investigators have assumed that the Deacon number equals unity under adiabatic conditions; any deviation from unity was interpreted as a diabatic effect. The above results show that this is not necessarily the case. This can be important for the discussion of empirical micrometeorological data from an anemometer mast of constant height. Here, one has to be aware of the possibility that, under conditions of low surface-Rossby numbers, the thickness of the atmospheric boundary layer can be greatly reduced so that the top of the anemometer mast may reach into the region where the adiabatic profile structure deviates significantly from the logarithmic law.

The problem is directly related to the concept of the surface layer as the lowest stratum of the atmospheric boundary layer. Estimates of the thickness of the surface layer have been based on the relative momentum divergence, i.e., on a certain tolerably small value of $(\tau_0 - \tau)/\tau_0$; reference can be made to Lettau (1957). This is not a sufficient condition for the validity of the logarithmic law. Namely, a possible non-linearity in the height increase of the length scale of turbulence, also a change of wind direction with height, can be important. It follows from a discussion given by Lettau (1961; Table 6, page 161 and 163) that the effect of

Table 1. Deacon number (De) of scalar wind shear as a function of relative altitude (x, or $\zeta = 2x$), computed with the aid of relative scale of turbulence (F) and relative magnitude of friction velocity (T), based on Lettau's (1961) universal wind spiral solution for an adiabatic atmosphere.

x	ζ	F	T	De
3.2	6.4	0.0706	1.78	3.55
2.8	5.6	.0723	2.69	2.45
2.4	4.8	.0741	3.78	1.75
2.0	4.0	.0761	5.03	1.40
1.6	3.2	.0781	6.44	1.04
1.2	2.4	.0797	8.02	0.68
1.0	2.0	0.0800	8.87	0.51
0.9	1.8	.0799	9.31	0.46
0.8	1.6	.0795	9.83	0.43
0.7	1.4	.0786	10.43	0.40
0.6	1.2	.0771	10.68	0.41
0.5	1.0	.0746	11.14	0.43
0.4	0.8	0.0704	11.64	0.48
0.3	0.6	.0636	12.15	0.56
0.2	0.4	.0521	12.65	0.68
0.1	0.2	.0327	13.16	0.79
0.05	0.1	.0183	13.45	0.93
0.005	0.01	.00199	13.70	0.98
0.0005	0.001	.00020	13.74	1.00

shear-stress gradient seems to be partially compensated by the effect of the height decrease of the rate at which the length scale of turbulence increases away from the surface. This is made evident in equation (8) inasmuch as the first term on the right-hand side is positive (if $\zeta < 1.0$) while the second term is negative.

Some authors have taken a risk in referring to the region of micrometeorological interest as the "constant flux layer." However, the flux divergence (which accompanies any vertical flux originating or terminating at the lower boundary) is normally greater in the immediate vicinity of the interface than at any other level of the atmospheric boundary layer. This is especially true for the steady state flux of horizontal momentum (i. e., the negative shearing stress) in view of the equation of motion. Obviously, speaking of a layer of "constant momentum flux" results in a dilemma. Namely, the equation of motion states that the frictional force τ' (which equals the negative momentum-flux divergence) is not only different from zero, but at its absolute maximum value at the interface (where $V_0 = 0$), and τ' is still relatively large when $\vec{V} << \vec{V}_g$, that is, in the layer in which the above nomenclature would suggest that τ is height-independent and equal to τ_0. The conflict is avoided if we define the surface layer ($0 \leq z \leq h$) as that stratum of the boundary layer where the height-integrated flux divergence, specifically the quantity

$$\int_0^h \tau' \, dz = \tau_h - \tau_0$$

is so small in comparison with the boundary flux (specifically, τ_0) that the ratio $(\tau_0 - \tau_h)/\tau_0$ is within the limits of probable error of the τ_0-determination. The physical implication is that in this lowest substratum of the boundary layer the vertical profiles of air properties are practically completely controlled by the value of the boundary flux. However, the thickness of the surface layer at a given site must depend on conditions, and will also vary from site to site; this applies, with only slight qualification, also to the region in which the logarithmic law, equations (1a and 1b) holds true with sufficient accuracy.

The surface-layer concept can be readily applied to heat transfer (Q, ly/time, with the boundary value of $Q_0 \gtrless 0$). Also, a common surface layer thickness can be defined so that both $(Q_h - Q_0)/Q_0$ and $(\tau_h - \tau_0)/\tau_0$ are absolutely small in comparison to unity. If $\tau = \tau_0$ and $Q = Q_0$ in equations (6a) and (6b), and these equations are used to eliminate θ' and V' in equation (3), the following is obtained,

$$\underline{Ri} = -(gQ_0K)/(T_m c_p K_Q \tau_0 V') \quad . \qquad (9a)$$

It is customary to refer to $K_Q \underline{Ri}/K$ as the "flux Richardson number," which shall be denoted here by $\underline{RI}$. Thus, from equation (9a),

$$K_Q \underline{Ri}/K \equiv \underline{RI} = -(g Q_0)/T_m c_p \tau_0 V' \quad . \tag{9b}$$

Furthermore, it is also customary to define a characteristic length, L, of diabatic surface layer conditions which depends on the boundary fluxes in the following convenient form,

$$L = -\rho T_m c_p (\tau_0/\rho)^{\frac{3}{2}}/k g Q_0 \quad , \tag{9c}$$

so that equation (9b) can be written as

$$\underline{RI} = (\tau_0/\rho)^{\frac{1}{2}}/k L V' \quad . \tag{9d}$$

A non-dimensional independent variable corresponding to z/L was introduced by Lettau (1949). Later, and independently, the length L was employed by Monin and Obukhov (1954).

10.3 Model Assumptions in Terms of Diabatic Influence Function

As was stated in Section 10.1, the basic model assumption deals with wind shear (V') in the lower atmosphere, in the presence of surface heating or cooling, of intensity Q_0 (ly/time). Supplementary to concepts proposed by previous authors, it will also be considered that the flow near the earth/air interface will not be independent of the flow at greater heights. In other words, any diabatic surface layer is still considered as the lowest stratum of a boundary layer in which the wind distribution is governed by geostrophic motion as the ambient flow. In view of this let us define the "diabatic influence function" in the following dimensionless form

$$\varphi = \varphi^* V'/V'_a \quad . \tag{10}$$

As before, V'_a, the wind shear under adiabatic conditions, is assumed to be uniquely determined by the external conditions as given by the set of three values V_{go}, f, and z_0. Making V'_a a reference shear has the practical consequence that the effect of surface heating (or cooling) on actual shear (mean profile steepness) is isolated and expressed by the height-independent parameter φ^* in equation (10). This parameter φ^* must be a function of external conditions involving primarily Q_0, but possibly also V_{go}, f, and z_0.

The diabatic influence function φ in equation (10) is primarily a function of the Richardson number. Since $\underline{Ri}$, for any given Q_0, must be a function of height (excepting the unlikely special case (ii) of equation (5)),

it follows that φ is a function of height. Consequently, equation (10) permits us to interpret φ^* as the value of φ at that level z^* where V' equals V'_a. In other words, at height z^* the diabatic wind profile has the same tangent as the adiabatic wind profile, for a given micrometeorological site. For example, the V/V_{go} profiles illustrated on Fig. 1 suggest z^* values of about 200 to 400 cm for relatively weak lapse as well as relatively strong inversion. This consideration utilizes again the dual effect of a change from adiabatic to diabatic conditions, involving both curvature and mean profile-steepness. Related to this are climatological facts concerning the average diurnal variation of wind speed; there is a level of maximum diurnal amplitude, normally at 2 to 10 m — see Lettau (1949) — and a reversal of phase in the upper portion of the boundary layer; see the summary presented by Haugen and Lettau (1960). Thus, it is evident that empirical information on the value of z^* can be obtained from direct observations, especially V/V_{go}-profiles for a variety of Q_0 values including $Q_0 = 0$ or adiabatic conditions, at a given site.

For a physical interpretation of φ^* we consider that equation (1a) gives

$$k(z + z_0)V'_a = \sqrt{\tau_{oa}/\rho} \quad . \tag{11}$$

The diabatic influence function must approach unity with the approach to the interface. Therefore, for any degree of surface heating or cooling, it follows from equation (10) that

$$\lim_{z \to 0} V' = V'_a / \varphi^* \tag{12}$$

This implies that the definition of the Kármán constant is, in the most general form,

$$k = \lim_{z \to 0} [(\tau/\rho)^{\frac{1}{2}} / (z + z_0)V'] \quad . \tag{13}$$

Since $\tau = \tau_0$ at $z = 0$, it follows from equations (11), (12) and (13) that

$$\tau_0 = \tau_{oa} / \varphi^{*2} \qquad \text{or} \qquad \varphi^* = C_a/C \quad , \tag{14}$$

when the definition of the geostrophic drag coefficient for adiabatic (C_a) and diabatic (C) conditions is recalled; see equation (1b). Equation (14) demonstrates the physical significance of the parameter φ^*. Obviously, the knowledge of φ^* for a given set of external conditions (V_{go}, f, z_0, and Q_0) is the prerequisite for the prediction of ground drag under diabatic conditions. A tentative empirical dependency of C/C_a on bulk stability

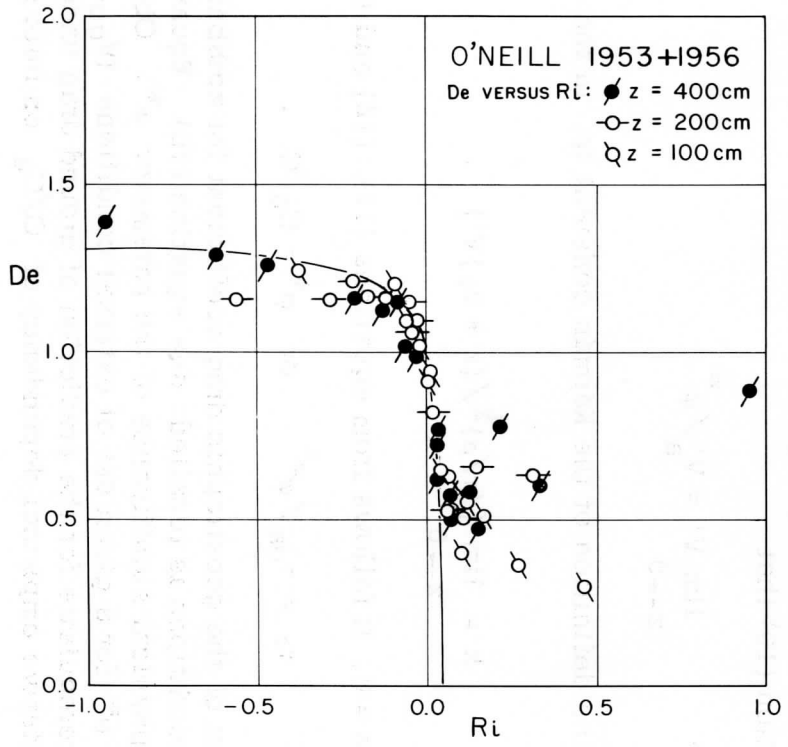

Fig. 5. Empirical relationship between Deacon and Richardson numbers as derived from observations at O'Neill. The indicated curve follows $\underline{De} = (1 - 18\,\underline{Ri})/(1 - 13.5\,\underline{Ri})$.

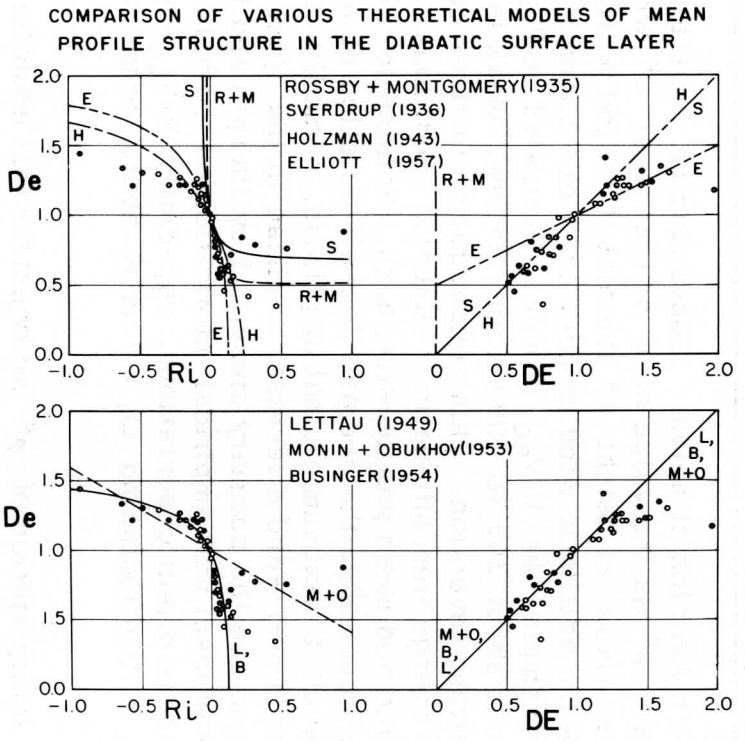

Fig. 6. Comparison of various theoretical models of mean profile structure in the diabatic surface layer. Points refer to observational data at O'Neill.

has been discussed by Lettau (1959); reference is also made to the discussion by Johnson (1962; see Section 7 of this report).

Another consequence of equation (10) can be derived with the aid of equation (4a), which defines the Deacon number of the wind profile. Upon solving equation (10) for V', and logarithmic differentiation,

$$\partial \log \varphi / \partial \log z = 1 - \underline{De} \quad . \tag{15}$$

Recalling equation (5), it follows from equation (15) that

$$\partial \log \varphi / \partial \log \underline{Ri} = (1 - \underline{De}) / (2\,\underline{De} - \underline{DE}) \quad , \tag{16a}$$

or, for the most frequently assumed special case that $\underline{De} = \underline{DE}$,

$$\partial \log \varphi / \partial \log \underline{Ri} = (1 - \underline{De}) / \underline{De} \quad . \tag{16b}$$

Equations (16a, b) are the basis for the conclusion that the diabatic influence function must be a unique-valued function of the Richardson number when the Deacon number is a unique-valued function of $\underline{Ri}$, or vice versa.

Before specifying such functions, $\underline{De}(\underline{Ri})$ and $\varphi(\underline{Ri})$, the general form of the diabatic wind profile equation shall be discussed. Upon solving equation (10) for V' and integrating with respect to height,

$$V = (k\varphi^*)^{-1} \sqrt{\tau_{oa}/\rho} \int_0^z (z + z_0)^{-1} \varphi \, dz \quad , \tag{17a}$$

or, considering the identity $z^{-1}\varphi = z^{-1} + z^{-1}(\varphi - 1)$,

$$V = (k\varphi^*)^{-1} \sqrt{\tau_{oa}/\rho} \, [\log_e(1 + z/z_0) + \Phi] \quad , \tag{17b}$$

where a convenient abbreviation is the identity

$$\Phi \equiv \int_0^z (z + z_0)^{-1} (\varphi - 1) \, dz \quad . \tag{18}$$

Equation (17b) represents the most general form of the diabatic wind profile equation in the surface layer.

If one looks at the great variety of proposed models for diabatic profile structure in the light of the above discussions, it is found that most authorities have used, either explicitly or implicitly, a dependence of the diabatic influence function on Richardson number of the simple mathematical form

$$\varphi = (1 + b\,\underline{Ri})^a \tag{19a}$$

Table 2. Summary of model characteristics for diabatic profile structure in the atmospheric surface layer, based on the same mathematical form for the diabatic influence function, $\varphi = (1 + b\,\underline{Ri})^a$.

Authority	Numerical Constants			Assumption for $\underline{DE}(\underline{De})$	Resulting Dependence $\underline{De} = \underline{De}\,(\underline{Ri})$
	a	b	(ab)		
Rossby & Montgomery (1935)	$\frac{1}{2}$	40	20	$\underline{DE} = 0$	$(1 + 40\,\underline{Ri})/(1 + 80\,\underline{Ri})$
Sverdrup (1936)	$\frac{1}{2}$	11	5.5	$\underline{DE} = \underline{De}$	$(1 + 11\,\underline{Ri})/(1 + 16.5\,\underline{Ri})$
Holzman (1943)	$-\frac{1}{2}$	- 11	5.5	$\underline{DE} = \underline{De}$	$(1 - 11\,\underline{Ri})/(1 - 5.5\,\underline{Ri})$
Monin & Obukhov (1954)	- 1	- 0.6	0.6	$\underline{DE} = \underline{De}$	$1 - 0.6\,\underline{Ri}$
Elliott (1957)	- 1	- 3.5	3.5	$\underline{DE} = 2\underline{De} - 1$	$(1 - 7\,\underline{Ri})/(1 - 3.5\,\underline{Ri})$
Panofsky[1] et al. (1960)	$-\frac{1}{4}$	- 18	4.5	$\underline{DE} = \underline{De}$	$(1 - 18\,\underline{Ri})/(1 - 13.5\,\underline{Ri})$

[1] The same model has been derived previously by Ellison (1957).

Differences in models exist primarily in the numerical values of the two constants, a and b, in equation (19a). The assumptions concerning interrelationship between $\underline{De}$ and $\underline{DE}$ vary slightly, but most frequently $\underline{De} = \underline{DE}$ is used. Logarithmic differentiation of equation (19a) yields

$$\partial \log \varphi / \partial \log \underline{Ri} = a\, b\, \underline{Ri} / (1 + b\, \underline{Ri}) \quad , \tag{19b}$$

or, in combination with equation (16b), after solving for $\underline{De}$,

$$\underline{De} = (1 + b\, \underline{Ri}) / [\, 1 + b(a+1)\, \underline{Ri}] \quad . \tag{20a}$$

If $a \neq -1$, and $|b\, \underline{Ri}|$ is large in comparison to unity, equation (20a) yields

$$\lim_{b\, \underline{Ri} \to \infty} \underline{De} = 1/(a + 1) \quad . \tag{20b}$$

According to Priestley (1955) and others, this limiting value exists and is significant in the approach to conditions of free convection. The Deacon number in the case of free convection equals $4/3$ which yields, in equations (20b), (20a), (19b), and (19a), $a = -1/4$. Thus, one of the numerical constants in equation (19a) is fixed by physical principles. The other appears to be of empirical nature. However, if $-1 < a < 0$, it follows that $-1/b$ is that Ri-value for which $\underline{De} = 0$ in equation (20a). As was discussed in Section 10.1, a zero value of the Deacon number indicates a strictly linear profile. For height-independent shearing stress, a linear wind profile would be a condition for truly laminar flow. However, in atmospheric boundary layers the case $\underline{De} = 0$ is neither necessary nor sufficient for laminar flow. A special physical significance could be attributed to $\underline{De} = 0$ only when this value would be approached asymptotically, which is not true in equation (20a). Therefore, any interpretation of the numerical constant b as corresponding to a "critical" value of Richardson number equal to $-1/b$ is not realistic.

The constant "b" in equation (19a) must be classified as strictly empirical. One method to determine b from observations is to consider that for very small values of $\underline{Ri}$ (very slight deviation from the adiabatic state) equation (20a) reduces to

$$\underline{De} \approx 1 - a\, b\, \underline{Ri} \quad . \tag{20c}$$

Thus, when "a" has been determined independently, the tangent at the curve $\underline{De}$ versus $\underline{Ri}$ at the point $\underline{Ri} = 0$ can be utilized to obtain the empirical constant b. In fact, it will be seen from the summary in Table 2 that comparatively the best agreement between various authorities exists in their estimate of the product $a \cdot b$. Table 2 summarizes also the assumptions made by different authors concerning the interrelationship between

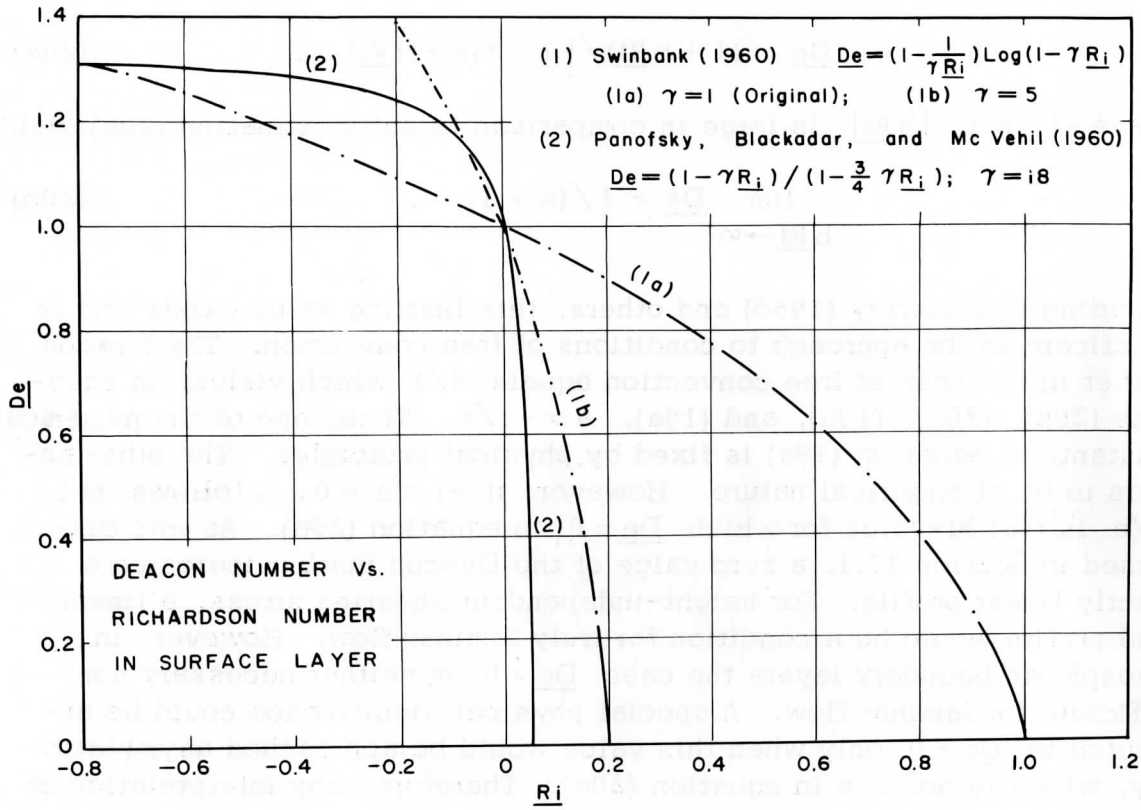

Fig. 7. Theoretical relation De versus Ri after Swinbank (for two indicated values of the constant γ), in comparison with the theoretical relation after Panofsky et al.

$\underline{De}$ and $\underline{DE}$. Reference is made to the discussion in connection with equation (5).

Several of the $\underline{De}(\underline{Ri})$ and $De(\underline{DE})$ relationships summarized in Table 2 are also illustrated and compared with observational data in Fig. 5 and Fig. 6. It is interesting to note that, with $\underline{DE} = \underline{De}$, the special value of $a = -1$ in equation (19a) — which does not produce a limiting $\underline{De}$-value for free convection — leads not only to a linear relationship between $\underline{De}$ and $\underline{Ri}$ (see the Monin-Obukhov model) but produces automatically in equation (18) that Φ is exactly a linear function of height z. Namely, by definition, $\Phi' = (\varphi - 1)/z$; if $\Phi = cz$, then $\Phi' = c$ whereupon $\varphi - 1 = cz$; thus, $\varphi' = c$, whereupon $\partial \log \varphi / \partial \log z = (\varphi - 1)/\varphi = 1 - \underline{De}$, or $\underline{De} = 1/\varphi$. On the other hand, $\underline{DE} = \underline{De}$, and $a = -1$ in equation (20a) and equation (19a), gives $\underline{De} = 1 - b\,\underline{Ri}$, and $\varphi = 1/(1 - b\,\underline{Ri})$; the last two equations necessitate, again, that $\underline{De} = 1/\varphi$ which was found above as a consequence of $\Phi = cz$.

The special case of Φ being a linear function of height (z) in equation (17b) is sometimes referred to as the "log-lin"-law. However, Fig. 5 and Fig. 6 provide sufficient evidence that the subsequent linear relationship between $\underline{De}$ and $\underline{Ri}$ is highly unrealistic. It must be concluded that the "log-lin"-law is, at best, an interpolation formula of severely restricted applicability. The method employed by Monin and Obukhov to test their theoretical model against observations has the great disadvantage, in comparison with plotting $\underline{De}$ versus $\underline{Ri}$, that, in their system of dimensionless parameters, the point of neutral stability is projected into infinity. Consequently they did not concern themselves with near-neutral conditions.

Fig. 6 also illustrates examples of models of diabatic profile structure which are not special cases of equation (19a), reference is made to Lettau (1949, 1952) and a similar model by Businger (1955). Another independent concept underlies the model suggested by Swinbank (1960), see Fig. 7. Swinbank's approach will be briefly outlined since he did not derive the $\underline{De}(\underline{Ri})$ function in his paper. Swinbank introduces a new height-dependent variable (x, having the dimension of length) by the requirement that in diabatic surface layers

$$V = k^{-1}\sqrt{\tau_0/\rho}\,\log_e x/x_0 \quad \text{or} \quad \partial V/\partial x = \sqrt{\tau_0/\rho}\,/kx \quad . \qquad (21)$$

The essential assumption is that

$$\partial V/\partial x = V' + \gamma g\, Q_0/c_p T_m \tau_0 \quad , \qquad (22)$$

where γ is a numerical constant which Swinbank postulated to be equal to unity, but which we prefer to carry along for later specification. Now, from general differentiation rules,

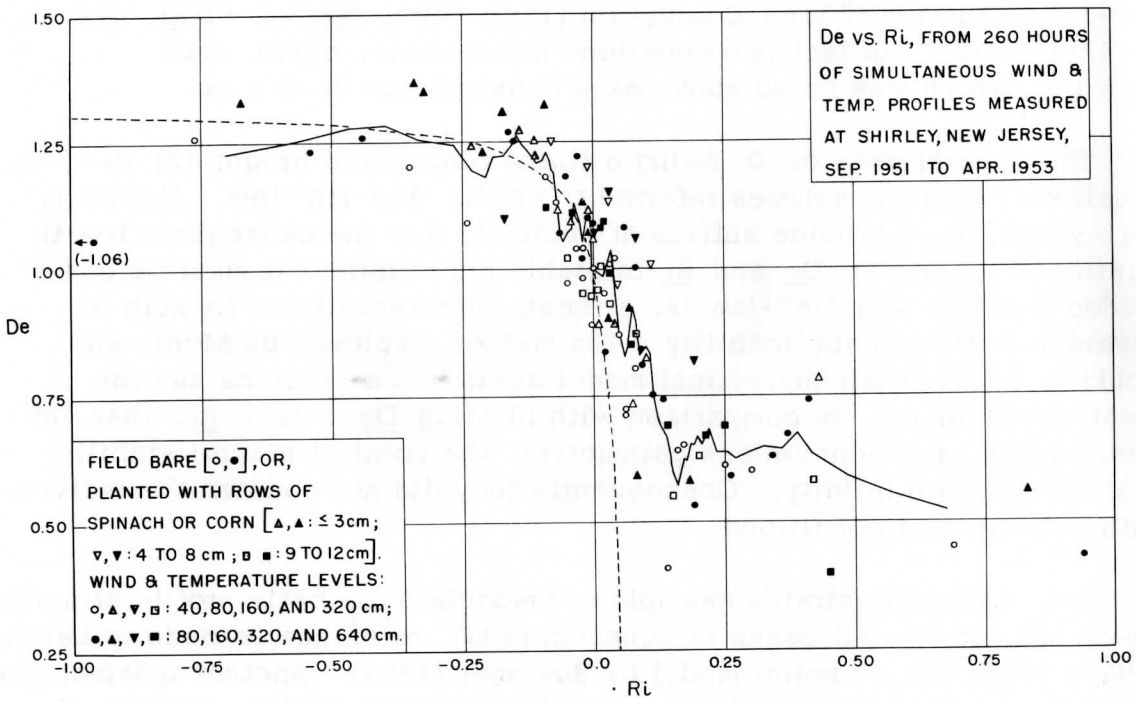

Fig. 8. Observational relationship between Deacon and Richardson numbers, from micrometeorological profile measurements over various surface structures. The full curve is a running-mean relationship, the dashed curve is the theoretical relationship after Panofsky et al.

$$V' = x' \, \partial V/\partial x \quad , \tag{23}$$

so that, after combination of equations (21), (22), and (23),

$$1 = x' - \gamma x/L \; ; \text{ or, integrated, } x = L(e^{y} - 1)/\gamma \, , \tag{24}$$

where y is a convenient abbreviation for $\gamma z/L$ and L is the same as defined in equation (9c). Consequently, the wind profile equation (21) is expressed as a function of height, and

$$V' = \gamma \sqrt{\tau_0/\rho} \, / k L (1 - e^{-y}) \quad , \tag{25}$$

which yields, upon logarithmic differentiation, and considering that $d \log z = d \log y$,

$$\underline{De} = y/(e^{y} - 1) \quad . \tag{26}$$

Now, on the other hand, using equation (9d) in combination with equations (21) and (25),

$$\underline{RI} = \sqrt{\tau_0/\rho} \, / k L V' = (1 - e^{-y})/\gamma \quad . \tag{27}$$

Finally, upon elimination of y with the aid of equations (26) and (27),

$$\underline{De} = (1 - 1/\gamma \, \underline{RI}) \log_e (1 - \gamma \underline{RI}) \quad , \tag{28a}$$

or, for $K = K_Q$, i.e., $\underline{Ri} = \underline{RI}$,

$$\underline{De} = (1 - 1/\gamma \underline{Ri}) \log_e (1 - \gamma \underline{Ri}) \quad . \tag{28b}$$

Equation (28b) is illustrated in Fig. 7 for $\gamma = 1$ (as originally suggested by Swinbank) and also $\gamma = 5$. Neither of these values produces satisfactory agreement with the empirical form of $\underline{De}(\underline{Ri})$ on Fig. 5.

Swinbank, as well as Monin and Obukhov, have claimed satisfactory agreement to exist between theoretical results, derived from their respective models, and observational data. The evidence provided here does little to support these claims. The discrepancy may be explained by the fact that these authors based their comparison on integrated results, or first-order derivatives, which procedure may have averaged out some characteristic detail. This supports the statement made in Section 10.1 that truly conclusive testings of diabatic profile structure can only be based on second-order derivatives such as curvature characteristics and Deacon numbers.

Practically all theoretical models of diabatic profile structure share one important feature. Namely, whenever they produce satisfactory results

Table 3. Theoretical dependence of φ, $\varphi\underline{Ri}$, $\underline{De}$, and Φ on Richardson number $\underline{Ri}$ for the diabatic influence function given as $\varphi = (1 - 18\underline{Ri})^{-1/4}$.

$\underline{Ri}$	φ	$\varphi\underline{Ri}$	$\underline{De}$	Φ
0.0555	5.623	0.312	0.004	3.716
.0554	4.347	.241	.011	2.343
.0553	3.840	.212	.018	1.905
.0552	3.536	.195	.025	1.660
.0551	3.323	.183	.032	1.496
0.055	3.162	0.1739	0.039	1.375
.054	2.445	.1320	.103	.870
.053	2.159	.1144	.162	.859
.052	1.988	.1034	.215	.731
.051	1.869	.0953	.263	.647
0.050	1.778	0.0899	0.308	0.584
.040	1.375	.0550	.609	.308
.030	1.214	.0364	.773	.188
.020	1.118	.0224	.877	.109
.010	1.051	.0105	.948	.049
0.000	1.000	0.0000	1.000	0.000
- .020	.926	- .0185	1.071	- .077
- .040	.873	- .0349	1.117	- .140
- .060	.833	- .0500	1.149	- .192
- .100	.733	- .0773	1.191	- .283
-0.15	0.721	-0.1082	1.223	-0.367
- .20	.683	- .1366	1.243	- .436
- .30	.629	- .1886	1.267	- .552
- .40	.591	- .2364	1.281	- .639
- .50	.562	- .2812	1.290	- .712
-0.60	0.540	-0.324	1.297	-0.775
- .70	.521	- .365	1.301	- .831
- .80	.505	- .404	1.305	- .880
- .90	.491	- .442	1.308	- .926
-1.00	.479	- .479	1.310	- .967

at negative and slightly positive Richardson numbers, they appear unrealistic at larger Richardson numbers — unrealistic in the sense that the empirical data fail to produce Deacon numbers which approach zero. Moreover, the empirical relationship between $\underline{De}$ and $\underline{Ri}$ seems to become erratic at $\underline{Ri}$ larger than approximately 0.1. This behavior is illustrated by the O'Neill data on Fig. 5. In order to show that there is little local effect, especially no significant effect of surface roughness in this relation, empirical $\underline{De}(\underline{Ri})$ values are also illustrated for another location, and for a variety of surface covers, computed from data published by Thornthwaite et al. and obtained at Shirley, New Jersey, 1951 to 1953, and evaluated by the author; see Fig. 8. However, the Shirley data seem to confirm the O'Neill data and we are left with the discrepancy between empirical and theoretical results at positive Richardson numbers. Obviously, along the general philosophy outlined in Section 10.1, we are forced to re-examine the logical structure of all models used. An attempt will be made in the next section to show that this examination must not necessarily lead to a revision of the mathematical form of the diabatic influence function, but will uncover a serious defect, in the customary neglect of ambient flow conditions and decreases in surface layer thickness which accompany any increase of stability.

10.4 Discussion of a Synthetic Windprofile Derived from Diabatic Surface Layer Theory

From the viewpoint outlined at the end of the preceding section it does not appear to matter greatly which of the various theoretical models of diabatic profile structure is selected for investigation. Let us take the model proposed by Ellison, and Panofsky et al. (see Table 2), in which the diabatic influence function is given by

$$\varphi = (1 - 18\,\underline{Ri})^{-\frac{1}{4}} \tag{29}$$

Mr. C. Hutchins of the Meteorology Department of the University of Wisconsin wrote a program (UWMD-020) using 1604 machine language for the computation of function values. The numerical integration to obtain Φ in equation (18) was performed employing the Gill method. Table 3 contains an extract of the tabulation of φ, $\varphi\underline{Ri}$, $\underline{De}$, and Φ which was produced by the "1604" in great detail. Note that the use of equation (29) is restricted to $\underline{Ri} < 1/18$.

The integration method to obtain Φ as a function of $\underline{Ri}$ was as follows. As shall be shown later — see equation (30b) — the product $\varphi\underline{Ri}$ is directly proportional to $(z + z_0)$. Thus, $d \log (z + z_0)$ in the defining equation (18) can be replaced by $d \log \varphi + d \log \underline{Ri}$. Finally, with the proper boundary conditions

$$\Phi = \varphi - 1 - \log_e \varphi + \int_0^{\underline{Ri}} (\varphi - 1)\, d \log_e \underline{Ri} \ ,$$

which was evaluated by the "1604" as a function of $\underline{Ri}$.

The listing of $\varphi \underline{Ri}$ is included to facilitate the practical application of the model. Namely, equations (9d) and (10) yield, after slight rearrangement of terms,

$$\varphi \underline{RI} = \varphi^* (\tau_0/\rho)^{\frac{1}{2}} / k L V'_a \quad . \tag{30a}$$

Thus, $\varphi \underline{RI}$, like $1/V'_a$, is a linear function of height in the surface layer. Let us assume that $K = K_Q$, i. e., $\underline{RI} = \underline{Ri}$. Then, upon expressing L by equation (9c) and consideration of equation (14), equation (30a) yields

$$\varphi \underline{Ri} = -(z + z_0)\, k\, g\, Q_0\, \varphi^{*3} / c_p \rho T_m (\tau_{oa}/\rho)^{\frac{3}{2}} \quad , \tag{30b}$$

which is not only strictly linear in $(z + z_0)$ but also predictable, when in addition to external conditions and boundary fluxes a value of φ^* is known. Note that the ground drag appears as its value under adiabatic conditions, which is related, via the wind-spiral theory, to the geostrophic or ambient speed.

As a concrete example let the external dynamic conditions of the theoretical wind-spiral solution be specified by the following set:

$$f = 1.458 \times 10^{-4}\ \text{sec}^{-1} \quad \text{(extreme or polar value)} \ , \tag{31a}$$

$$z_0 = 0.014\ \text{cm} \quad \text{(typical of an extended snow field)} \ , \tag{31b}$$

and

$$V_{go} = 12\ \text{m/sec} \quad \text{(moderate or normal speed)} \ . \tag{31c}$$

Then, the surface-Rossby number $\underline{Ro_0}$ is 5.9×10^8, or $\log_{10} \underline{Ro_0} = 8.77$. Using the tables prepared by Lettau (1961) it is found that for the deviation of the surface wind from the isobars $\alpha_{oa} = 16.8°$, and geostrophic drag coefficient $C_a = 0.025$, which produces $\sqrt{\tau_0/\rho} = 30$ cm/sec, i. e., $(\tau_{oa}/\rho)^{3/2} = 27 \times 10^3\ \text{cm}^3/\text{sec}^3$. The unit-height coefficient is $C_Z = 90.8 \times 10^{-5}$, which gives $Z = 75$ m, a relatively low value due to the assumed smoothness of the surface; reference concerning the use of Z can also be made to Section 10.2.

Let an additional set of prescribed values specify the thermodynamic conditions,

$$c_p \rho T_m = 0.080 \text{ cal/cm}^3 \text{ (or ly/cm)} , \tag{31d}$$

$$Q_0 = -3 \times 10^{-4} \text{ ly/sec} = -0.018 \text{ ly/min} = -26 \text{ ly/day} , \tag{31e}$$

and $$z^* = 200 \text{ cm} . \tag{31f}$$

This magnitude of surface heat flux Q_0, like the other specified conditions, is roughly corresponding to what may apply to the antarctic snow field in the vicinity of the South Pole; reference can be made to Dalrymple, Lettau and Wollaston (1962). With the above formulations (31a through 31f), all necessary and sufficient requirements for the verification of a theoretical model of diabatic profile structure are completed. The procedure to obtain a synthetic wind profile will now be outlined in successive steps.

Remembering that at $z = z^*$ we have $\varphi = \varphi^*$ and $\underline{Ri} = \underline{Ri}^*$, equation (30b) yields

$$\underline{Ri}^*/\varphi^{*2} = -z^* k g Q_0 / c_p \rho T_m (\tau_{oa}/\rho)^{\frac{3}{2}} = 0.011 , \tag{32a}$$

where the numerical values in formulations (31a to f) are used, z_0 is neglected in comparison with $z^* = 200$ cm, and $k g = 400 \text{ cm/sec}^2$. Note that $\underline{Ri}/\varphi^2$ is a unique-valued function of $\underline{Ri}$, which, in turn, determines uniquely the term $\varphi \underline{Ri}$. A few test computations of $\underline{Ri}/\varphi^2$ with the aid of Table 3, and if necessary, slight interpolations, in view of the result of equation (32a), yielded

$$\underline{Ri}^* = 0.0532 ; \quad (\varphi \underline{Ri})^* = 0.117 ; \text{ and } \varphi^{*2} = 4.80 . \tag{32b}$$

Now, recall that in the surface layer theory $\varphi \underline{Ri}$ is a strictly linear function of height; this yields

$$\varphi \underline{Ri} = z (\varphi \underline{Ri})^* / z^* , \tag{32c}$$

when again z_0 is neglected. Starting from the known values at z^* — see equations (32b) — we obtain $\varphi \underline{Ri}$ at all desired levels z; then, with the aid of Table 3, or by direct calculation, the values of $\underline{Ri}$, $\underline{De}$, and Φ are determined at the same levels.

The next step involves the computation of the diabatic wind profile, equation (17b), for the chosen external conditions, using equation (14) to obtain $\sqrt{\tau_0/\rho}$ as $\sqrt{\tau_{oa}/\rho} / \varphi^* = 30.0/2.19 = 13.7$ cm/sec. Results of the computation are listed in Table 4. and produce the synthetic wind profile $V(z)$. For comparison, the last column of Table 4 contains the corresponding values of the adiabatic wind profile (i.e., V_a, for $Q_0 = 0$), using equation (1b). Even though the assumed rate of surface cooling —

Table 4. Predicted diabatic profile structure in the lowest 8 m above a snow field for surface cooling and other external conditions as specified in the text.

z cm	φ Ri	Ri	De	Φ	$\ln(z/z_0)+\Phi$	V cm/sec	V_a cm/sec
800	.468	.05553	.001	7.50	18.45	631	822
700	.410	.05552	.002	5.50	16.32	559	813
600	.351	.05551	.003	4.20	14.86	507	800
500	.292	.05548	.006	3.20	13.68	460	786
400	.234	.05538	.013	2.22	12.48	426	770
300	.166	.0549	.046	1.28	11.25	385	748
200	.117	.0532	.150	.86	10.46	358	718
100	.058	.0414	.581	.33	9.20	315	666
50	.029	.0250	.830	.15	8.33	285	614

Table 5. Rectangular components of the diabatic wind profile from Table 4; computed values of components, and magnitude, of shearing stress, and distribution of corrected Deacon and Richardson numbers.

z cm	u cm/sec	v cm/sec	τ_x/ρ cm^2/sec^2	τ_y/ρ cm^2/sec^2	τ/ρ cm^2/sec^2	$De^{(c)}$	$Ri^{(c)}$
800	510	372	124	9	124	.26	.084
700	451	329	129	20	130	.18	.080
600	410	298	133	31	137	.14	.076
500	378	274	137	43	143	.13	.073
400	344	251	141	55	151	.11	.069
300	311	220	144	68	159	.13	.065
200	289	211	147	81	168	.20	.058
100	254	186	150	95	177	.61	.044
50	230	167	151	102	182	.83	.026
0	0	0	152	111	188	1.00	.000

see formulation (31e) — is relatively low, a significant reduction in wind-speed can be noticed. With $\varphi^{*2} = 4.8$, the ground drag under these cooling conditions is reduced to 21% of the adiabatic value of approximately 0.9 dynes/cm^2. Curvature and steepness of the diabatic profile conform with the theoretical results derived from the assumed shape of the diabatic influence function, equation (29). The question arises, is the theoretical profile structure realistic?

It may be noted that the synthetic V-profile in Table 4, when directly used for back-computation of Deacon numbers, does not reproduce exactly the theoretical values of $\underline{De}$ but only their general trend. The discrepancy appears to be caused by some systematic error in the machine computation of Φ, which, at the present time, has not yet been resolved. However, this is immaterial for the following discussion.

The major point is that, with the reduction in wind speed due to surface cooling, the geostrophic departure becomes significantly larger than for the adiabatic case. Using numerical integrations of the equation of motion in component form,

$$\tau'_x = -\rho f v \quad ; \quad \text{and} \quad \tau'_y = \rho f (u - V_{go}) \quad ,$$

where $u = V \cos \alpha_0$ and $v = V \sin \alpha_0$, the stress components, and $\tau = (\tau_x^2 + \tau_y^2)^{1/2}$ can be obtained, since the boundary values were known. Table 5 lists computed data for the lowest 8 m over the snow field under the same conditions examined before, but for a deviation angle between surface wind and isobars of $\alpha_0 = 36°$. It will be remembered that for adiabatic conditions — see formulations (31a to c) — $\alpha_{oa} = 16°$. However, the use of any α_0 smaller than about 33° would have caused τ_y to go through zero to negative, at heights below 8 m, which was considered unlikely.

Even for the chosen $\alpha_0 = 36°$, a significant decrease of shearing stress with height exists in the lowest 8 m, much stronger than for the adiabatic case; this is caused by the sizable reduction of ground drag, due to the factor of $1/\varphi^{*2}$. This means that the thickness of the surface layer is greatly reduced. Obviously, this necessitates the addition of a correction term in the actual Deacon number computation, mainly due to $\partial \log \sqrt{\tau/\rho} \,/\, \partial \log z$. Correspondingly, the Richardson number in a modified form of equation (30b) will be affected (increased) by the existing momentum-flux divergence. Estimates of corrected values for $\underline{De}$ and $\underline{Ri}$ as a function of height are listed in the last two columns of Table 5. The important fact results that the corrected $\underline{Ri}^{(c)}$ is not any more limited by a "critical" value, while the corrected $\underline{De}^{(c)}$ decrease with height only to a minimum value significantly above zero, and begin to re-curve and increase with height at higher levels. In principle, this behavior of the

Deacon number corresponds closely to the findings of Dalrymple, Lettau, and Wollaston (1962) in their detailed analysis of the several hundred of hourly wind profiles under strong inversion conditions, observed by Dalrymple in the lowest 8 m layer at the South Pole in 1958.

A similar re-curving of the Deacon number, at somewhat larger heights, occurs also for adiabatic conditions as was discussed in Section 10.2 and illustrated in Fig. 4. In the adiabatic boundary layer, the causes of the re-curving are well understood. For the diabatic case, especially strong inversion, with geostrophic flow conditions remaining unchanged, it is natural to assume that the reduction of ground drag causes a decrease in surface layer thickness. Then, the ambient flow conditions begin to affect the profile structure. This fact has apparently never been considered in a theoretical model. If sometimes it has been stated that the wind profile structure for strong inversion defies description, it can now be said that the physical reason for this statement is not a default of surface layer theory, but the reduction in surface layer thickness, and the subsequently appearing effect of the dynamical interrelationship between flow near the surface and at greater heights, which previously has been neglected.

10.5 Conclusions

The major conclusion is that in a theory of the diabatic wind profile structure near the ground, it is not permissible to ignore the flow conditions at greater heights. For strong inversion the reduction in surface layer thickness of the wind field, due to ground drag decrease and increase in geostrophic departure, produces significant effects in the vertical distribution of Deacon numbers. It is the disregard of this effect in previous models which has occasioned the statement that the wind profile under stable conditions (positive Richardson numbers) seems to defy description. Actually, the condition of re-curving Deacon number profiles corresponds to distributions which exist also in the adiabatic boundary layer at some intermediate levels.

Future work will have to deal with the clarification of several related problems such as the development of models of diabatic profile structure without empirical constants which will necessitate the consideration of turbulence structure concepts, the closer investigation of the dependency of geostrophic drag coefficient on bulk-stability, and the extension of theoretical wind-spiral solutions to include defined diabatic conditions in the entire atmospheric boundary layer.

10. 6 References

Businger, J. A., "On the structure of the atmospheric surface layer," J. Meteor., 12, 553, 1955.

Businger, J. A., "A generalization of the mixing-length concept," J. Meteor., 16, 516, 1959.

Dalrymple, P., H. Lettau, and S. Wollaston, "South Pole micrometeorology program, Part II: Data evaluation," Techn. Report, Quartermaster Res. and Eng. Center, Natick, Mass. (To be published 1962.)

Deacon, E. L., "Vertical profiles of mean wind in the surface layer of the atmosphere," Geophys. Memoirs, No. 91, 1953.

Elliott, W. P., "A comparison of some approaches to the diabatic wind profile," Trans. Amer. Geophys. Union, 38, 21, 1957.

Ellison, T. H., "Turbulent transfer of heat and momentum from an infinite rough plate," J. Fluid Mech., 2, 456, 1957.

Haugen, D. A., and H. Lettau, "Wind," Sec. 1 of Chapter 5 in Handbook of Geophysics, revised edition, The Macmillan Co., New York, 1960.

Holzman, B., "The influence of stability on evaporation," Ann. New York Acad. Sci., 44, 13, 1943.

Kao, S-K., "Transfer of momentum vorticity," "Turbulent transfer in the boundary layer of a stratified fluid," J. Meteor., 16, 497, 1959.

Lettau, H., "Isotropic and non-isotropic turbulence in the atmospheric surface layer," Geophys. Res. Paper No. 1 (GRD, Cambridge, Mass.), 1949.

Lettau, H., "The present position of selected turbulence problems in the atmospheric boundary layer," Geophys. Res. Paper No. 19 (GRD, Cambridge, Mass.), 49, 1952.

Lettau, H., "Summary of non-dimensional characteristics of boundary layer theory," Sec. 7.5 in Exploring the Atmosphere's First Mile, Vol. I, Pergamon Press, New York and London, 1957.

Lettau, H., "Wind profile, surface stress, and geostrophic drag coefficients in the atmospheric surface layer," p. 241 in Advances in Geophysics, Vol. 6, Academic Press, New York and London, 1959.

Lettau, H., "Theoretical wind spirals in the boundary layer of a barotropic atmosphere," Annual Report, Studies of the Three-Dimensional Structure of the Planetary Boundary Layer, Contract DA-36-039-SC-80282 (USEPG, Fort Huachuca, Arizona), University of Wisconsin, 1961.

Monin, A. S., and A. M. Obukhov, "Dimensionless characteristics of turbulence in the surface layer," Akademia Nauk SSSR. Geofis. Trudy, No. 24 (151), 163, 1954.

Neumann, J., "Richardson's number and the Monin-Obukhov wind profile," J. Meteor., 18, 808, 1961.

Panofsky, H., A. K. Blackadar, and G. E. McVehil, "The diabatic wind profile," Quart J. Roy. Meteor. Soc. (London), 86, 390, 1960.

Priestley, C. H. B., "Free and forced convection in the atmosphere near the ground," Quart. J. Roy. Meteor. Soc. (London), 81, 139, 1955.

Rossby, C-G., and R. Montgomery, "The layer of frictional influence in wind and ocean currents," Mass. Inst. Techn., Meteor. Papers, 3, No. 3, 1935.

Sverdrup, H. U., "The eddy conductivity of the air over a smooth snow field," Geofys. Publ., 11, No. 7, 1936.

Swinbank, W. C., "Wind profile in thermally stratified flow," Nature (London), No. 4723, 186, 433, 1960.

INDEX OF DISTRIBUTION

Commanding General
ATTN: Staff Assistance
U. S. Army Ordnance Missile Command
Div, Signal Office (ORDXM-DR)
Redstone Arsenal, Alabama 1

Commanding General
ATTN: ORDXM-RRA
U. S. Army Ordnance Missile Command
Redstone Arsenal, Alabama 1

Director, Meteorology Dept.
University of Arizona
Tucson, Arizona 1

Director, U. S. Water Conservation Lab
Agricultural Research Service
U. S. Dept. of Agriculture
Route 2, Box 816-A
Tempe, Arizona 1

Department of Agricultural Cml and Soils
University of Arizona
Tucson, Arizona 1

Commanding General
ATTN: STEEP-AA
U. S. Army Electronic Proving Ground
Fort Huachuca, Arizona 2

Commanding Officer
Electronics R & D Activity
Fort Huachuca, Arizona 50

Commander
U. S. Navy Electronics Lab
ATTN: Dr. M. Halstead
San Diego 52, California 1

Officer-in-Charge
Meteorological Curriculum
U. S. Naval Post Graduate School
Monterey, California 1

Director, Pacific Southwest Forest & Range Experiment Station
U. S. Department of Agriculture Forest Service
P. O. Box 245
Berkeley 1, California 1

Director, Meteorology Dept.
University of California at Los Angeles
Los Angeles 24, California 1

Director, U. S. Salinity Lab
P. O. Box 672
ATTN: Dr. L. A. Richards
Riverside, California 1

Department of Irrigation
University of California
Davis, California 1

Dept. of Agricultural Engineering
University of California
ATTN: Dr. F. A. Brooks
Davis, California 1

Meteorology Dept.
San Jose State College
San Jose, California 1

Chief, Radio Propagation Lab
U. S. National Bureau of Standards
Boulder, Colorado 1

Librarian, National Center for Atmospheric Research
Boulder, Colorado 1

Dept. of Civil Engineering
Colorado State University
Fort Collins, Colorado 1

Director
ATTN: M. Martinelli, Jr.
Rocky Mountain Forest & Range
Experiment Station
U. S. Department of Agriculture
Forest Service
Room 221, Forestry Building
Colorado State University
Fort Collins, Colorado 1

Director, Meteorology Dept.
Florida State University
Tallahassee, Florida 1

Director, Southern Piedmont Soil
Conservation Field Station
U. S. Dept. of Agriculture
P. O. Box 33
Watkinsville, Georgia 1

Meteorology Dept.
University of Hawaii
Honolulu, Hawaii 1

Commander
USAF Air Weather Service
Scott Air Force Base, Ill. 1

Director, Meteorology Dept.
The University of Chicago
Chicago 37, Illinois 1

Department of Agronomy
Iowa State University
ATTN: Dr. R. H. Shaw
Ames, Iowa 1

Commandant
ATTN: Archives
U. S. Army Command and
General Staff College
Fort Leavenworth, Kansas 1

Commanding General
ATTN: U. S. Army Ballistic
Research Laboratories
Aberdeen Proving Ground
Aberdeen, Maryland 1

Director
U. S. Army Chemical Corps
Opns Research Gp
U. S. Army Chemical Center
Edgewood, Maryland 1

Director, Soil & Water
Conservation Div.
Agricultural Research Service
U. S. Dept. of Agriculture
Beltsville, Maryland 1

Director, Dept. of Civil
Engineering
Johns Hopkins University
Baltimore 18, Maryland 1

U. S. Army Quartermaster
R & E Command
Natick, Massachusetts 1

Director, Geophysical
Research Directorate
ATTN: CRZD
USAF Cambridge Rsch Center
Hanscom Field
Bedford, Massachusetts 2

Executive Secretary
American Meteorological Society
45 Beacon Street
Boston 8, Massachusetts 1

Director, Meteorology Dept.
Massachusetts Institute of
Technology
Cambridge 37, Mass. 1

Dept. of Meteorology
Massachusetts Institute of Technology
Round Hill Field Station
South Dartmouth, Mass. 1

Director, Meteorology Dept.
University of Michigan
Ann Arbor, Michigan 1

University of Minnesota
ATTN: Dean Spilhouse
Minneapolis, Minnesota 1

Commanding Officer
ATTN: Army Mobility Research Center
U. S. Army Corps of Engineers
Vicksburg, Mississippi 1

Director, Meteorology Dept.
St. Louis University
St. Louis, Missouri 1

Dept. of Geophysics
Washington University
St. Louis, Missouri 1

Department of Soils
University of Missouri
Columbia, Missouri 1

Commanding Officer
Army Research Office-Durham
Duke Station
Durham, North Carolina 1

Commanding Officer
U. S. Army Corps of Engineers
Cold Regions Research & Engineering Lab, Box 282
Hanover, New Hampshire 1

USA CRREL CE-Library
P. O. Box 282
Hanover, New Hampshire 1

Commanding General
ATTN: SELRA/SL-ADT
USA Electronics Command
Ft. Monmouth, N. J. 1

Commanding General
ATTN: SELRA/SL-ENC
USA Electronics Command
Ft. Monmouth, N. J. 6

Commanding General
ATTN: SELRA/SL-RE
USA Electronics Command
Ft. Monmouth, N. J. 1

Commanding General
ATTN: SELRA/SL-DP
USA Electronics Command
Ft. Monmouth, N. J. 1

Commanding Officer
ATTN: SELMS-ADJ
USA Electronics Materiel Support Agency
Ft. Monmouth, N. J. 1

Commanding Officer
ATTN: SELMS-PA-1
USA Electronics Materiel Support Agency
Ft. Monmouth, N. J.
(Unclass. only) 1

Commanding Officer
ATTN: Chief, Met Div; Surveillance Dept.
U. S. Army Electronics R & D Agency
Fort Monmouth, N. J. 2

Commandant
ATTN: Weather Br, DST
U. S. Army Signal School
Fort Monmouth, New Jersey 1

Commanding Officer
U. S. Army Electronics
R & D Laboratory
Fort Monmouth, N. J. 1

Commanding Officer
USA Electronics R & D Activity,
White Sands
White Sands, New Mexico 1

Commanding Officer, U. S.
Army Signal Missile Support
Agency
ATTN: Chief, Missile Meteor-
ology Div.
White Sands, New Mexico 2

Commanding General
ATTN: Office of Ordnance
Mission (ORDBS-OM-SS)
White Sands Missile Range
White Sands, New Mexico 1

Director, Meteorology Dept.
Cornell University
Ithaca, New York 1

Director, Meteorology Dept.
New York University
University Heights
New York 53, N. Y. 1

Soil & Water Conservation
Research Division
Agricultural Rsch Service
U. S. Dept. of Agriculture
Cornell University, Bailey Hall
Ithaca, New York 1

President
U. S. Army Artillery Board
Fort Sill, Oklahoma 1

Commandant
ATTN: Metro Div, Target
Acquisition Dept
U. S. Army Artillery &
Missile School
Fort Sill, Oklahoma 1

Atmospheric Science Branch
Scientific Research Institute
Oregon State College
Corvallis, Oregon 1

Director, Meteorology Dept.
Pennsylvania State University
University Station, Pa. 1

Dept. of Oceanography and
Meteorology
The Agricultural and Mechanical
College of Texas
College Station, Texas 1

Electrical Engineering
Research Laboratory
The University of Texas
Austin, Texas 1

Commanding Officer
ATTN: Chief, Meteorology Div
U. S. Army Chemical Corps
Proving Ground
Dugway, Utah 2

Department of Agronomy
Utah State University
ATTN: Dr. S. A. Taylor
Logan, Utah 1

Dept. of Meteorology
University of Utah
Salt Lake City, Utah 1

Commanding General
ATTN: ATSIG
U. S. Continental Army Command
Fort Monroe, Virginia 1

Commanding General
ATTN: ATINT-CID Weather Br.
U. S. Continental Army Command
Fort Monroe, Virginia 2

Commanding General
ATTN: 16th Weather Squadron
U. S. Continental Army Command
USAF Air Weather Service
Fort Monroe, Virginia 1

Commanding Officer
ATTN: Chief, Tech Svcs Div
U. S. Army Transportation
R & E Command
Fort Eustis, Virginia 1

Armed Services Technical
Information Agency
Arlington Hall Station
Arlington 12, Virginia 10

Commander
2d Weather Group
USAF Air Weather Service
Langley Field, Virginia 1

Officer-in-Charge
U. S. Naval Weather
Research Facility
U. S. Naval Air Station
Norfolk, Virginia 1

Chief, U. S. Army SigC
Operations Research Office
The Johns Hopkins University
6935 Arlington Road
Bethesda, Maryland
Washington 25, D. C. 1

Commanding Officer
ATTN: Earth Sciences Division
Department of the Army
Washington 25, D. C. 1

Deputy for Defense Research
& Engineering
ATTN: Geophysical Sciences
Office of the Secretary of Defense
Washington 25, D. C. 1

Chief, Research and Development
ATTN: CRD/M Army Research
Office
Department of the Army
Washington 25, D. C. 5

The Quartermaster General
ATTN: Research Br, R&E Div
Department of the Army
Washington 25, D. C. 1

Chief of Engineers
ATTN: Chief, Engineer R&D Div
Department of the Army
Washington 25, D. C. 1

Commander
U. S. Naval Rsch Laboratory
(Code 7100)
Washington 25, D. C. 1

Director, Atmospheric Sciences
Program
National Science Foundation
Washington 25, D. C. 1

Chief
U. S. Weather Bureau
Washington 25, D. C. 7

Chief
National Aeronautics and Space
Administration
Washington 25, D. C. 1

Director, Federal Aviation Agency
ATTN: Records Officer
Bureau of Research & Development
Washington 25, D. C. 1

Director, National Rsch Council
National Academy of Sciences
2101 Constitution Avenue
Washington 25, D. C. 1

Chief, Fallout Studies Branch
Division of Biology & Medicine
Atomic Energy Commission
Washington 25, D. C. 1

Director, Meteorology Dept.
University of Washington
Seattle, Washington 1

Climatic Center, USAF
ATTN: CCCAD
Air Weather Service (MATS)
Annex 2, 225 D Street, SE
Washington 25, D. C. 1

Director, Meteorology Dept.
University of Wisconsin
Madison, Wisconsin 1

Dept. of Soils
University of Wisconsin
ATTN: Dr. C.B. Tanner
Madison, Wisconsin 1

AD _____ Accession Nr _____

Department of Meteorology, University of Wisconsin, Madison
STUDIES OF THE THREE-DIMENSIONAL STRUCTURE OF THE PLANETARY BOUNDARY LAYER by H. H. Lettau and others.
Final Report (1 July 1959 through 30 September 1962)
Pub. December, 1962, USAEPG Technical Program, DA Project 3A99-27-005.
222 p. incl. illus. tables. Unclassified report.

This report contains a series of nine individual papers presenting the results of continued investigations of the three-dimensional structure of the planetary boundary layer. Special attention is given to the horizontal variations of the boundary exchanges of masses, momentum, and energy (or heat) which are induced by surface characteristics. Work accomplished during three years under the contract has been devoted to four general subtasks: (1) Ground-based instrumentation, (2) Airborne instrumentation, (3) Micrometeorological measurements, and (4) Theoretical work, including data evaluation and analysis.

UNCLASSIFIED

1. Micrometeorology — Energy balance
2. Micrometeorology — Surface roughness
3. Micrometeorology — Instrumentation
4. Turbulent Boundary Layer — Mathematical model

Contract DA-36-039-SC-80282

UNCLASSIFIED

AD _____ Accession Nr _____

Department of Meteorology, University of Wisconsin, Madison
STUDIES OF THE THREE-DIMENSIONAL STRUCTURE OF THE PLANETARY BOUNDARY LAYER by H. H. Lettau and others.
Final Report (1 July 1959 through 30 September 1962)
Pub. December, 1962, USAEPG Technical Program, DA Project 3A99-27-005.
222 p. incl. illus. tables. Unclassified report.

This report contains a series of nine individual papers presenting the results of continued investigations of the three-dimensional structure of the planetary boundary layer. Special attention is given to the horizontal variations of the boundary exchanges of masses, momentum, and energy (or heat) which are induced by surface characteristics. Work accomplished during three years under the contract has been devoted to four general subtasks: (1) Ground-based instrumentation, (2) Airborne instrumentation, (3) Micrometeorological measurements, and (4) Theoretical work, including data evaluation and analysis.

UNCLASSIFIED

1. Micrometeorology — Energy balance
2. Micrometeorology — Surface roughness
3. Micrometeorology — Instrumentation
4. Turbulent Boundary Layer — Mathematical model

Contract DA-36-039-SC-80282

UNCLASSIFIED

AD _____ Accession Nr _____

Department of Meteorology, University of Wisconsin, Madison
STUDIES OF THE THREE-DIMENSIONAL STRUCTURE OF THE PLANETARY BOUNDARY LAYER by H. H. Lettau and others.
Final Report (1 July 1959 through 30 September 1962)
Pub. December, 1962, USAEPG Technical Program, DA Project 3A99-27-005.
222 p. incl. illus. tables. Unclassified report.

This report contains a series of nine individual papers presenting the results of continued investigations of the three-dimensional structure of the planetary boundary layer. Special attention is given to the horizontal variations of the boundary exchanges of masses, momentum, and energy (or heat) which are induced by surface characteristics. Work accomplished during three years under the contract has been devoted to four general subtasks: (1) Ground-based instrumentation, (2) Airborne instrumentation, (3) Micrometeorological measurements, and (4) Theoretical work, including data evaluation and analysis.

UNCLASSIFIED

1. Micrometeorology — Energy balance
2. Micrometeorology — Surface roughness
3. Micrometeorology — Instrumentation
4. Turbulent Boundary Layer — Mathematical model

Contract DA-36-039-SC-80282

UNCLASSIFIED

AD _____ Accession Nr _____

Department of Meteorology, University of Wisconsin, Madison
STUDIES OF THE THREE-DIMENSIONAL STRUCTURE OF THE PLANETARY BOUNDARY LAYER by H. H. Lettau and others.
Final Report (1 July 1959 through 30 September 1962)
Pub. December, 1962, USAEPG Technical Program, DA Project 3A99-27-005.
222 p. incl. illus. tables. Unclassified report.

This report contains a series of nine individual papers presenting the results of continued investigations of the three-dimensional structure of the planetary boundary layer. Special attention is given to the horizontal variations of the boundary exchanges of masses, momentum, and energy (or heat) which are induced by surface characteristics. Work accomplished during three years under the contract has been devoted to four general subtasks: (1) Ground-based instrumentation, (2) Airborne instrumentation, (3) Micrometeorological measurements, and (4) Theoretical work, including data evaluation and analysis.

UNCLASSIFIED

1. Micrometeorology — Energy balance
2. Micrometeorology — Surface roughness
3. Micrometeorology — Instrumentation
4. Turbulent Boundary Layer — Mathematical model

Contract DA-36-039-SC-80282

UNCLASSIFIED